2021

Straining the flatland: novel physics from strain engineering of atomically thin graphene and molybdenum disulfide

BOSTON UNIVERSITY

COLLEGE OF ENGINEERING

Dissertation

STRAINING THE FLATLAND: NOVEL PHYSICS FROM STRAIN ENGINEERING OF ATOMICALLY THIN GRAPHENE AND MOLYBDENUM DISULFIDE

by

MOUNIKA VUTUKURU

B.S., Boston University, 2015
M.S., Boston University, 2018

Submitted in partial fulfillment of the

requirements for the degree of

Doctor of Philosophy

2021

Approved by

First Reader

Anna K. Swan, PhD
Associate Professor of Electrical and Computer Engineering
Associate Professor of Physics
Associate Professor of Materials Science and Engineering

Second Reader

David J. Bishop, PhD
Professor of Electrical and Computer Engineering
Professor of Physics
Professor and Division Head of Materials Science
and Engineering
Professor of Mechanical Engineering
Professor and Biomedical Engineering

Third Reader

Roberto Paiella, PhD
Professor of Electrical and Computer Engineering
Professor of Materials Science and Engineering

Fourth Reader

Xi Ling, PhD
Assistant Professor of Chemistry
Assistant Professor of Materials Science and Engineering

The Road goes ever on and on,
Down from the door where it began.
Now far ahead the Road has gone,
And I must follow, if I can,
Pursuing it with eager feet,
Until it joins some larger way,
Where many paths and errands meet.
And whither then? I cannot say.

- Bilbo Baggins
"A Long-expected Party,"
Lord of the Rings: The Fellowship of the Ring

అమ్మ కోసం
For my mother.

Acknowledgments

If there's one thing you can learn from my thesis, it's that materials are only as strong as their bonds allow them to be. I'm no different: my strength comes entirely from the bonds I have with these extraordinary people.

To Anna: Thank you for your unwavering support for all my endeavors, within the lab and without. I know I haven't been the ideal PhD student, and, at times, I was difficult to work with. Thank you for your patience with me. You ask me each year to help with the ECE Open House, and I always say yes. I do like meeting new people and all that, but mostly, I want to make sure I share some advice that mattered the most to me throughout my time as a graduate student: choose the right advisor for you. For me, having you as my advisor, my mentor, my *friend*, is really what made this whole thing worthwhile. Thank you for teaching me what it is to be a good scientist, educator, and ally. I so look forward to sharing all my success with you down the road.

To Prof. Bishop: I (quite literally) wouldn't be here if wasn't for you. When I received an email from you and Anna in my senior year asking if I'd considered graduate school, I didn't think I'd fit in well. But you've always acknowledged my ideas and work, and made me feel welcome as a scientist. It's been a pleasure working with you and your group. Thank you for seeing potential in me, I hope I have lived up to your expectations and faith.

To all my colleagues, comrades-in-arms: You've all been an absolute pleasure to work with. Hossein, I'm grateful for our discussions on the science as well as the frustrations of 2D materials. Your part in this work has been substantial, coming in at the 11th hour for both of us. Jason, thank you for being a great mentor in the lab for me. I learned a lot from you, and I'm grateful for your guidance in the formative years of grad school. Marco, thank

you for being an incredibly patient colleague and friend! There's been many rough patches over the years. But in the face of it all, you've always been encouraging, steadfast, willing to lend a hand. These are admirable skills in a PhD student, and you are an exceptionally talented one. I'm glad to leave the lab I've called home for the past six years in your safe hands. May the road rise up to meet you in all your endeavors.

To Kara and Zhanna: Thank you for all the times you helped me turn off my overactive brain and be a normal person again. You guys have been my rock these past few years. I love you guys for checking in on me, dragging me out of the lab when I needed to pause, and keeping me sane. There's so many adventures to look forward, and I look forward to sharing them with you.

To Pudu and Bhavna: Your friendship has meant the world to me, and all the miles between us pale in comparison. I've seen you both so little these past few years, and I know I've missed some important things. But to me, it feels like we've not really missed a day since 9th grade guitar lessons after school. I love you guys; thank you for being such a constant source of love and support for me. I'm so excited for the future, for all of us.

To my grandmother, Vani, and my uncle, Srinivas: You helped me move in to BU, nearly 10 years ago. You told me to be careful and to study well, and I promised I would. Here I am! I so wish you could be here to see me right now, to cheer me on. I know you would be proud.

To Giri mama, Sudha atta, Jyostna atta, my cousins Sindhu, Sailu, Karthik, and Samhitha: You've always been the first to wish me success and make sure I was happy. I know I'll never want for anything with family like you. Thank you for your love!

To Leela, Thammu, Pippin, my dancing electrons. I love you all so much, and I thought of you guys a lot when I was alone in the lab at 2 a.m. Pandemic or not, this past year I spent at home with you guys has been the happiest of my 6 years. We got to do so much, and I got to really be present in the family again; not just as a Facetime picture. I'm so

excited for all the amazing things you will do, and I'm looking forward to being present for all these moments from now on.

Finally, to Amma, the strongest person I know. I love you so much. You've taught me to be brave, to be kind, to work hard, and to never lower my voice. You've faced so many hardships to bring me here. I owe everything I accomplish to you, Amma. Every time I look at the letters "Dr." in front of my name, I'll think of you, and all the love that you give me to propel me forward. I dedicate this work to you.

In my mother tongue, Telugu, saying "thank you" is somewhat of an ordeal. There's no good way to say "thank you for everything" without coming off as very stiff and formal. We're not too great at expressing this emotion, it would seem, and we definitely feel awkward expressing thanks to friends and family. But even though it is extremely formal, one translation of "Thank you" is the word "Dhanyavaadam." Etymologically, it literally means "I am blessed." In acknowledging all of these bonds, I will use it here, as it could not be more apt.

Dhanyavaadalu,
Mounika

STRAINING THE FLATLAND: NOVEL PHYSICS FROM STRAIN ENGINEERING OF ATOMICALLY THIN GRAPHENE AND MOLYBDENUM DISULFIDE

MOUNIKA VUTUKURU

Boston University, College of Engineering, 2021

Major Professor: Anna K. Swan, PhD
Professor of Electrical and Computer Engineering
Professor of Physics
Professor of Materials Science and Engineering

ABSTRACT

2D materials like graphene and MoS_2 are atomically thin, extremely strong and flexible, making them attractive for integration into strain engineered devices. Strain on these materials can change physical properties, as well as induce exotic physics, not typically seen in solid-state systems. Here, I probe the novel physics arising from distorted lattices of 2D materials, strained by nanopillars indentation and microelectromechanical systems (MEMS), using Raman and photoluminescence (PL) spectroscopy. From nanopillars strained multilayer MoS_2, I observe exciton and charge carrier funneling due to strain, inducing dissociation of excitons in to free electron-hole pairs in the indirect material. Using MEMS devices, I dynamically strain monolayer and multilayer graphene. Multilayer graphene under MEMS strain showed signatures of loss in Bernal stacking due to shear of the individual layers, indicating that MEMS can be used to tune the layer commensuration with tensile strain. From these methods and results, I further explore applications of strain on 2D materials such as electron-hole plasma formation, optimized pseudo-magnetic fields (PMFs)

generated in monolayer graphene strained by MEMS, using machine learning, and even straining of low-dimensional materials.

Nanopillars provide non-uniform, centrally biaxial strain to multilayer MoS_2 transferred on top. Raman E^1_{2g} and PL red-shift across the pillar confirms 1-2% strain in the material. I also observe a softening in the A_{1g} Raman mode and an enhancement in the overall PL with an increase in radiative trions, under strain. The changes in these charge-dependent features indicates funneling of charge carriers and neutral excitons to the apex of the pillar, as strain locally deforms the band structure of the conduction and valence bands. DFT calculations of the band structure in bilayer MoS_2 under biaxial strain shows the conduction band is lowered, further increasing the indirectness of multilayer MoS_2. This should cause the PL intensity to decrease, whereas experiments show a dramatic increase in MoS_2 PL intensity under strain. I theorize that this is due to a dissociation of excitons into free electron-hole pairs. The increase in charge carrier and exciton densities due to strain leads to a renormalization of the local band structure and increased dielectric screening, which supports free electron-hole recombination at the K-point without momentum restrictions. In turn, increased recombination induces high intensity PL, which opens attractive opportunities for utilization in optoelectronic devices.

MEMS chevron actuators can dynamically strain 2D materials, which I demonstrate through uniaxial strain in CVD and exfoliated graphene. I use a novel microstructure assisted transfer technique which can deterministically place materials on non-planar surfaces like MEMS devices. Building on previously reported 1.3% in monolayer MoS2 from our group, I report tunable 0.3% strain in CVD monolayer graphene and 1.2% strain in multilayer exfoliated graphene using MEMS chevron actuators, detected by Raman spectroscopy. The asymmetric-to-symmetric strain evolution of the 2D phonon line shape in multilayer graphene is evidence of changes in interlayer interactions, caused by shearing between layers. This demonstrates that MEMS can be used to tune the commensuration in

few layer 2D materials, which is a promising avenue towards Moiré engineering.

These methods and results open a host of opportunities for application of strain engineered 2D materials in novel devices. Strong localization of carriers and quasiparticles in MoS_2 shows promise in creating electron-hole plasma with long lifetime. Using machine learning, I also simulate optimal monolayer graphene geometries for generating strong, uniform pseudo-magnetic fields by MEMS strain. The coupled use of finite-element methods, variational auto-encoder, and auxiliary neural network accelerates the search for PMFs in strained graphene, while optimizing the graphene shape for fabrication through electron-beam lithography. This experimental and simulated work creates a road-map for rapid advancement in zero-field quantum Hall effect devices using graphene-integrated MEMS actuators.

Contents

List of Tables

List of Figures

List of Abbreviations

AC	.....	Armchair
AFM	.....	Atomic Force Microscopy
CAD	.....	Computer Aided Design
CPD	.....	Critical Point Drying
CVD	.....	Chemical Vapor Deposition
DI	.....	De-ionised
EBL	.....	Electron Beam Lithography
FEA	.....	Finite Element Analysis
FIB	.....	Focused Ion Beam
FLG	.....	Few Layer Graphene
hBN	.....	Hexagonal Boron Nitride
HF	.....	Hydrofluoric Acid
IR	.....	Infrared
LCM	.....	Lumped Circuit Model
MEMS	.....	Microelectromechanical Systems
ML	.....	Machine Learning
PDMS	.....	Polydimethylsiloxane
PL	.....	Photoluminescence
PMF	.....	Pseudo-magnetic Field
PMMA	.....	Poly(methyl methacrylate)
PPA	.....	Poly(phthalaldehyde)
PPC	.....	Polypropylene carbonate
RIE	.....	Reactive Ion Etching
SD	.....	Standard Device
SEM	.....	Scanning Electron Microscope
STM	.....	Scanning Tunneling Microscope
STS	.....	Scanning Tunneling Spectroscopy
TEM	.....	Transmission Electron Microscope
TIS	.....	Thermal Isolation Stage
UV	.....	Ultraviolet
ZZ	.....	Zig-zag
$\mathbb{R}^2$	.....	the Real plane

Chapter 1

Introduction

The flatland is the world of atomically thin materials. Although it is generally thought that the mechanical exfoliation of graphene in 2004 using ordinary scotch tape broke open the field (Novoselov et al., 2004), the real theoretical impetus for studying atomically thin materials came much earlier (Khveshchenko, 2001; Gorbar et al., 2002; González et al., 1994). As early as the 1940s, scientists theorized the existence of atomically thin layers of graphite which could posses unique semi-metallic properties (Wallace, 1947). Initially graphene was theorized to be unstable at room temperature due to thermal fluctuations leading to displacement of atoms (Landau, 1937; Peierls, 1935). The isolation of graphene showed that experimentally stable 2D materials were possible as they existed in a quenched, metastable state with interatomic bonds were strong enough to counteract the thermal fluctuations (Mermin, 1968; Geim and Novoselov, 2007). Following quickly on the heels of its isolation from graphite, the “2D material" gained critical momentum when the 2010 Nobel Prize in Physics was given to Andre Geim and Konstantin Novoselov for their “groundbreaking experiments regarding the two-dimensional material graphene." (Novoselov et al., 2005b)

Graphene is not just an atom thick material with extraordinary high tensile strength (Frank et al., 2007; Lee et al., 2008; Cao et al., 2020) and electrical conductivity (Chen et al., 2008; Morozov et al., 2008). It is an ordinary material capable of extraordinary physics. The metallic field effect was first demonstrated in graphene, showing that an externally applied voltage could reliably switch the material from 2D electron to hole gases

(Novoselov et al., 2004). Unraveling the band structure of graphene showed that its electrons were Dirac fermions, mimicking the behavior of relativistic particles with no inertial mass (Neto et al., 2007). The electronic structure around 6 equivalent high symmetry points (K and K') in momentum space were shown to exhibit linear dispersion (Novoselov et al., 2005a). As a direct consequence of this linear dispersion, it was shown that quantum Hall effect (QHE) manifests in graphene at room temperatures. This is highly unusual as the QHE had hitherto been realized in systems under extreme conditions of temperatures near 0 K and high magnetic field (Zhang et al., 2005; Novoselov et al., 2007). Recently, bilayer graphene twisted at a “magic angle" induced either superconductive or correlating insulator behavior, as a function of gated electron (or hole) density (Cao et al., 2018b; Cao et al., 2018a). Hence, this simple material opens the doors to a rich and diverse array of physical phenomena.

Today, graphene is one of a family of more than 100 atomically thin crystalline materials, which span the length of the electronic and optical spectrum. As stated earlier, graphene is a semi-metallic conductor, as it lacks a bandgap. Hexagonal boron nitride (hBN) posses a large band gap, and is therefore an insulator. In addition, as an atomically smooth substrate with minimal dangling bonds and charge traps, hBN acts as an excellent atomically thin dielectric (Dean et al., 2010). Transition metal dichalcogenides are materials with band gaps spanning the visible range between 400 to 700 nm (Wang et al., 2012). They are comprised of 3 strongly-bonded atomic planes, with two chalcogen layers (sulfur, tellurium, selenium) interspersed with a middle layer of Group V & VI transition metals like (Molybdenum or tungsten) (Liu et al., 2013; Ramasubramaniam, 2012). MXenes are a relatively new class of 2D materials with high conductivity and hydrophilicity, comprising of transition metals combined with nitrides, carbides or a combination of the two (Naguib et al., 2014; Anasori et al., 2015). Hence, the basic building blocks of all modern electronics, diodes and transistors, can be effectively thrive in the flatland of 2D materials.

In this thesis, I concentrate on straining the flatland and studying the novel physics that arises from deformation on atomically thin lattices. The application of strain to tune physical properties is not, in itself, a new idea: it has been a well-demonstrated mechanism in low dimensional films for over 70 years (Smith, 1954). A well-known example from the early 2000s is the use of strained Silicon in CMOS transistors developed by Intel Corp., in an effort to continue Moore's Law (Mistry et al., 2004) at increasingly small gate dimensions. Here, the epitaxially induced strain in the active region enhanced electron and hole mobility and decreased ion impurity scattering. The use of unaxially strained silicon in the source-drain region of their 90 nm logic technologies dramatically improved device performance and recorded world-record setting drive currents (Ghani et al., 2003).

Consequently, the application of mechanical strain on 2D materials has been of gaining interest in electronics and condensed matter physics because of their unique strain-dependent material properties. For example, strain on graphene can yield changes in properties like thermal conductivity (Chen et al., 2014), electronic structure (Pereira and Castro Neto, 2009; Choi et al., 2010), and can even result in fascinating phenomena such as pseudo-magnetic field generation (Levy et al., 2010; Guinea et al., 2010). Likewise, strain on TMDCs is very appealing for observing a multitude of novel physics. The two-dimensional (2D) structure limits dielectric screening so that Coulomb interactions for photo-generated quasiparticles are strong even at room-temperature (Lin et al., 2014; Chernikov et al., 2015b). Strain-engineering is an exciting avenue to explore these materials, owing to their layer-dependent band structure from direct bandgap for monolayers to indirect bandgap for two or more layers (Mak et al., 2010a; Splendiani et al., 2010), combined with their strength, flexibility (Bertolazzi et al., 2011), and ability to sustain strain. Studies have demonstrated large bandgap tunability with uniaxial (Conley et al., 2013) or biaxial (Lloyd et al., 2016) strain, including transition from direct to indirect bandgap at readily achievable strain levels. Recently, generating non-uniform strain fields has received

considerable interest because of the possibilities presented by local distortion to the band structure. Of particular interest is the spatial manipulation of neutral and charged excitons by strain funneling (Feng et al., 2012). Depending on the valance- and conduction-band response to strain, it is possible to either concentrate excitons or spatially separate electrons and holes (Feng et al., 2012; Fu et al., 2014). This could open doors for strained TMDCs to be used in a wide-array of optoelectronic devices such as light-emitting diodes (Ross et al., 2014; Lien et al., 2018), solar cells (Feng et al., 2012; Liu et al., 2018), lasers (Ye et al., 2015), and excitonic switches(Zhang et al., 2014b; Yang et al., 2019; Unuchek et al., 2018).

Strain can be generated in these materials through a variety of mechanisms: bendable substrates (Polyzos et al., 2015; He et al., 2013), pressurizing over holes (Lloyd et al., 2016), and piezoelectric substrates (Hicks et al., 2014; Hui et al., 2013), to name a few. Recently, microelectromechanical systems (MEMS) are being utilized to impart strain on suspended materials. MEMS actuators are reliable in terms of their output force and displacement, have an established fabrication process (Cowen et al., 2013), and can be easily integrated into existing electronics. Materials such as carbon nanotubes (Lu et al., 2004; Lu et al., 2006), metallic nanobeams (Pant et al., 2011), thin films (Saleh et al., 2015), graphene (Goldsche et al., 2018), and MoS_2 (Christopher et al.,) have been tested using a variety of different MEMS actuator configurations.

Studies on strain-funneling in TMDCs have utilized controlled wrinkling (Castellanos-Gomez et al., 2013), nanobubbles (Tyurnina et al., 2019; Blundo et al., 2020), pressurizing membranes (Kumar et al., 2015; Kovalchuk et al., 2020), or nanopillars (Chaste et al., 2018; Wang and Ma, 2020; Kern et al., 2016; Li et al., 2015). Early studies observed the funnel effect in few-layer MoS_2 but did not report on enhancement of PL intensity due to exciton funneling (Castellanos-Gomez et al., 2013). Following Feng *et al.*, recent studies have concentrated on creating very localized strain profiles on suspended films by using

AFM tip indentation. Studies on non-uniform strain in WS_2 reported that charge-funneling is a more dominant mechanism than exciton funneling, resulting in an increase in trion production (Harats et al., 2020), while others showed modest increase in PL intensity due to exciton funneling in monolayer WSe_2 (Moon et al., 2020). Monolayer MoS_2 on nanocones showed promising signatures of intensity enhancement from exciton funneling, but at modest strains of 0.2-0.5% (Li et al., 2015). Finally, multilayer MoS_2 on nanopillars showed efficient strain-induced enhancement in the intensity attributed to exciton funneling, but did not report on concentration of charges due to funneling (Mangu et al., 2017).

In this thesis, I concentrate on two methods of applying strain and interesting physical consequence to the 2D materials strained by each method. This manuscript is organized as follows: Chapter 2 will detail fabrication of $MoS2_2$ strained on top of nanopillars and their optical characterization. Chapter 3 demonstrates extraordinary results in the light-matter interactions induced in nanopillar-strained MoS_2. Chapter 4 describes a MEMS as a novel way to introduce strain to materials. Chapter 5 focuses on methods to integrate atomically thin materials with MEMS. Chapter 6 shows strain introduced to CVD monolayer graphene and exfoliated few layer graphene via MEMS. Finally, Chapter 7 details interesting applications brought about from methods in this thesis and some preliminary results.

Despite their amazing potential to solve some of humanity's most critical problems, it is a long and strange road from lab to real-world devices for 2D materials. With the methods and results presented here, I hope to make the path a bit more clearer, uncover some oddities along the way, and bolster the hope to realizing the “2D material revolution" that has long been heralded.

Chapter 2

Nanopillar-strained MoS_2

2.1 Introduction

In this chapter, I focus on a method of generating non-uniform strain in MoS_2: by deformation on nanopillared substrates. I discuss nanopillar fabrication from SiO_2/Si substrates and the transfer of MoS_2 on top. Strain is characterized by optical signatures from Raman and PL and compared with finite element analysis models. I demonstrate optimal Raman and PL fitting using Voigt profiles. I discuss the effect of interference in the optical signatures, which has a crucial role to play in understanding the complete opto-electronic picture of these samples. Using spatially-resolved optical characterization on ~ 27 different samples, 1-4 layer MoS_2 are analyzed and compared to modeling to develop a statistical intuition for geometry and strain on these samples. These results will lay the foundation for significant results presented in the next chapter on charge and exciton funneling and extraordinary PL enhancement in nanopillar-strained MoS_2.

2.2 Nanopillar Fabrication and MoS_2 Transfer

Nanopillars were fabricated on SiO_2/Si substrates using electron beam lithography (EBL) and reactive ion etching (RIE). The substrates, originally of 334 *nm* oxide thickness, were coated with a resist (polymethyl methacrylate or PMMA) and exposed to an electron beam, creating roughly square shape patterns in an array. RIE then creates 130 *nm* height pillars after lithography. Thus, the thickness of the oxide at the pillar and substrate is 334 *nm*, and

204 *nm* respectively. See Appendix A.1 for AFM characterization of the nanopillars. The resulting substrate contains arrays of roughly square shaped nanopillars of side length 300 *nm*, with 7 μm of separation between each pillar. The process flow is illustrated in Fig. 2·1 and details on the process parameters can be found in Appendix A.1.

MoS_2 is grown via physical vapor deposition on SiO_2/Si substrates, using MoS_2 powder. See Appendix A.3 for information on PVD process flow. The deposition on a standard 1 cm^2 chip usually results in the formation of several areas of growth, easily identifiable under an optical microscope. This includes areas of full-coverage monolayer domain, as well as areas where individual geometrically-defined shapes are formed.

The area where the domains form well-defined shapes (usually triangular, rhombus, or other polygon) should be selected for transfer over the nanopillars. These regions contain multilayer and monolayer flakes, as shown in Fig. 2·2(b). In order to maximize the number of strained regions, the domains should also be large enough such that a large number of pillars are simultaneously covered ($\geq 30\ \mu m$).

Once a suitable region on the growth substrate containing optimally sized flakes is identified, the transfer procedure can begin. As grown MoS_2 is first coated with polypropylene carbonate (PPC). PPC acts as a suitable transfer polymer because it is pliable, easy to clean using solvents, and has a low glass transition temperature which allows the material to flow. Using water-based float release techniques, the membrane of PPC+MoS_2 is lifted off the substrate, as described in Chapter 5. Care should be taken when determining the size of the area to transfer, as too large a membrane will be unstable to handle during transfer and could result in tearing or irreversible wrinkling. Fig. 2·3 shows the transfer process and the resulting sample.

The substrate is initially on a copper heating stage set at 40 °C. After the membrane of PPC+MoS_2 makes contact with the substrate, the temperature of the copper heating stage is raised in increments of 10 °C to a final temperature of 90 °C (beyond the PPC glass

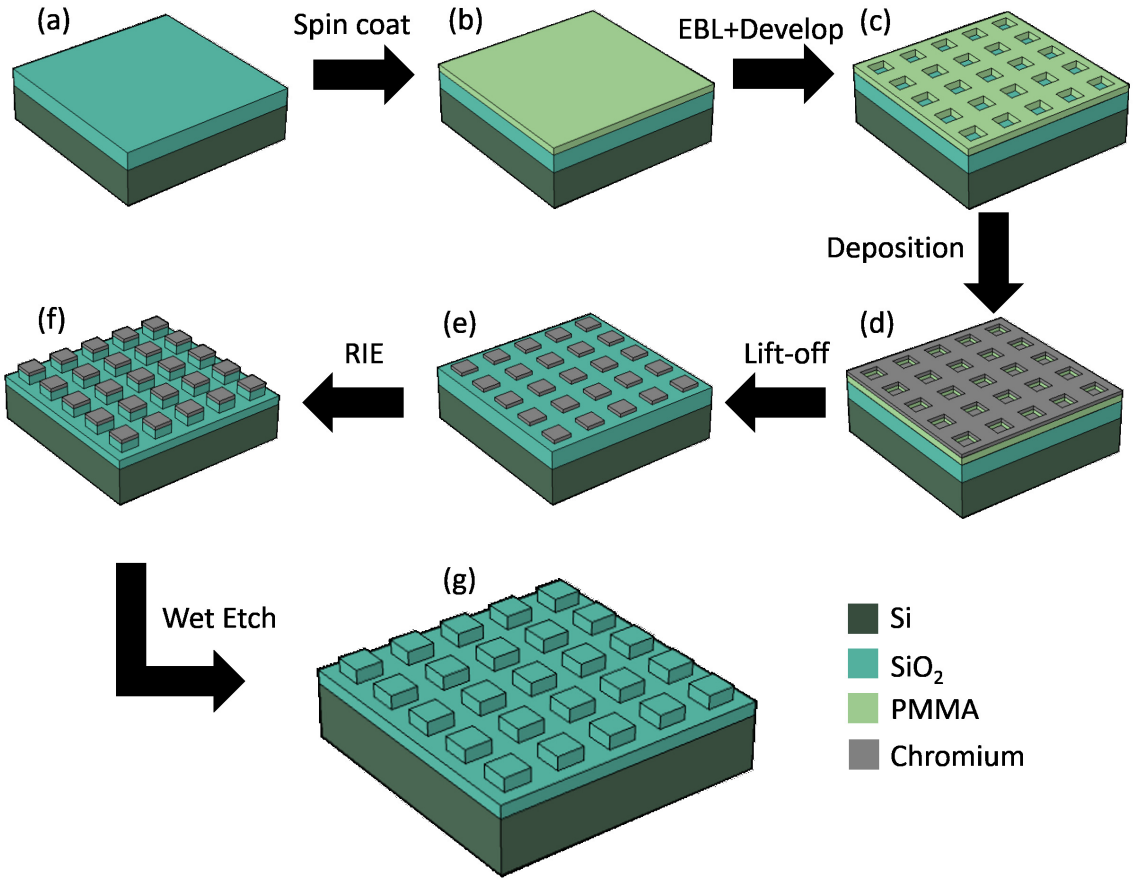

Figure 2·1: Fabrication Flow of Nanopillars. (a) Silicon substrate with 334 *nm* thick SiO_2. (b) Spin coat PMMA. (c) Electron-beam lithography defines an array of squares of side length 300 *nm* spaced 7 μm apart. With PMMA acting as a positive resist, development in IPA+MIBK removes the squares exposed by EBL. (d) 50 nm thick Chromium is deposited on the entire substrate. (e) Acetone is used to lift-off PMMA, leaving behind array of chromium squares. (f) Reactive ion etching etches the SiO_2 substrate down to 204 *nm*, leaving the chromium regions relatively untouched. (g) Chromium is removed using a wet etchant, leaving behind the final device: 130 *nm* height SiO_2 nanopillars on a Si substrate.

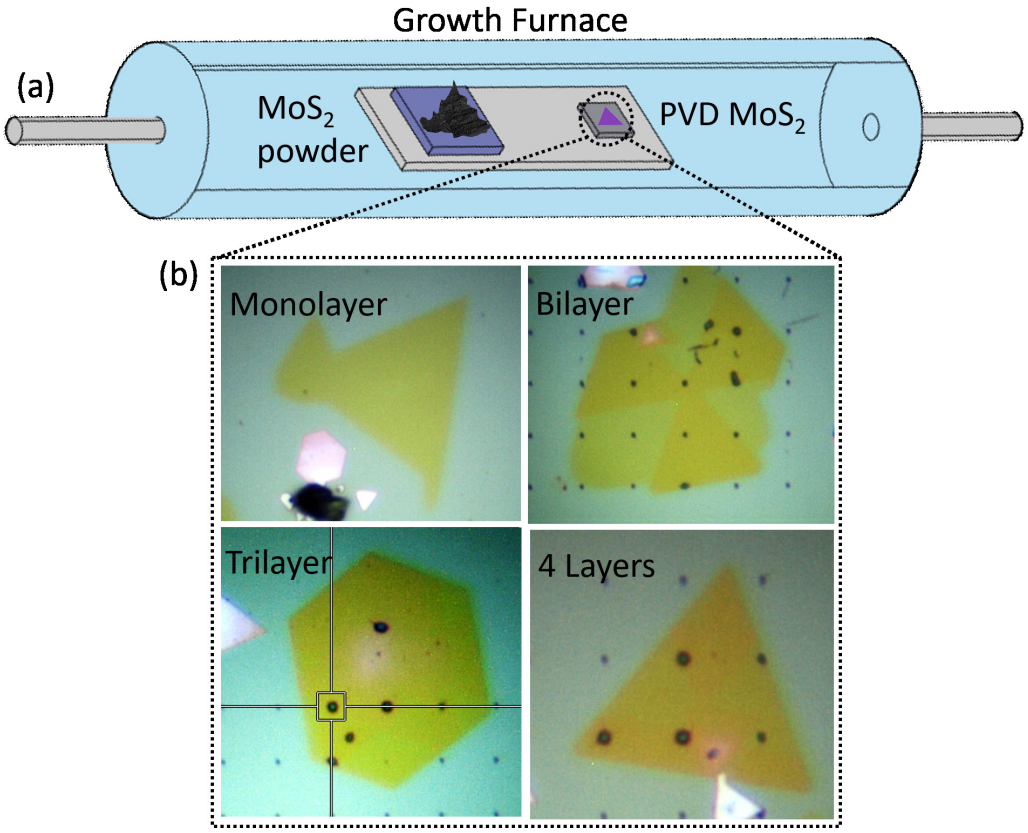

Figure 2·2: PVD Mo_2 Optical Images. (a) MoS_2 is grown by physical vapor deposition in a growth furnace using MoS_2 powder. The deposition on a SiO_2/Si substrate yields several regions of PVD MoS_2. (b) Optical images of 1-4 layer MoS_2 samples are shown. Note: these images are post-transfer on to the nanopillared substrate.

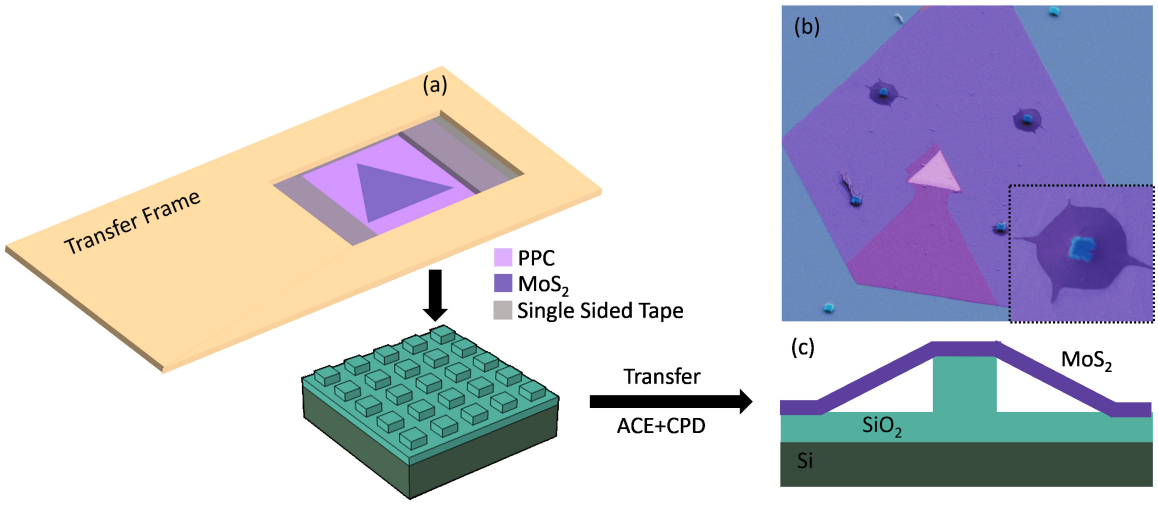

Figure 2·3: Transfer of MoS_2 on to Nanopillared Substrate. (a) Using PPC-based transfer techniques, a large region is transferred over the nanopillared substrate, encapsulating several pillars simultaneously. (b) Colorized SEM image showing multilayer MoS_2 (purple) transferred on top of a group of nanopillars (blue) with “tented" region (dark purple). Inset: Closer look at a single covered nanopillar. (c) Cross-sectional schematic showing formation of a “tented" region.

transition temperature). The PPC is allowed to fully release from the transfer frame, and the transfer frame is lifted away. The polymer residue is removed using acetone and undergoes critical point drying. The resulting sample after transfer is shown in Fig. 2·3(b). While monolayer MoS_2 conforms closely to the pillar, the multilayer flakes are stiffer, and an area around the nanopillars is suspended. The inset of Fig. 2·3(b) shows a colorized SEM image of one of our samples: a group of nanopillars (in blue) fully covered by multilayer MoS_2 (in purple). The darker purple region around the pillar is suspended material, stretching $\sim 1\ \mu m$ from the top of the pillar to the substrate. We refer to the suspended portion of the material as the “tented" region. The schematic in Fig. 2·3(c) shows a cross-section of this region. MoS_2 is strained by the nanopillars, and the strain reaches beyond the edge of the suspended region because of insufficient friction to hold it firmly in place (Kitt et al., 2013; Wang et al., 2015). As shown in the Fig. 2·3(b), the MoS_2 flakes are large enough to encapsulate several nanopillars.

2.3 Optical Characterization: Raman and Photoluminescence Response

2.3.1 Local Optical Measurements

A continuous wave laser with $\lambda = 532\ nm$ and a full width at half-maximum (FWHM) of $0.53\ \mu m$ was used for local Raman and PL measurements. Appendix A.4 shows determination of the laser beam waist determined by a knife-edge experiment. As the laser spot is larger than the pillar dimension, the resulting spectral response will be a convolution over the laser beam. This is an averaging effect that tends to underestimate the true value of strain or energy shifts of the material on the pillar. The laser power was 270 μW or lower for all measurements, which we determined produced no thermal shifting in the peaks while maintaining high signal-to-noise. All measurements reported here are taken in an ambient lab environment at room temperature. The resulting PL and Raman is either imaged or sent to a spectrometer. We observe the spectral response from this sample by a

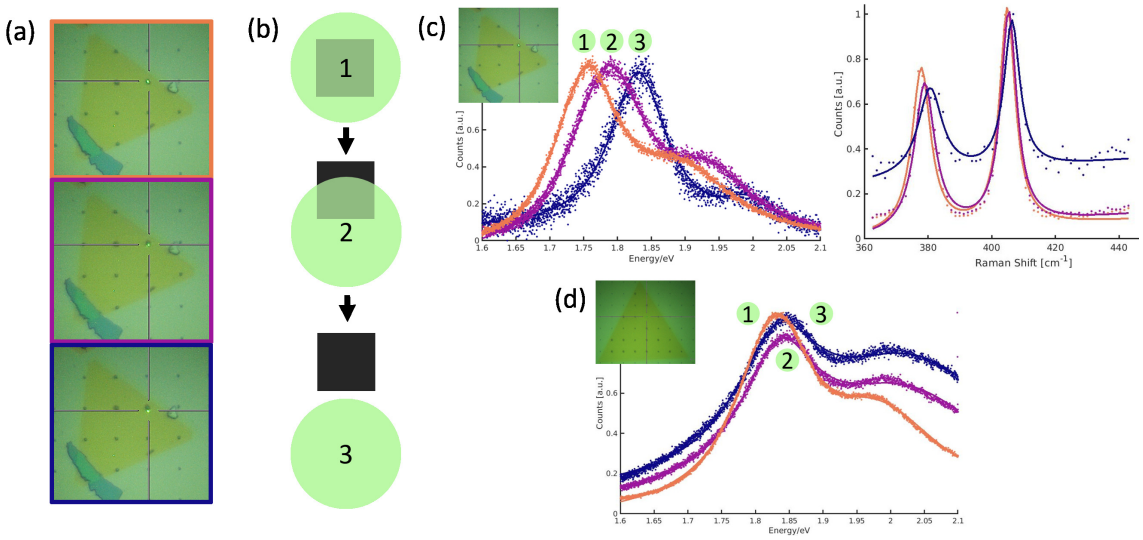

Figure 2·4: Path of Photoluminescence Measurements over Pillars. (a) Optical images of a 4 layer MoS_2 domain over nanopillars. The green spot within the cross-hairs indicates the position where the spectra are collected. (b) Schematic representing corresponding position of the laser over the pillar (1) directly on top of the pillar, (2) roughly at the edge of the pillar, and (3) off the pillar, roughly 1 μm away. (c) Normalized PL and Raman of response of the 4 layer sample from the 3 positions. The spectral response on top of the pillar shows a strong red-shift for both PL and Raman, compared to the substrate. (d) Normalized PL of monolayer MoS_2, showing minimal strain.

long-working distance 100x objective (NA 0.7). The spectrometer diffraction gratings used are 2400 l/mm for Raman, and 1200 l/mm for PL. The signal is passed through a 50 μm slit and detected on a thermoelectrically cooled CCD. Fig. 2·4(a) shows optical images of a 4 layer MoS_2 flake covering a portion of the nanopillar array, where each image corresponds to a location of the laser on pillar seen in Fig. 2·4(b). The respective normalized PL and Raman spectra taken on top of the pillar, at an edge, and off the pillar (on the substrate) for a 4 layer flake are shown in Fig. 2·4(c). Changes to the spectral features of PL and Raman (position, area, and FWHM etc.), are immediately apparent. The spectra on the pillar (orange) are red-shifted compared to the substrate (blue) as a consequence of the strain, while the spectra (purple) in between shows an intermediate strain level. Interestingly, not all samples show strain, as can bee seen in Fig. 2·4(d) which shows a monolayer MoS_2 on a nanopillar.

In order to elucidate the effects of the pillar on MoS_2, we perform spatially resolved optical measurements along a one-dimensional path, with 100 nm step sizes. Typically scan lengths range from $y =$ -3 μm to $y = 3$ μm, with the pillar centered at $y = 0$ μm, as shown in Fig. 2·5(a). The optical image of a trilayer MoS_2 flake is also shown. As the step size is a fraction of the laser beam waist, the resulting spectra will be over-sampled across the pillar. We collect the PL response from substrate to pillar in nearly-identical positions and step size as the Raman scans, as shown in Fig. 2·5(b&c), which follows the path indicated by the arrow in Fig. 2·5(a).

2.3.2 Thickness of multilayer MoS_2

It is clear from Fig. 2·4 that strain is not ubiquitous across all samples, and is especially dependent on the thickness of the MoS_2. Here, I discuss determining the thickness of MoS_2 using Raman. As a non-destructive method, Raman spectroscopy is suitable to determine thickness without the need for additional characterization through AFM or TEM.

To determine sample thickness, we use the difference in energies of the unstrained

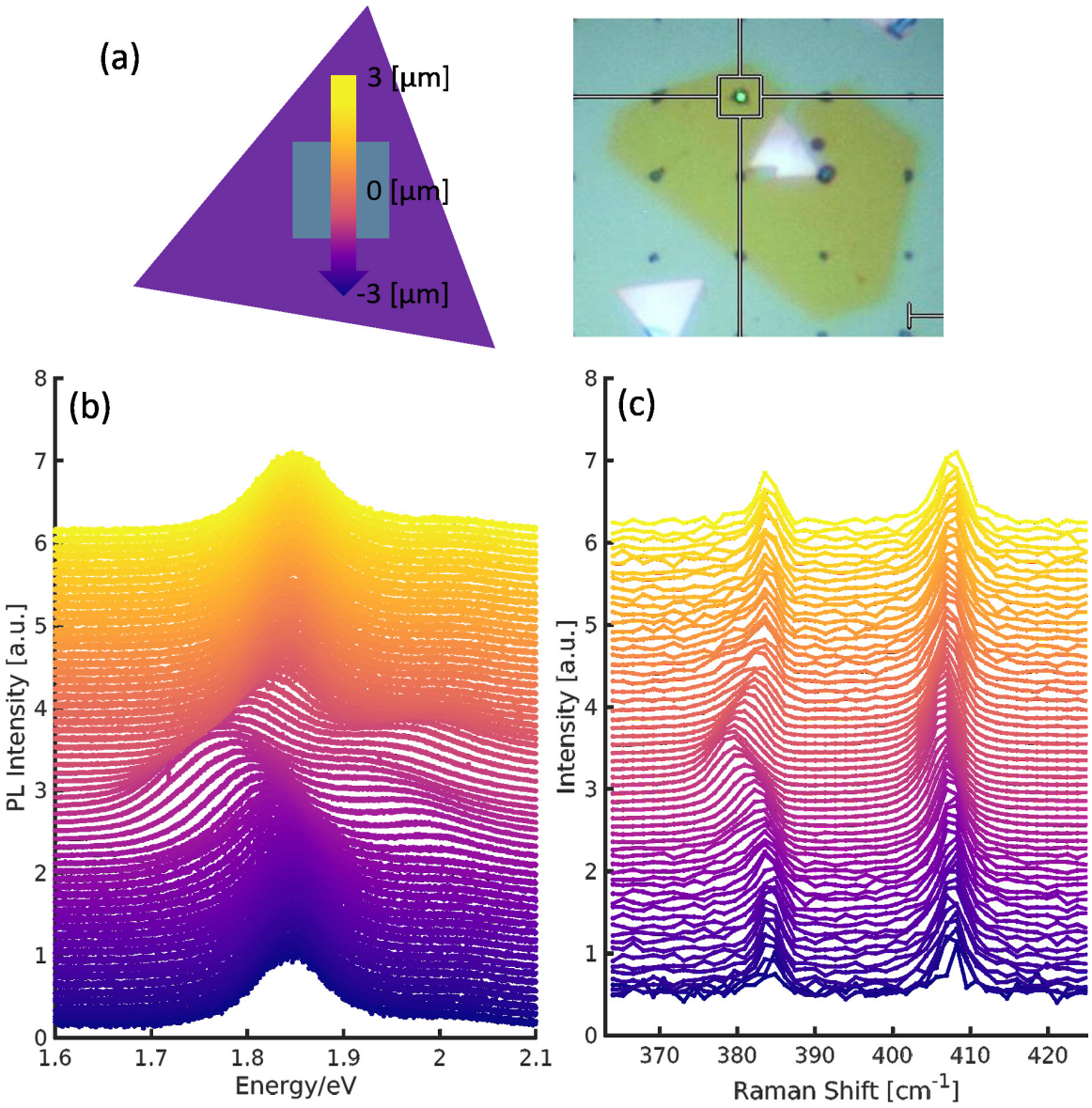

Figure 2·5: Spatially-resolved of Photoluminescence and Raman Measurements from Nanopillar-strained trilayer MoS_2. (a) Schematic of line scam over the pillar. Optical image of trilayer MoS_2 on nanopillars. The green laser spot indicates pillar position at $y = 0$ μm. (b & c) Normalized PL and Raman from $y =$ -3 μm to $y = 3$ μm, across the nanopillar.

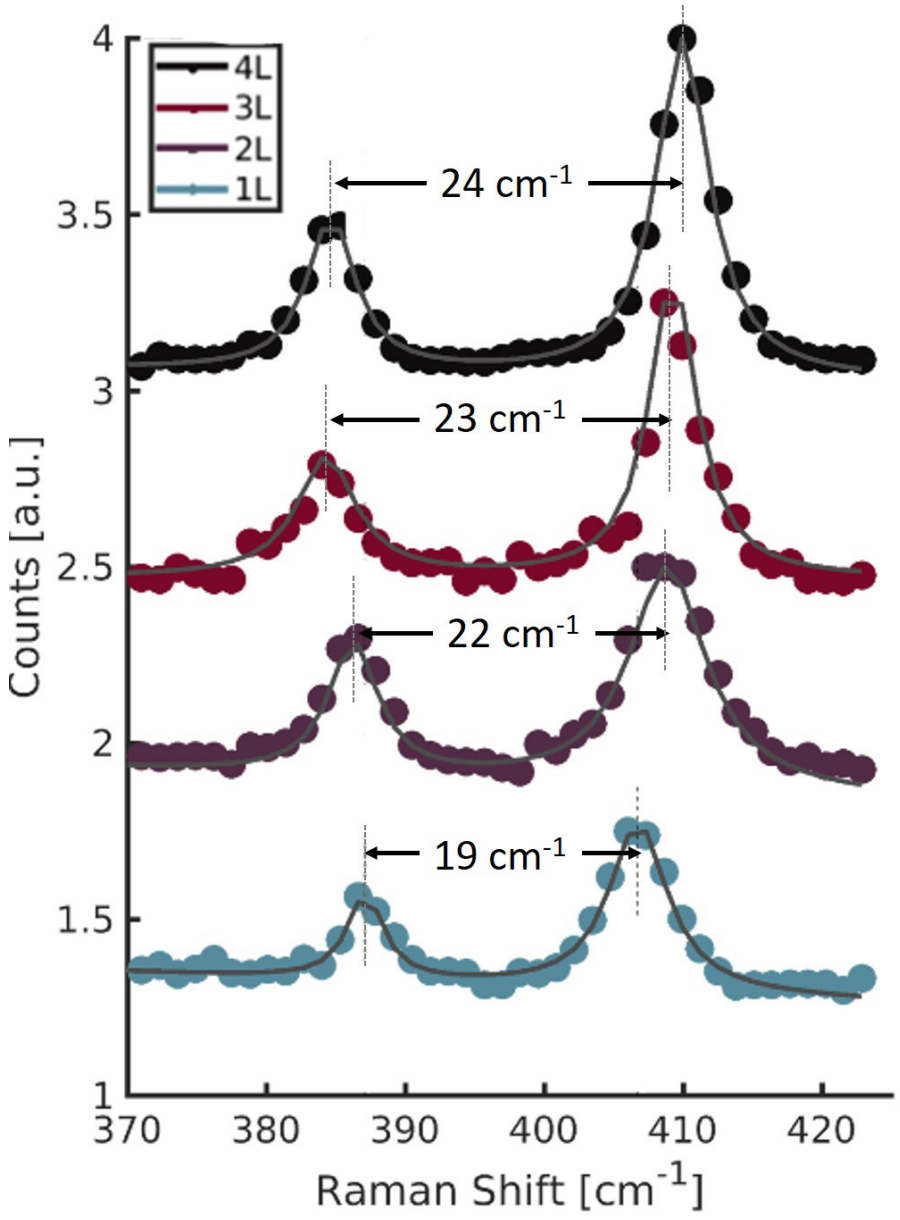

Figure 2·6: Raman Spectra from Multilayer MoS_2. A_{1g}-E^1_{2g} for 1-4 layers of MoS_2 observed in our unstrained samples are shown here.

Raman active phonon modes (Li et al., 2012; Lee et al., 2010), A_{1g}-E^1_{2g}, which is sensitive to layer thickness. Fig. 2·6 shows the peak separation of these Raman modes for 1-4 layer samples, taken on the unstrained regions of MoS_2.

2.3.3 Fitting Spectral Data

A thorough investigation on appropriate fitting for Raman and PL should be performed in order to correctly interpret the data and its constituent parts, and to prevent “over-fitting" of data. Here, we discuss the characteristic line shapes of Raman and PL spectra and the best fitting method to employ for them.

The line shape of spectral lines from 2D materials typically undergo lifetime broadening, and, under external factors such as macroscopic strain, temperature, or pressure, can also broaden due to increased rate of collisions. These effects can usually be modeled by Lorentzian profiles. However, the spectral size of the Raman peaks of MoS_2 are typically on the order of the resolution of the instrument. In addition, when the broadening is inhomogeneous, for example due to ensemble averaging of different strains in a diffraction limited laser spot, the Lorentzian line shape does not fully capture the shape of the PL. Hence, the Voigt line shape is most appropriate for fitting both Raman and PL in multilayer MoS_2. A Voigt function is a convolution between a Lorentzian and a Gaussian (Posener, 1959). Hence, the Raman and PL spectra are fit with Voigt profiles to extract intensity, position, and FWHM of the data (Fig. 2·7) (Ulrich et al., 1997; Michail et al., 2016). See Appendix A.5 for specific details on how the fitting is performed.

For the Raman, 2 Voigt functions, for the E^1_{2g} and A_{1g}, are utilized to fit the data (dashed lines in Fig. 2·7(a&b)). For the PL, 3 Voigt functions are used, corresponding to the neutral excitons (A & B) and the charged trions (T). As seen in Fig. 2·7(c), the substrate PL is fit well with 2 Voigt functions, and hence the fitting automatically reduces the trion contribution to a minimum. The solid black line is the sum of the fitting of individual Voigt line shapes. The residual error (shown below the spectra, in pink) shows that the resultant fit

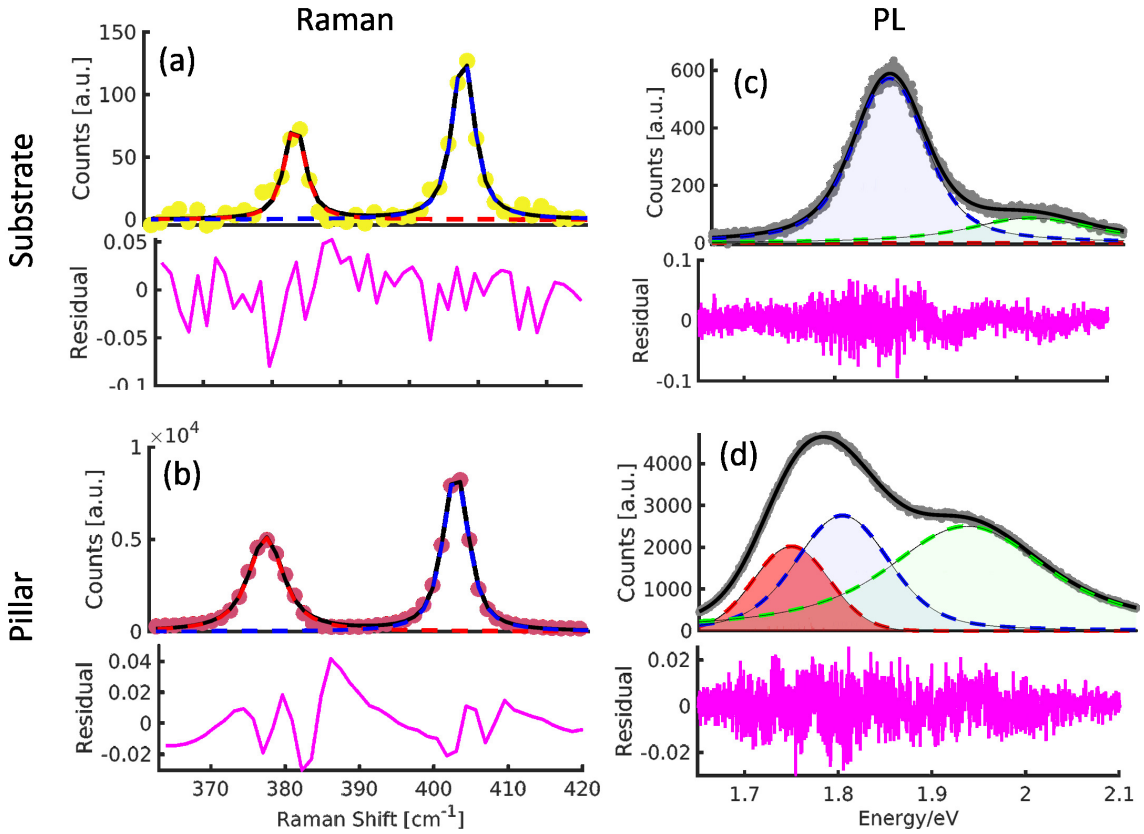

Figure 2·7: Fitting and Residuls for Raman and PL Raman spectral data fit with 2 Voigt profiles on the (a) substrate and (b) pillar. PL spectral data with 3 Voigt profiles on the (c) substrate and (d) pillar.

captures the data reasonably well. In comparison, purely Lorentzian fitting shows higher residuals and does not effectively capture the broadening of the spectral features as effectively (Fig. A·6(a&b)). Likewise, as seen in Fig. A·6(c), using only 2 Voigt peaks to fit the PL on the pillar gives high residuals, showing that the presence of a low energy tail (the trion peak) necessitates fitting using 3 Voigt peaks.

2.3.4 Laser Power Studies

Laser heating manifests as a red-shift of the exciton energy that can get mistaken for the effect due to strain. Hence, it is necessary to maintain a low enough power to negate laser heating red-shift in PL and Raman, while maintaining a quality of signal-to-noise ratio to allow for meaningful fitting of the data. For these studies, The laser power is kept at 270 μW or below for all measurements in order to minimize laser heating effects.

Another consideration to be made for optimal laser power is the effect of thermal heating and expansion on the morphology of the MoS_2 on top of the pillar. This is illustrated in Fig. 2·8(a). The material is originally suspended between the top of the pillar and the substrate, ie., the “tent" region. The friction and adhesion energy of the MoS_2 on the substrate produces the suspended “tent" region around the pillar, which has been seen to extend up to 1 μm from the pillar in some instances. However, with sufficient laser power, the material can undergo thermal expansion due to laser heating. This can release the adhesion between the material and the substrate, and as a result, the “tent" region collapses. Consequently, the material becomes more conformal around the pillar. The images under the optical microscope are shown below the schematics in Fig. 2·8, where the specific pillar under consideration is circled. There is a very noticeable decrease in the dark “spot" around the pillar when the morphology of the tent region changes abruptly under laser heating. This is most likely due to the changing interference conditions of the material due to different air gap. When the tent collapses, there is a release in the long-range strain of the multilayer on top of the pillar. In Fig. 2·8(b), I show PL taken on top of the pillar as a function of laser

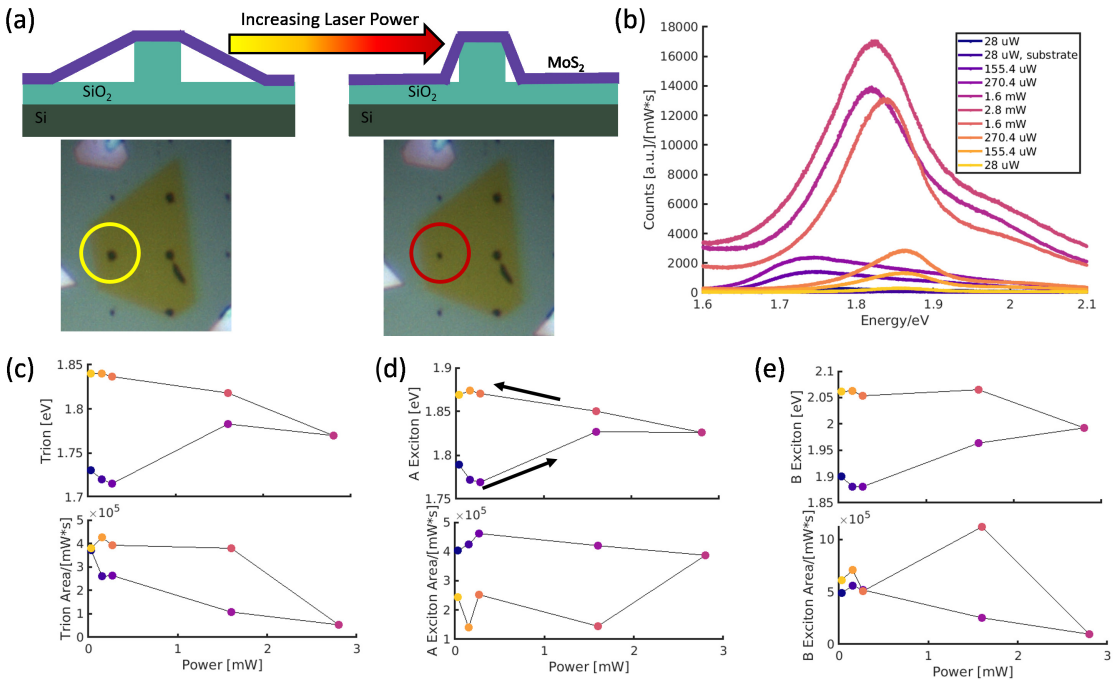

Figure 2·8: Laser Power Dependence of Pillar-strained Multilayer MoS_2 (a) Schematic of changes to MoS_2 "tent" region due to increasing incident laser power. Respective optical images are shown below. (b) Changes to PL with increasing optical power from 28 μW to 2.8 mW, and back to 28 μW. (c-e) Trion, A and B exciton peak position and normalized integrated area, as a function of incident laser power.

power, from 28 μW to 2.8 mW, and then back down to 28 μW. The extract trion, A, and B exciton peak positions and normalized areas are shown in Fig. 2·8(c-h), where the color of the points correspond to the laser power indicated in Fig. 2·8(b). As the laser power increases from 28 μW to 270 μW, all 3 spectral features on top of the pillar down shifts very slightly due to thermal heating (Fig. 2·8(c-e)). The peak area of each spectral feature, normalized by laser power and integration time, rises for the neutral excitons but is seen to decrease in this region for the trion (Fig. 2·8(f-h)).

When the incident laser power is 1.6 mW, the “tent" region collapses, and the long-range strain of the material is released. This causes the PL peak energies of all 3 spectral features to blue-shift to a higher, unstrained energy. As the power cycles back from a maximum power of 2.8 mW to 28 μW, the spectral features continue to blue-shift, indicating a decrease in the laser-induced heating in the material. No hysteresis is observed when cycling back and forth in incident laser power, indicating that the collapsed tent region is a permanent morphological change in the nanopillar-strained material.

It is important to note that, while the long-range strain is no longer present in the material due to the collapsed tent, the material is still strained due to the presence of the pillar. In fact, due to the material being more conformal on top of the pillar, the corners and sides of the material should undergo considerably more strain than when the material is tented. However, this strain cannot be observed optically, due to the near-normal incidence of the laser and the diffraction limit of the laser beam. Additionally, the laser power that will induce a tent collapse for different pillars is indeterminate. 270 μW, the standard laser power used in the next sections and chapter, was enough to induce this change to some pillars while others were unaffected. The stability of the long-range strain in each pillar seems to be contingent a number of factors such as the adhesion energy and friction, thickness of the multilayer, length of the tent etc. A more thorough investigation on these different factors is needed to elucidate the exact nature of tent stability.

For the present, optical experiments on nanopillar-strained MoS_2 should use incident powers $\leq 270\mu W$, which should be decided on the basis of optimal signal-to-noise ratio. Additionally, signal-to-noise can be marginally improved even for lower powers by taking $\geq$3 spectra at each spot and averaging them. For more data on laser power studies done on MoS_2 on nanopillars, see Appendix A.6.

2.3.5 Edge Determination Using Polarized Raman

Physical properties of multilayered TMDCs can be altered on changes to the relative twist, stacking order, and sliding of individual basal planes. Misalignment between layers strongly modulates interlayer coupling which induces changes in vibrational, optical, and electronic. Hence, knowing the crystallographic orientation is important to fully characterize the properties of devices using TMDCs. The PVD MoS_2 in this work is generally grown with an edge orientation that is ubiquitous throughout the transferred portion of the sample.

In Fig. 2·9(a), I show a prototypical multilayer sample on top of the nanopillar. It can be clearly seen that the edges of the sample make angles of 120°. In crystallographic structures of this type, when two edges are separated by 60°or 120°, they share the same chirality (either armchair or zigzag). But which of the two orientations is this sample? Here, I conduct a polarized Raman study to determine the chirality of the edge. I use a linearly polarized 532 nm laser, with its initial polarization oriented along the x-axis, as indicated in Fig. 2·9(a). Using a half-wave plate, I rotate the axis of polarization of the laser, while maintaining its linearity. I collect the Raman spectra from the MoS_2 sample as a function of polarization angle. Fig. 2·9(b&c) show the change in intensity of the Raman active phonon modes, A_{1g} and E^1_{2g} (respectively), as a function of polarization angle. The E^1_{2g} phonon mode is independent of polarization angle. Under strain, however, it becomes strongly dependent on the polarization when under uniaxial strain, as the strain breaks the in-plane symmetry and lifts the degeneracy of the E^1_{2g} mode. Though the strain on top of the pillar is biaxial, due to the inhomogeneity in strain, the Raman E^1_{2g} mode exhibits a

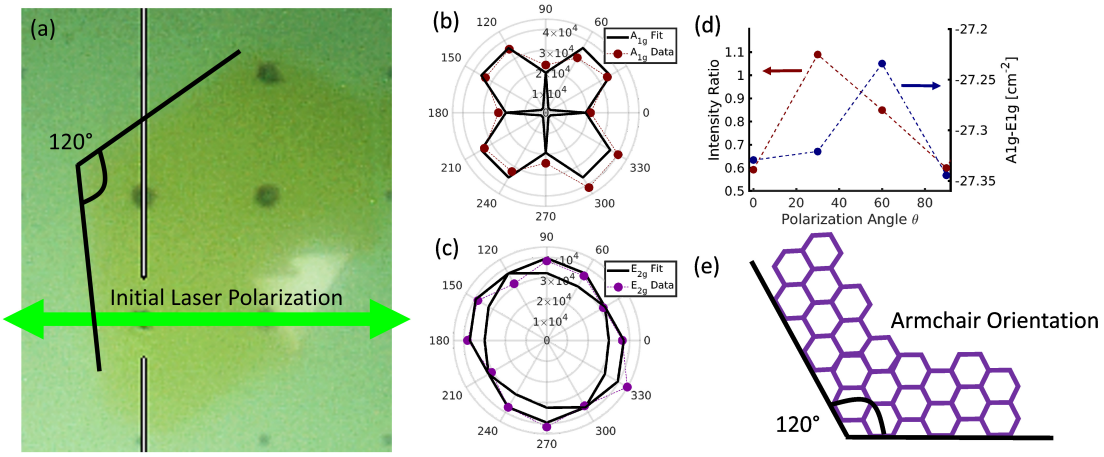

Figure 2·9: Polarization Dependence of Multilayer MoS_2 (a) Multilayer MoS_2 sample with linear polarization aligned with the x-axis. The angle of the edges is measured 120°. (b&c) Intensity of A_{1g} and E^1_{2g} for different polarization angles θ =0°to θ =360°. (d) Intensity ratio A_{1g}/E^1_{2g} and difference in Raman energies $A_{1g} - E^1_{2g}$ for θ =0°to θ =90°. (e) Illustration of MoS_2 armchair edge chirality oriented along a 120°angle, corresponding to the edge of the sample in (a).

slight anisotropic variation with polarization. The difference in phonon modes $A_{1g} - E^1_{2g}$ shows a slight variation with respect to polarization, as shown by the blue data points in Fig. 2·9(d). This can also be attributed to the strain on top of the pillar. In addition, the E^1_{2g} mode has been shown to exhibit anisotropy in intensity due to stacking order. By contrast, the Raman A_{1g} phonon mode follows the polarization of the laser: the intensity is minimum when the polarization of the laser is orthogonal to the scattered light. Following Li *et al.*, we can see that the intensity ratio (red data points in Fig. 2·9(d)) corresponds to the armchair orientation of MoS_2, as illustrated in Fig. 2·9(e). Further experiments using polarized Raman would help elucidate interesting features, such shear between layers, and changes to interlayer coupling due to the non-uniform strain induced by the nanopillar. The setup for varying the laser polarization and the resulting Raman spectra can be seen in Appendix A.7.

2.4 Interference Effects on Optical Spectroscopy

2 dimensional films are deposited on substrates with a transparent dielectric, e.g. SiO_2, to provide an interference cavity to make the films visible to the naked eye or microscope by a color change. In this study we are using a substrate where the oxide layer has been patterned and etched to have evenly spaced nanopillars. The thickness variation between the etched substrate and the nanopillars makes for different interference conditions. Since we are interested in the PL enhancement on the pillars from diffusion and funneling, we need to account for the differences in interference conditions (Yoon et al., 2009; Zhang et al., 2015). I gratefully acknowledge Zhuofa Chen in the Swan Lab and Celalattin Yardukal in the Unlu Lab for these results.

There are three distinct regions as illustrated in Fig. 2·10(a): Film directly on the substrate (air/MoS_2/SiO_2/Si), films with a varying thickness air gap between the film and substrate, the "tent" region, (air/MoS_2/air/SiO_2/Si); and the film on the pillar (air/MoS_2/SiO_2/Si).

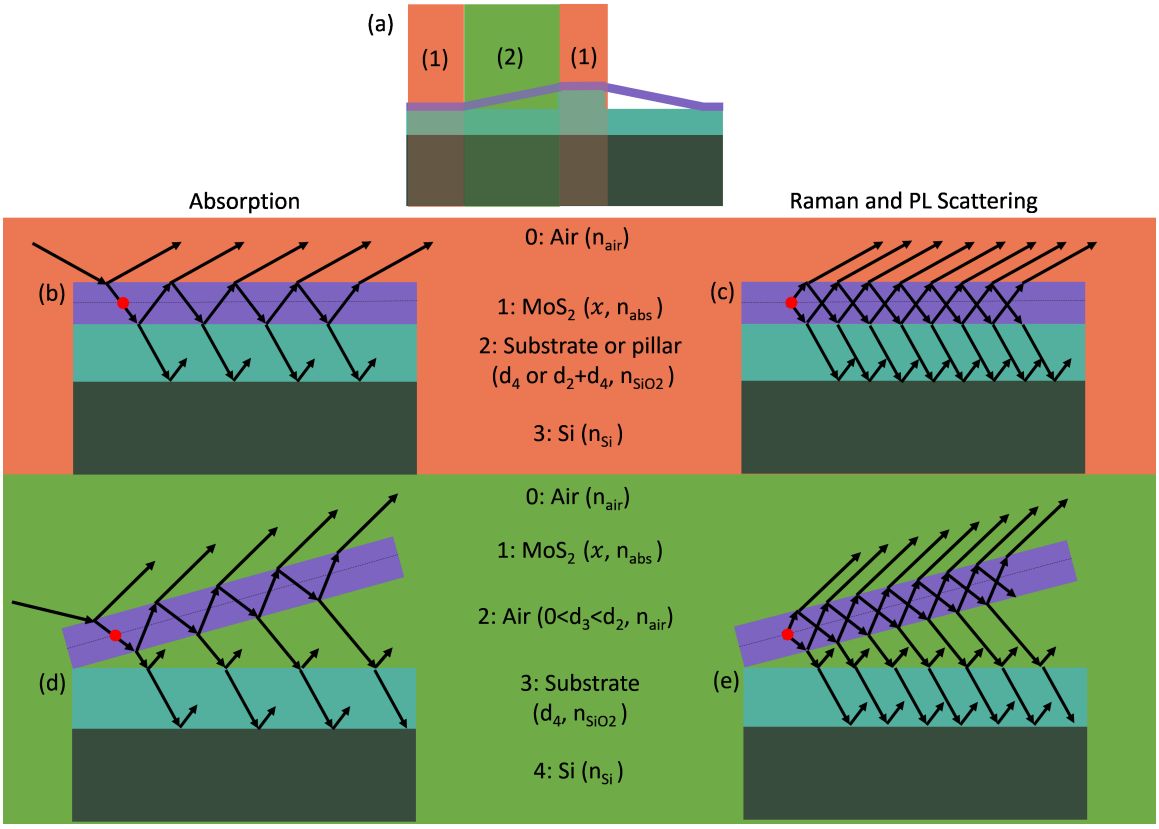

Figure 2·10: Schematic of Interference Regions and Multi-reflection Models. (a) Regions with differing interference conditions. (b&c) Multi-reflection model for incident and emitted light in the absorption and scattering processes for regions (1). (d&e) Multi-reflection model for incident and emitted light in the absorption and scattering processes for regions (2).

The incident light and the outgoing PL intensity and is decreased or enhanced due to interference. The enhancement factor of the three regions are first calculated point by point, and later the results are convoluted with the Gaussian laser beam, which is significantly larger than the pillar itself and the sampling region consists both the pillar region and the tent region.

The PL enhancement factor is calculated by integrating the product of the absorption factor and the scattering factor. The absorption factor originates from the interference of the incident laser since the laser goes through multiple reflections inside the 2D material and the underlying cavities. The scattering factor originates from the interference of the emission light which goes out as well as going through multiple reflections inside different interfaces.

2.4.1 (1) Pillar and substrate regions: Air/MoS_2/SiO_2/Si

The net absorption factor can be calculated by summing up multiple terms of the reflected light using Airy‘s formula, as shown below:

$$F_{ab} = t_{abs} \frac{e^{i\beta_{abs,x}}(e^{-2i\beta_{abs,x}} + r_{abs,1}e^{-2i\beta_{abs}})}{1 + r_{abs,1}r_{abs,2}e^{-2i\beta_{abs}}} \tag{2.1}$$

where t_{abs}, $r_{abs,1}$, $r_{abs,2}$ are the Fresnel transmission and reflection coefficients calculated using the matrix method. $r_{abs,1}$ is the reflection coefficients on the MoS_2 surface and $r_{abs,2}$ is the reflection coefficient on the SiO_2 surface. We use abbreviations $\beta_1 = \frac{2\pi d_1 n_{abs}}{\lambda}$ and for a specific depth (x) in the MoS_2 layer, $\beta_x = \frac{2\pi x n_{abs}}{\lambda}$, λ is the wavelength of the incident light. We also consider the dispersion of the MoS_2 refractive index. n_{abs} is the refractive index of MoS_2 at the excitation wavelength λ.

The net scattering factor can be calculated by summing up all the outgoing light using the Airy‘s formula, as shown below:

$$F_{sc} = t_{sc} \frac{e^{i\beta_{sc,x}}(e^{-2i\beta_{sc,x}} + r_{sc,1}e^{-2i\beta_{sc}})}{1 + r_{sc,1}r_{sc,2}e^{-2i\beta_{sc}}} \tag{2.2}$$

where t_{sc}, $r_{sc,1}$, $r_{sc,2}$ are the Fresnel transmission and reflection coefficients calculated using matrix method at the emission wavelength λ_{sc}. For example, the A exciton of trilayer MoS_2 excited by 532 *nm* laser has an energy of 1.85 *eV*, then $\lambda_{sc} = 670$ *nm*. We use similar abbreviation β_{sc} and $\beta_{sc,x}$ at the emission wavelength. The absorption and scattering processes for this region are illustrated in Fig. 2·10(b&c).

2.4.2 (2) Tent region: Air/MoS_2/Air/SiO_2/Si

The absorption factor and the scattering factor is calculated using the same formulas for F_{ab} and F_{sc}, as described above. The difference is that one more layer (air gap) needs to be added to the matrix formulation when calculating the Fresnel transmission and reflection coefficients t_{abs}, $r_{abs,1}$, $r_{abs,2}$ and t_{sc}, $r_{sc,1}$, $r_{sc,2}$. The absorption and scattering processes for this region are illustrated in Fig. 2·10(d&e).

2.4.3 Numerical aperture NA

Note that we also consider the effect of numerical aperture (NA). For the specific NA used in our experiment (0.7), the maximum incident angle is calculated by $\theta_{max} = \arcsin(NA) \approx 1.1$ rad. The above transmission and reflection coefficients are calculated at a specific incident angle and the final absorption factor is calculated by integrating through incident angle from 0 to θ_{max}. The total enhancement factor is calculated by integrating the square of the product of absorption factor and scattering factor through the thickness of the MoS_2 layer.

$$F = \int_0^{d_1} \mid F_{ab}F_{sc} \mid^2 dx \tag{2.3}$$

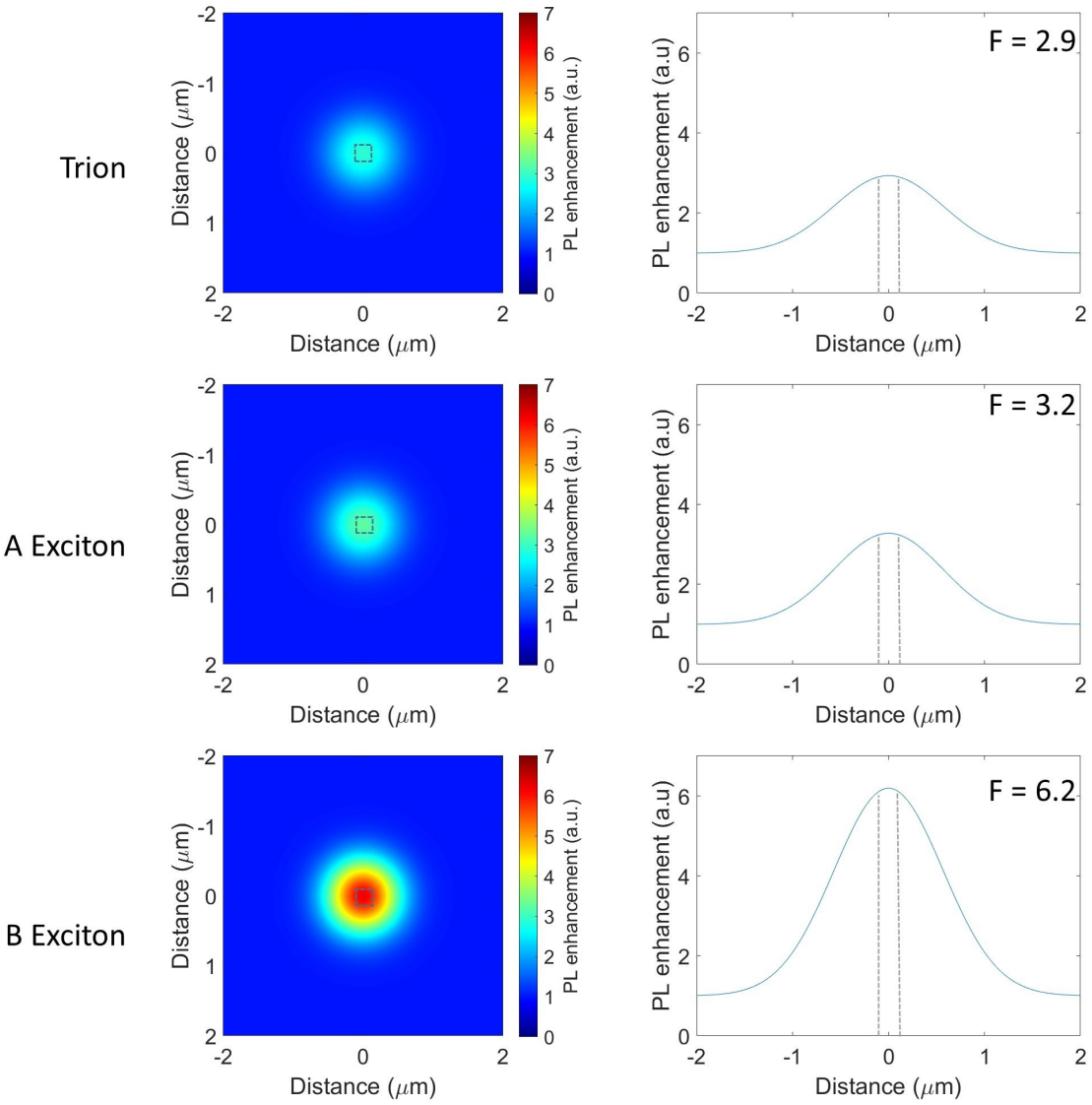

Figure 2·11: PL enhancement simulation results of the trion, A exciton, and B exciton.

2.4.4 Gaussian laser beam spot profile

Since the laser beam size is much larger than the pillar size, we need to integrate the local enhancement factor with the illuminated region. Thus, we use a mesh grid (covering the pillar, tent, and substrate regions) and the enhancement factor at each pixel is calculated. The final enhancement factor is then calculated through convolution process.

Fig. 2·11 shows the simulation results of the trion, A exciton, and B exciton interference signal enhancement, computed according their energies in the main text. The left figure is the 2D spatial image of the PL enhancement in a 2 μm by 2 μm region. The bright spot in the center is the convolution results of the PL enhancement on the pillar. The right is the cross cut of the left figure. The simulation results show that PL enhancement of the trion, A, exciton, and B exciton is 2.9, 3.2, and 6.2, respectively.

2.5 Strain in 1-4 Layer MoS_2

In this section, I characterize the strain in multilayer MoS_2 using spatially resolved line scans across the pillar. Fig. 2·12 shows the Raman and PL analysis of a trilayer MoS_2 sample over a nanopillar. Raman and PL spectra were taken across the sample in steps of 0.1 μm, and then fitted with Voigt profiles. The Raman active phonon modes (E^1_{2g} and A_{1g}) of MoS_2 provide information on number of layers (Lee et al., 2010; Li et al., 2012), strain in the material (Conley et al., 2013; Lloyd et al., 2016), as well as information on changes in concentration of charges (Chakraborty et al., 2012; Ardekani et al., 2019). Fig. C·3(a) shows that both Raman active phonon modes soften from the substrate to the 300 nm pillar region (blue bar). The in-plane E^1_{2g} phonons respond mostly to strain. The out-of-plane A_{1g} mode red-shifts with charge and does not soften significantly with strain (Ardekani et al., 2019).

We plot the calculated strain across the pillar in Fig. 2·12(b). The strain in the material varies from $\varepsilon = 0\%$ on the substrate at one end of the scan (± 3 μm), to a nominal max

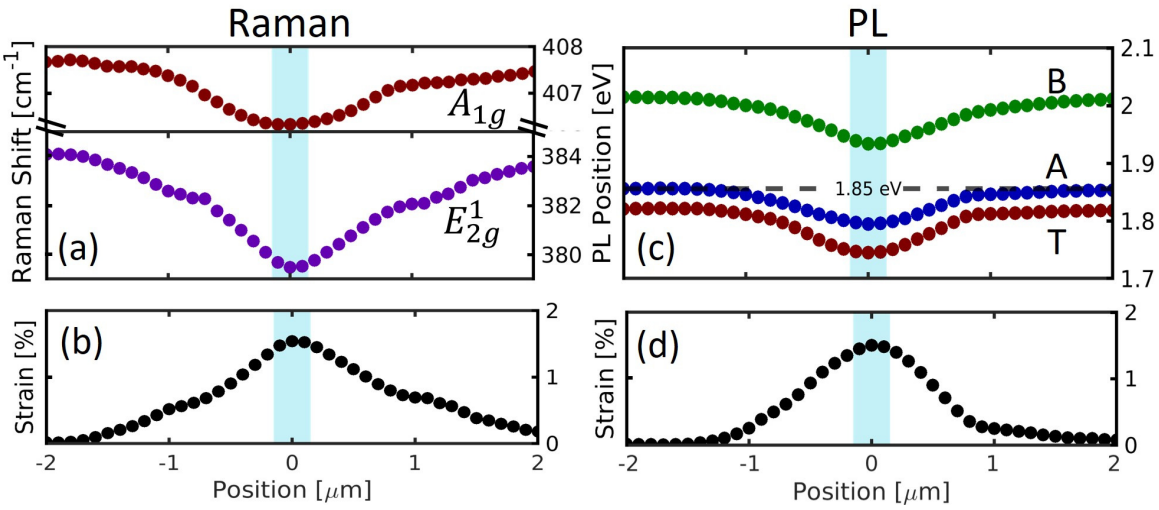

Figure 2·12: Raman and PL Energy Shifts. (a)E^1_{2g} and A_{1g} line scans show phonon softening across the pillar (blue). (b) Raman strain profile with max $\varepsilon = 1.55\%$. (c) PL line scans show energy red-shifts for A and B excitons and charged trions T from substrate to the pillar. (d) Strain profile from PL A exciton position, max $\varepsilon = 1.51\%$.

value of $\varepsilon = 1.55\%$. This strain value is a lower limit of the maximum local strain due to the convolution of the laser spot with the strain profile. The strain extends $\pm 2\ \mu m$ on either side of the pillar, yielding an average strain gradient of $0.78\ \%/\mu m$ for this particular pillar. Note that the convolution of the strain profile with the laser spot extends beyond the suspended tent region, indicating a long-range strain gradient is established by the pillar. In the next chapter, we analyze the correlation between the E^1_{2g} vs. A_{1g} phonon modes to decouple charge and strain effects, and construct a strain-charge ($\varepsilon - n$) correlation diagram (Michail et al., 2016; Chae et al., 2017; Kim et al., 2020; Lee et al., 2012).

Next, we consider the shift in phonon and PL energies from across the pillar. The strain extracted from the Raman E^1_{2g} and the PL A exciton (Lloyd et al., 2016) are closely matched. However, The distribution of strain over the pillar slightly differs between the two. This could be because the presences of charges causes partial conversion of excitons to trions, while the E^1_{2g} is largely unaffected by the presence of charge. In addition, discrepancies between Raman and PL scan locations can change overall strain distribution.

Fig. C·3(c) shows the peak positions for the characteristic neutral excitons (A and B) (Coehoorn et al., 1987) and charged trions (T) (Mak et al., 2013). In our unstrained trilayer sample, we observe these features at 1.85 eV, 2.01 eV, and 1.82 eV, which agree with previous optical studies (Golovynskyi et al., 2020; Splendiani et al., 2010). In Fig. C·3(c), we show that these spectral features red-shift due strain from substrate to pillar. The A exciton energy shift from 1.85 eV on the substrate to 1.79 eV on top of the pillar, corresponding to a maximum strain(Lloyd et al., 2016) of $\varepsilon = 1.51\%$ (Fig. C·3(d)), closely corroborates the strain value extracted from Raman. Following Fig. 2 in the main text, we illustrate the shift in phonon and PL energies from across the pillar for the 2 and 4 layer samples (Fig. 2·13, 2·14). The strain extracted from the Raman E^1_{2g} and the PL A exciton (Lloyd et al., 2016) are closely matched. However, The distribution of strain over the pillar slightly differs between the two. This could be because the presences of charges causes

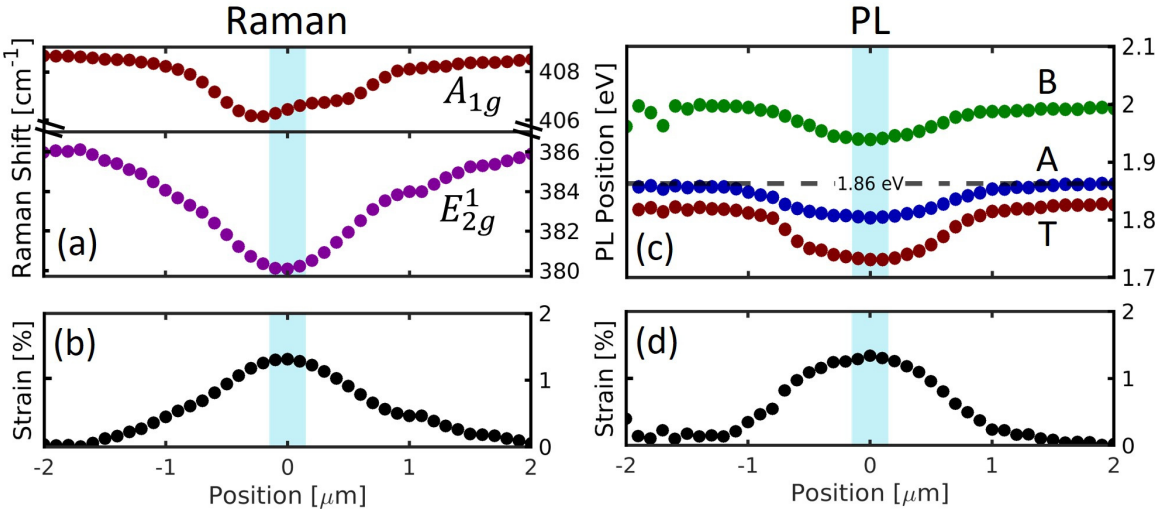

Figure 2·13: Bilayer MoS_2.

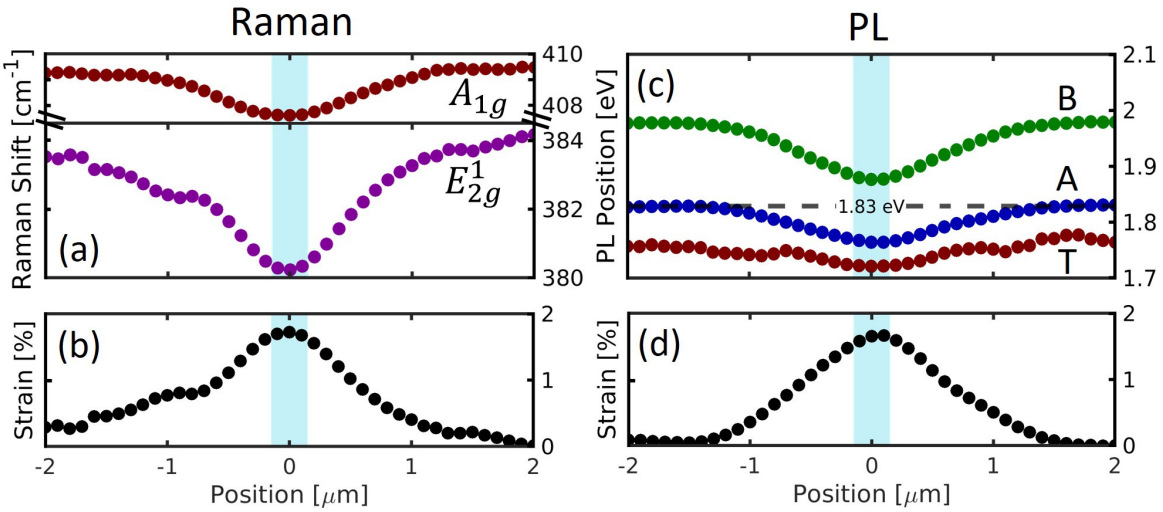

Figure 2·14: 4 Layer MoS_2.

partial conversion of excitons to trions, while the E^1_{2g} is largely unaffected by the presence of charge. In addition, discrepancies between Raman and PL scan locations can change overall strain distribution.

2.6 Finite Element Modeling of Strain

We use COMSOL Multiphysics ™to simulate the inter-coupled structural and electronic behavior of multilayer MoS_2 under deformation by the nanopillar. The model takes the following inputs: thickness of trilayer MoS_2 $d_1 = n \times 0.65nm$ (where n is the number of layers, and 0.65 nm is the thickness of monolayer MoS_2), Young's modulus $E = 238\ GPa$, Poisson's ratio $\nu = 0.25$, density $\rho = 5.06\ g/cm^3$. A circular MoS_2 flake is simulated, with radius $3\mu m$. This matches the extent of the line scans performed to optically characterize the material in the previous section. A series of parameterized tests where the tent region and the initial strain due to transfer in the material was varied. The solution was on a triangular mesh, with a density determined by a series of convergence studies. The resulting solution was compared with the data extracted from optical measurements, as seen in the previous section. The best fit set of pre-strain and tent values for 3 multilayer samples are shown in Fig. 2·15. Specific details on modeling can be found in Appendix A.8.

Fig. 2·15(a,c,&e) show the 3D distribution of strain in Mo_2 deformed due to a nanopillar of height $H = 130\ nm$, as function of increasing layer thickness ($n = 2,3,4$). The deformation in the z direction was scaled by 2.5 to adequately show strain profile across the pillar. The maximum strain is calculated to be $\varepsilon_{max} = 1.85\%$, 2.14%, and 2.58% for 2, 3, and 4 layer MoS_2, respectively. It is clear that the maximum strain is seen at the corners of the pillar. This is because the sharp corners of the pillar cause a localized increase in the stress concentration at that point. In reality, the corners of the pillar are smoother. Hence, the maximum strain calculated by the FEM is the ideal strain for infinitely sharp corners. From the corners, the strain radially decreases towards the center of the pillar, and also de-

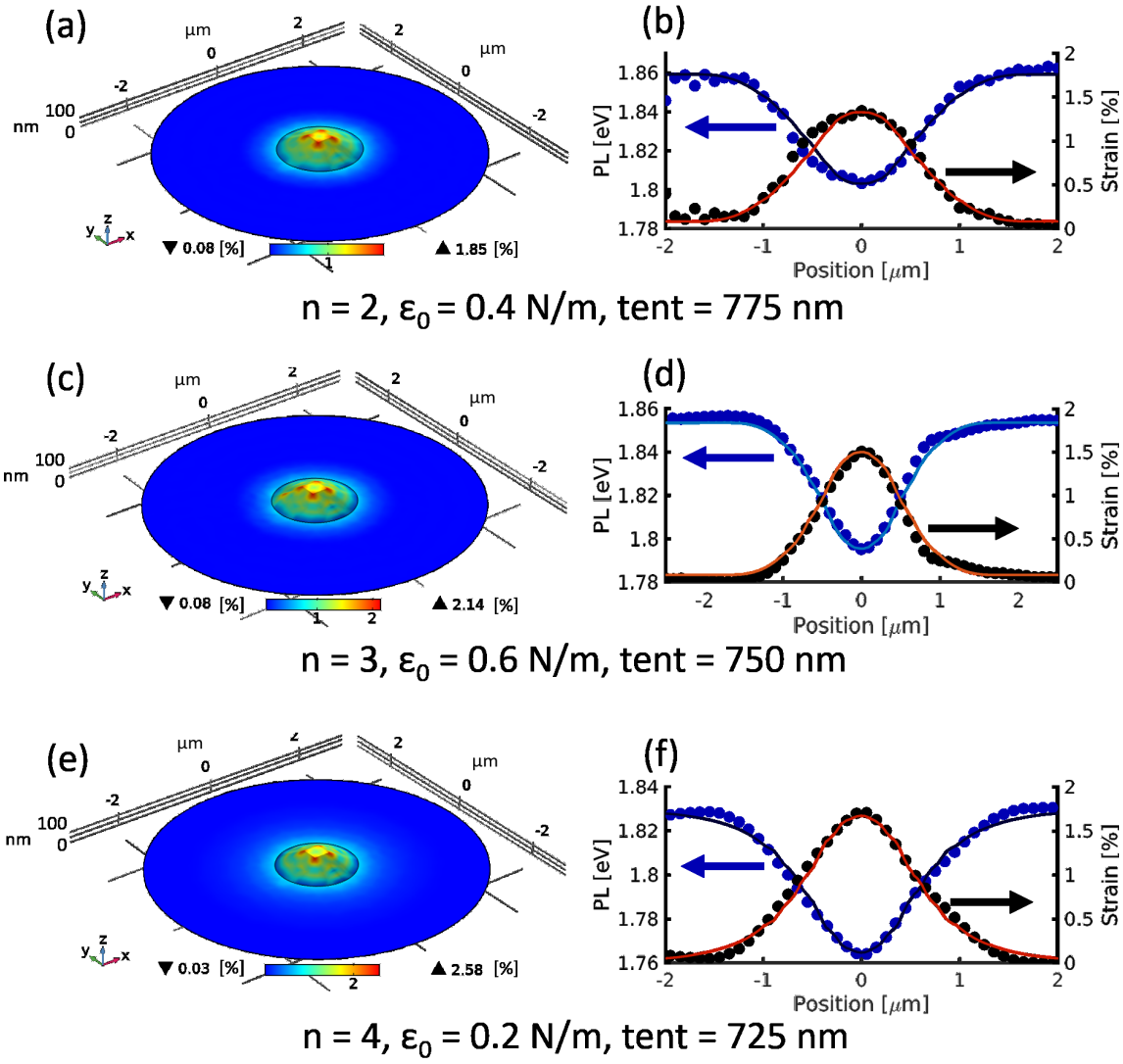

Figure 2·15: FEM of Strain in Multilayer MoS_2 3D strain distribution and corresponding line scan across the pillar from $y = -2\ \mu m$ to $y = 2\ \mu m$ calculated by FEM on (a&b) 2 layer, (c%d) 3 layer, and (e&f) 4 layer MoS_2. The solid lines are the results of the COMSOL simulation while the data points are experimental results from PL.

creases as a function of distance from the pillar. The strain clearly extends beyond the tent region (indicated by the inner circle). Furthermore, as the thickness of the layer increases, the strain extends to a greater extent beyond the suspended “tent" region. This corroborates our findings that friction is insufficient to hold the material in place (Kitt et al., 2013; Wang et al., 2015). On an atomic level, frictional force is proportional to the area of contact between the material and the underlying substrate. As the material thickness increases, the conformation with the (relatively) rough substrate decreases due to increasing bending stiffness. As a result, frictional force decreases as a function of increasing thickness. At $\pm$ 3 μm, the sample has a minimum strain of $\varepsilon_{min} = 0.08\%$, 0.08%, and 0.03%. This shows that a long-range strain gradient is established.

Fig. 2·15(b,d,&f) shows the comparison between data and the FEM simulation in closer detail. Here, I extract the calculated strain (solid orange line) and PL energy shifts (solid blue line) across a line cut centered on the pillar from $y =$ -2 μm to $y = 2$ μm, to match the data from optical measurements seen in the previous section. Additionally, the solution at each point is averaged over a circle of diameter 530 *nm*, to match the averaging over the Gaussian laser beam in the experimental setup. From comparison with the data points, it is clear that the finite element modeling effectively captures the effect of strain in the material very well.

In Fig. 2·16, I compare experimental results of 27 different line scans on 1-4 layer MoS_2 to simulations. This includes: four monolayer samples, twelve bilayer samples, four trilayer samples, and seven 4 layer samples. Fig. 2·16(a) differentiates the 27 line scans by 1-4 layers plotted as a function maximum strain, extracted from the Raman E^1_{2g}. The maximum strain for each layer thickness is 0.3%, 1.48%, 1.87%, 2.04% for 1-4 layers, respectively. The lowest maximum strain, out of 27 samples, was 0.09 % from a monolayer flake. The thicker samples show consistently high strain, while, in the the monolayer samples, the strain is below 0.5%. This is likely a consequence of the negligible bending

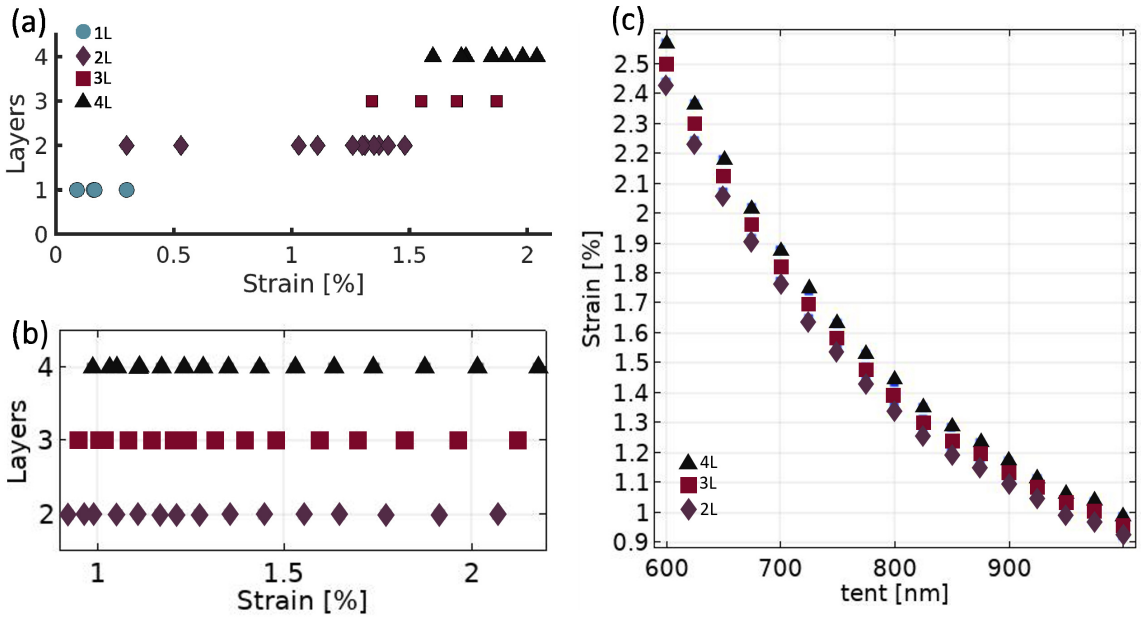

Figure 2·16: Relation between Strain and Tent Length for 27 line scans (a) 1-4 layer samples as a function of maximum strain in each layer. Strain is calculated from the Raman E^1_{2g} as shown in the previous section. Circle = 1 layer, diamond = 2 layers, square = 3 layers, triangle = 4 layers. (b) FEM calculated maximum strain in 2-4 layers. The strain is variable due to different tent lengths. (c) Maximum strain in 2-4 layer samples as a function of tent length, showing an inversely proportional relationship.

stiff of the monolayer samples. As a result the lower bending stiffness, The monolayer samples are more likely to have smaller tent sizes, and conform more closely to the pillar. The strain is therefore localized around the corners or sides of the pillars. Hence, when averaged over the Gaussian laser beam, the strain appears negligible. The maximum strain increases with increasing layer thickness, and can be matched with the FEM simulation results in Fig. 2·16(b) for 2-4 layer samples. This shows how strain can vary in samples of the same thickness covering different pillars, and provides an explanation for the variability we observe in the experimental data. Fig. 2·16(c), shows the maximum strain as from 2-4 layer samples calculated by FEM as a function of tent length.

It is clear that the tent length has a significant impact on the maximum strain observed in the material due to the nanopillar: maximum strain is inversely proportional to the tent length. Interestingly, the difference between 2-4 layers is more evident at smaller tent lengths, showing that the scaling stiffness starts to play a more important role in the deformation of the multilayer sample. Another variable that could impact the strain distribution is the amount of pre-strain in the sample due to growth, handling, or transfer of the MoS_2. This can also vary across different thickness of MoS_2. Increasing the pre-strain in the simulations only serves to “narrow" the strain distribution without effecting the overall peak strain value, as seen in Appendix A.8. Overall, these results show that by successfully modeling strain and comparing with real experimental data, finite element simulations can be utilized as a predictive tool to understand the expectant strain distribution and build an intuition for the morphology of multilayer materials deformed by nanopillars, without having to degrade the sample quality by imaging it under an SEM or conducting time-consuming AFM measurements.

2.7 Conclusion

In this chapter, I establish SiO_2/Si nanopillars as an efficient method to induce non-uniform strain in 2D materials. Although nanopillar strain for monolayers needs more investigation, multilayers are effectively strained between 1-2% using nanopillars of this design. Future endeavors in this direction can easily use the finite element modeling developed in this chapter to simulate strain in different pillar geometries, heights, and aspect ratios. It is important to understand the effect of interference for new geometries, as is demonstrated in this chapter.

In the next chapter, I investigate extraordinary enhancement in the photoluminescence in multilayer MoS_2 strained by nanopillars. I build on the methods developed in this chapter and investigate how charges and excitons are funneled to the region of maximum strain on top of the pillar. The resultant PL shows an increase in trion contribution, indicating that the localization of charges in the presence of neutral excitons increases the conversion of the latter to charged trions. The enhancement in 2-4 layers and it's origins are discussed, showing that the nanopillar-strained MoS_2 is a facile platform to observe unique light-matter interactions in indirect 2D materials.

Chapter 3

Photoluminescence enhancement from strain-induced charge and exciton funneling in multilayer MoS_2

3.1 Abstract

Non-uniform strain on multilayer TMDCs is an exciting path towards practical optoelectronic devices, as it combines the advantages of localized control of optical and electronic properties with ease of fabrication. However, the weaker photoluminescence (PL) due to their indirect nature poses a challenge to their application. Here, we demonstrate extraordinary enhancement of PL from multilayer MoS_2 under non-uniform strain generated by nanopillars. We observe charge and exciton funneling to the pillar strain-apex. The screening from the increased exciton and charge density lowers the exciton binding energy and renormalizes the band gap. Hence, we attribute the dramatic increase in PL to dissociation of bound excitons to free electron-hole pairs, showing that non-uniform strain on multilayers can effectively manipulate the nature of light-matter interaction in these atomically thin materials.

3.2 Introduction

In this work, we locally strain multilayer MoS_2 using nanopillars to explore funneling and diffusion in a prototypical indirect-gap 2D semiconductor. We find excitons in multilayer MoS_2 funnel towards the strain apex, even several micrometers from the pillar where the

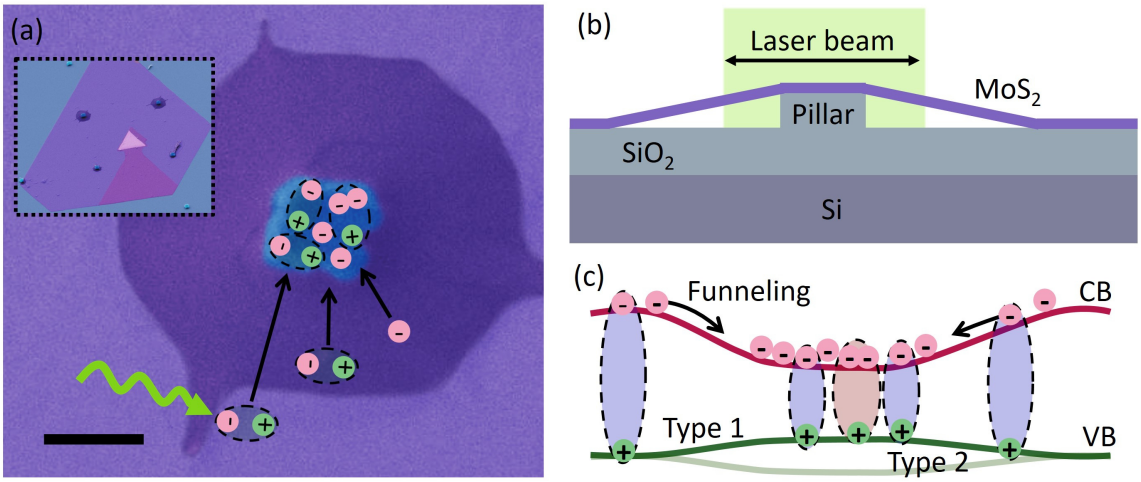

Figure 3·1: MoS_2 strained by nanopillars. (a) Colorized SEM image showing multilayer MoS_2 (purple) on top of nanopillar (blue) with "tented" region (dark purple). Scale bar is 300 *nm*. Inset: Nanopillar array covered by a large PVD MoS_2 domain. (b) Cross-sectional schematic. (c) Illustration of band-bending and funneling caused by local strain in the material.

strain gradient is very small. The strain profile also funnels charge to the strain apex, with a resultant increase in trion PL intensity. Overall exciton PL intensity is dramatically enhanced. The PL enhancement for multilayer MoS_2 at the strain apex is in stark contrast to the reduction expected from other effects. For example, excitons are converted to fast-decaying trions in the presence of excess charges. Strain–induced changes in the band structure makes the electronic structure more indirect, and the higher probability of exciton-exciton decay due to larger exciton density should also result in lower PL intensity. We discuss the PL enhancement below, concluding that the most likely reason is dissociation of excitons into free electron-hole pairs, due to charge and exciton screening.

The Raman and PL strain considered here follow from the 2-4 layer samples in Section 2.5 in the previous chapter. See Appendix B.1 for spectra from this sample, and other multilayers.

3.3 Strain-charge correlation map

The simultaneous red-shift of both Raman active phonon modes indicates that there is interplay of strain and charge in the system. Hence, it is necessary to decouple these effects in order to understand the structural and electronic changes in MoS_2. We construct a $\varepsilon - n$ correlation, or a Lee diagram (Lee et al., 2012), to optically separate the strain and charge. These axes are constructed from a linear transformation of the A_{1g} vs. E^1_{2g} positions (Michail et al., 2016; Chae et al., 2017; Sercombe et al., 2013).

First, let us quantify the strain on the Raman active phonon modes. Consider the strain tensor components ε_{ij} as defined by the infinitesimal strain theory,

$$\varepsilon_{ij} = \frac{1}{2}(u_{ij} + u_{ji}) \tag{3.1}$$

where u_{ij} define the displacement vector components in-plane. Solving the secular equation, we obtain the relative phonon energy shift for the E^1_{2g} from,

$$\Delta\omega(E^1_{2g}) = \Delta\omega(E^1_{2g})^h \pm \frac{1}{2}\Delta\omega(E^1_{2g})^s \tag{3.2}$$

where $\Delta\omega(E^1_{2g})^h$ and $\Delta\omega(E^1_{2g})^s$ are the phonon peak shifts from hydrostatic and shear strains, respectively.

The Gruneisen parameter γ and shear deformation potential β for the E^1_{2g} are defined as:

$$\gamma(E^1_{2g}) = -\frac{1}{\omega_0(E^1_{2g})}\frac{\partial\omega(E^1_{2g})^h}{\partial\varepsilon_h} \tag{3.3}$$

$$\beta(E^1_{2g}) = \frac{1}{\omega_0(E^1_{2g})}\frac{\partial\omega(E^1_{2g})^s}{\partial\varepsilon_s} \tag{3.4}$$

where the hydrostatic and the shear components of applied strain are $\varepsilon_s = \varepsilon_{xx} + \varepsilon_{yy}$ and $\varepsilon_s = \sqrt{(\varepsilon_{xx} - \varepsilon_{yy})^2 + 4\varepsilon^2_{xy}}$. Given biaxial strain ($\varepsilon_b = \varepsilon_{xx} = \varepsilon_{yy}$) and assuming no anisotropic distortion ($\varepsilon_{xy} = 0$), we see a vanishing shear strain in our system. Hence, given Gruneisen parameters from literature(McCreary et al., 2016; Kim et al., 2020; Lloyd et al., 2016), we can calculate the phonon energy shifts from Eqn. 3.2 as,

$$\Delta\omega(E^1_{2g}) = -2\gamma(E^1_{2g})\omega_0(E^1_{2g})\varepsilon_b \tag{3.5}$$

Following Eqns. 3.2-3.5 for the A_{1g} yields an analogous relationship,

$$\Delta\omega(A_{1g}) = -2\gamma(A_{1g})\omega_0(A_{1g})\varepsilon_b \tag{3.6}$$

Now, let us consider the relative shifts in phonon energies from changes in carrier concentration, which can be written as,

$$\Delta\omega(E^1_{2g}) = k_n(E^1_{2g})\Delta n \tag{3.7}$$

$$\Delta\omega(A_{1g}) = k_n(A_{1g})\Delta n \tag{3.8}$$

where $k_n(E^1_{2g})$ and $k_n(A_{1g})$ are the carrier concentration shift rates for the E^1_{2g} and A_{1g} phonon modes, respectively (Chakraborty et al., 2012; Miller et al., 2015).

We can therefore formulate a linear combination of Eqn. 3.5-3.8 to get the total relative shift of Raman active phonon modes in the presence of strain and charge,

$$\Delta\omega(E^1_{2g}) = -2\gamma(E^1_{2g})\omega_0(E^1_{2g})\varepsilon_b + k_n(E^1_{2g})\Delta n \tag{3.9}$$

$$\Delta\omega(A_{1g}) = -2\gamma(A_{1g})\omega_0(A_{1g})\varepsilon_b + k_n(A_{1g})\Delta n \tag{3.10}$$

The system of equations in 3.9&3.10 represents a linear transformation connecting the relative energy shift to strain and charge. Hence, we can express an equivalent system of equations as,

$$\varepsilon_b = \frac{k_n(A_{1g})\Delta\omega(E^1_{2g}) - k_n(E^1_{2g})\Delta\omega(A_{1g})}{2\gamma(A_{1g})\omega_0(A_{1g})k_n(E^1_{2g}) - 2\gamma(E^1_{2g})\omega_0(E^1_{2g})k_n(A_{1g})} \tag{3.11}$$

$$\Delta n = \frac{\gamma(A_{1g})\omega_0(A_{1g})\Delta\omega(E^1_{2g}) - \gamma(E^1_{2g})\omega_0(E^1_{2g})\Delta\omega(A_{1g})}{\gamma(A_{1g})\omega_0(A_{1g})k_n(E^1_{2g}) - \gamma(E^1_{2g})\omega_0(E^1_{2g})k_n(A_{1g})} \tag{3.12}$$

where, $k_n(E^1_{2g})$ and $k_n(A_{1g})$ are the electron shift rates, $\gamma(E^1_{2g})$ and $\gamma(A_{1g})$ are the Gruneisen parameters, $\omega_0(E^1_{2g})$ and $\omega_0(A_{1g})$ are the mean phonon positions, and $\Delta\omega(E^1_{2g})$ and $\Delta\omega(A_{1g})$ are the relative phonon energy shifts of the E^1_{2g} and A_{1g} phonons, respectively.

Table B.1 in Appendix B shows the respective values used in Eqns. 3.11&3.12 to construct the $\varepsilon - n$ correlation maps for 2-4 layer MoS_2.

Fig. 3·2 shows the $\varepsilon - n$ correlation extracted from 2-4 layer samples of MoS_2 on nanopillars. The respective SEM images of the samples show variations in “tent" region, shape of pillar, and presence of wrinkles in the 2D material due to transfer. The samples

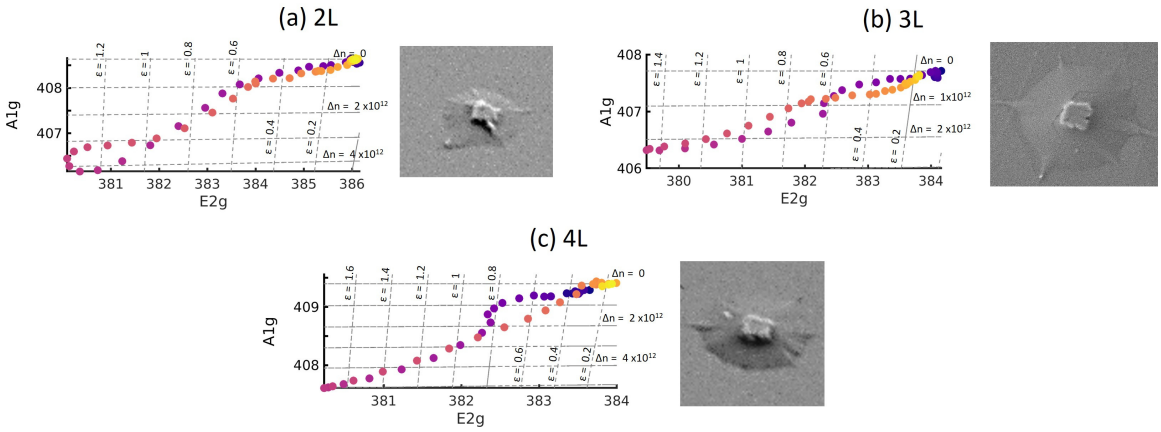

Figure 3·2: SEM images, and $\varepsilon - n$ correlation for 2-4 Layer MoS_2 on Nanopillars. $\varepsilon - n$ diagrams from (a) 2 layer, (b) 3 layer, and (c) 4 layer MoS_2 on nanopillars, along with SEM images of respective samples.

show a maximum strain of ε =1.3-1.7%, while the change in charge carrier concentration is Δn = 4.2, 2.1, 4.9 $\times 10^{12}$ cm^{-2} for 2, 3, and 4 layers, respectively.

3.4 Diffusion and Drift in Nanopillar-Strained MoS_2

Next, we use non-local PL imaging to directly observe exciton strain-funneling on trilayer MoS_2. I thank Hossein Ardekani in the Gundogdu Lab at NCSU for these results. The laser excitation is focused by a 0.7 NA objective to a diffraction limited spot of $\sim$0.45 μm while the PL from a large area is imaged on a CCD. Further details on these experiments can be found in Appendix B.3. The sample is scanned from y = -3 μm to y = 3 μm in 0.1 μm steps, and directly across the pillar in the center.

Fig. 3·3(a),(c), and (e) show three different positions of the laser, indicated by the yellow circle. Fig. 3·3 (b),(d), and (f) show the corresponding normalized profile of the PL intensity along the vertical axis . The position of the pillar at $y = 0$ is indicated by the blue bar. The laser beam (lavender peak inside the intensity profile) with width $w_0 = 0.45$ μm is significantly narrower than the PL intensity profile $w_{PL} = 0.91$ μm, which shows that the excitons readily diffuse from the generation area during their lifetime (Pulizzi et al., 2001; Xie et al., 2012). In Fig. 3·3(a), the laser spot is at y = -2 μm, and a slight asymmetry in the PL intensity can be seen in Fig. 3·3(b), with the tail of the PL intensity reaching the pillar location 2 μm away. In Fig. 3·3(c), when the laser spot is y = -1 μm away, the PL intensity profile (Fig. 3·3(d)) shows a secondary PL peak arising at the pillar position. When the excitation is coinciding with the pillar location (Fig. 3·3(e&f)) the PL line shape at the pillar is significantly narrower than on the substrate (Fig. 3·3(a&b)). The non-local PL imaging results indicate both strong exciton diffusion and drift from funneling. The peak broadening of the PL compared to the laser line-width is a measure of the diffusion, with a diffusion length $\sim \sqrt{w_{PL}^2 - w_0^2} = 1.0$ μm on the substrate. The funneling is evidenced by the asymmetry in the PL line-shape. The asymmetry in the PL intensity profile is visible as

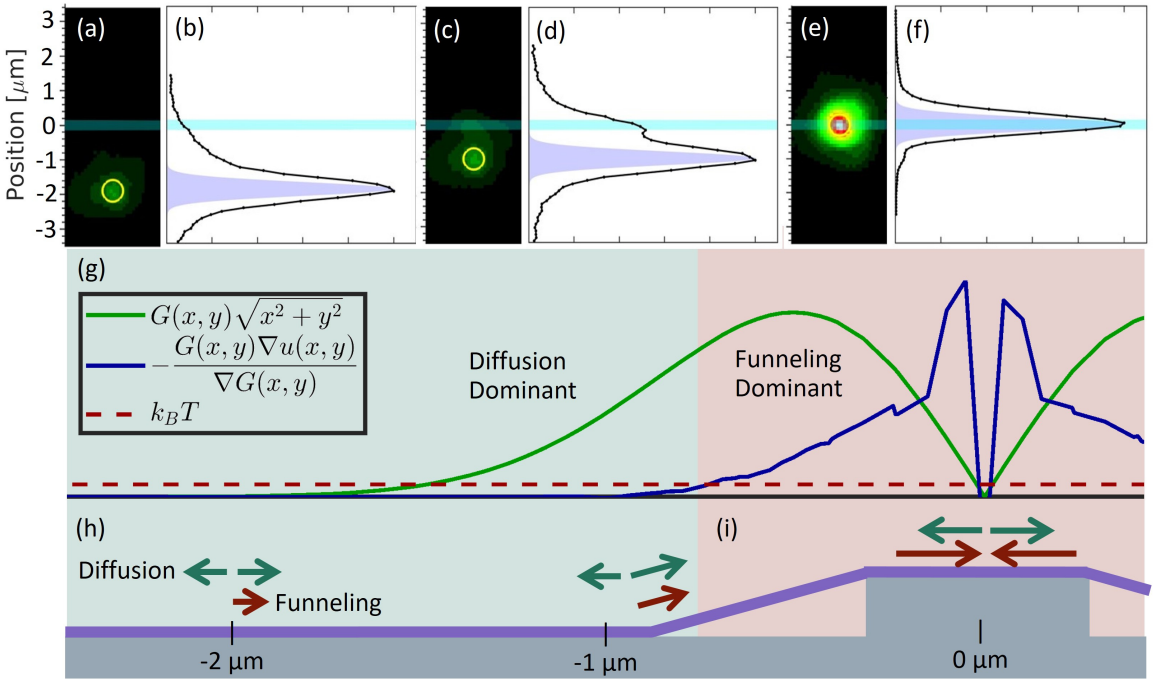

Figure 3·3: Non-local PL Imaging. (a-f) 3 different excitation positions and their resulting intensity profiles. (g) Ratio of drift and diffusion currents as a function of position from pillar (blue line) compared to k_BT at room temperature (red dashed line). (h-i) Schematic of interplay between diffusion (green arrow) and strain-induced funneling (red arrow) at the corresponding excitation position.

soon as the excitation spot starts to overlaps with strain profile (as shown in Fig. C·3(b)), well outside the suspended tent region. This indicates a zone outside the suspended region with strain due to slipping(Kitt et al., 2013; Wang et al., 2015).

In semiconductor devices, motion of charge carriers (electrons or holes) are dictated by two types of forces: diffusion and drift. For TMDCs, we can apply similar rationale to motion of excitons in the material. Due to a concentration gradient, a current is established where carriers move from an area of high concentration to area of low concentration. In our material, a concentration gradient is established due to the generation of excitons from to the Gaussian laser beam as well as by spatial localization of excitons. Therefore, diffusion current density for excitons,J_{Diff}, is governed by Fick's first law of diffusion which relates diffusive flux to the concentration gradient:

$$\vec{J_{Diff}} = -q\nabla \cdot (D_{exc} n_{exc}(x,y)) \tag{3.13}$$

where q is elementary charge, D_{exc} is the diffusion coefficient for excitons, and $\nabla n_{exc}(x,y)$ is the concentration gradient of excitons, and $\nabla = (\frac{\partial}{\partial x}, \frac{\partial}{\partial y})$. Here, we consider the MoS_2 to be a homogeneous, isotropic medium. Therefore, diffusion coefficient does not vary in space. Diffusion current exists even when there is no applied electric field, as it only depends on a spatial variation in concentration of excitons, and the direction of diffusion depends on the gradient of the concentration of excitons.

On the other hand, drift current is a result of an electromotive force imposed on charge carriers in the presence of an applied electric field. In our material, the applied electric force is a consequence of the band bending induced by strain in the material. Hence, a drift current is established, pointing in the direction of maximum strain. The drift current density, J_{Drift}, is governed by Ohm's law,

$$\vec{J_{Drift}} = -q\mu n_{exc}(x,y)\nabla u(x,y) \tag{3.14}$$

where μ is the mobility of excitons, and $u(x,y)$ is the strain-induced change to the band-gap. The diffusion coefficient and mobility are related by Einstein relation

$$D_{exc} = \mu k_B T_{RT} \tag{3.15}$$

where, k_B is the Boltzmann's constant, and T_{RT} is room temperature.

To ascertain the extent of funneling dominant behavior, we consider the ratio of the diffusion and drift currents(Harats et al., 2020). The ratio $\vec{J_{Diff}}/\vec{J_{Drift}}$, gives rise to the inequality:

$$D_{exc}\nabla n_{exc}(x,y) + \mu n_{exc}(x,y)\nabla u(x,y) < 0 \tag{3.16}$$

$$\Rightarrow -\frac{n_{exc}(x,y)\nabla u(x,y)}{\nabla n_{exc}(x,y)} > k_B T_{RT} \tag{3.17}$$

Considering an instantaneous laser generation, the exciton density can be therefore be equated as $n_{exc}(x,y) = G(x,y)$. Hence, Eqn. 3.17 can be re-written as:

$$k_B T_{RT} < -\frac{G(x,y)\nabla u(x,y)}{\nabla G(x,y)} \tag{3.18}$$

Here, $\nabla u(x,y)$ is the change in bandgap due to strain which is proportional to the funneling (drift) force, and $\nabla G(x,y)$ is proportional to the diffusion. From Eqn. 3.18, it can be see that drift dominates over diffusion when the left side of the inequality is greater than the thermal energy at room temperature, ie., $k_B T_{RT} = 25\ meV$. Using our finite element model of the strain in the trilayer sample, we plot both sides of the inequality in Fig. 3·3(g) as a function of position from the pillar. Fig. 3·3(g) shows that funneling-induced drift of excitons is dominant from $y < \pm\ 0.8\ \mu m$ from the pillar (red region). Beyond this, the exciton movement is dominated by diffusion (green region). This is illustrated by the schematic of the diffusion and funneling in Fig. 3·3(h&i), where the diffusion and funneling strength

is represented with different length green and red arrows, respectively. The competition between diffusion and strain-induced drift dictates the extent of PL broadening atop the pillar. In addition, a larger diffusion coefficient is expected for suspended material(Newaz et al., 2012; Kojima et al., 2019). At the apex of the pillar (Fig. 3·3(i)), the PL peak width is considerably smaller compared to on the substrate due to the strength of strain-induced band-bending concentrating excitons to the apex. Owing to the highly localized exciton density in this region, the outward diffusion is also stronger. Hence, the funneling at the strain apex is strong enough to counteract diffusion pressure that is here larger than on the substrate.

3.5 PL Enhancement and Charge Funneling

Next we consider the increase in PL intensity and the emergence of a sizable trion peak at the strain apex. From the $\varepsilon - n$ correlation map, we extract the spatial variation of charge density, shown in Fig. 3·4(a). It shows a substantial charge accumulation at the pillar of $\sim \Delta n = 2.1 \times 10^{12} cm^{-2}$. The strain gradient extends several μm beyond the pillar, and therefore collects charge from a large area. The accidental doping in these samples is likely electrons (Mouri et al., 2013), which is also supported by the band structure change with strain, as illustrated in Fig. 3·1(c). The downward deformation of the conduction band is larger than the change in the valence band, though it is not clear whether the valence band bends up with strain to capture holes (Type 1 funnel), or down, to repel them (Type 2 funnel) (Feng et al., 2012). Further experiments to change the dominant carrier concentration using gating (Lien et al., 2019) could provide clarification on the type of charge funneling observed.

In addition to the strain-related red-shift of the PL, the funneled charge accumulation at the pillar manifests in the appearance of a trion PL peak which is nearly non-existent on the substrate. Fig. 3·4(c),(d) show the raw PL spectra on the substrate and from the center of

the pillar. The substrate PL intensity has been multiplied by a factor of 15 to be visible. The trion contribution is shown by the red area. The PL trion-to-exciton ratio increases at the top of the pillar as a consequence of conversion of localized excitons to trions in the presence of an abundance of funneled charge carriers. This observation is in agreement with recent work on AFM tip-strained WS_2, which also demonstrated strain-funneled charge carriers causing increased exciton-trion conversion (Harats et al., 2020).

It is clear that the PL intensity at the strain apex is significantly enhanced, and by comparing the raw data, the enhancement of the PL intensity is a factor of 15. However, we need to first account for the difference in interference conditions between MoS_2 on the substrate and in the pillar region. We normalize the exciton and trion peaks by the interference enhancement (see Chapter 2, Section 2.4). The resulting total PL intensity on the pillar still shows a remarkable enhancement of 4.5 times compared to the substrate (Fig. 3·4(b)).

Qualitatively similar results are observed on the bilayer and 4 layer samples. Charge funneling (Fig. 3·5(a) & 3·6(a)) and a concomitant increase in trions on top of the pillar (Fig. 3·5(b) & 3·6(b)) is ubiquitous also in the bilayer and 4 layer samples of strained MoS_2. The PL spectra from the substrate shown in (Fig. 3·5(c) & 3·6(c)) were multiplied by 10x and 7.5x, respectively, demonstrating that the PL is enhanced for other multilayers as well. After accounting for interference effects as described in the previous section, the resultant PL enhancement for the bilayer is 380% (Fig. 3·5(b)). For the 4 layer, the total PL enhancement is 210% (Fig. 3·6(b)). From Fig. 3·5&3·6, it can be seen that the PL enhancement is inversely proportional to the extent of charge funneling on top of the pillar, which indicates that radiative processes are limited by presence of charges.

In Fig. 3·7, I compare the diffusion vs. drift behavior for 2-4 layers, using the strain calculated from the finite element models described in the last chapter. The purple, blue, and pink solid lines of Fig. 3·7(a) represent the $\vec{J_{Diff}}/\vec{J_{Drift}}$ for 2, 3, and 4 layers, respectively,

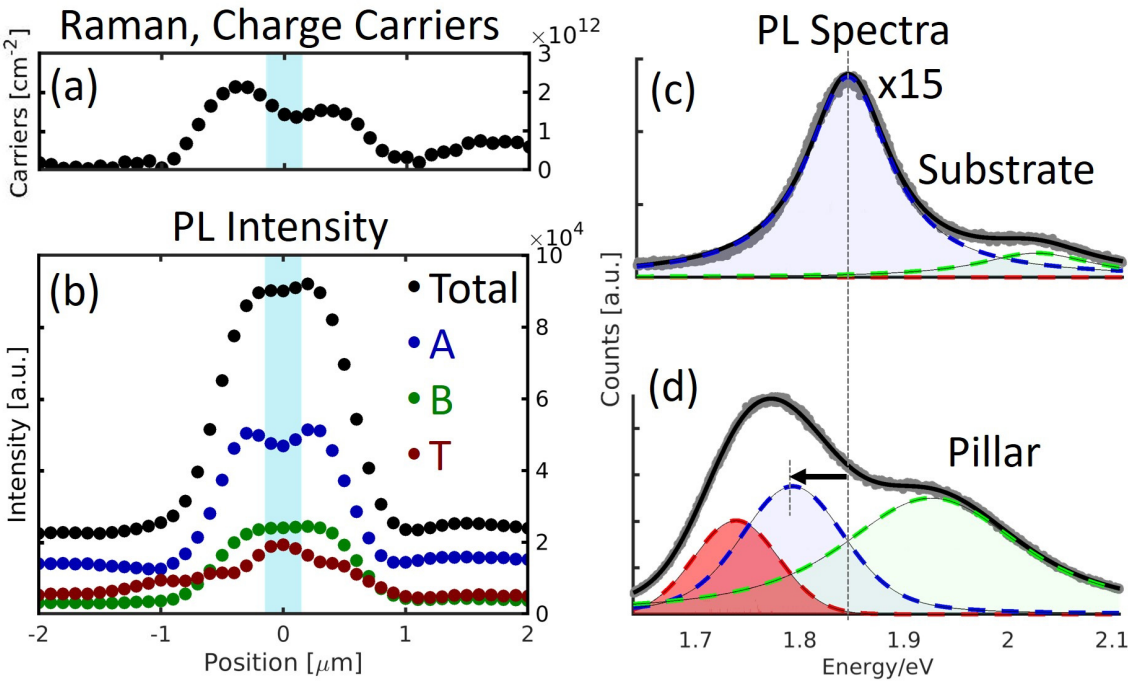

Figure 3·4: Charge Funneling and PL Enhancement. (a) Raman-extracted charge carrier concentration. (b) PL enhancement on the pillar. The total PL (black) shows a 4.5x enhancement from substrate to pillar, after normalization by interference effects. (c) Representative spectra from the substrate and (d) on top of the pillar with an increase in trions (red).

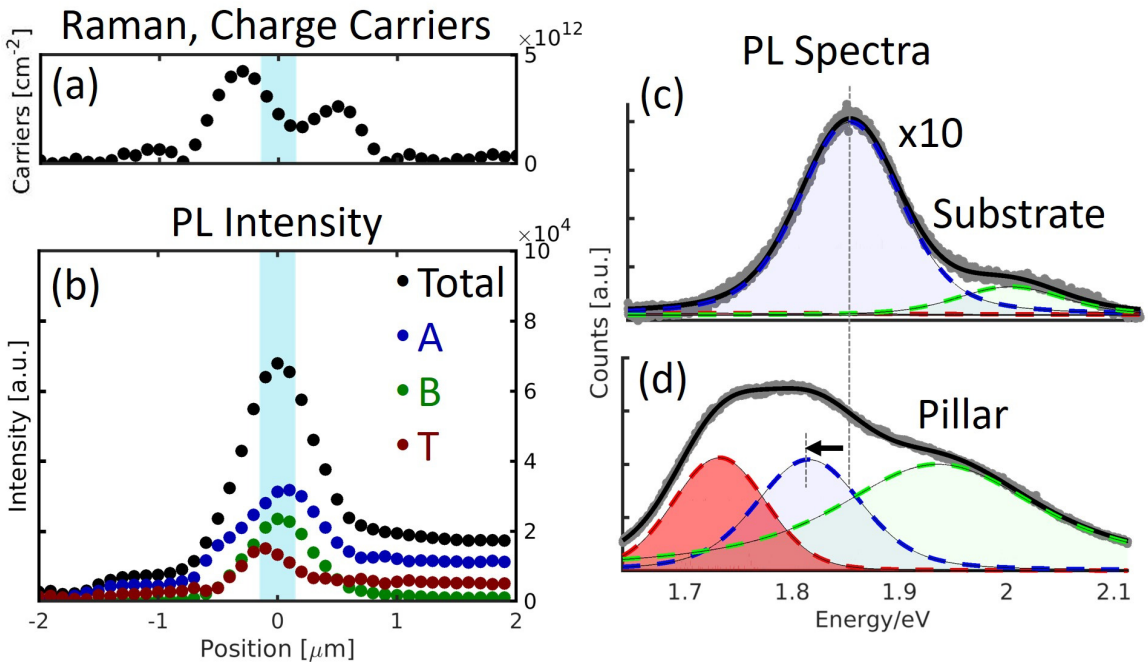

Figure 3·5: Bilayer MoS_2.

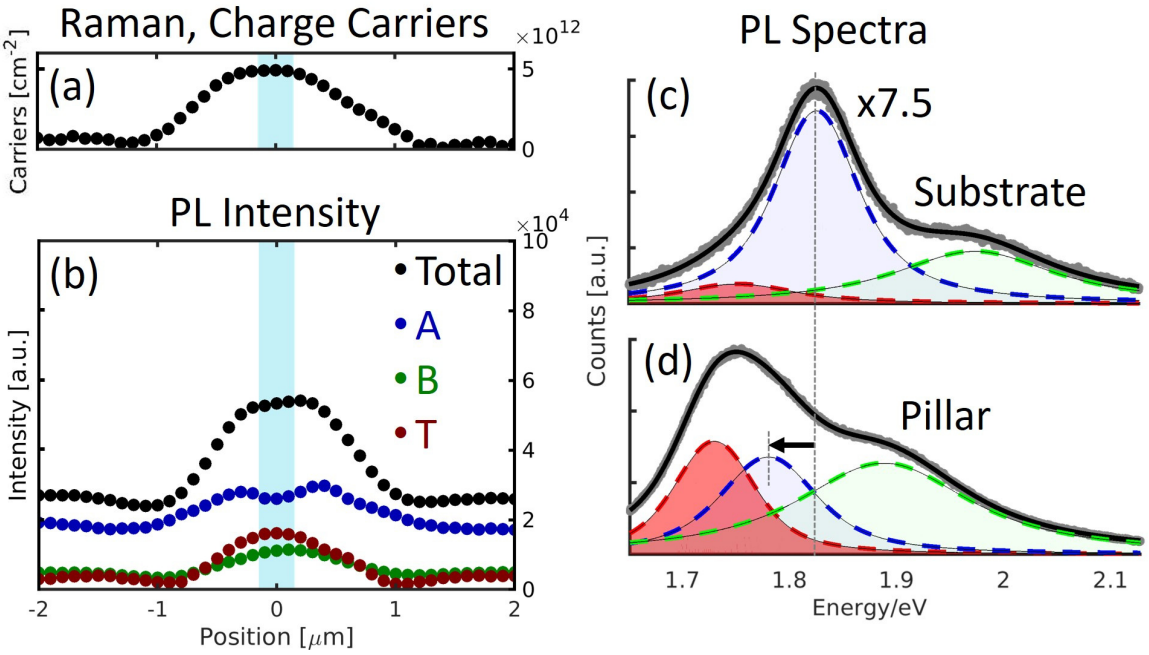

Figure 3·6: 4 Layer MoS_2.

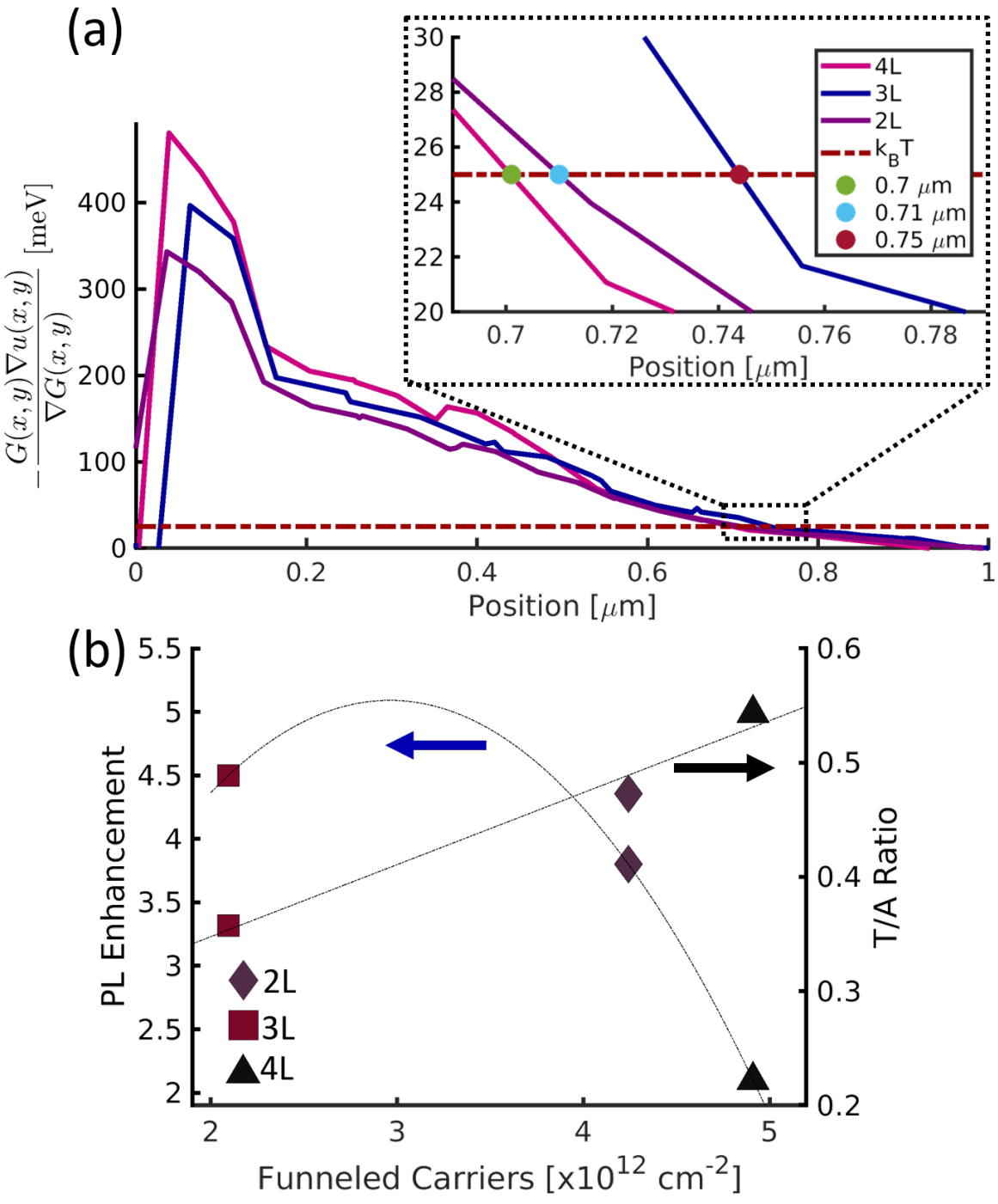

Figure 3·7: Simulated Diffusion vs Drift for 2-4 layers.

plotted as a function of position from the pillar. Close to the pillar, drift-dominant behavior is shown to increase with number of layers, $4L > 3L > 2L$. This is a consequence of the higher maximum strain exhibited by thicker materials, as seen in the last chapter. However, as the ratio of diffusion vs. drift approaches the thermal energy level at room temperature (red dashed line), the drift dominant behavior changes such that $3L > 2L > 4L$. The inset in Fig. 3·7(a) zooms in on this area. The drift lengths are 0.71 μm, 0.75 μm, 0.70 μm for 2-4 layers, respectively. This indicates that the trilayer MoS_2 funnels excitons over a region 50 nm greater than that of the 4 layer sample. These results corroborate the total PL enhancement seen in the 2-4 layer samples. Fig. 3·7(b) shows PL enhancement and Trion vs. A Exciton ratio as a function of the funneled charges. The PL enhancement follows the trend indicated by the drift lengths: $3L > 2L > 4L$. The exact increase in density of excitons due to this 50 nm region is the subject of future finite element analyses.

3.5.1 Origin of the Extraordinary PL Enhancement

It is important to note that we cannot explain the increase in PL intensity by funneling alone. The number of excitons created by the laser beam is fixed by the excitation density and the interference conditions. Hence, we need to consider possible changes in the non-radiative and radiative decay rates in the presence of local strain, exciton and charge accumulation. In monolayer MoS_2, the PL intensity drops with increased strain as a consequence of the electronic band structure becoming more indirect (Conley et al., 2013). In multilayer MoS_2, this trend continues with the bandgap becoming more indirect with strain (Lloyd et al., 2016). Hence, bandgap changes are not favoring higher PL intensity.

In the absence of quenching defects, the major contributions to the non-radiative rates are exciton-exciton annihilation, and trion annihilation (Javey et al., 2020; Lien et al., 2019). Here, we have both an increase in trions (due to the charge funneling and exciton-to-trion conversion) and highly localized excitons, which should lower the PL intensity. Doping-controlled studies have shown that compensating the accidental charge via a gate

voltage removes non-radiative decay channels (Lien et al., 2019). Here, we observe a higher charge density. Therefore, the 450 % PL increase is unlikely to be due to a reduction in the non-radiative rate, since the increased charge and exciton concentration at the strain apex would increase the non-radiative rate.

The effective lifetime of excitons at room temperature is much larger than what the oscillator strength would indicate, and therefore the effective radiative rates are much lower. This is due to momentum conservation; no exciton with momentum outside the light-cone can decay radiatively (Christopher et al., 2017). It is conceivable that the strain causes non-quenching trapping sites. By trapping an exciton at a local site, the excitons become bright. The strain profile produced by the pillar localizes excitons to a large area, not a point, so the strain localization is not sufficient to confine excitons to within the light cone and cannot account for the PL enhancement. If the exciton dispersion became steeper, a larger fraction of K-points would fall within the light cone, and would increase the PL yield somewhat. However, this would require the exciton mass to decrease, but the expectation is instead a small increase in exciton mass with strain (Rosati et al., 2021).

We believe that the most likely reason for the PL intensity increase comes from excitons dissociating into unbound electrons and holes (Chernikov et al., 2015a). Unlike excitons, band-to-band transitions do not have a stringent near-zero momentum requirement. Band-to-band transitions would require breaking the exciton binding energy, which is of the order of several 100 *meV* for suspended monolayer films (Chernikov et al., 2014). In low-dimensional materials, the strong Coulomb interactions are sensitive to external dielectric screening as well as internal charge screening. This will greatly affect the very strong exciton binding energy. In addition, the screening will renormalize the bandgap by hundreds of meV (Chernikov et al., 2015a). Interestingly, the energy of the exciton to bandgap transition is left almost unchanged since the bandgap renormalization (BGR) and reduction of binding energy nearly compensate each other(Raja et al., 2017; Gao and

Yang, 2017; Kane and Mele, 2004; Spataru and Léonard, 2010; Gao et al., 2016). The strain concentrates charge and excited quasiparticles, providing extra screening in the film, which will further reduce the exciton binding energy to allow free electron-hole pairs. Due to the tendency of bandgap and binding energy effect to cancel each other, spectral changes would not be obvious. Pump-probe studies or transient PL and reflectance experiments could further elucidate the origin of the strain-induced PL enhancement in these multilayer materials, and will be the basis of further studies.

3.6 Conclusion

In summary, we report on funneling of excitons and charge carriers in multilayer MoS_2 on nanopillars. Unlike previous studies, we show strong non-uniform, long-range strain $\varepsilon =$ 1.3-1.7 %, extending over 2 μm from the apex of the pillar, resulting in both charge carrier concentration and strongly enhanced PL. Using non-local PL imaging, we directly observe the interplay between diffusion and funneling-induced drift of excitons over a large region $\geq$2 μm. Overall PL intensity, normalized by the interference effects, shows a 450% difference from substrate to pillar, despite the more indirect nature of the strained material. We conclude that the most likely explanation for this behavior is direct band-to-band transitions of electron-hole pairs around the direct gap due to charge and exciton screening.

Controlling the localization of excitons and charge carriers is of particular interest for exploring novel physics and new optoelectronic devices. Earlier work on monolayer MoS_2, where expansion caused a direct-to-indirect transition, demonstrated that an electron-hole plasma (EHP) or electron-hole liquid (EHL) state could be reached at sufficiently high excitation densities (Bataller et al., 2019; Yu et al., 2019). Our samples would be amenable to explore this effect. Non-uniform strain profiles arising from different pillar geometries, or dynamically modulating strain through thermally-isolated MEMS devices (Christopher et al., ; Vutukuru et al., 2019), could improve the steering of localized excitons and charge

carriers, opening new doors in “straintronics" using excitons.

Chapter 4

Microelectromechanical Actuators

4.1 Introduction

Microelectromechanical systems (MEMS) possess all the functionalities of existing techniques for employing strain with the added advantages of being finely controllable and easily integrated into electronic devices due to their established commercial manufacturing process. MEMS actuators that operate by electrocapacitive or electrothermal action provide displacements in-plane suitable for straining 2D materials. Electrocapacitive "comb-drive" actuators consist of a series of interdigitated fingers acting as microcapacitors, and they are popularly utilized for their zero DC power usage and hence low operating temperatures. This type of actuator has recently been utilized for straining graphene to 0.24% (Goldsche et al., 2018). However, the actuation voltages run high for electrocapacitive actuators (>20V) and the resulting force is only on the order of μN, all while taking up significant chip area (Ye et al., 1998).

Electrothermal actuators, such as chevron actuators, are a strain platform with high output force (on the order of mN) and displacement with low operating voltages and device footprint (Sinclair, 2000). The viability of this platform has already been investigated for strain engineering of metal thin films (Zhu et al., 2006; Abbas et al., 2012; Saleh et al., 2015), carbon nanotubes or nanowires (Zhu and Espinosa, 2005; Lu et al., 2006; Espinosa et al., 2007; Brown et al., 2009), and monolayer MoS_2 (Christopher et al.,). A significant drawback to electrothermal actuators is the generation of heat as a means to produce displacement, with actuator temperatures that can swing from room temperature to $\sim$800

°C (Que et al., 1999). To use chevron actuators for 2D strain engineering, it is crucial to include thermal management of the 2D films as mechanical and structural properties of the materials are altered with temperature. Furthermore, thermal management design needs to take into account whether the device is operated in air or vacuum. Previous work which model and test operation of MEMS electrothermal actuators in SEM or TEM (Espinosa et al., 2007; Zhu et al., 2006), has to contend with vacuum conditions which removes one conduction pathway (via air). Other work which consider actuation in air use heat sink beams which decrease actuation of the device (Qin and Zhu, 2013). Another solution with reasonable temperature management and high output displacement uses cascading actuators but at the cost of a very large device footprint (Abbas et al., 2012).

Here we present an in air chevron actuator device design with a thermal isolation stage (TIS). This design maintains the 2D material strain device stage near room temperature without sacrificing output displacement and force, as confirmed through finite element simulation, analytical modeling, and measurement. The TIS device is compared with a standard device (SD) without the thermal isolation stage. We have improved the thermal management significantly compared to previous designs with a less than 10 °C increase at the 2D strain device stage at the highest actuation voltage while maintaining the high output displacement ($\sim$2.5 μm) of our standard device.

4.2 Device Architecture

Our MEMS devices are fabricated by the well-established PolyMUMPS process (Cowen et al., 2013), composed of three layers of highly degenerately doped surface micromachined polysilicon on a silicon nitride substrate interceded with sacrificial oxide layers. On dissolution of the oxide layers in an HF bath, two polysilicon layers are free to move and are suspended off the underlying substrate by 2 μm. Fig. 4·1 shows SEM images of two chevron-type electrothermal microactuators. The standard device has two stages: the

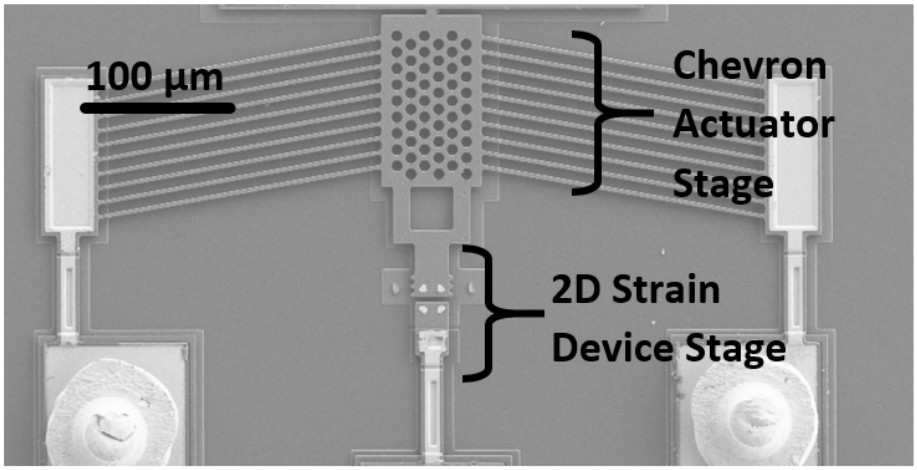

(a)

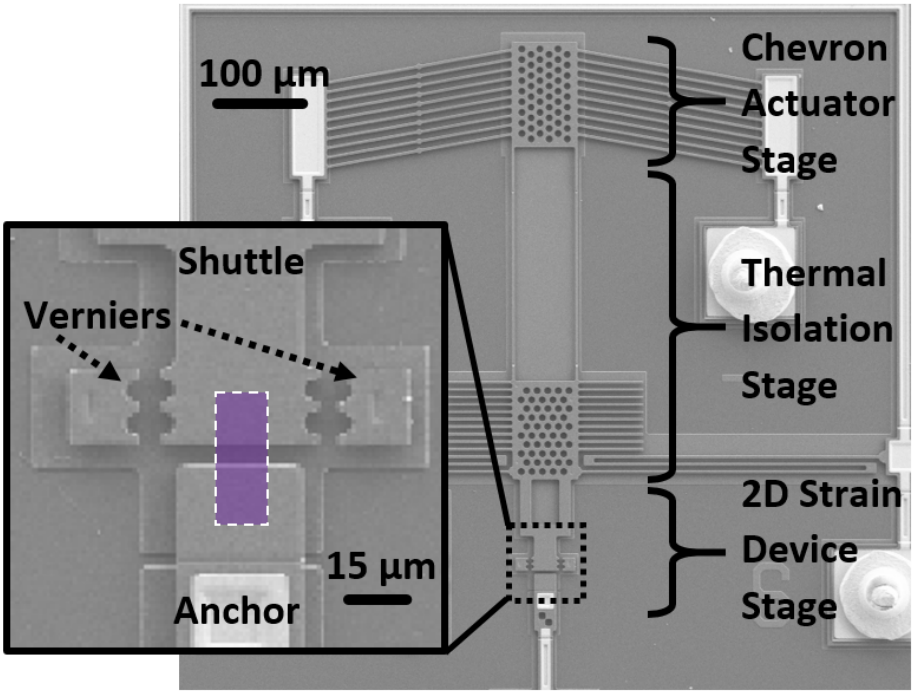

(b)

Figure 4·1: SEM images of (a) Standard Device (SD) and (b) Thermal Isolation Stage (TIS) Device. In the TIS device, the 2D strain device stage is isolated from the heat generated by the chevron actuator by the thermal isolation stage. The bright colored regions at the ends of the chevron actuator stage are the gold pads for electrical connection. **Inset**: The 2D material Strain Device Stage with a fictitious 2D film in purple spanning the gap between the anchored stage and the moving stage. The scalloped edges provides a visual vernier.

chevron actuator stage, and the 2D strain device stage. Our TIS device adds a thermal isolation stage between these two stages.

The chevron actuator stage consists of 10 pairs of released polysilicon beams, angled like chevrons, connected to a movable central shuttle. The two sets of chevron beams are anchored at either end to the substrate, where gold contact-pads provide electrical contact. When a voltage is applied across these terminals, the current passing through the beams generates Joule heating due to the resistivity of polysilicon. Free to move, these beams undergo thermal expansion, displacing the whole suspended device laterally from its equilibrium position. The angle of the chevron beams, here at 10 °from the horizontal, directs the majority of the co-planar motion in the y-direction along the substrate (Que et al., 1999).

The 2D strain device stage, seen in Fig. 4·1(b) inset, consists of a shuttle attached to the chevron actuator stage and an anchor point separated by 3 μm. Here, a suspended 2D film can be reliably strained between the moving actuator and the fixed anchor point. The scalloped edges act as verniers which provide optical evaluation of the motion.

Fig. 4·1(b) shows the TIS device, where a thermal isolation stage is placed between the actuator and sample stage. When designing a thermal isolation stage, there are several issues that need to be taken into consideration. One issue is that if the thermal isolation stage effectively shunts heat from the actuator, the actuation will suffer due to thermal loading (Qin and Zhu, 2013). Another consideration is the extra die space that is needed to physically isolate chevron actuator from the strain stage. This TIS device combines many conventional designs used for thermal management (Saleh et al., 2015; Zhu et al., 2006; Pant et al., 2012; Qin and Zhu, 2013; Zhu and Chang, 2015) with the goal of not affecting displacement for a given power, and still maintaining a relatively compact device footprint. The device was designed to operate in air, taking advantage of high thermal conductivity via the air gap between the suspended device and the substrate.

The added TIS does not compromise the actuation compared to the SD, as shown in Fig.

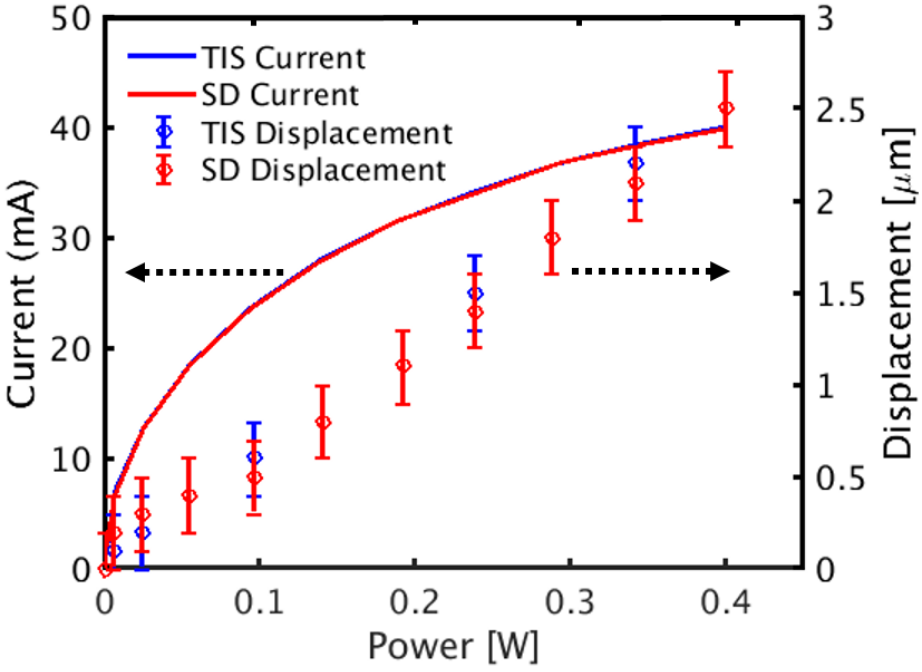

Figure 4·2: Measured current (solid line) and displacement (circles) of the SD and TIS device. Current is measured across the two terminals of the chevron actuator while the displacement is experimentally determined optically using a standard microscope. Error bars for displacement data are 200 nm, corresponding to the imaged camera pixel size.

4·2. The current generated by voltage actuation is identical for the SD and TIS device, as seen by the overlapping solid lines. The displacement vs input power is measured optically using the built-in verniers, as seen in the inset of Fig. 4·1(b). The displacement (circles) as a function of input power is also identical within the accuracy of the optical measurement (which could be further improved using digital image correlation methods (Naraghi et al., 2007)). The maximum displacement for both SD and TIS device is determined to be 2.5 μm at 0.4 W (10 V) of input power. Hence, the TIS device does not degrade the output displacement. During tensile testing of samples, the resulting strain should be corroborated by optical spectroscopy methods like Raman and photoluminescence since samples might slip. These two methods to measure strain have already been employed in monolayer MoS_2 using the TIS device (Christopher et al.,).

4.3 Multiphysics Finite Element Modeling and Analysis

When designing these devices, finite-element modeling is a useful tool to understand the displacement, current, and thermal profile response to a voltage input to the device. We use COMSOL Multiphysics to simulate the full geometry of the devices, accessing the Joule heating and thermal expansion modules. Finite-element modeling of both device designs were done to capture the integrated electrical, thermal and structural changes of device under actuation. Fig. 4·3 is a COMSOL Multiphysics model of our TIS device showing the essential features.

Structurally, the anchor points shown in the model are the fixed constraints for the devices, while the suspended device is allowed to nonlinearly expand through a temperature-dependent coefficient of thermal expansion. Thermal boundary conditions on the devices allow for thermal conduction through the polysilicon, and via air to the silicon nitride substrate which is constrained to room temperature. Conduction through air and silicon are dominant, so that convection and radiation can be ignored (Geisberger et al., 2003). Due

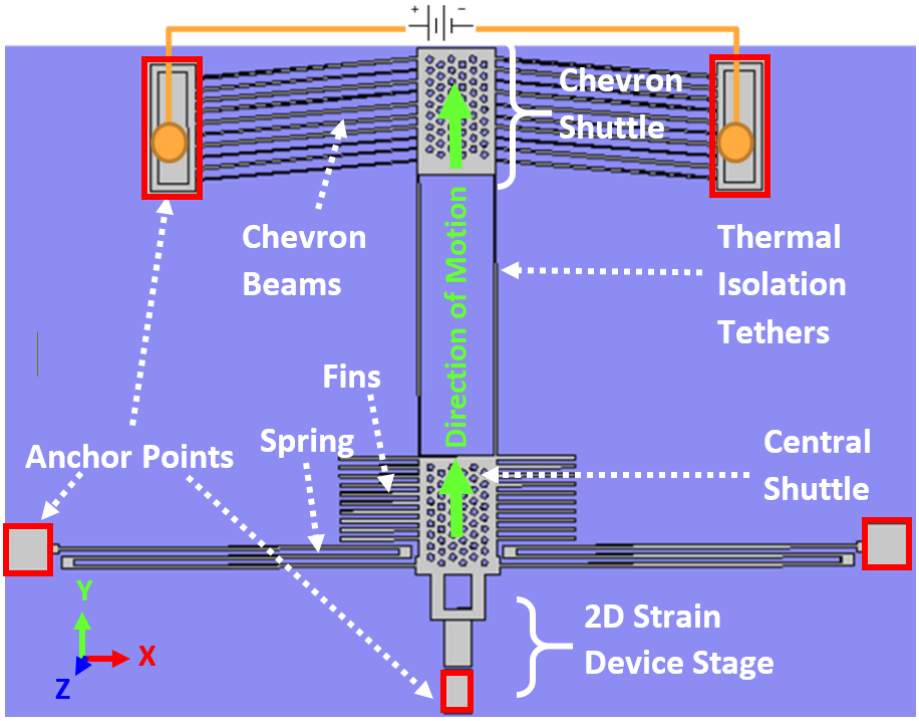

Figure 4·3: COMSOL Multiphysics model of the TIS device with the different components labeled. All components are free to move except the anchored parts (boxed in red). The joule-heated chevron actuator stage (top) shows the electrical contact points (yellow circles). The green arrows indicates the indicating direction of motion of the actuator. The purple background is the Nitride substrate which is assumed to remain at room temperature under actuation.

to the short air column under the suspended device, conduction through air is very efficient at removing heat at higher temperatures. In contrast, the conduction through polysilicon is less efficient at higher temperatures. Detailed discussion of the heat transfer mechanism through the TIS device is presented in Sec. slowromancapv@.

Electrically, an electric potential is applied across the chevron actuator between 0 to 10 V. The electrical conduction through the device is modeled with a temperature-dependent linearized resistivity, using reference resistivities given by PolyMUMPS fabrication processing with each run. The accuracy of our model relies on the temperature-dependent material properties that dictate the electro-thermo-mechanical physics in the device. Furthermore, for polysilicon, these material properties are related to dopant concentration and temperature (McConnell et al., 2001; Geisberger et al., 2003), and are nonlinear within the typical actuation range of our devices. Table slowromancapi@ in the Supplementary Material details the material properties used in the simulation.

The resulting model closely captures the displacement and IV characteristics of the fabricated devices. For 0.4 W (10 V) of input power, the SD and TIS device measured a displacement of 2.5 μm. The FEA model estimated a displacement 2.7 μm and 2.6 μm for the SD and TIS device, respectively. Hence, the improved TIS design is comparable in both displacement and power intake to the original device, from which we can conclude that the thermal isolation stage does not significantly diminish the motion of the shuttle. Simulated and measured displacement and IV characteristics for the SD and TIS can be found in Fig. 2 in the Supplementary Material.

4.4 Thermal Measurements

To measure the temperature of the microstructures, we used two thermal metrology methods. IR thermometry provides a large-area view of the devices which is useful for distinguishing regions of high temperature in a rapid and qualitative way. However, IR ther-

mometry lacks the temperature range and spatial resolution to resolve smaller areas on the devices, such as chevron beams or thermal isolation tethers. Raman thermometry is valid through the whole temperature range and has high spatial resolution, but assessing temperatures over large areas is time-consuming. The large-area overview and distinct hotspots of the device are easily identifiable with the use of IR while the Raman can be used to determine temperatures of smaller components. Hence, the two methods work in a complementary fashion to fully capture the thermal profile of our devices.

4.4.1 Infrared Thermometry Measurements

In order to provide a large-area overview of the temperatures in our devices, we actuated the devices using an Optotherm IS640 thermal imaging camera with 5 μm resolution, giving a field of view of 3.2 x 2.4 mm at a working distance of 20 mm. The thermal camera, equipped with an amorphous Si microbolometer detector, operates within the long-wavelength infrared range from 7-14 μm. Emissivity for the suspended polysilicon microstructures were calibrated by recording the thermal image at different stage temperatures using a Peltier thermal stage. The emissivity of the polysilicon for our microstructures was measured to be e = 0.4. This falls in the range of possible spectral emissivities calculated for silicon of 0.4 to 0.71 (Sato, 1967; Abedrabbo et al., 1998; Zhang, 2000), and is taken to be constant within the operating temperature range of this device.

Fig. 4·4 shows the devices under the thermal imaging camera when actuated to 0.14 W (5 V). It is clear that without the thermal isolation stage, the 2D strain device stage is heated to 50% of the hottest chevron beam temperature, as seen in the SD images. On the other hand, the 2D strain device stage on the TIS device remains close to room temperature for the same actuation conditions.

The optics of the system are calibrated to most accurately measure temperatures within the range of 10-300 °C. Chevron actuators such as ours are known to go to temperatures in excess of 700 °C, rendering the IR imaging as an ineffective thermal metrology technique

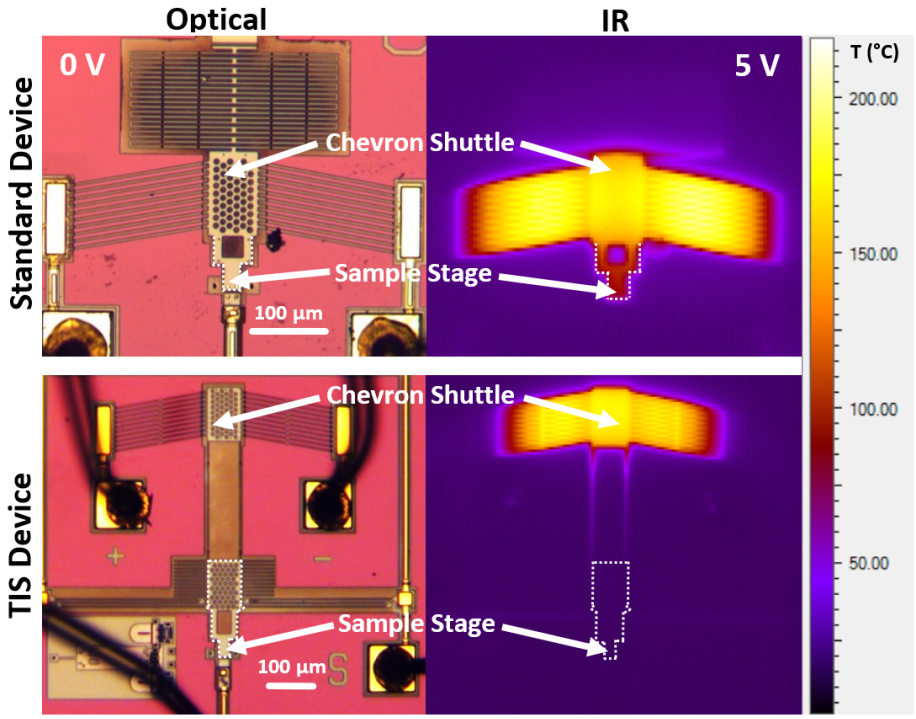

Figure 4·4: Optical and thermal images of the activated SD and TIS devices. Left column: Optical images of un-activated devices (0 V). Right column: IR thermographs of the activated devices (5V). Temperature is denoted by the color gradient scale from 0-230 °C.

in the high input power regime. Furthermore, the spatial resolution of the system at 5 μm/pixel is at its far-field diffraction limit. This is another restriction as components of our device such as the chevron beams and thermal isolation tethers have dimensions between 2-3 μm, making it difficult to assess temperature in those localized areas.

It is clear from the IR thermal profile that the thermal isolation stage is efficient in removing the heat generated by the chevron actuator stage in the TIS device. For 0.14 W input power, the temperature along the thermal isolation tethers drops from 190 °C at point A to 21.4 °C (room temperature) at point B, as shown in Fig. 4·5. The temperature decrease is nonlinear and drops by $\sim$ 40% in the first 10th of the thermal isolation tether. This temperature drop is mainly due to conduction through air and not the conduction through the beam, as discussed in section slowromancapv@. The thermally isolated 2D strain device stage (outlined with a dashed white line) is indistinguishable from the background in the thermal image indicating it remains at $\sim$RT.

4.4.2 Raman Thermometry Measurements

Raman spectroscopy is a well-established thermal metrology tool for polysilicon microdevices (Serrano et al., 2006; Sarua et al., 2006; Kearney et al., 2006). It has high spatial resolution, comparable to the minimum device dimensions, as well as high temperature accuracy. In polysilicon, the Raman active mode is $\omega_0 \sim$520 cm^{-1} which linearly red-shifts with increase in temperature within the typical actuation range of the MEMS actuators. The temperature change ΔT has been calibrated to be at a rate of approximately $C_{Stokes} =$ -0.0232 cm^{-1}/ °C (Abel et al., 2007a) so that $\Delta T = \Delta\omega / C_{Stokes}$, where $\Delta\omega$ is the shift of the silicon peak from ω_0.

The Stokes peak position of this Raman mode is also sensitive to stresses in the material. However, free-standing, fully flexible MEMS actuators grown by low-stress LPCVD techniques have been shown to have negligible stress-induced bias on the peak shift (Abel et al., 2007b). Effects of internal stresses on the coefficient of Stokes shift are therefore

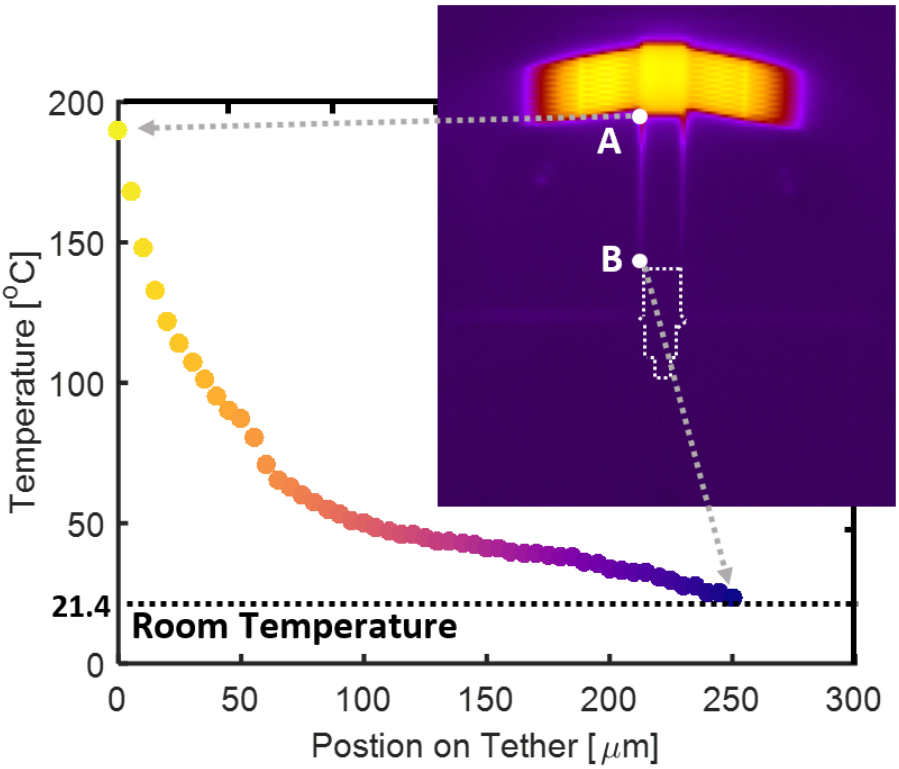

Figure 4·5: Wide-view IR temperature measurements along a tether. From Point A at the start of the tether near the chevron shuttle to point B near the 2D strain device shuttle, the temperature profile is mapped for the TIS device actuated to 0.14 W (5 V). We see that the temperature near the shuttle starts at $\sim$ 180 °C (point A) and dissipates to room temperature (21.4 °C) at point B. Color scale same as in Fig. 4·4.

justifiably neglected in calculating temperature. Raman measurements were conducted in-situ on the devices under actuation using a confocal microRaman system (Renishaw Inc). The devices were illuminated using an Argon ion laser, λ =514.5 nm excitation, using an Mitutoyo 100x objective (0.58 μm beam waist). An irradiation power of 1 mW was used, which did not measurably optically heat the sample. The scattered signal is detected on a thermoelectrically cooled CCD detector. The spectral pixel resolution is 1 cm^{-1}/pixel, while the measurement resolution was two orders of magnitude better (Srikar et al., 2003). 20 spectra were taken for each data point, yielding a consistent photoelectron count of 8×10^3. The standard deviation on each data point was less than 0.01 cm^{-1}, hence the error bars are not visible in the graph. Fig. 3 in the Supplementary Material demonstrates the effect of temperature on the Stokes peak of the polysilicon as measured from the center of a chevron beam.

4.4.3 Temperature Profile Comparison

In order to quantify how well the TIS device works for mitigating large operating temperatures, we take a closer look at the area of interest- the 2D strain device stage of the microactuator. The IR image in Fig. 4·4 shows that the 2D strain device stage of the SD experiences high temperatures due to proximity to the actuated chevron beams. Thermal dissipation mechanisms are inefficient over the short range of the device. The 2D strain device stage of the TIS device, on the other hand, is thermally protected from the chevron actuator stage by the thermal isolation stage. We compared the temperature range of the center of the 2D strain device stage through Raman thermometry, shown in Fig. 4·6. Even at the highest chevron actuator temperature (735 °C), the 2D strain device stage of the TIS device increases by less than 10 °C, reaching a maximum temperature of 30 °C. By comparison, the 2D strain device stage of the SD increases in temperature by more than 180 °C, reaching a maximum temperature of 202 °C. Such temperatures in the region of a 2D film to be tested will affect its mechanical, thermal and/or optical properties. Raman

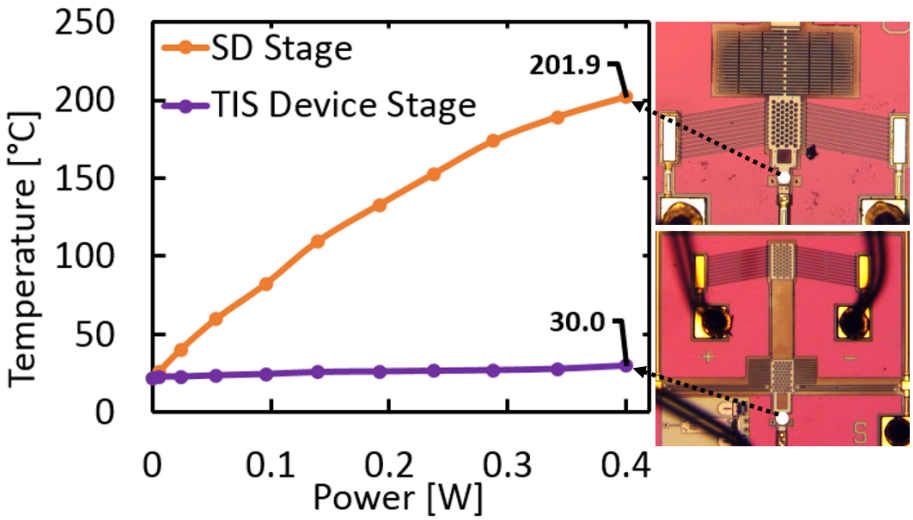

Figure 4·6: Raman thermometry of the SD and TIS device devices at the center of the 2D strain device stage. SD device: The temperature of the 2D strain device stage increases by 180 °C under device actuation. TIS device: The temperature of the 2D strain device barely increases due to the addition of the thermal isolation stage. For both devices, the maximum temperature is at the chevron beams (735 °C).

thermometry of multiple points of the TIS device is shown in Fig. 4·7. While the 2D strain device stage is thermally isolated, the chevron beams and chevron shuttle reach maximum temperatures of 736 °C and 469 °C respectively.

Comparison of Raman and IR thermometries with finite-element simulation of the temperature of the fifth chevron beam shows good agreement, as seen in Fig. 4·8. Experimental measurements using IR were limited to 0.19 W (6 V) power input to keep within the calibrated temperature range of the Optotherm IS640 camera. The slightly lower temperature from the simulated data compared to the measurements are attributed to the uncertainty in the temperature-dependent polysilicon materials parameters used in the simulation. For example, variation in dopant concentration, or grain size in the polysilicon would lead to changes in the phonon mean free path. This would result in changes in thermal conduction and hence in the resulting temperatures (Geisberger et al., 2003).

4.5 One-dimensional heat transfer and Lumped Thermal Circuit Analysis

The goal of a thermal isolation stage is to avoid a temperature increase at the 2D strain device stage without thermally loading the chevron shuttle significantly, which would decrease the actuator motion at a given power. In this section, we discuss the effectiveness of the thermal isolation stage design. As the core functionality of electrothermal actuators, these devices generate high amounts of heat, particularly at their hottest points on the chevron beams. Our improved design capitalizes on the high output force/displacement of the standard design while simultaneously mitigating high temperature at the sample end. The added thermal isolation stage acts as a voltage divider circuit which shunts heat directly to the substrate via air to prevent the heat from reaching the 2D strain device stage. We use one-dimensional heat transfer analysis in a simple lumped circuit model (LCM). This analysis provides simple, back-of-the-envelope calculations for designing thermal iso-

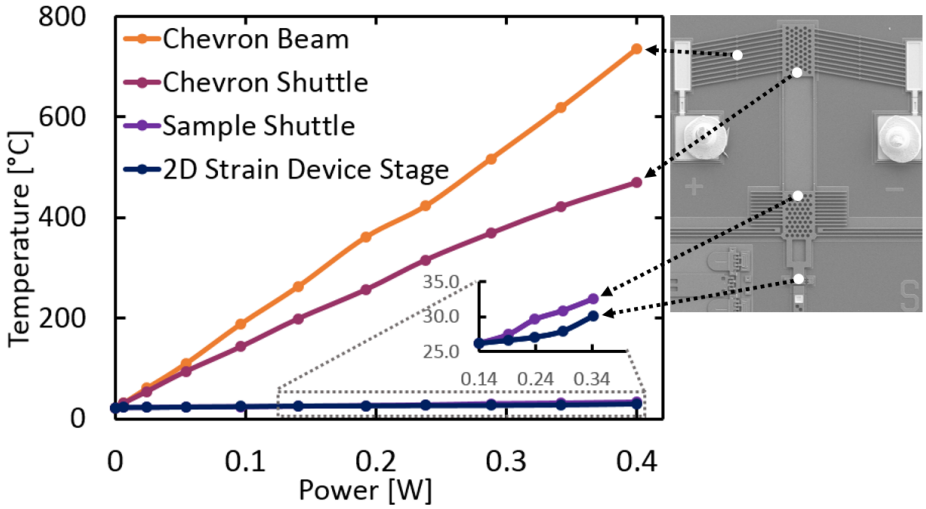

Figure 4·7: Temperature breakdown for the different stages of the TIS device. At 0.4W (10 V) input power, the highest temperatures are generated at the chevron beams, around 730 °C. The chevron shuttle at full actuation has a maximum temperature of around 470 °C. However, temperatures at the sample shuttle and 2D strain device stage rise to a maximum temperature of about 32 °C and 30 °C, respectively. Thus, the thermal isolation stage successfully circumvents the high temperatures generated by the chevron actuator stage during device actuation.

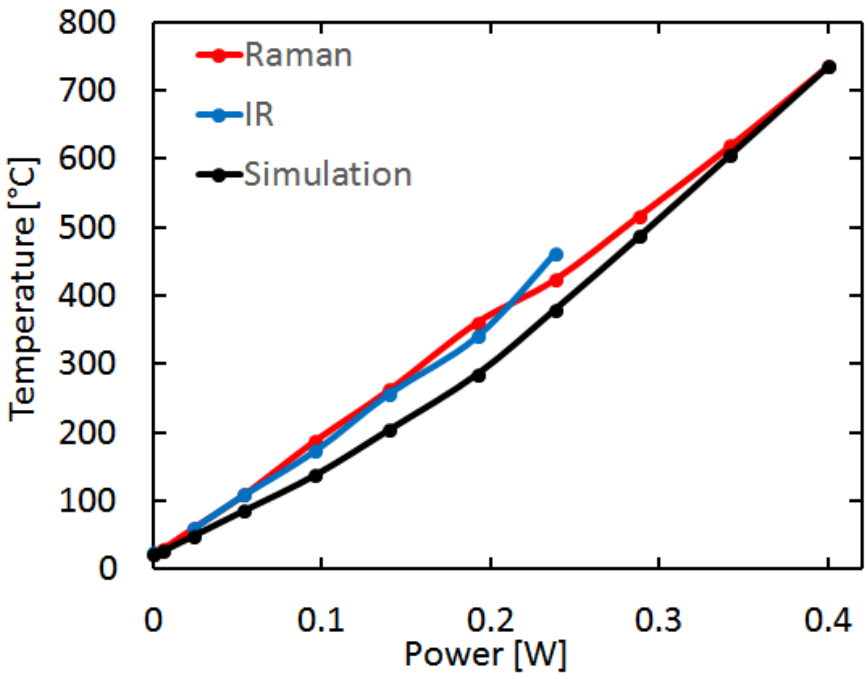

Figure 4·8: Comparison between measured and calculated temperature using IR, Raman and FEA. The temperature at the center of the 5th chevron beam of the TIS device was monitored as a function of input power. IR, Raman and FEA show good temperature agreement. IR measurement was limited to 0.19 W (6 V) to keep within the temperature limit of the IR camera.

lation stages under desired constraints, e.g., reducing die space. The thermal circuit model is useful for quickly assessing the heat transfer of different designs, since full device simulations using FEA as seen in Sec. slowromancapiii@ are time consuming.

We begin with considering the mechanisms of one-dimensional heat transfer. Thermal convection and radiation are assessed to be negligible in the temperature range considered, compared to thermal conduction through air and polysilicon (Geisberger et al., 2003). Heat flux q due to conduction in a material is proportional to the temperature difference ΔT. The heat transfer along an element in one dimension can then be written as:

$$q = -k\frac{A}{\Delta x}\Delta T \tag{4.1}$$

where k is the material's thermal conductivity, A is the area normal to heat flow and Δx is length of heat flow. Using the analogue to electrical circuits, we consider the temperature gradient to be analogous with the voltage difference and heat flow to be analogous with electrical current. Thus, we can set up an Ohm's Law relation for a thermal circuit:

$$\Delta T = q \cdot R_{thermal} \tag{4.2}$$

The thermal resistance $R_{thermal}$ can therefore be calculated by:

$$R_{thermal} = \frac{\Delta x}{k \cdot A} \tag{4.3}$$

We model the components of the TIS as thermal resistors, as seen in Fig. 4·9, and use Eqn. (4.3) to calculate their values. There are two conduction pathways to the silicon nitride substrate: through the polysilicon, and through air. At high temperatures, conduction through air dominates over conduction through polysilicon, while the opposite is true for lower temperatures.

Using accurate temperature-dependent conductivity values to calculate resistances would

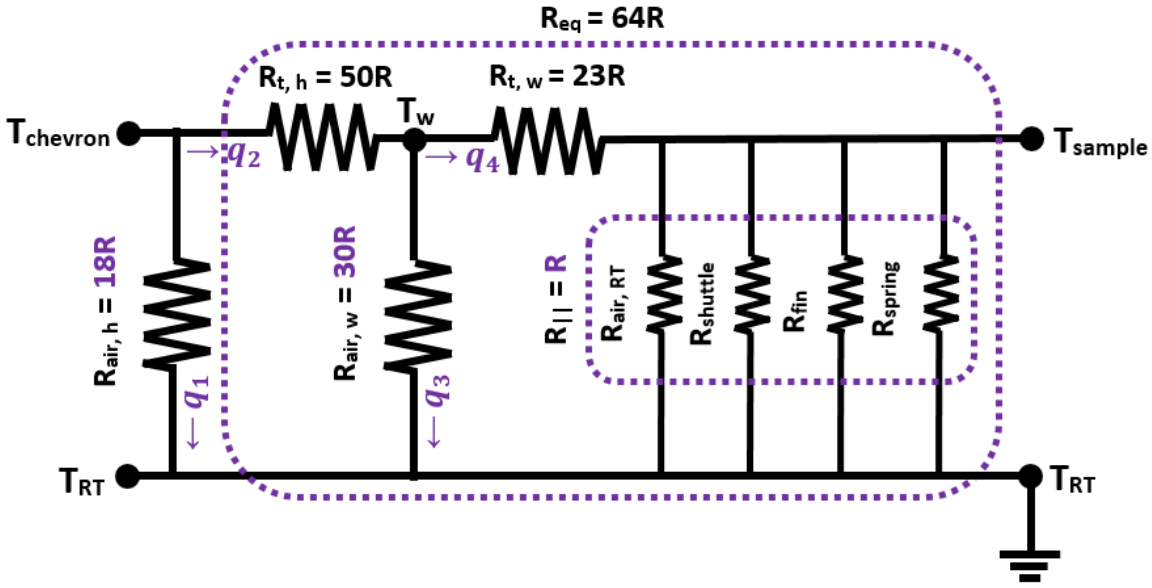

Figure 4·9: TIS device as a lumped circuit thermal divider. The tether resistors $R_{t,h}$ and $R_{t,w}$ conduct heat through the Si tethers. $R_{air,h}$, $R_{air,w}$ and $R_{air,RT}$ in purple conduct heat from the tether through the air-gap to the substrate at room temperature T_{RT}, likewise for central shuttle and resistances ($R_{shuttle}$, R_{fin}). R_{spring} conducts heat through the spring and air. The heat currents are denoted by q_i.

result in a complex model where temperatures would have to be known *a priori*. In order to keep the model simple but predictive, we use only three conductivities: hot, warm and room temperature values. The resistances of the first half of the tether, $R_{t,h}$ and $R_{air,h}$, correspond to the conductivities at the hot chevron shuttle, $T_{chevron}$. We use IR thermometry to guide the conductivity choice for the second part of tether. The temperature T decreases quickly with position x along the tether. Hence, we pick the warm temperature in the middle of the tether, T_w, as roughly 1/4 of $T_{chevron}$, and the corresponding resistances to be $R_{t,w}$ and $R_{air,w}$. This choice works reasonably well for the temperature measurements along the tether for a number of input powers, as seen in Fig. 5, the Supplementary Material. For simplicity, the rest of the thermal isolation stage used room temperature (T_{RT}) values for thermal conductivities.

Now that we have determined the resistances based on geometry and conductivities, we can use the LCM to calculate the temperature of interest at the 2D strain device stage is T_{sample}. A summary of our circuit analysis variables and resistances can be found in Table slowromancapii@ in the Supplementary Material. Details of k_{si} and k_{air} as a function of input power and temperature can also be found in Fig. 6 in the Supplementary Material.

As seen in Fig. 4·9, an equivalent resistance $R_{||}$ can be used to replace the four mutually parallel resistances $R_{air,RT}$, $R_{shuttle}$, R_{fin}, and R_{spring}. We can also make an equivalent resistance, R_{eq}, for our circuit as indicated by the dashed line in purple in Fig. 4·9. In order to design an effective thermally isolated device in air, the TIS design should shunt a large portion of the heat through air in order to prevent it from reaching the 2D strain device stage; that is, to make $q_1 > q_2$ and $q_3 > q_4$. Finally, $R_{||}$ should be small compared to $R_{t,w}$ to keep T_{sample} as close room temperature as possible. We also want the overall resistance of the TIS to be high enough so that the TIS does not significantly thermally load the actuator.

Using the previously defined resistances, the T_{sample} can be related to $T_{chevron}$ as:

$$\Delta T_{sample} = \frac{R_{||} R_{air,w}}{R_{eq}(R_{t,w} + R_{||} + R_{air,w})} \Delta T_{chevron} \tag{4.4}$$

Details on the derivation can be found in Section slowromancapi@ in the Supplementary Material. Using the calculated resistance values for the highest input power where $T_{chevron} = 469.2$ °C, we find:

$$\Delta T_{sample} = 0.8\% \Delta T_{chevron} \tag{4.5}$$

According to the LCM, at the highest input power, the 2D strain device stage increases in temperature by $<1\%$ of the temperature generated at the chevron shuttle, which corresponds to T_{sample} = 25.3 °C. This is reasonably close to the measured value of 30 °C and is useful for a first pass of designing the thermal isolations stage.

In Fig. 4·10, we compare the measured temperatures (Raman) of the 2D strain device stage with the LCM and FEA simulations for different chevron beam temperatures. The effectiveness of the TIS stage is confirmed using all temperature analysis methods. Both the LCM and the FEA simulation slightly underestimate the temperature of the 2D strain device stage. As mentioned in Sec. slowromancapiv@, this discrepancy could be due to variations in polysilicon material properties. In addition, the substrate is constrained to be at room temperature for the LCM and the FEA simulations. However, the substrate could be heating up slightly as result of the device actuation, which would raise the overall temperature of the 2D strain device stage as measured by Raman. To maintain the substrate at room temperature and bring the measured temperature closer to the simulation, the entire die can be mounted on a thermal electric cooler (Christopher et al.,). Details of the calculations for a second input power as well the general trend of the percentage increase in temperature and ΔT_{sample} as it varies with input power can be found in Table slowromancapiii@ and Fig. 7 in the Supplementary Material.

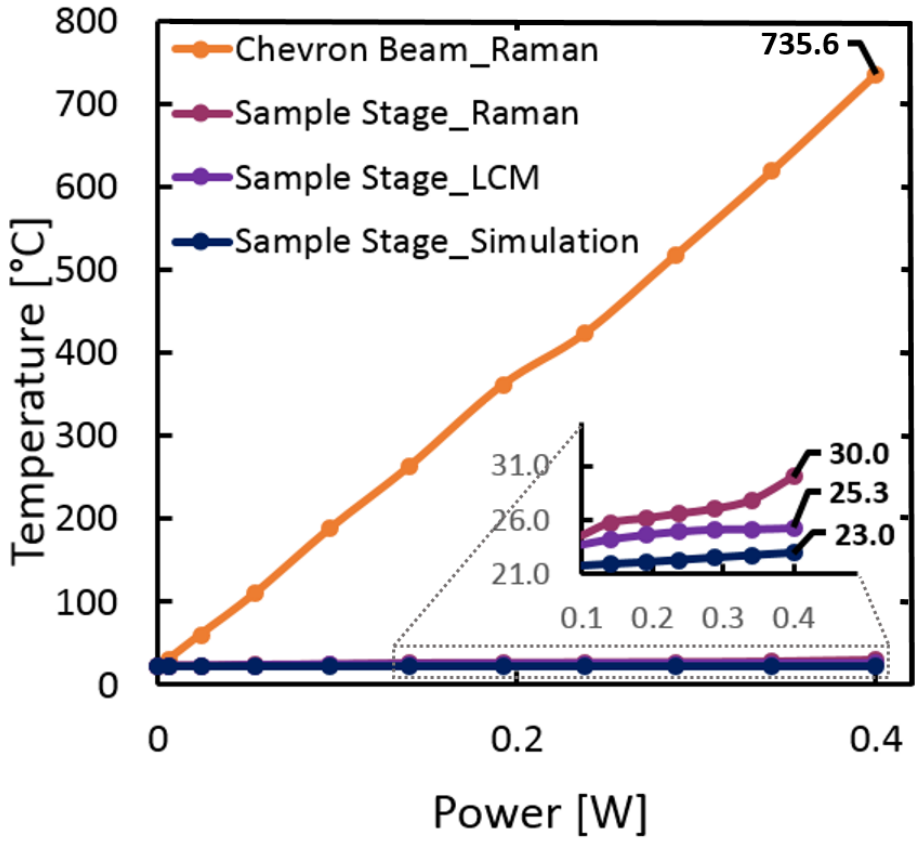

Figure 4·10: Comparison of chevron beam and 2D strain device stage temperatures. Chevron beam temperature is measured through Raman thermometry. 2D strain device stage temperature is measured by Raman, and predicted by the LCM, and FEA simulation. **Inset:** The measurement, 1D-LCM, and FEA of the 2D strain device stage are closely matched.

4.6 Conclusion

We have presented a thermally isolated device for use in air that does not compromise the output displacement ($\sim$2.5 μm) achieved by our standard design. Despite the added thermal isolation stage, our design remains compact, occupying a 600 μm x 700 μm footprint. As determined by our thermal metrology techniques, we observe a temperature increase of $\leq$ 10 °C from room temperature on our 2D strain device stage at actuation temperatures of 735 °C. Our FEA modeling predicts we could achieve $\leq$ 2 °C of increase in temperature at the sample end if we maintain the substrate at room temperature. Hence, our modeling and thermal analysis shows that the TIS device is a suitable, thermally isolated platform to strain engineer 2D materials.

Finally, we have developed a simple lumped thermal circuit model for analyzing the thermal isolation stage. The LCM is good for estimating initial device parameters, even though it is a highly simplified model. Our model is sufficient for a first order approximation for analyzing the effectiveness of the thermal isolation stage. To quickly evaluate different design ideas, the LCM would useful for future work on optimizing TIS devices, using back-of-the-envelop calculations instead of time-consuming simulations.

Chapter 5

2D Material Integrated MEMS Devices

5.1 Abstract

We report a new transfer method for 2D materials from a growth substrate onto non-planar, non-supported target substrates, such as released MEMS devices. We utilize a polymer membrane together with a direct-laser written microstructure to transfer materials onto areas of flexible, released microactuators without damage to the MEMS device or the 2D materials. Our transfer method allows precise placement of the 2D film on the device, uniform distribution of the stamping force during transfer, and small contact footprint between the microstructure and MEMS which minimizes contamination. Here, we demonstrate the precision transfer of 2D materials with near non-existent contamination of the MEMS. Successful transfer of monolayer MoS_2 and few layer graphene is demonstrated through spatially resolved Raman spectroscopy, photoluminescence mapping, and SEM imaging of the 2D materials on the MEMS actuators, with the MEMS remaining fully functional.

5.2 Introduction

MEMS actuators are micromachined devices made of polysilicon and nitride base, interspersed with sacrificial oxide layers. In order to actuate the devices, the oxide layers must be dissolved in hydrofluoric acid; this is the so-called ¨release˝process. The actuator, seen in Figure 5·1 is comprised of three parts: 2D strain device stage, thermal isolation stage, and chevron actuator stage. When the power is applied across the ball-bonded pads shown

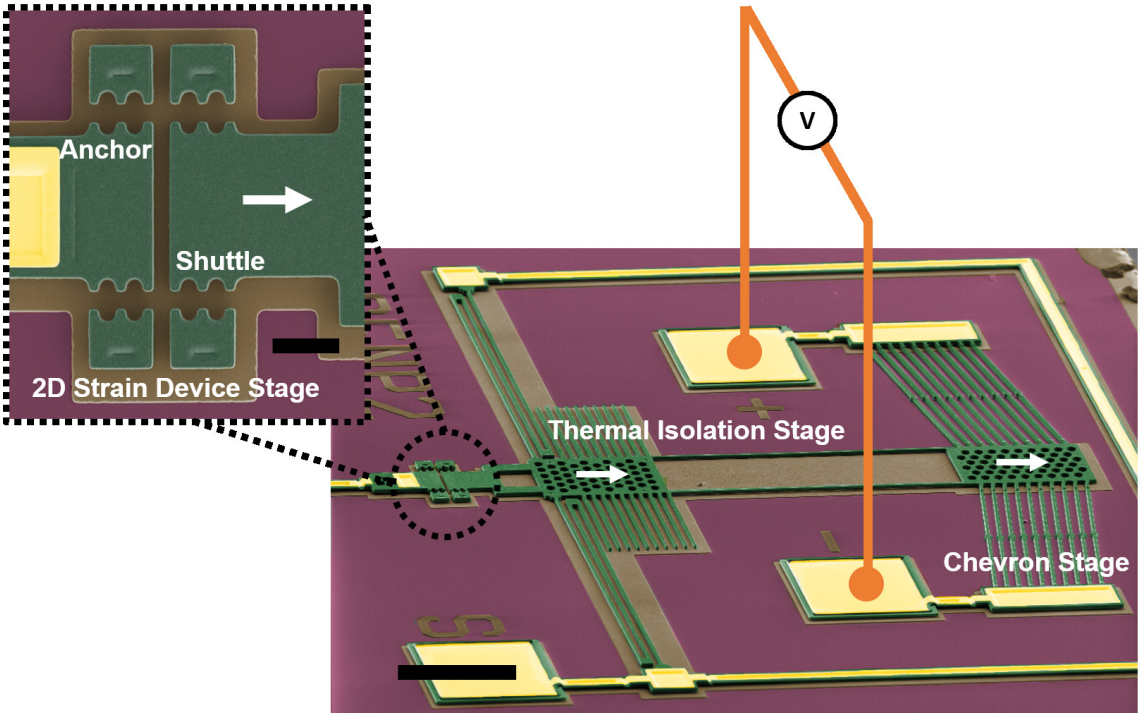

Figure 5·1: False color SEM image of a MEMS electrothermal actuator. The actuator consists of 3 parts: 2D strain device stage (inset), thermal isolation stage, and Chevron stage. The device moves in-plane in the direction of the white arrows when given an input voltage across the gold ball-bonded pads. Scale bar is 100 μm **Inset**: The 2D strain device stage consists of a shuttle, attached to the moving actuator, and an unmoving anchor. A 2D film suspended across the gap between anchor and shuttle can be reliably strained. Scale bar is 10 μm

in gold, the beams in the chevron stage undergo thermal expansion due to Joule heating and move the released part in-plane, in the direction of the white arrows. The thermal isolation stage separating these stages ensures that the 2D material being strained remains isothermal and is unaffected by the high temperatures generated at the chevron stage (Vutukuru et al., 2019). The 2D strain device stage, shown in the inset of Figure 5·1, consists of the shuttle, movable under actuation of device, and an unmoving anchor point, separated by a gap. Given adequate anchoring, 2D materials supported on the shuttle and anchor points can be strained reliably across this gap. For the purposes of studying strain in fully-suspended materials through optical methods like Raman spectroscopy, the gap was designed to be 3 μm. These actuators are very strong in-plane, capable of high output forces in the *mN*s (Sinclair, 2000). However, due to the large surface-to-volume ratio, these actuators are fragile and prone to buckling and breaking under forces applied normal to the plane.

5.3 Building on Existing Transfer Techniques

Several techniques for integrating 2D materials into devices have been developed. Early methods utilize wet-etching of metal growth substrate and polymers like poly (methyl methacrylate) (PMMA) to transfer 2D films onto flat substrates (Reina et al., 2008; Liang et al., 2011; Li et al., 2009) or for suspending samples (Lin et al., 2011). Wet transfer methods without the use of polymers were also devised for large-area 2D material transfer while preserving electrical properties (Lin et al., 2014; Zhang et al., 2016). Alternative polymers such as poly(propylene) carbonate (PPC), poly(phthalaldehyde) (PPA), or paraffin were also trialed in order to create more atomically clean, wrinkle-free transfers (Wang et al., 2013; Wood et al., 2015; Leong et al., 2019). Dry transfer methods can be useful for reducing contamination, such as for forming sealed microchambers (Suk et al., 2011), van der Waals heterostructures (Pizzocchero et al., 2016), or flexible devices (Fernández et al., 2018; Fechine et al., 2015). Delamination transfer techniques of 2D materials without wet-

etching of underlying metal may be favorable for reducing ionic impurities that percolate on graphene during the etch process (Yang et al., 2015; Marta et al., 2016). Direct transfer or roll-to-roll mechanisms have been invented to streamline the device fabrication process without any intermediate steps (Martins et al., 2013; Shivayogimath et al., 2019).

The low out-of-plane force tolerance of released microactuators renders conventional transfer techniques of 2D materials unfeasible, for example the polymer “stamp" method which utilizes a polydimethylsiloxane (PDMS) block on a glass slide, mounded by tape. However, this transfer method is best used for flat substrates, where the stamping force is evenly distributed during the transfer. For non-planar, released substrates like MEMS devices, this stamping force is enough to cause damage to the structure and lead to buckling of the movable parts. In addition, the sizes of the stamps are on the order of several hundred micrometers, resulting in a large footprint of contamination. Traditional transfer methods could be used by transferring before release onto a rigid MEMS device, followed by wet-etch of the oxide layers in HF. However, we have found that the HF used in subsequent degrades the 2D material properties. Hence, a modified transfer procedure is necessary to accommodate non-planar devices with movable, fragile parts while also keeping the 2D film unharmed during transfer.

Here, we introduce a specially designed polymer microstructure that forms part of a universal, deterministic transfer method for 2D materials. We use direct laser writing to print a 3D polymer microstructure which allows us to custom design around the specifications of the MEMS device. See y Information for more details on the microstructure. This microstructure is combined with a polymer membrane for deterministic transfer of materials onto non-planar surfaces like MEMS devices, with no impact to the device’s functioning while maintaining 2D film’s quality. We integrate monolayer MoS_2 grown by physical vapor deposition (PVD) and few layer graphene (FLG) with MEMS electrothermal actuators to demonstrate the versatility of this transfer system for atomically thin and layered mate-

rials. We confirm that the materials maintain quality by Raman and PL spectroscopy. SEM imaging on materials post transfer also shows that the transfer process does not introduce wrinkles or contamination which could affect the electronics of the strained devices. The DLW microstructure can be redesigned and printed to be compatible with different strain platforms. Moreover, this method is universal for 2D materials on flat growth substrates such as SiO_2, and can be used to transfer and suspend TMDCs, graphene, or other layered materials on to MEMS actuators for strain engineering.

5.4 Transfer Procedure

5.4.1 Microstructure Assembly

The transfer method we present here adds the microstructure to the polymer transfer method developed by Wang *et. al.* (Wang et al., 2013). A PDMS cube of 1 *mm* side length is placed on top of a glass slide, as is shown in Fig. 5·2. Using clear tape, the PDMS is domed such that it's highest point can be easily determined by the formation of Newton rings when touching a flat surface such as SiO_2 substrate. When making contact with the target substrate, the highest point of the domed PDMS cube will be the point of first contact with the substrate, barring extreme deformation of the PDMS where the 3D microstructure is places.

Using a probe tip inserted into the keyhole, we place the microstructure on the taped PMDS dome at it's peak. UV curable glue is introduced to the base of the microstructure using a micropipette. The arrays of pedestals wick the glue into the channels on the underside of the microstructure through capillary action. Without the pedestals, the glue will not evenly distribute as a thin layer under the microstructure. The microstructure is glued securely to the tape under UV light exposure. Optical images and further details of this process can be found in the Supplementary Information. A schematic of the resulting assembly is shown in Fig. 5·2.

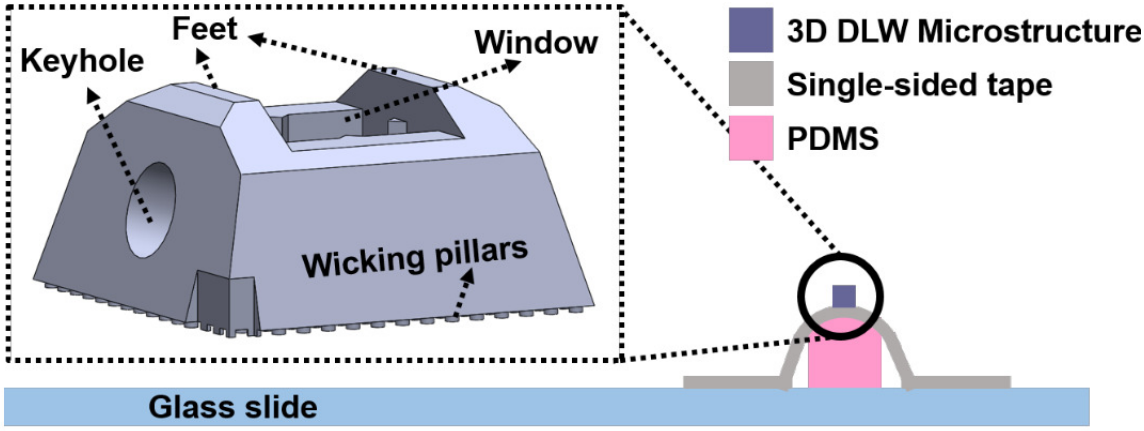

Figure 5·2: Schematic of the microstructure attached to the tape-domed PDMS block on a glass slide. The clear tape is pressed around the PDMS, causing it to dome. The microstructure is placed at the highest point and attached with UV curable glue that wick evenly under thep pillars. The optical window allows for precise placement of the 2D film. The feet will be the only contact points between the microstructure and the substrate.

This assembly can be reused hundreds of times for transferring materials, as it can be easily rinsed to clean off polymer residue from the transfer process, using common organic solvents like isopropyl alcohol or acetone. However, there is a gradual degradation of the UV glue from repeated solvent cleaning, limiting the lifetime of the assembly after hundreds of transfers. Mechanical impact (too strong pressure applied during transfer, sideways impact etc) can deform or peel off the microstructure from the tape.

5.4.2 2D Film Transfer Preparation

Here, we consider the approach to prepare PVD MoS_2 for transfer from SiO_2, as an example. The procedure can be applied to other TMDCs as well as for exfoliated layered materials, like graphene.

After growth, a suitable MoS2 flake is identified using optical methods (Castellanos-Gomez et al., 2010). We spin coat polypropylene carbonate (PPC) on top, (see Supplementary Information for PPC recipe and spin information) which yields an even coating of PPC of 1 μm thickness. PPC is a common polymer used in the transfer of 2D materials because of the strong adhesion between the PPC and the 2D material. In addition, PPC has a low glass transition (around 40 °C) temperature which can be exploited for tuning the adhesion strength, even before the polymer melts (Kinoshita and Moriya, 2019). Using a 60 μm probe tip (T-4-60 Picoprobe from GGD Industries Inc.), we introduce cuts in the polymer around the desired flake. These are strain-relief cuts and are essential for transfer on to the MEMS, as described in the next section. We use the DI H_20 float release technique to lift the membrane of PPC+MoS_2. See Supplementary Information for details on this procedure.

The membrane with the MoS_2 is then transferred on to the microstructure assembly (Fig. 5·3(a) and (b)). In order to have the MoS_2 on the top, the single-sided tape holding the PPC+MoS_2 membrane is flipped and reattached to the transfer frame. Using a micropositioner, the membrane on the transfer frame is carefully brought in contact with the

microstructure on the glass slide, as shown in Fig. 5·3(a). The 2D material is centered in the window of the microstructure, and the strain relief cuts are aligned to the sides of the microstructure legs. The polymer film outside the window is allowed to conform over the domed PDMS block. Finally, the single sided tape meets the glass slide which adheres the membrane to the stack, as seen in Fig. 5·3(b).

This assembly requires significant deformation of the polymer film around the microstructure, which could irreparably stretch, wrinkle, or tear the 2D material. This is where the strain relief cuts are useful. They relieve tension as the cuts can open a gap to accommodate stretching, keeping the film taut. The legs of the microstructure provide anchor points for the film also limits tensions to the supported film as the polymer is conformed outside of the microstructure. The result is a supported wrinkle-free 2D film, ready to be transferred.

5.4.3 2D Material Transfer on to MEMS

The transfer system as shown in Fig. 5·3(b) is ready to transfer the 2D material onto any arbitrary substrate. We use a transfer station fitted with microscope, micropositioners, copper integrated with a heater to facilitate the transfer (see Supplementary Information for setup details). The heating of the copper stage serves two purposes: to fine-tune position in z through thermal expansion of the copper stage with heating, and to melt the PPC. The glass slide is flipped and inserted in to a micropositioner such that the 2D material is the first to make contact with an underlying substrate. The slide is confirmed be to horizontal using a level. As the assembly is comprised of materials that are transparent (i.e., glass slide, PDMS, tape, polymer), the 2D material is clearly visible through the central window of the microstructure (See Supplementary Information for optical image of transfer). Here, we transfer the 2D material onto 2D strain device stage of the MEMS electrothermal actuator, as shown in Fig. 5·3(c).

It is important to increase the hydrophilicity of the MEMS substrate in order to have

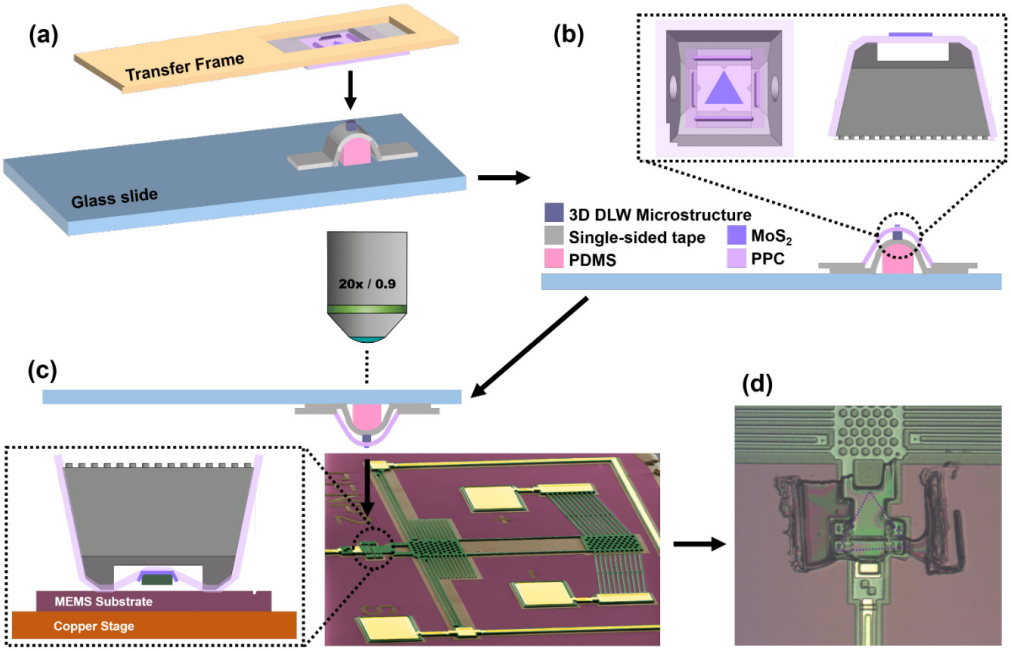

Figure 5·3: Transfer of the 2D Material onto the MEMS.(a) The PPC+MoS_2 is transferred on to the microstructure assembly, with the MoS_2 aligned in the center of the microstructure, and facing up after flipping the PPC film. (b) The single-sided tape (adhesive side facing down) adheres to the tape on the microstructure, securing the membrane on to the assembly, additionally aided by the strain release cuts. (c) The final 2D material transfer assembly is used to transfer the material on the 2D Strain Device Stage of the MEMS device. As the microstructure makes contact with the MEMS substrate (purple), the PPC deforms around the released actuator stage (green). (d) When the microstructure is lifted off, the PPC and MoS_2 (outlined in pink) in contact with the MEMS device remains behind.

good contact and adhesion of the 2D material to the strain stage. Therefore, immediately before transfer, the MEMS device is plasma-ashed in oxygen (Huang et al., 2015). The device is placed on the copper stage initially heated to 40 °C, the glass transition temperature of PPC. This temperature ensures that the PPC will be soft and pliable as it makes contact with the MEMS device. The combination of the strain relief cuts and glass transition temperature allows for huge deformation of the polymer membrane without inducing stresses in the 2D material, similar to kirigami of 2D materials (Blees et al., 2015; Hanakata et al., 2016). See Supplementary Information for optical images during transfer. When the transfer system first makes contact with substrate, the membrane starts to change color due to changing interference conditions caused by the contact. After contact, the heating stage temperature is raised in steps of 10 °C, to a final temperature of 90 °C. This also causes the copper stage to undergo thermal expansion mostly in the z-direction, but also results in some lateral displacement. This temperature step size is sufficient to slowly melt the PPC off the microstructure onto the MEMS device, while also making minor adjustments to the positioning of the 2D film in case the material moves off the target due to this slight lateral movement of the underlying stage. The setup is kept at 90 °C for 15 minutes, to allow for the PPC film to completely detach from the microstructure. The transfer system is then slowly lifted off the MEMS subdie. The 2D film in contact with the MEMS device covered with melted PPC remains behind, as seen in Fig. 5·3(d).

The only area with polymer residue at the end of the transfer process is a $30\,\mu m$ x $50\,\mu m$ area on the 2D strain device stage and the footprints of the microstructure on the substrate. Other methods of transfer mentioned above, such as using a polymer stamp, cause polymer residue and contamination length scales on the order of millimeters due to the large transfer contact footprint. By contrast, our method has a very small footprint of polymer residue. Using acetone and liquid CO_2 critical point drying, we remove the polymer from the 2D film, while preventing the film for tearing or stiction of the MEMS device (Tas et al., 1996;

Velasco et al., 2009; Velasco et al., 2011).

In order to remove the polymer from the 2D film, the MEMS subdie must be immersed in acetone. However, allowing the devices to air dry or using N2 after immersion in a liquid could damage the device. Capillary forces due to submersion in liquid can tear the suspended material or cause these released devices to adhere to the underlying substrate, a phenomenon known as stiction (Tas et al., 1996). Stiction and tearing of the 2D film can be prevented by critical point drying (CPD) (Velasco et al., 2009; Velasco et al., 2011). CPD uses liquid CO_2 to ensure that the phase transition of liquid to gaseous state happens around the triple point instead of directly crossing the interface, preventing surface tension from destroying the devices.

Using this method, we have successfully transferred exfoliated FLG and PVD MoS_2. We confirm that the materials are transferred without damage with optical imaging, SEM, and using spectroscopy (Raman and PL) on our transferred material. In the next section, we will discuss results of some our successful transfers.

5.5 Transfer Results

Results of reliable transfer were assessed using SEM imaging, Raman and PL spatial mapping of MoS2 and graphene transferred on to the MEMS devices.

Figure 5·4 shows a false-color SEM image of MoS_2 transferred on to MEMS. Our MEMS devices have a fixed anchor and movable shuttle, separated by 3 μm to allow for tunable strain manipulation (Vutukuru et al., 2019; Christopher et al.,). The MoS_2 was PVD grown, and is a large triangular domain that is monolayer expect for a small region in the center where a second layer growth appears. A very large area of this monolayer, 30 μm x 3 μm, is fully suspended across the shuttle and anchor of the MEMS device, as seen in purple in Fig. 5·4. The suspended region shows no tears and very little wrinkling, indicating that the transfer procedure maintained the integrity of the MoS_2 during the complicated

road from growth substrate to target substrate. Polymer residue is also non-existent, indicating that the PPC is cleanly removed by acetone. Furthermore, the SEM image of the entire MEMS device whole shows no changes from before the transfer process, contamination or otherwise.

To analyze the optical properties of the transferred MoS_2, we use confocal, spatially resolved photoluminescence and Raman spectroscopy over the suspended region. We used a continuous wave 532 nm laser with low laser fluence (26 μW) to avoid heating the suspended material. Our measurement raster scans over the entire suspended region as well as some area over both supported ends, with a step size of 1 um. The complete map contains 30 x 5 points.

The PL spectrum of MoS_2 consists of two exciton peaks (A and B) emerging from direct-gap transitions at the K-point of the Brillouin Zone, between the conduction band minima to two spin-orbit split valence band maxima (Mak et al., 2010a). In cases where there is an abundance of charged particles, decay of bound quasiparticles of two elecrons and one hole, called trions (T), also contribute to the spectrum (Mak et al., 2013; Christopher et al., 2017). Figure 5·4(a) shows the PL spectrum fit with two Lorentzians corresponding to the two excitonic contributions. We did not observe a significant trion peak. The A and B excitons, indicated by the blue and green dashed lines, are centered around 1.84 and 1.98 eV, respectively. The solid black line is the sum of the contributing peaks, which fits the experimental data with high accuracy.

Similarly, the Raman spectrum of MoS_2 has two phonon modes, $E^1{}_{2g}$ corresponding to the in-plane vibration of S atoms with respect to Mo, and A_{1g} corresponding to the out-of-plane vibration of S atoms (Li et al., 2012). Fitting with Voigt peaks, we found these features at $385 cm^{-1}$ and 405 cm^{-1} in our sample, as seen in Fig. 5·4(b).

Figure 5·5 shows PL and Raman maps of the position, as well as the position histogram of the suspended MoS_2. Fig. 5·5(a) and (b) show the positions of the fitted A and B

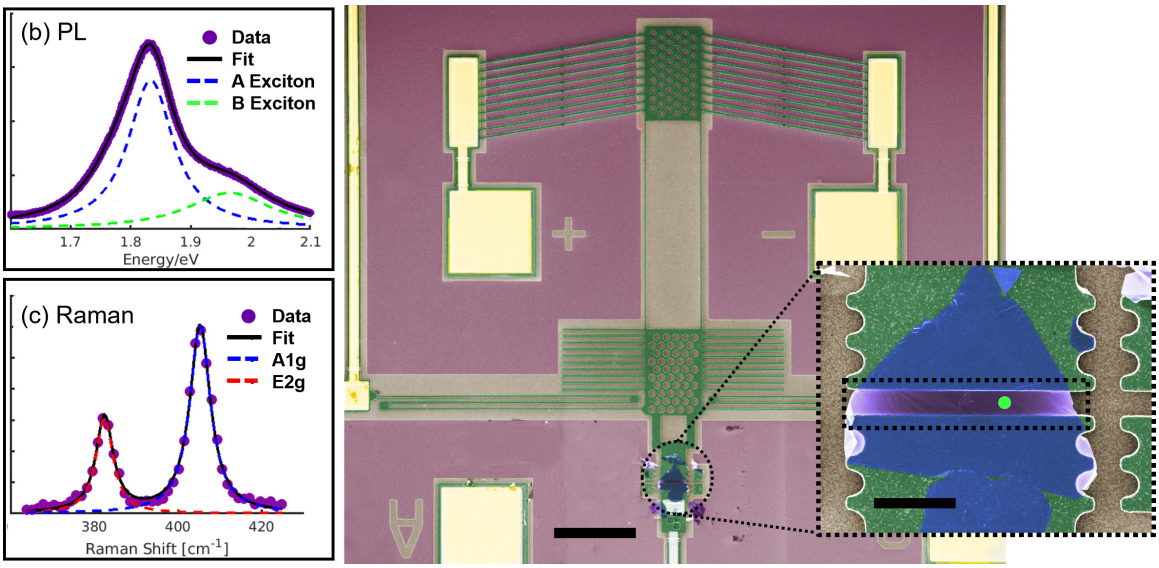

Figure 5·4: False Color SEM Image of 2D Material transferred on to MEMS. The PPC polymer only contaminates the region around the 2D strain device stag, and is easily removed using acetone immersion of the MEMS subdie followed by critical point drying. **Inset**: The MoS_2 suspended across the gap on the 2D strain device stage. The outline shows the PL and Raman mapped region. The area of the suspended region is approximately 30 μm x 3 μm. (a) and (b) show representative PL and Raman spectra, taken on the suspended region at the green dot.

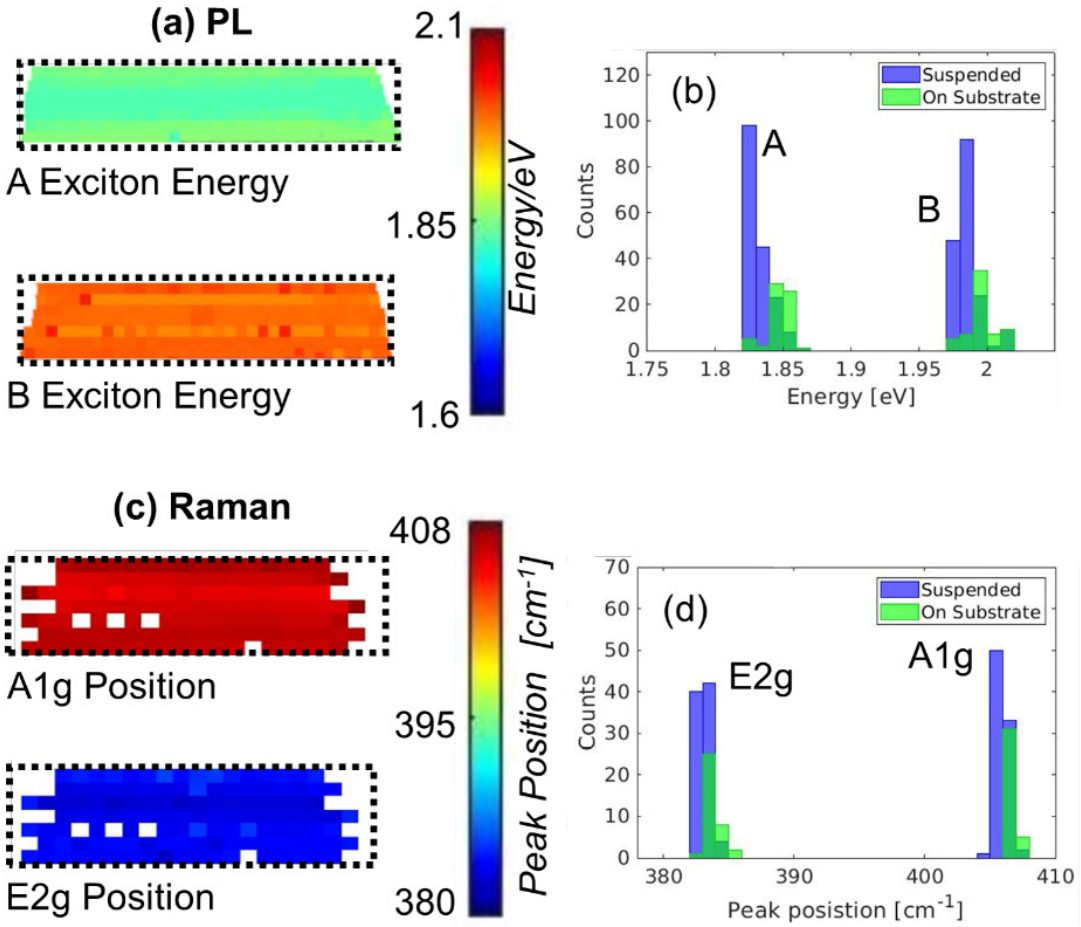

Figure 5·5: Spatially Resolved Photoluminescence and Raman Mapping of Suspended MoS_2. The spectra were collected in the region outlined by the dashed line. (a) and (c) are the intensities of the A and B excitons, obtained by fitting the mapped region. Likewise, (f) and (h) are the intensities of the A_{1g} and $E^1{}_{2g}$.The intensity maps show that the suspended area has high PL and Raman intensity, with a small few layer growth in the center where the PL is weaker. (b) and (d) show the position of the A and B excitons throughout the mapped region, while (g) and (i) show the Raman phonon mode positions. The consistent coloring of the region shows that the peaks have not shifted in energy, indicating a nearly strain-free sample.(e) and (j) show histograms of the exciton and phonon peak positions, separated into substrate and suspended regions.

excitons of the resulting PL, while (c) and (d) show $E^1{}_{2g}$ the A_{1g}. The uniform coloring of these maps shows that these peak positions do not drastically change from supported to suspended MoS_2. Hence, the material over the gap is negligibly strained.

We further illustrate this in Fig. 5·5(e) and (f), which shows the distribution of these peak position separated into suspended and substrate regions. The A exciton on the substrate is centered around 1.85± 0.008 eV, while the suspended region is minimally downshifted to 1.84 ± 0.009 eV. The B exciton is centered around 1.99 ± 0.01 eV on the substrate and 1.98 ± 0.01 eV on the suspended region. The $E^1{}_{2g}$ phonon is centered at 385.8 ± 0.6 cm^{-1} on the substrate and at 385.1 ± 0.6 cm^{-1} in the suspended region. The A_{1g} phonon is found at 406.0 ± 0.4 cm^{-1} and 405.9 ± 0.5 cm^{-1} on the substrate and the suspended area, respectively. Given the small standard deviations around the mean positions, the peaks positions indicate negligible strain in the sample compared to as grown MoS_2, in the range of $\sim$ 0.15-0.17% uniaxial strain (Mak et al., 2010a; Christopher et al.,). This strain corresponds well with the strain calculated from the PL and Raman data.

Finally, we apply the same technique to transfer few-layer graphene on MEMS. Optical images during the transfer process can be found in the Supplementary Information. In Figure 5·6, we show a colorized SEM image of the transferred few-layer graphene flake suspended on the MEMS 2D strain device stage. The flake consists of a few-layer graphene region in pink (5-10 layers) attached to a bulk piece of graphite. This demonstrates that layered structures can be picked up as a whole, even if they are not uniformly thick.

Raman mapping was done on the thinner region of the sample, over the suspended and supported fewlayer graphene region indicated by the dashed black line. Consistently high intensity of the 2D and G phonons can be seen in Fig. 5·6(a) and (c), which corresponds to the part of the graphene that is suspended. The supported ends of the graphene, however, exhibits very low intensity due to substrate interference quenching the signal. As a result, the fitting of the spectra from the substrate becomes less reliable causing the peak position

distribution to be broad. This can be seen in the Fig. 5·6(b-d). The suspended region has a very uniform peak coloring, and the histogram in Fig. 5·6(e) shows that the G and 2D peaks are centered around 1583.9 $\pm$ 0.5 cm^{-1} and 2704.4 $\pm$ 1.3 cm^{-1}. From the standard deviation the strain in the suspended region is $\sim$ 0.01%, calculated assuming strain is uniaxial in nature.

5.6 Conclusion

We demonstrated a new approach to transferring 2D materials, MoS_2 and FLG, from a growth substrate to a complex target substrate, like MEMS actuators. The transfer procedures uses a novel DLW microstructure that minimally interacts with the MEMS device. The procedure also uses PPC to maintain 2D material quality during transfer. Our procedure allows precision placement of the 2D material, producing large suspended regions without damage. The residue footprint is also minimal compared to other transfer techniques, and the overall procedure does not damage the freestanding MEMS actuator.

We have previously applied this transfer procedure to transfer MoS_2 onto a MEMS electrothermal actuator, and demonstrated 1.3% strain in the monolayer (Christopher et al.,). Our method is universal and can be applied to transfer layered materials, such as graphene, WS_2, or other TMDCS, as PPC has been demonstrated as an efficient pick-and-place polymer for 2D materials. In addition, heterostructures and twisted layers can be transferred with no alterations to the transfer procedure. Our technique allows for the integration of 2D materials with MEMS actuators for applying strain in suspended materials, opening a pathway to explore exotic physics in these unique systems.

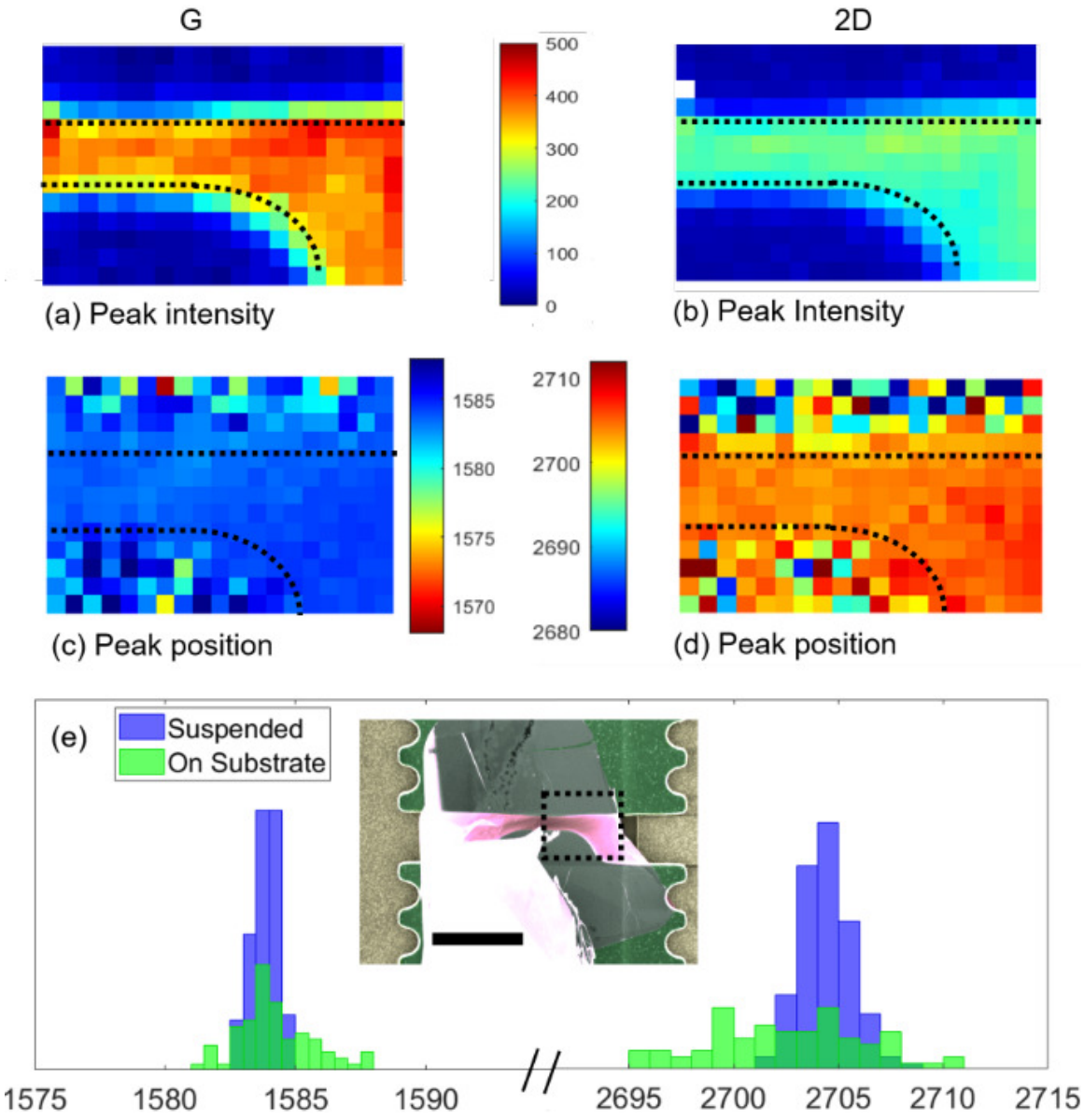

Figure 5·6: Spatially Resolved Raman Mapping of Suspended FLG and Histogram of Peak Positions. A colorized SEM image of the sample stage where graphene was transferred is shown. The region where Raman informatin was collected is outlined with the dotted black line. (a) and (c) are the intensities of the 2D and G phonon modes, obtained by using a Voigt fit on the mapped region. The intensity maps show uniform color from the suspended region, demonstrating high intensity. (b) and (d) show the position of the 2D and G phonons throughout the mapped region. Again, the suspended region is uniform.

Chapter 6

2D Materials Strained with MEMS

6.1 Introduction

The MEMS actuators and the optimized integration process using the polymer microstructure have successfully strained PVD monolayer MoS_2 to 1.3% (Christopher et al.,). The anchoring method used was simply the viscoelastic polymer PPC, which provided adequate mechanical coupling to reliably strain the 2D material on power of the electrothermal actuator. Beyond this level of strain, the mechanical coupling dissipates and the 2D material slips relative to the polymer. However, the PPC also dampens the actuation of the MEMS device, which could be a hindrance to directly observing strain in the 2D material as a function of applied voltage.

In this chapter, I briefly introduce microriveting as an improved anchoring technique. Using this technique, I will demonstrate the dynamic, and reversible straining of CVD monolayer graphene to 0.3%. Ideally, the microriveting technique should allow for remarkably increased mechanical coupling in the 2D material, and should result in more strain. In order to capitalize on the capabilities of the MEMS actuator, I use the microstructure to transfer exfoliated multilayer graphene to the MEMS 2D strain device stage. The actuator strains the multilayer to 1%, despite non-ideal behavior incurred during the fabrication process. Interestingly, the optical response of strained multilayer graphene shows signatures of decoupling and shear between layers. This process shows that MEMS devices can be used to tune commensuration between layered materials, opening the doors to “twistronics" with MEMS strained 2D materials. Some fabrication process steps are a bottleneck to

improving the maximum strain. I will describe these prospective improvements Appendix E.6.

6.2 Straining CVD Monolayer Graphene

In this section, I demonstrate strain in CVD monolayer graphene using the MEMS actuator. The graphene was purchased from GrollTex and assessed for quality using Raman spectroscopy. Monolayer graphene is grown on both sides of a copper foil, and the total supplied portion is a square area with a side length of 8 *cm*. The entirety of the GrollTex is affixed to thermal release tap to provide stiffness and also aid in the transfer process. In order to maximize the graphene, I cut small, square portions to use at a time, with dimensions slightly bigger in than the side length of the MEMS subdie, ~ 2 *cm*. Triple thick PMMA is spun on top of the graphene, using the recipe described in Appendix A.1.1. The graphene layer on the backside of the foil is etched in oxygen plasma ash. The PMMA+graphene+copper foil substrate is affixed to the transfer frame and float released in copper etchant to remove underlying copper foil. Subsequently, the PMMA+graphene membrane is thoroughly rinsed in DI water and dried in a dessicator for 1 hour. This prepares the monolayer graphene ready for integration with the MEMS device.

6.2.1 Fabrication

The transfer process here will not utilize the microstructure process described in the previous chapter. Instead, I will follow the “Post-G Method" previously developed by J. Christopher in the Swan Lab. This fabrication process allows us to fabricate several devices simultaneously, improving on the fabrication time and yield.

Fig. 6·1(a) shows the fabricated subdie, a square substrate with side length approximately 1.5 *cm*. On each subdie, 6 MEMS actuators of different variations in the 2D strain device stage are micro-machined, as seen in Fig. 6·1(b). Three devices are plain 2D strain

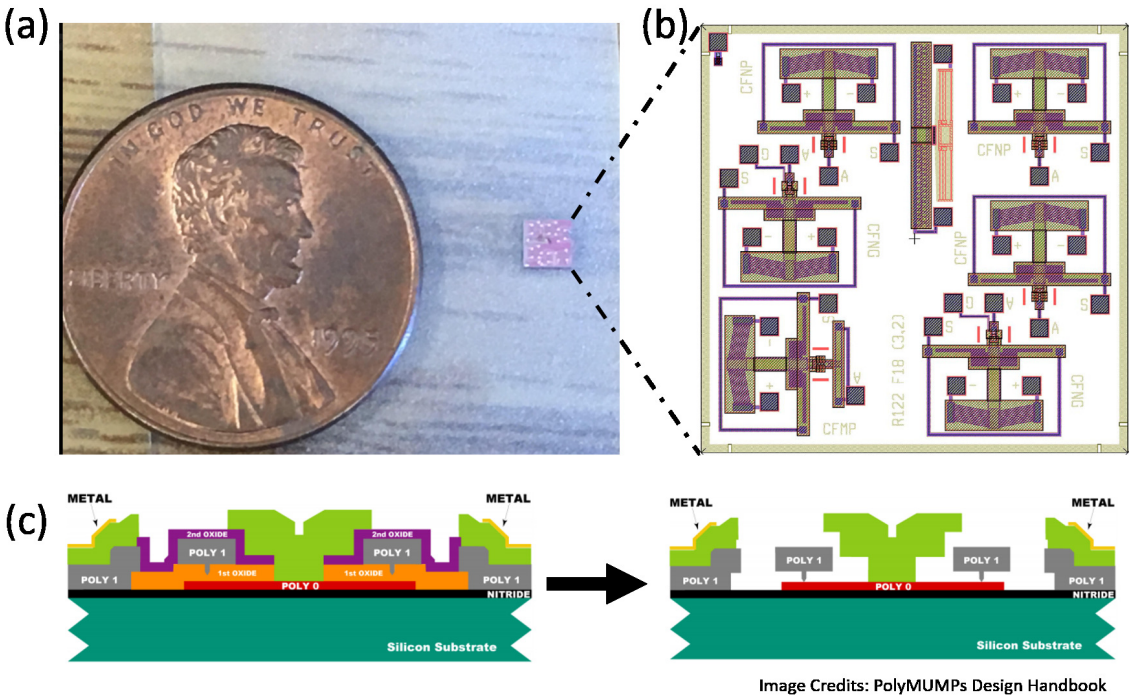

Figure 6·1: MEMS Subdie and Release. (a) Photograph of the MEMS subdie (in purple) fabricated through the PolyMUMPs process at MEMSCap foundry, compared to a US penny. (b) Each MEMS subdie contains 6 optimally placed actuators of different variations. (c) The subdie is fabricated and released in HF to allow movement in the device when actuated.

device stages, with a straight-edged gap region. These are labeled CFNP. Two devices are fabricated to allow electrical back-gating, and are called CFNG. Finally, one device (CFMP) is fabricated with a force meter, which can allow one to measure the Young's modulus by tensile strain in a material. For our the present time, the 2D material integrated MEMS devices will utilize the CFNP devices, in order to simplify the strain studies. The subdies are micro-machined with 3 polysilicon interspersed with oxide layers that are sacrificially released in HF acid, as shown in Fig. 6·1(c).

First, the MEMS devices are individually tested electrically using probe tips to ensure that the HF has fully released the movable polysilicon layers of the device. In Fig. 6·2(a), I ascertain that the device is functioning properly by optically observing the 2D strain device stage in relation the stationary verniers. At full actuation, the gap in the device will have increased by 2 μm. At a maximum input voltage of 10 V, the device draws a current of 38.8 mA. In this actuation range, the device exhibits linear motion.

To prepare for transferring 2D materials, the hydrophilic nature of the MEMS substrate is improved by a 15 minute oxygen plasma ash, which also helps in atomically cleaning the surface. The previously prepared PMMA+graphene membranes are transferred over the entire subdie on the copper stage heated to an initial temperature of 90 °C. As the membrane makes contact with the MEMS subdie, subtle changes in color due to interference effects will assure good contact has been established. Contact on all devices is ensured after the subdie is subsequently heated at 180 °C for 15 minutes, as seen in Fig. 6·2(b).

Next, all devices on the subdie are patterned using EBL, following the procedure outlined in A.1.2. The 2D strain device stage is patterned in a desired shape across the gap, in addition to patterning holes on the anchor and shuttle, as seen in Fig. 6·2(c). In order to free the actuator from under the PMMA, we also expose a pattern shaped to each device, as seen in Fig. 6·2(d). Since these two patterns are of vastly different sizes, they should be executed in separate steps in order to minimize errors in misalignment of the two patterns. In

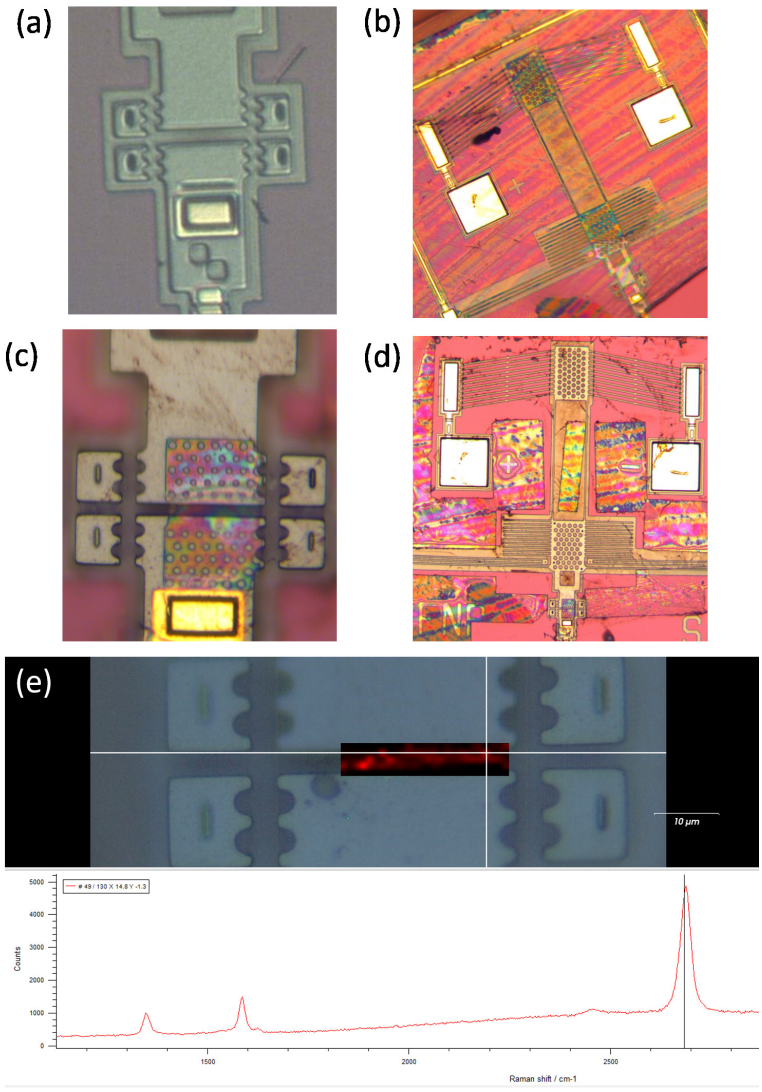

Figure 6·2: Fabrication of CVD Monolayer Graphene Integrated MEMS Actuator. (a) Actuation test prior to fabrication. (b) Transfer of CVD Graphene and PMMA membrane over entire subdie. (c&d) Post EBL, development, and RIE. (e) Raman map post ACE and CPD. The map shows position of the 2D peak across the gap region.

addition, the alignment guidelines outlined in Appendix A.1.2 should be considered. After exposure, the regions dosed by the electron beam will be removed during the development, which exposes the underlying graphene in all these regions. The graphene is removed using reactive ion etching, using the procedure detailed in E.1. It is essential to keep the MEMS subdie in the center of the RIE chamber, aligned with glass slides. This ensures an even etch over the entire subdie.

Subsequently, a course Raman map should be done as a quality control step. In Fig. 6·2(e),the area in red across the gap shows the $2D$ peak of graphene. The relative position of the $2D$ peak is consistent over the gap.As the region is contiguous across the gap, it shows that the material has not torn or washed away thus far during the fabrication process. Over the anchor and the shuttle region, the interference effect diminishes the signal intensity. Individual spectra on either end of the gap still shows the presence of graphene. However, looking at a spectra in one point on the gap shows a presence of the D peak. This indicates that the fabrication process introduces defects in the material. In Appendix E.6, I discuss possible ways to maintain quality during the fabrication process.

The final steps of the riveting process start by micropositioning a custom silicon nitride shadow mask over each device. As seen in Fig. 6·3(a), the windows of the shadow mask align over anchor and shuttle, making sure to cover the gap where the graphene is exposed. The 1 μm silicon nitride layer is sufficiently thin to allow the alignment over the MEMS device with microscopic precision, as seen in Fig. 6·3(b). After proper alignment over the CFNP device, the MEMS is ready to undergo electron-beam deposition. A thin layer of Chromium is first deposited as an adhesive layer. Subsequently, a layer of gold is deposited to rivet the 2D material. The e-beam deposition uses the recipe detailed in Appendix E.2. A CFNP device with gold riveting on the 2D strain device stage is shown in Fig. 6·3(c). Finally, the device is ready for actuation after ball bonding with gold wire, as shown in the photograph in Fig. 6·3(d).

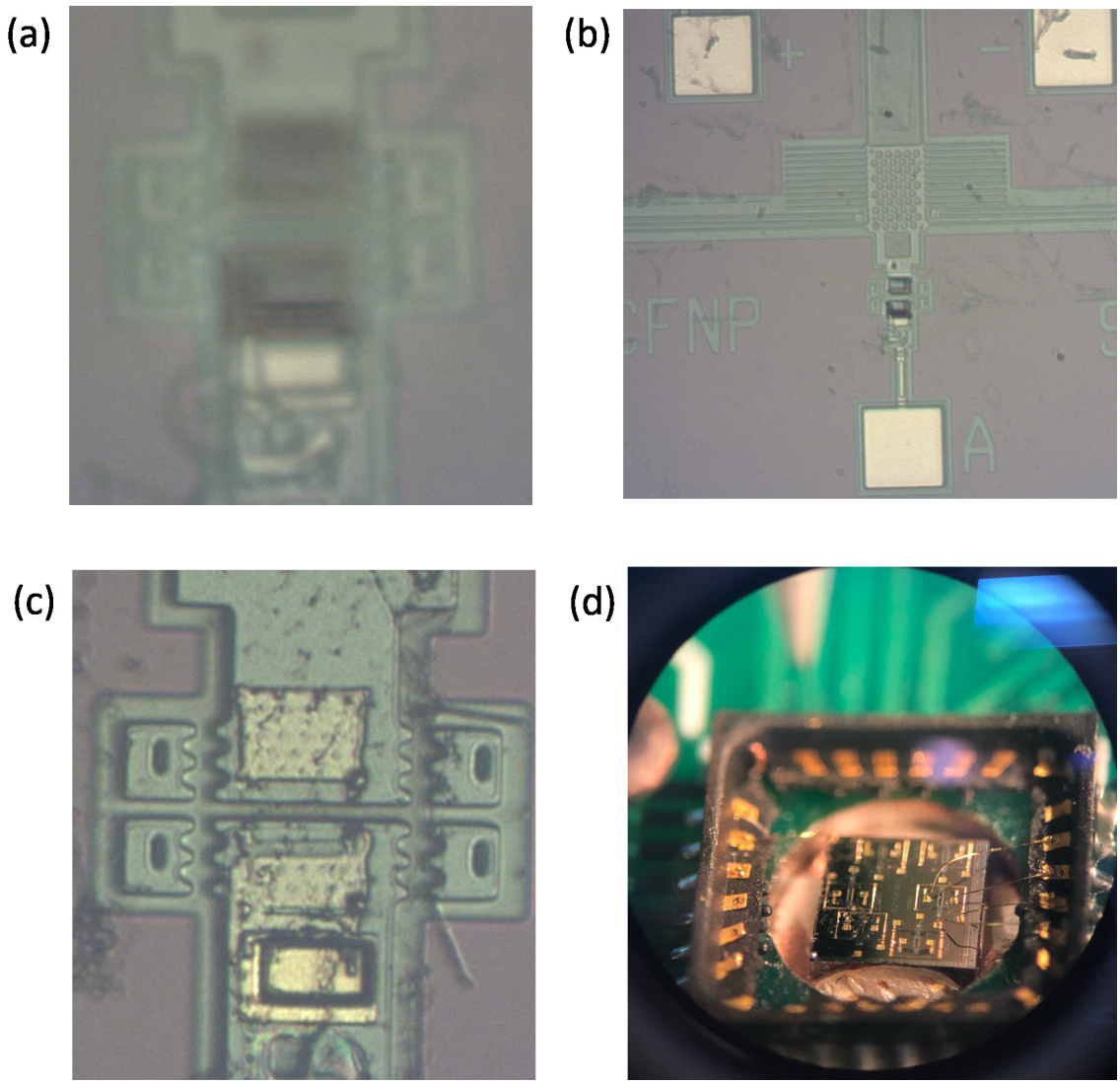

Figure 6·3: Gold Riveting and Ball Bonding of the MEMS device. (a) Custom silicon nitride shadow mask is aligned over the MEMS 2D strain device stage, with the anchor and shuttle ends on either side of the gap exposed to Gold deposition. (b) The shadow mask prevents metal deposition on other areas of the MEMS device, while the 1 μm thin silicon nitride is transparent to allow alignment with micrometer resolution. (c) Gold deposition with an underlying thin adhesive layer of chromium is deposited over the anchor and shuttle sides of the 2D strain device stage. (d) The device under the optical microscope showing ball bonded pads, ready for electrical actuation.

6.2.2 Raman Spectroscopy of Monolayer Graphene under Strain

In this section, I will describe the strain response of monolayer CVD graphene uniaxially strained by a MEMS device to 0.3%, determined through Raman spectroscopy. These measurements were taken device labeled G11 CFNP2, using the B11 Renishaw spectrometer, the setup of which is described in Appendix E.3.

In an ideal thermally-isolated MEMS chevron actuator, the maximum displacement at an input power 0.4 W (or 10 V) is 2.5 μm. This behavior is thoroughly investigated in Chapter 4. We can calculate the displacement per mW as 4.3 nm for an ideal device. In order to properly ascertain strain in the material from Raman spectroscopy, the strain steps per mW of input power should be chosen such that the shift of the Raman peaks can be easily discerned while maintaining while ensuring that the strain is smoothly varying. Quickly increasing power is likely damage both the actuator as well causing tears in the material. I decided that a strain step size of 0.05% is optimal. For this strain step on an originally 3 μm gap in the TIS device, each strain step should induce a displacement of 1.5 nm in the device. Hence, the step size in input power for a 0.05% strain step will be 0.34 mW. If we monitor the Raman $2D$ peak of graphene, which is more strain-sensitve than the G peak and has a rate of shift of 64 $cm^{-1}/\%$ strain, we can expect each step input power to shift the peak by 3.2 cm^{-1}. Given the FWHM of the peak and the spectral resolution of the grating, this shift in the peak should be easily discernible. For 1% strain in the device, we should input only need to give an input power of 6.34 mW or 1.32 V.

After making electrical connections from the ball-bonded MEMS in a ceramic dual-inline package to a Kiehtley 2400 power source, we first measure the resistance across the beams of the Chevron actuator by allowing a small current to pass through the contacted pads. The initial resistance informs us on the state of the device after the lengthy fabrication process, whether the device is fit to be actuated or if it has collapsed or electrically broken at some point. For this device, I measured an initial resistance of 273 Ω. This is higher than

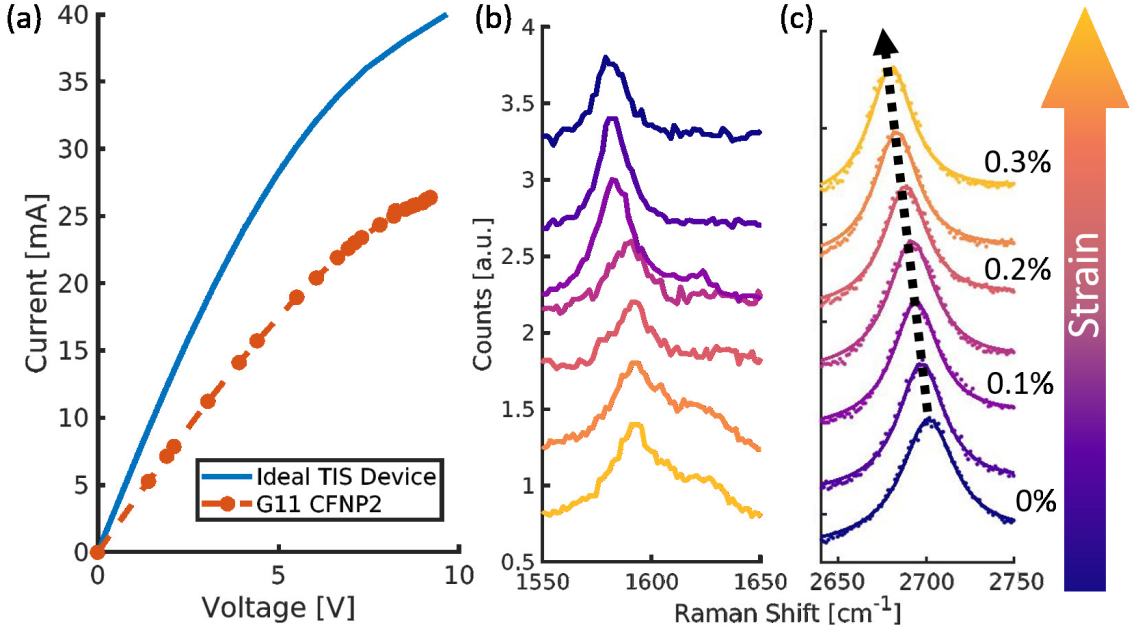

Figure 6·4: Strain Response of CVD Monolayer Graphene. (a) IV Characteristic of G11 CFNP2 compared to and Ideal TIS device. (b&c) *G* and 2*D*peak evolution as strain increases on the sample from 0 to 0.3%.

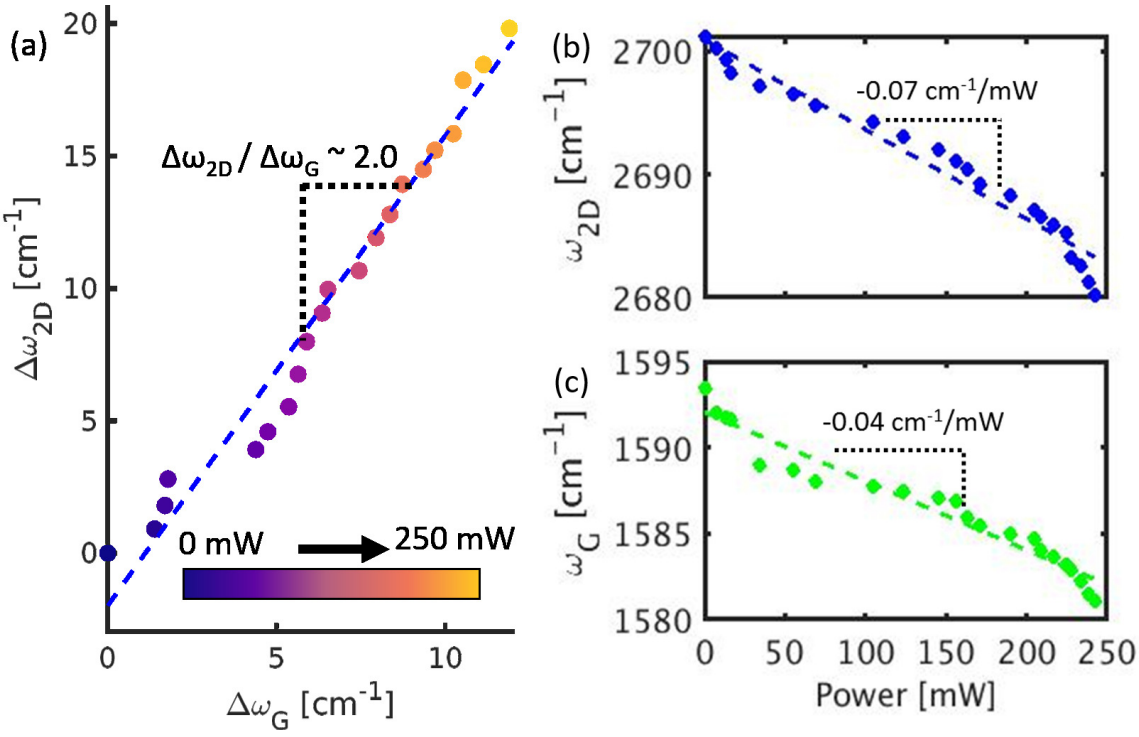

Figure 6·5: Strain Response and Repeatability. (a) Correlation of Ratio 2*D* to *G* peak shift from mean position at 0% strain, as the device is actuated from 0 to 250 mW. Inset shows extracted ratio of Gruneisen parameters, which matches previous experiments. (b&c) Rate of shift of the 2D and G phonon as a function of input power to the device, over 2 runs.

the resistance of an ideal device ($\sim$250Ω). This is the first indication that the fabricated device will exhibit non-ideal behavior during actuation.

Indeed, after several attempts to actuate the device using a small power step size, I determined the device needed higher input powers than is typical to move, possibly as a result of the fabrication process changing the device parameters. As a result, although G11 CFNP2 did actuate and show movement in the 2D strain device stage, the IV characteristics showed a significant disparity compared an ideal TIS device, as shown in Fig. 6·4(a). The blue solid line shows the behavior of an ideal TIS device, characterized in Chapter 4 while the orange data points are from current device. At a maximum input power of 243 mW (9.2 V or 26.4 mA), I observed the G peak to shift from 1593 cm^{-1} to 1581 cm^{-1}, as seen in Fig. 6·4(b). Likewise, the $2D$ peak shifted from 2701 cm^{-1} to 2680 cm^{-1}, as seen in Fig. 6·4(c). The G peak has less than half the sensitivity of the $2D$ peak with regards to strain, shifting at a rate of $\sim$ 31 cm^{-1}. In addition, due to the presence of defects, a D' peak appears as a shoulder off the G peak, as seen in the low strain spectra in Fig. 6·4(b). The effect of strain on the D' peak is not well-studied, so I rely on the $2D$ peak to inform on the strain in the system. In the linear regime, we can determine the strain using the red-shifting of the more strain-sensitive Raman $2D$ peak as (Mohiuddin et al., 2009):

$$\varepsilon = -\frac{\Delta\omega_{2D}}{\omega_{2D}^{0}\gamma_{2D}(1-\nu)} \tag{6.1}$$

where ω_{2D}^{0} is the original, unstrained position of the $2D$ peak, $\Delta\omega_{2D}$ is the shift of the $2D$ peak from the original position, $\gamma_{2D} = 3.55$ is the Gruneisen parameter for the $2D$ phonon, and $\nu = 0.33$ is the Poisson's ratio of suspended monolayer graphene. From the shift of the $2D$ peak, using 6.1, the maximum strain induced in monolayer graphene was determined to be 0.32%. As input power in the device was approaching the limit for the linear operating regime of the actuator, I refrained from increasing the power at this point and cycled back down to 0 mW.

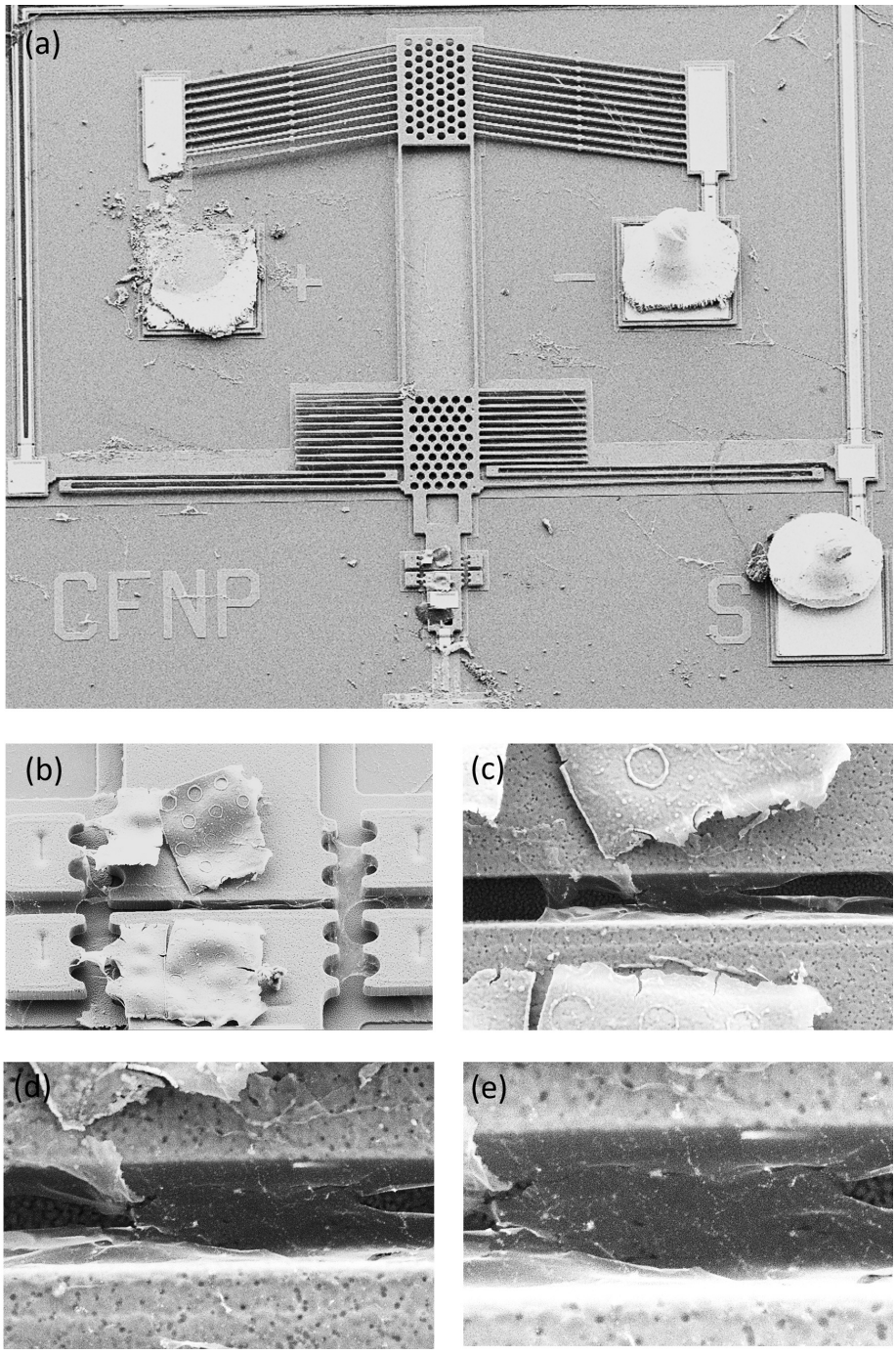

Figure 6·6: G11 CFNP2 Failure. (a) Overview of the device showing broken Chevron beams. (b&c) Gold microrivets popped off the 2D strain device stage. (d&e) Monolayer graphene is torn.

Typically, uniaxial strain lifts the degeneracy in the G band, and the peak splits in to G^- andG^+. This does not occur for the $2D$ peak. However, the strain levels seen in this device are not sufficient to split the G peak. Hence, we need another basis of determine the whether the strain from the $2D$ peak is accurate. Fig. 6·5(a) shows the correlation of $2D$ peak shift vs. G peak shift, $\Delta\omega_{2D}$ vs. $\Delta\omega_G$. The ratio of these frequencies gives the ratio of Gruneisen parameters, γ_{2D}/γ_G, which I determined as approximately 2 for G11 CFNP2. This value agrees with previous studies on uniaxial strain in graphene (Cheng et al., 2011; Goldsche et al., 2018; Mueller et al., 2017). Finally, I tested the repeatability of this experiment by cycling the input power from 0 to 0.24 W. Fig. 6·5(b&c) shows rate of shift of the $2D$ and G peak as a function of input power, extracted over two separate cycles. The repeatability of the device shows that MEMS is a reliable platform to dynamically strain materials.

Unfortunately, the behavior of the device degraded after sitting in ambient conditions for greater than 24 hrs. Images in Appendix E.4 show the extent of the change to the device. The main changes were to the riveting metal, which “popped" off the substrate on the anchor and the shuttle. In addition, the whole movable device seems to have been dragged closer to the anchored part. As a result, the material across the gap either broke is folded by compression of the gap. Fig. 6·6(a) shows an overview of the device under SEM. The ball bonds need to be removed using a probe tip in order to place the device under the SEM. This process can sometimes damage the device, as can be seen in the broken Chevron beams in Fig. 6·6(a). Figures 6·6(b-e) looks progressively closer at the material across the gap. In Fig. 6·6(b), we can see that the riveting metal has cracked, deformed, and popped off the substrate. In Fig. 6·6(c), the riveting metal has broken the graphene layer on the anchor and substrate ends. Looking closer at a contiguous region of graphene across the gap, Fig. 6·6(d&e), there is evidence of residue or dirt on the material, along with tears and folds. This shows that there are still areas of improvement for the fabrication process and considerations for after actuation, in order to maintain longevity for the 2D material

integrated MEMS device. These are included in detail in Appendix E.6.

6.3 Straining Exfoliated Few Layer Graphene

The mechanical strength of the CVD monolayer graphene could likely be a bottleneck for its implementation with the MEMS device, given the extensive fabrication pipeline. In order to capitalize on the capabilities of the MEMS device as a robust straining platform, I tested its durability with exfoliated few layer graphene. Exfoliated graphene is unlikely to have intrinsic defects or disorder that will occurs in CVD materials, so it maintains the high tensile strength that graphene is known for. However, the trade off in utilizing exfoliated monolayer graphene is in handling, transfer, and most importantly, in yield. Sizes for exfoliated monolayers can range from 10-40 μm in length with extensive trial and effort. Despite using the microstructure, alignment and transfer on top of the MEMS device is difficult given the high transparency of monolayers. Here, few-layer graphene has the benefits of ease of handling and opacity which help in damage-free transfer, without comprising on the fascinating strain-tunable properties of naturally occurring graphene.

6.3.1 Fabrication

Few layer graphene is exfoliated on SiO_2/Si substrates. The pick and transfer procedure follows the integration process detailed in Chapter 5. After transferring and removal of the transfer polymer (PPC), a triple-thick membrane of PMMA is transferred on to the entire subdie. The procedure for obtaining PMMA films is detailed in Appendix E.5. As before, PMMA acts as a resist for electron beam lithography. Following the patterning, development, and reactive ion etching process described in the previous section, I obtain the material transferred and etched in the desired shape. Fig. 6·7(a&b) shows optical microscope images of a few layer graphene sample transferred on to the 2D strain device stage of a CFNP device. The sample also has an attached bulk graphite flake, which I will

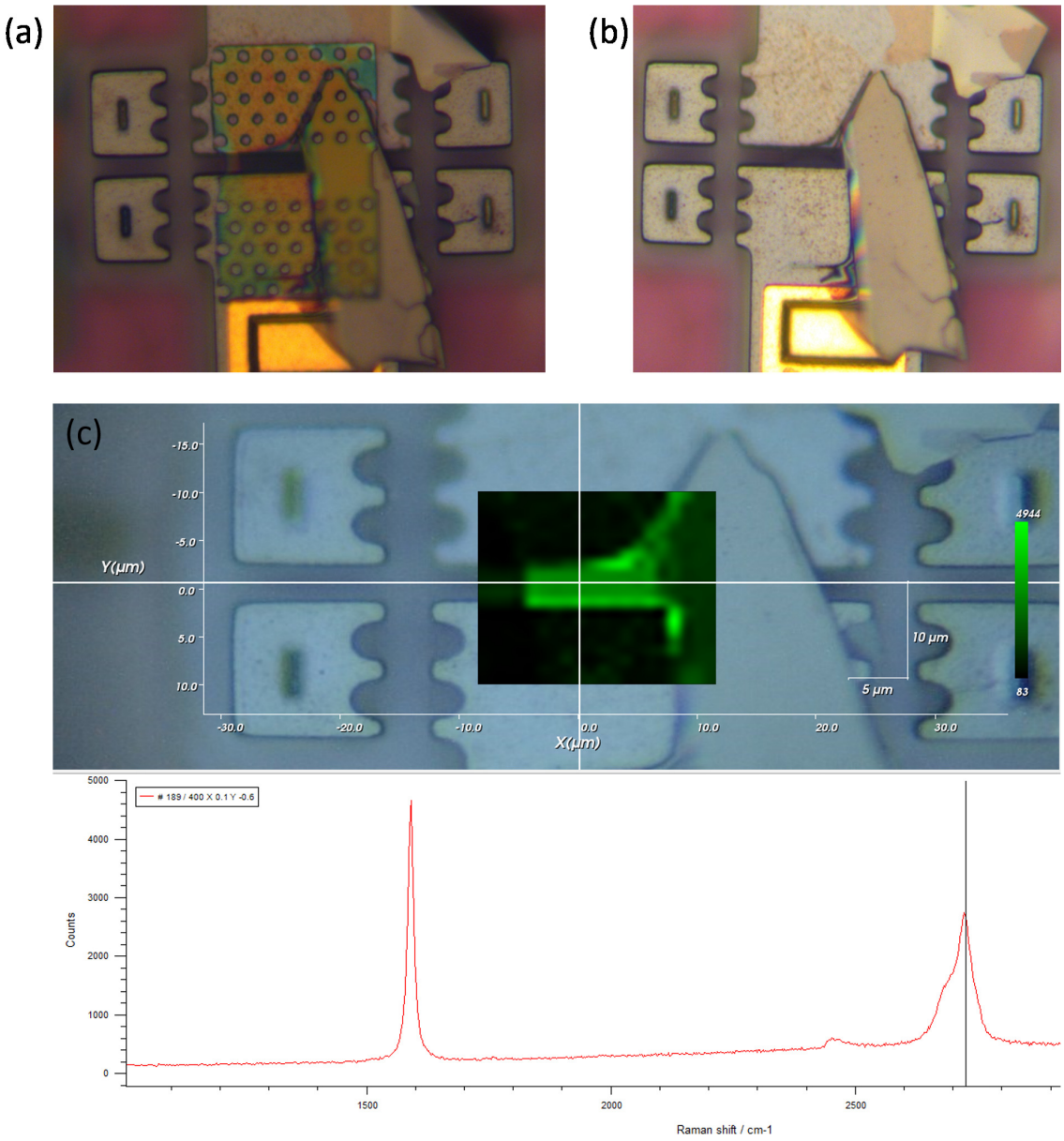

Figure 6·7: Fabrication of Few Layer Graphene on MEMS

avoid during optical measurements. From the interference pattern under the PMMA in Fig. 6·7(a), we can distinguish that the few layer graphene flake has large areas firmly on the substrate of the anchor and shuttle. These large areas of contact help in minimizing slipping during strain.

The RIE process was not adapted to completely etch through the few layer graphene sample. While this meant that riveting the material in place during actuation would not be possible, this helped in mechanically releasing the graphene layers, as I will describe in the latter section. In Fig. 6·7(b), the device has gone through acetone removal of the PMMA for $>$ 24 hrs, followed by critical point drying. Once, again quality assurance through Raman map was done to make sure the material is contiguous across the gap. Fig. 6·7(c) shows the Raman map of the intensity of the $2D$ peak in the transferred sample. Looking at an individual spectra, it can be seen that the sample is indeed multilayer graphene based on the ratio of the $2D$ peak and the G peak. The exact number of layers in flake will need to be determined by other methods such as AFM.

6.3.2 Raman Spectroscopy of Few Layer Graphene under Strain

The device was electrically ball-bonded. As before, measuring resistance across the Chevron actuator stage allows us to make an initial assessment on the state of the device. Using a small current through the device, I measured a resistance of 181.5 Ω. This is significantly lower than the typical resistance across the Chevron, which indicates that the device will be exhibit non-ideal actuation. The device is will need to take in more input power to generate the same in order to generate displacement through thermal expansion of the Chevron beams. As such, extra care must be taken to account for any aberrant behavior, such as smaller than usual strain steps and monitoring the temperature of the device to prevent over-heating. This section will describe the strain response of exfoliated few layer graphene uniaxially strained by a MEMS device to 1.2%, determined through Raman spectroscopy. These measurements were taken on device labeled G34c CFNP3.

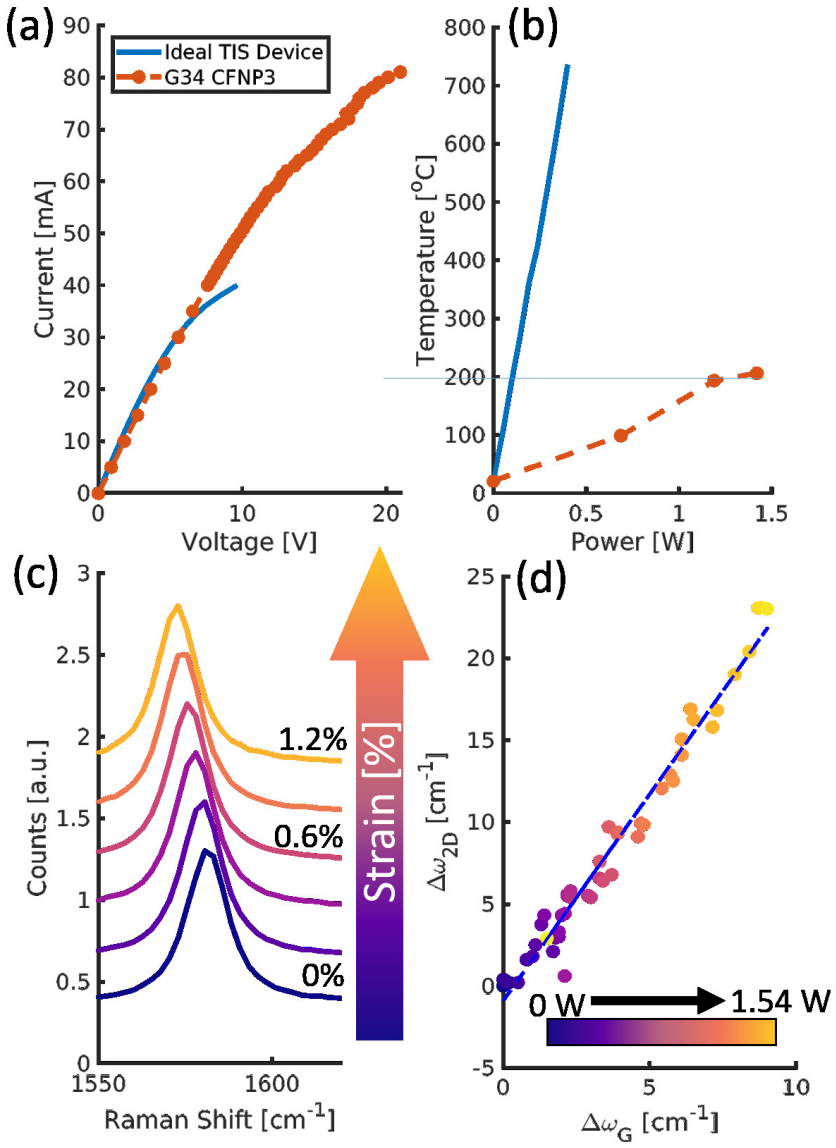

Figure 6·8: G34c CFNP3 under Actuation. (a) IV characteristic of the device, compared to an ideal TIS device. (b) Comparison of beam center temperatures of an ideal TIS device and G34c CFNP3. (c&d) Evolution of Raman spectra with increase in input power, focusing on *G* and 2*D* phonon softening induced from strain on the material.

Fig. 6·8 shows the electrical and optical response of G34c CFNP3 under actuation. As indicated by the initial resistance, the device required higher input voltage than is typical to generate appreciable displacement. Though typical Chevron actuators of this design undergo irreversible damage beyond 13 V, this device was able to go beyond that limit while still maintaining a linear actuation response. The device was actuated to a maximum 19.5 V which generated 79 mA, as shown in Fig. 6·8(a). By monitoring the temperature of the Chevron beam, it is clear these aberrant IV characteristics are because the device is heating up atypically. In Fig. 6·8(b), we see the temperature of a Chevron beam in G34c CFNP3 compared to an ideal TIS device shown in Chapter 4. The maximum temperature of a Chevron beam at the highest input power of 1.54 W was 224 °C. For a typical TIS deivce, this temperature is reached at an order of magnitude less input power, $\sim$ 0.14 W. The most likely issue is polymer or some other residue that is acting like a thermal sink in the region of the Chevron stage. Following the rationale behind 1-dimensional heat transfer in thin structures from Chapter 4, it is likely that the polymer/residue caused heat to flow through this alternate path of lower thermal resistance, as opposed to through the Chevron beams. As a result, the Chevron beams need higher actuation voltage to undergo sufficient thermal expansion for strain.

Fig. 6·8(c) shows select spectra of the few layer graphene under device actuation, focusing on the evolution of the *G* peak under increasing power to the device. As expected, the *G* peak shows softening in response to strain (Mak et al., 2010a; Zhou et al., 2013; Mak et al., 2010b). I extract the peak position of the *G* peak using a single Voigt peak fit. The evolution of the *G* peak with strain is only confined to the position, while the strain does not appreciably alter the area of the peak or FWHM. Although uniaxial strain easily lifts the degeneracy of the *G* phonon in monolayer graphene, this effect is less pronounced as the layer numbers increase (Mohiuddin et al., 2009; Tsoukleri et al., 2009; Metzger et al., 2010). As a result, few layer graphene does not experience optical visible splitting or

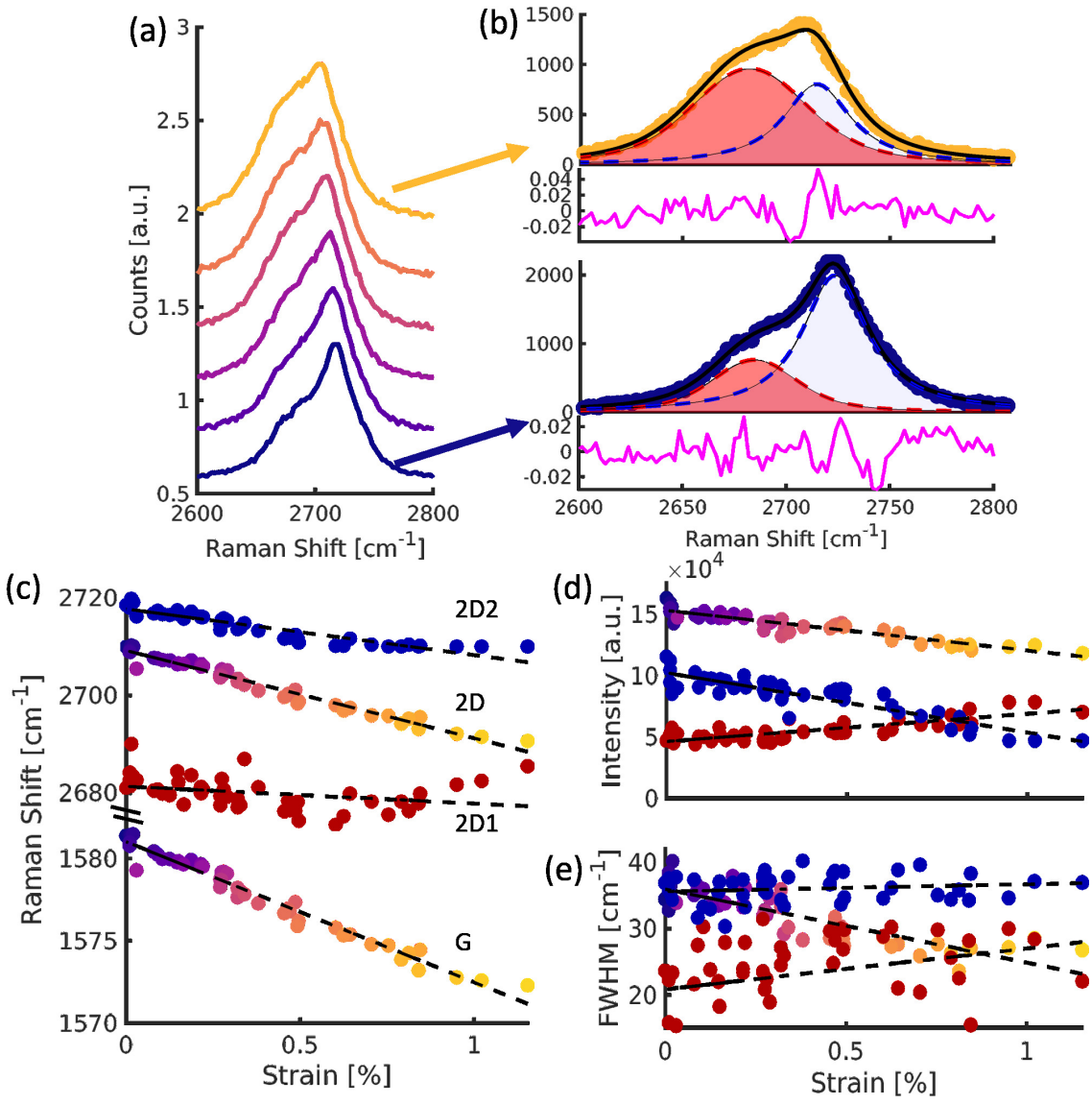

Figure 6·9: Few Layer Graphene Spectral Response Under Strain.

change in the G peak, as can be seen in Fig. 6·8(c). For a preliminary understanding of the phonon shift, I use a single Voigt profile to fit the 2D peak. fig. 6·8(d) shows the correlation between the spectral shift of the $2D$ versus G peak. The maximum shift at 1.54 mW was 21 cm^{-1} and 8 cm^{-1} for the $2D$ and G peak respectively. For a monolayer material, this would produce a strain of less than 0.5%, however the rate of shift is significantly lower for few layer materials (Gong et al., 2012; Gong et al., 2013). Using a rate of shift from previous studies on few layer graphene, I extract a maximum strain of 1.2% from the red-shift at the final input power.

However, it is easily discernible that the $2D$ peak shows appreciable changes to the area and FWHM as strain is increased, as is shown in Fig. 6·9(a). In few layer and bulk graphite, the $2D$ peak can be fit using 2 peaks, lower energy $2D_1$ and higher energy $2D_2$ (Ferrari et al., 2006; Ferrari, 2007; Ferrari and Basko, 2013). In Fig. 6·9(b), I show representative Raman spectra at 0 and 1.2% strain, focusing on the $2D$ peak. The lower energy $2D_1$ component, in red, shows significant changes when the material is strained. The $2D$ peak as a whole evolves to a more “symmetric" peak under strain. Fig. 6·9(c-e) shows the extracted change to position, intensity, and FHWM for the individual components of the $2D$ peak. The $2D_2$ component and the $2D$ peak on the whole decrease in intensity under strain, whereas the $2D_1$ shows a contrasting trend nearly doubling in intensity. As a whole the $2D$ peak becomes narrower under strain, from $\sim$ 35 cm^{-1} to 22 cm^{-1}. However, the $2D_1$ peak increases in width under strain by approximately 10 cm^{-1}. To a lesser extent, the $2D_2$ peak also increases by about 5 cm_{-1}. In the next section, I discussion possible origins of these trends, as well as the outcome of the device G34c CFNP3.

6.3.3 Interlayer Shear and Device Fracture

The Raman response of strain on few layer graphene was previously investigated in nanocomposites and embedded in polymer matrices(Gong et al., 2012; Gong et al., 2013; Androulidakis et al., 2019). Graphitic materials have shown to effectively lend their strength to poly-

mer composites or for reinforcing in metals. (Sreenivasulu et al., 2018; Anagnostopoulos et al., 2015; Anagnostopoulos et al., 2019; Wang et al., 2016).

Intriguingly, the effect of strain on multilayers of graphene shows signatures of loss in stacking order between layers due to inefficient transfer of strain from the straining polymer to the multilayer system. During mechanical exfoliation, the majority of multilayer samples created are Bernal stacked; a stacking order more energetically favored compared to rhombohedral or non-Bernal order (Bernal, 1924; Torche et al., 2017; Tiberj et al., 2011; Shibuta and Elliott, 2011; Cong et al., 2011). Gong. et. al. have shown that few layer graphene can undergo reversible loss in Bernal stacking order as a result of shearing strain between layers (Gong et al., 2012; Gong et al., 2013). When a multilayer material is uniaxially strained by elongation of an underlying substrate, the stress transfers to the layer immediately in contact first. The material will lengthen (or compress) in the direction of the strain, while contracting in the opposite direction in proportion to the Poisson's ratio. The strain from the first layer transfers to next, but the transfer of strain is only 70% efficient to every subsequent layer. Considering that the penetrating depth of the 532 nm laser is larger than the thickness of the few layer graphene, the optical determination of the strain in the system should yield an average value dominated by the top most layers, and not the true maximum strain on the layer in contact (Ni et al., 2008; Klar et al., 2013; Smausz et al., 2017).

The optical response of the loss in stacking order produced a distinct change in the line shape of the 2D peak, which evolved from an asymmetric shape to more symmetric as a result of loading strain on to the sample. In Fig. 6·10(a) shows representative line shape as a function of strain, fitted with 2 Voigt spectra. The distinct two peak structure at 0% strain evolves to a more symmetric peak at 1.2% strain. As a result, the Bernal stacking order is lost under strain, as shown in Fig. 6·10(b). The effect can be visualized by imagining few layer graphene as a deck of cards, as shown in Fig. 6·10, where individual cards are

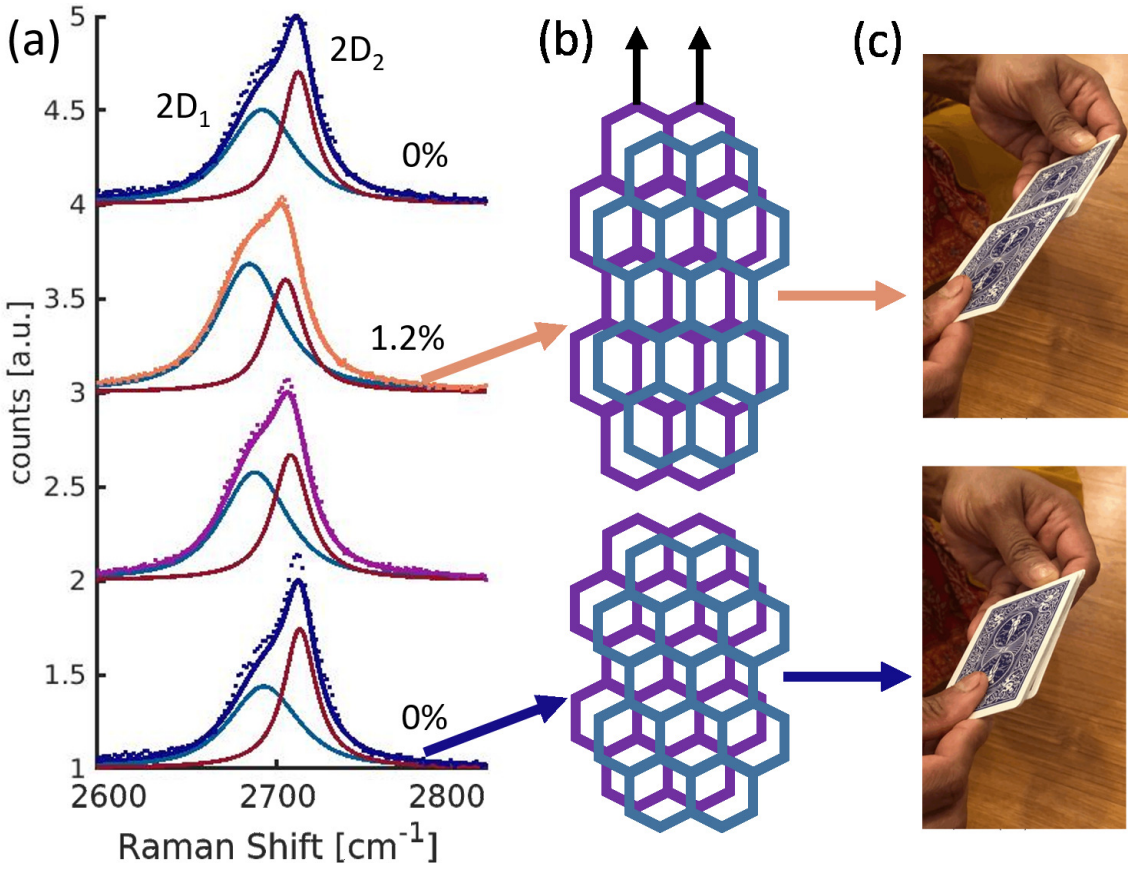

Figure 6·10: 2D Peak Evolution with Strain of Few Layer Graphene.

weakly coupled monolayer graphene. The layers in contact with the substrate strain to a greater extent compared to the layers on top, introducing relative shear between the layers. Previous studies have shown that the graphene/graphene interface for bulk graphite has a shear yield as low as 0.03 MPa (Soule and Nezbeda, 1968). So two questions to consider here are: is the Chevron actuator capable of exceeding the shear yield and inducing the interfacial slip, and can the few layer graphene remain anchored to the actuator without slipping during the course of actuation?

For the first question, I compare the the force needed to strain the material and the output force of the actuator. From one-dimensional expansion calculations of a heated rod, we can calculate the maximum pull force a single Chevron beam F_{beam} of the actuator stage (Lai2004, Que1999) from:

$$F_{beam} = AE\alpha T_{max} l \tag{6.2}$$

where A is the Chevron beam's cross-sectional area, and E is the Young's modulus of the polysilicon, α is the coefficient of thermal expansion, T_{max} is the maximum temperature of the beam extracted from Raman thermometry (Fig. 6·8(b)), and l is the initial length of the beam.

The total force of the Chevron stage $F_{Chevron}$, with $n = 10$ beams angled at $\theta = 10\ ^{\circ}$, is calculated as:

$$F_{Chevron} = nF_{beam} \sin\theta \tag{6.3}$$

Hence, I can calculate the total output force for the TIS device from Eqn. 6.3 as ~ 4 mN.

If we model the few layer graphene as a spring, we can estimate the spring constant from linear elastic theory using Hooke's law as:

$$k_{FLG} = \frac{EA}{d} \tag{6.4}$$

where $E =$ is the Young's modulus of few layer graphene, $A = w \times t$ is the cross-sectional area of the few layer graphene (w is the width of the suspended portion of the flake, t is the thickness), and d is the length of the flake, equal to the initial gap in the 2D strain device stage (Zhou et al., 2013). For simplicity, I will assume that the sample is 10 layers thick, as the Raman spectra of the unstrained sample is very similar to optical signatures of this thickness in the literature (Ferrari, 2007). From Eqn. 6.4, the spring constant of few layer graphene can therefore be calculated as 6.8 kN/m. To produce 1.2% strain in the material, we should expect a required force $F = k_{FLG}\Delta x = 0.31$ mN. Hence, the Chevron actuator is capable of providing adequate force to strain the few layer material.

Secondly, the question of whether anchoring is sufficient is answered through the final outcome of the device G34c CFNP3. Fig. 6·11 shows the SEM image of the device after sudden failure of the device at the maximum input power. The device experienced sudden breakdown and the strain was entirely released. The likely reason is that the residue or polymer holding the actuator back spontaneously released its hold on the device, causing a surge of high power through the device. Fig. 6·11(a) shows an overview of the device, with areas that have broken either during actuation or during removal of the ball-bonding wires (springs, Chevron stage shuttle). Despite these sources of failure, the material has adhered as a whole on the anchor and shuttle side of the Chevron device (Fig. 6·11(b)). The shuttle and anchor stages are misaligned in the y-direction, which implies the material adhered to such an extent as to "twist" the floating device under strain. Interestingly, a closer look of at the material across the gap, in Fig. 6·11(c), shows how the material experienced a perfect break on the end attached to the shuttle end. This implies that the material was indeed anchored to the 2D strain device stage with considerable adhesion force.

The question remains as to the cause of such extraordinary adhesion. The likely can-

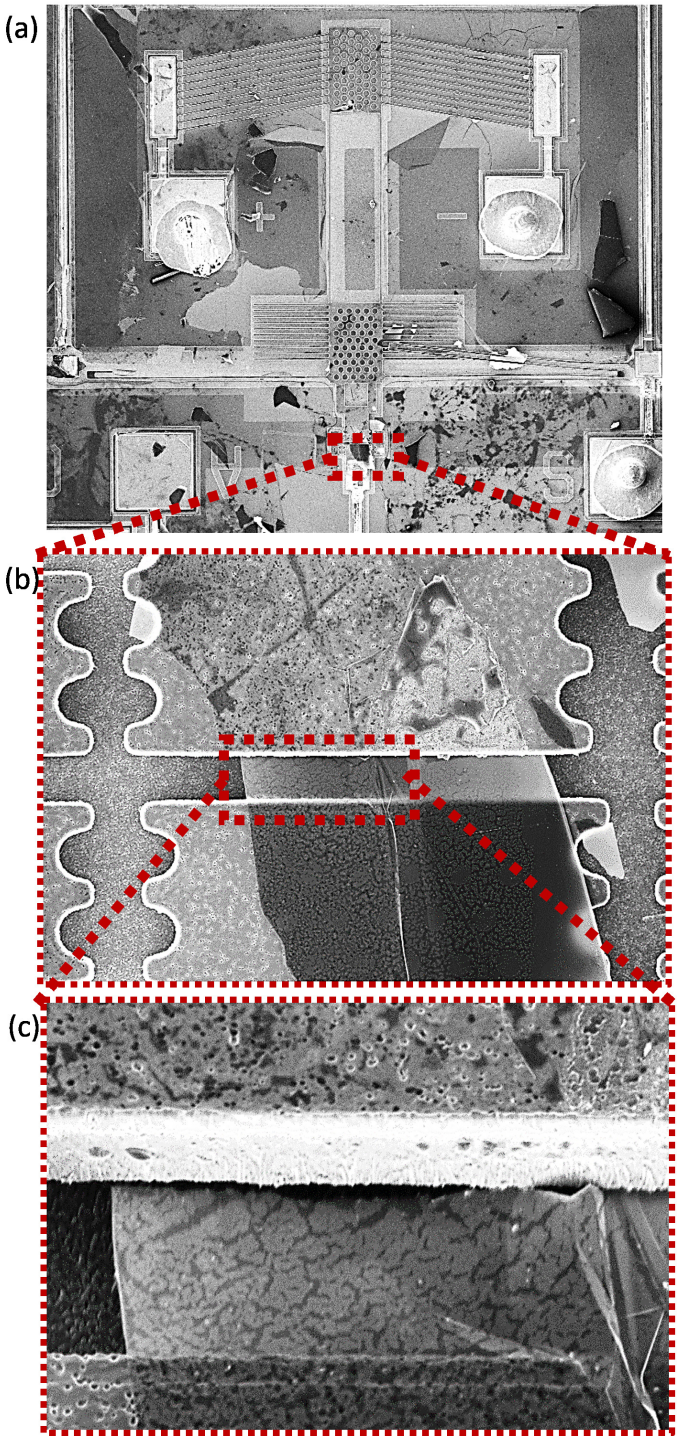

Figure 6·11: G34c CFNP Device Failure.

didate is that the reactive ion etching thinned successive regions of the few layer material. The thinner regions have greater frictional force, and will be more anchored to the substrate (Kitt et al., 2013; Wang et al., 2016). The initial PMMA transfer membrane would cause these regions to better conform with the substrate. Further studies using this method would provide clarification as to the nature of the adhesion force and its anchoring efficiency. This and other improvements and modifications are explored in Appendix E.6.

6.4 Conclusion

In this chapter, I describe two 2D material integrated MEMS devices, using CVD monolayer graphene and exfoliated few layer graphene. The CVD monolayer graphene was strained to 0.3% using MEMS, while 1.2% strain was observed in few layer graphene. Both devices exhibited non-ideal behavior as a result of the fabrication process. These issues will need to be overcome in order to see more reproducible results. However, these initial results show promise that the fabrication pipeline is almost there.

MEMS actuators pose many advantages over existing strain methodologies, and it has the potential to really advance the field of “straintronics" with 2D materials. While there are still many challenges to unlock this full potential, there are already many prospective applications made possible by the results from my thesis and other works from the Swan Group at Boston University. In the next chapter, I will propose some interesting applications and areas of exploration using the methods and results in this thesis (nanopillars and MEMS). The preliminary results will lay the groundwork for future experimentation and device prototyping.

Chapter 7

Applications of Strain on 2D Materials

7.1 Introduction

In my thesis, I have spent a considerable amount of time investigating, characterizing, and optimizing two different methods to strain materials: nanopillars, and MEMS actuators. I have also shown optical signatures of interesting physical phenomena arising from strain on materials, such as funneling of quasiparticles and charge carriers, and decoupling of multilayers. Nevertheless, establishing reliable methods of straining atomically thin materials is only half the battle. Utilizing them to probe unique strain-emergent properties will prove to be the real task, with more far-reaching importance. In this chapter, I will propose some applications of strain on 2D materials using the methods tried and tested in my thesis, to motivate further research in this direction. With effort, building on techniques and methods established thus far, I believe these prospective applications are on the horizon, and will mark a watershed moment in the timeline for “straintronic" technologies.

7.2 Electron-hole Plasma Formation in MoS_2 on Nanopillars

Transition metal dichalcogenides are an amenable platform to study many interesting physical phenomena such as transport, light matter interactions, and phase transitions. Applying strain through nanopillars is a powerful yet facile “knob" to tune these properties. Nanopillars cause localized changes to electrical and optical fields in the materials, and can control formation, motion, and lifetime of quasiparticles like excitons and trions. In this thesis, I

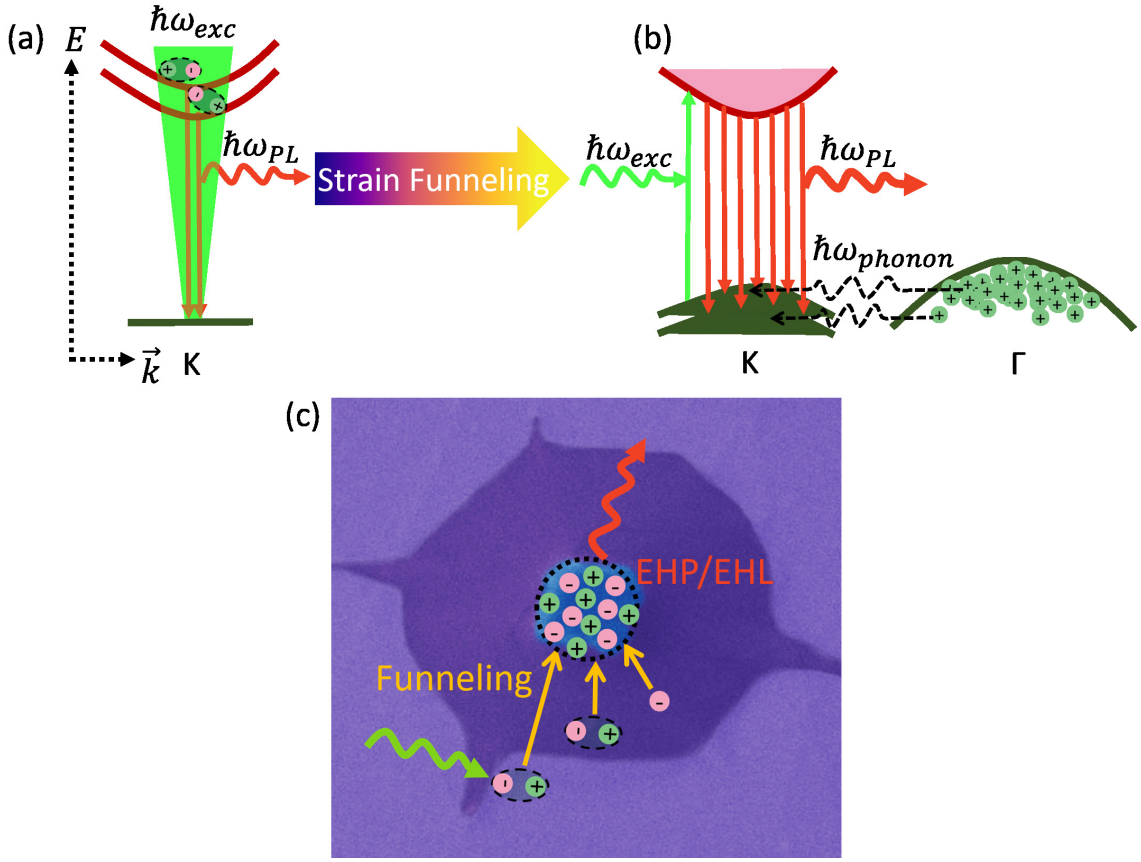

Figure 7·1: Dissociation of Excitons in Strained MoS_2 on Nanopillar. (a) Excitons are momentum-restricted, and brightly luminescent within the light cone. (b) As strain funnels charges and excitons to an area, the excitons dissociate in to free electron-hole pairs. Recombination of electron-hole pairs is not restricted by the light cone and causes much brighter PL. (c) Localization of charges and excitons through funneling can cause a phase transition into electron-hole plasma or electron-hole liquid in nanopillars.

have demonstrated how non-uniform local strain in multilayer MoS_2 can cause accumulation of charges, excitons, and form trions in a region. Uniquely, evidence of dissociation of excitons in to free-electron hole pairs was shown as a driving force behind the extraordinary photoluminescence enhancement in strained multilayers of MoS_2. Further exploration of this phenomenon is of great interest in the optoelectronics community. In particular, nanopillar-strained multilayer Mo_2 is a potential platform to observe many-body interactions and novel phase transitions 2D materials.

Typically, excitons in TMDCs such as MoS_2 are highly stable at room temperature under a range of population densities, due to their strong binding energy. However, beyond a certain threshold population density, the excitons can undergo Pauli blocking and dissociate into free-electron hole pairs (Steinhoff et al., 2017; Chernikov et al., 2015a; Zhai et al., 2012). The ionization of excitons in to free charge carriers increases the dielectric screening in the system, and can cause a quantum mechanical phase transition (or Mott transition) into a dense ensemble state known as the electron-hole plasma (Shah et al., 1977; Snoke, 2008). A further phase transition occurs at even higher photogeneration rates, where the electron-hole plasma condenses in to a strongly-correlated Fermi liquid, known as the electron-hole liquid (Nagai and Kuwata-Gonokami, 2002; Staehli, 1976; Arp et al., 2017).

Fig. 7·1(a&b) shows the consequence of this phase transition as an evolution in the band structure. Under 0% strain, the exciton is a quasiparticle that recombines within a narrow light cone of the incoming laser, $\hbar\omega_{exc}$ (Fig. 7·1(a)). This “bright" exciton recombination emits a photon, $\hbar\omega_{PL}$, whose emission energy can be tuned by the application of strain. Under non-uniform strain, the excitons funnel during their lifetime and localize in the band minima. In the presence of funneled charge carriers, the increase in dielectric screening causes dissociation of excitons in to electron-hole pairs. This marked by extremely strong recombination around the K point, unrestricted by the narrow light cone of the laser (Fig.

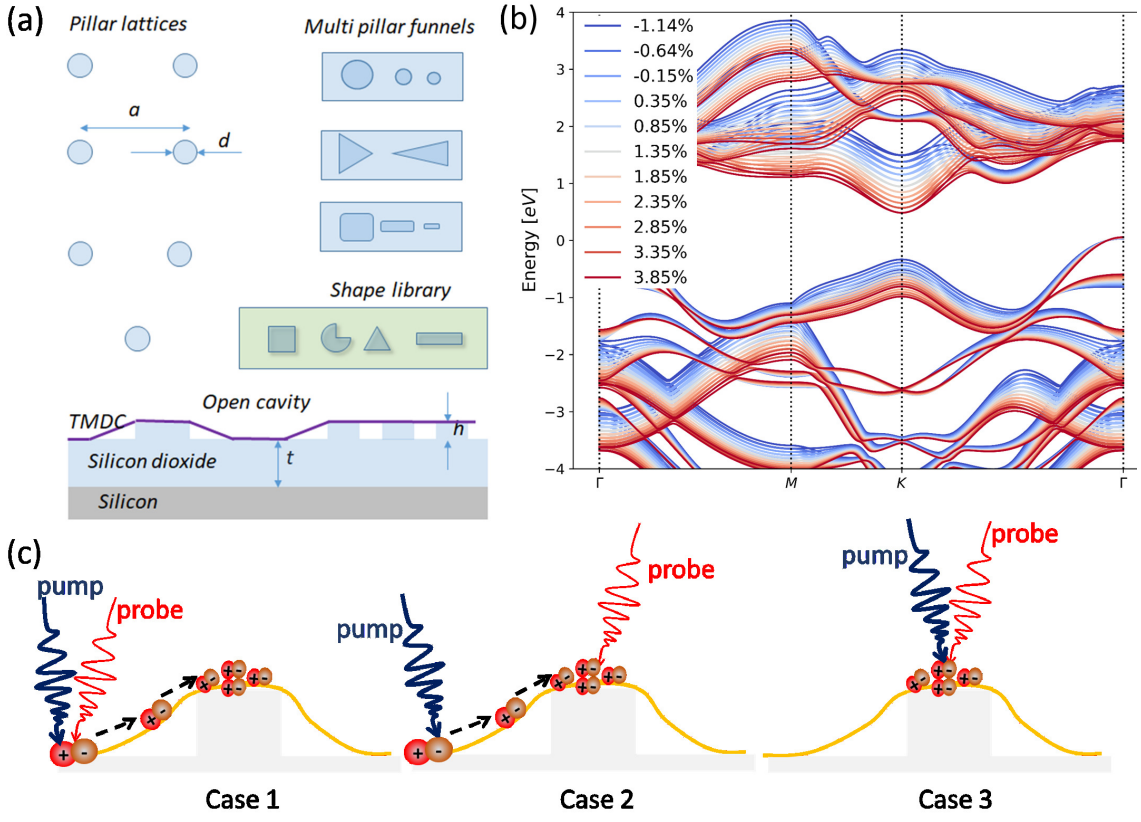

Figure 7·2: Experimental and Theoretical Toolkit. (a) Nanopillar shapes, aspect ratios, and spacing can be designed using EBL. (b) Insight into the band structure evolution of indirect MoS_2 under biaxial will be complementary to the experimental thrust. (c) Pump-probe experiments and time-resolved spectroscopy will further reveal the nature of the light-matter interaction in nanopillar-strained MoS_2.

7·1(b)). By harnessing the power of localization of carriers and quasiparticles, we can effectively promote the formation of the electron-hole plasma, on demand, as illustrated in Fig. 7·1(c) (Bataller et al., 2019; Yu et al., 2019; Yu et al., 2020).

Further experiments in this area could be directed towards fabrication of new pillar geometries, as shown in Fig 7·2(a). A whole host of shapes could be investigated in order to increase funneling strength, stimulate brighter photoluminescence, or even cause directional flow of electron-hole droplets. The SiO_2/Si platform is amenable to electrostatic gating experiments, and top gates can be constructed using the silicon nitride mask method utilized for the MEMS riveting procedure. As a foundation to the experimental work, theory behind the band structure evolution for multilayers under biaxial strain will need to be established to really understand the dynamics of carriers in the system (Rustagi and Kemper, 2018). Fig. 7·2(b) shows initial results from biaxial strain applied to bilayer MoS_2. I gratefully acknowledge the Kemper Group at NCSU for the calculation, and supporting these experimental works with their theoretical methods. Further optical experiments, using pump-probe and transient reflectance studies (Fig. 7·2(c)), will fill in the gaps about the nature of the material under non-uniform strain (Zipfel et al., 2020).

7.3 Pseudo-magnetic Fields in MEMS-Strained Monolayer Graphene Designed Using Machine Learning

Pseudo-magnetic field generation is an extraordinary phenomenon in strained graphene. PMF arises as a consequence of non-uniform strain on the electrons in graphene, where the electrons feel a effective potential from the application of strain and start to precess in a cyclotron orbit as in a real magnetic field (Guinea et al., 2010; Novoselov et al., 2007; Schomerus and Fal, 2013). A seminal paper by Levy *et. al.* first captured this phenomenon when they demonstrated pseudo-magnetic fields in excess of 300 T, created by graphene nanobubbles on Pt (Levy et al., 2010). Using scanning tunneling spectroscopy, the local

electronic structures of strained graphene was characterized, revealing a series of strong peaks spaced by more than 100 meV. These peaks arise from a large, relatively uniform pseudo-magnetic field induced by strain, which mimics the effects of the real magnetic field applied perpendicular to the graphene sheet. This peak separation demonstrated that the electron orbits in the system are quantized, equating to Landau levels in a magnetic field. Interestingly, the mechanism of strain application here is by exploiting the thermal coefficient mismatch between graphene and the substrate. Evidently, this isn't an efficient mechanism to reproduce in a device setting. The mechanism of strain has to be more deliberate than this in order to really utilize the consequence in devices (Verbiest et al., 2015; Zhu et al., 2015).

As described in Chapter 4, integration of 2D materials with MEMS devices gives extraordinary control to fabricating and designing custom strain configurations. By adapting the MEMS platform or shaping the graphene with electron beam lithography, we can create strain fields that induce a non-vanishing vector potential. Here, I will describe advances in numerical simulations of the PMF in suspended graphene, in way that could enable future experimental work to probe its strength, tunability and localization (Settnes et al., 2016b; Settnes et al., 2016a; Settnes et al., 2017).

We simulate strain in graphene using finite element analysis, using a coupled structural and partial differential equations solver. In Fig. 7·3(a&b), I demonstrate two different geometries in particular that we can realize in our device setup, by either changing the CAD design of the MEMS or shaping graphene through lithography. Fig. 7·3(a) shows graphene patterned such that the width of the membrane varies in the y direction. Developed by Zhu *et. al.*, the shape function is calculated to achieve large regions of uniform pseudo-magnetic field (Zhu et al., 2015). Fig. 7·3(b) shows graphene that has an effective wedge shape. This geometry is easily realizable through redesigning the 2D strain device stage. Both these geometries are drawn and simulated in COMSOL Multiphysics. On the edges clamped to

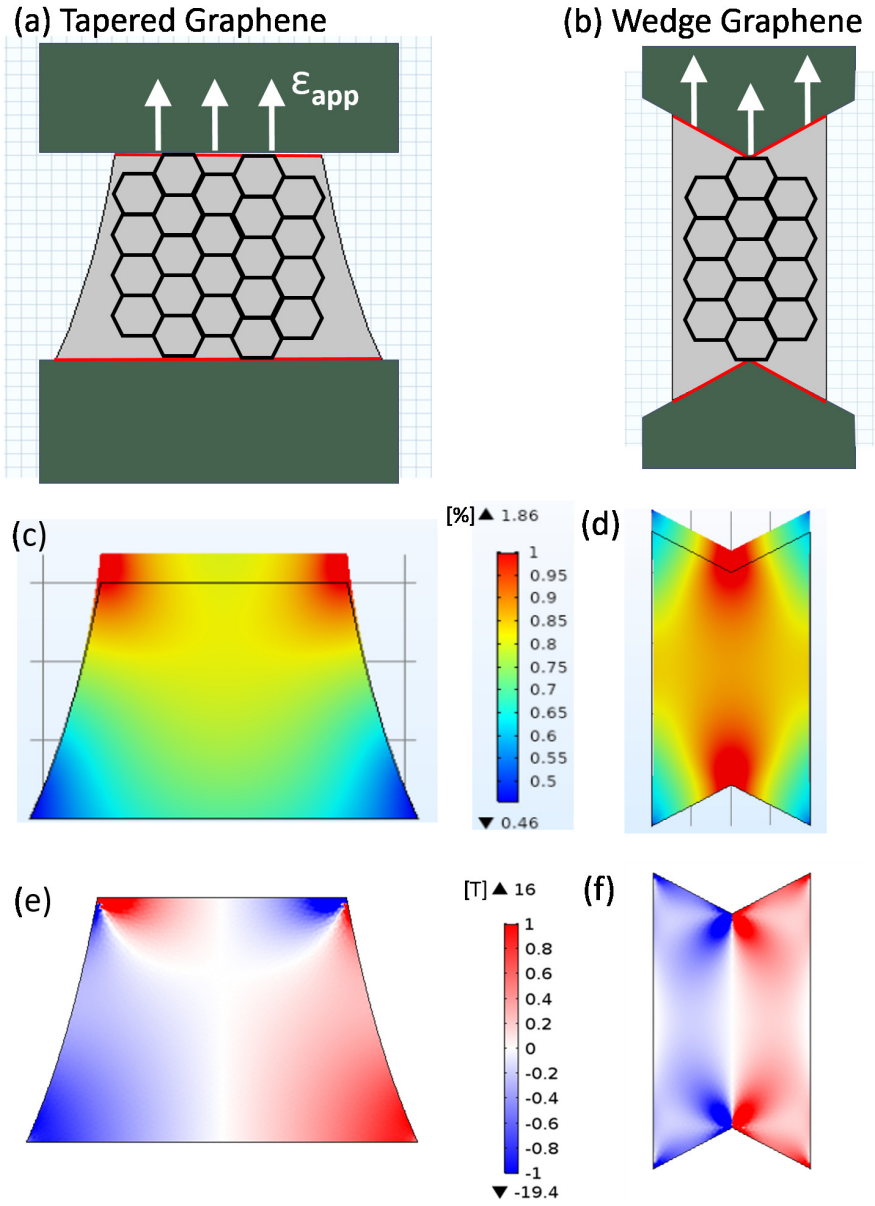

Figure 7·3: Finite Element Modeling of PMF in Graphene. (a&b) Schematic of graphene geometries and strain direction. (c%d) First principal strain distribution from application of 1% strain. (e&f) Calculated PMF profile.

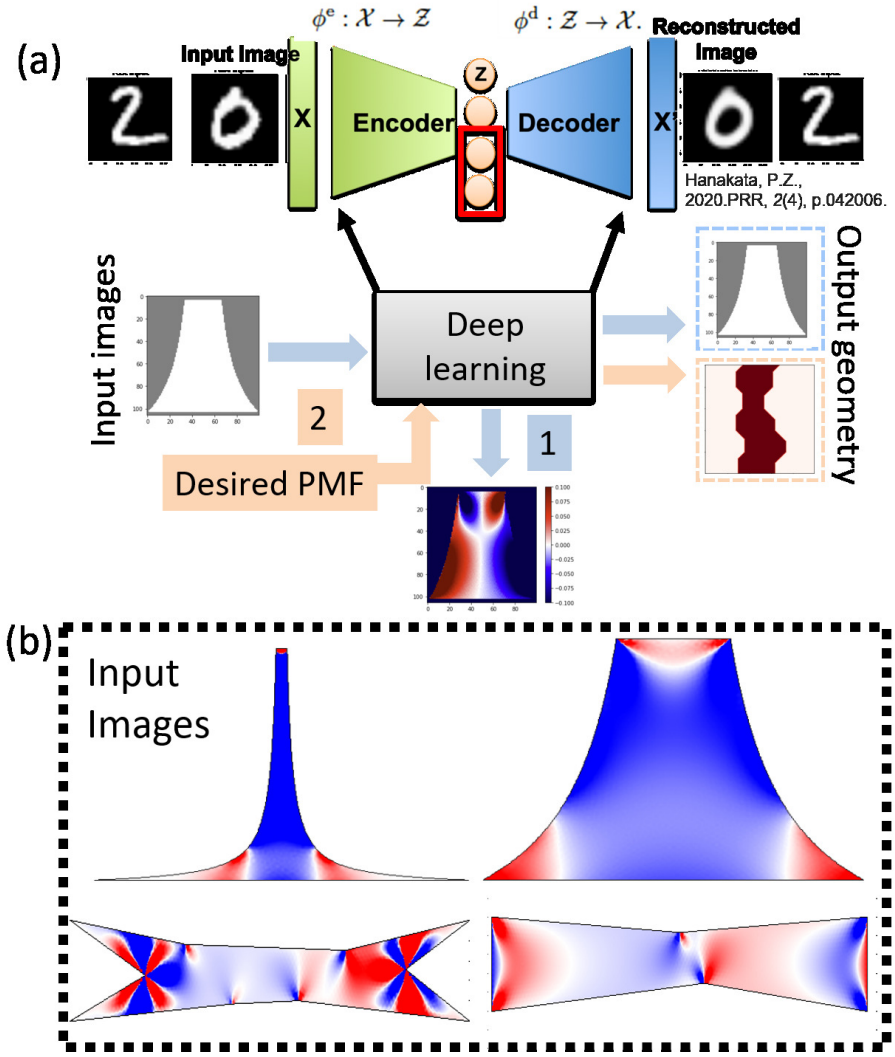

Figure 7·4: Designer PMFs in Graphene through Deep Learning. (a) Workflow of deep learning model using a variational autoencoder to classify, simulate, and predict optimal graphene geometries for specified PMF distributions. (b) Input models generated through finite element modeling.

the MEMS 2D strain device stage (shown in red), the side length of the graphene is constrained. However, the transverse length and longitudinal width are allowed to expand or contract according to the Poisson's ratio. Fig. 7·3(c&d) shows the geometry strained to 1%, which has been demonstrated as a realizable strain for our MEMS device. The deformation is exaggerated using a scaling factor to more effectively show how the material deforms under uniaxial strain. The strain is applied along the zig-zag edge of the graphene. We restrict the strain in the simulation to small applied strains to stay within the bounds of the continuum elasticity model. Hence, the strain is slowly varying so it is completely captured using infinitesimal strain theory without the use of non-linearity in the finite element modeling. The exception to this is in the corners of the graphene, where there is a sharp breakdown in linear elasticity due to size constriction. We neglect these affects as these are not experimentally realizable strains. At this step, the structural mechanics module gives the strain tensor components we need to compute the pseudo-vector potential.

Next, I use the partial differential equations interface to compute the curl of the vector potential directly. The generated PMF for both geometries of graphene is shown in Fig. 7·3(e&f). The two profiles show significant regions where we can expect the PMF to be fairly uniform. Furthermore, these are large pieces of graphene compared to sizes considered in other works. Although PMF strength scales inversely with the length of the graphene ribbon (Stegmann and Szpak, 2016; Uchoa and Barlas, 2013), we can still realize strong fields within these geometries. Furthermore, we can easily fabricate even smaller regions within the limits of EBL, thereby increasing the field by as much as 30 times. Interestingly, we can see edge states starting to arise from where the sign of the PMF reverses. These are regions where counter-propagating edges currents arising from K and K' valleys can be harnessed to make quantum valley hall devices (Zhu et al., 2014; Zhang et al., 2014a; Hsu et al., 2020). These features are dependent on length of the graphene, as well as the rotation of the graphene lattice with respect to the strain direction (Zhang et al., 2017).

Finite element methods have proven invaluable in understanding strain configuration, deriving vector potentials from the strain tensor, and calculating the effective pseudo-magnetic field. However, this clearly necessitates an *a priori* knowledge of a strain field in order to know that it will induce the non-vanishing vector potential under uniaxial strain. Apart from straightforward configurations, as seen in Fig. 7·3(b), or extensive theoretical work into designing an ideal geometry, as in Fig. 7·3(a), it is has hard to develop an "intuition" for what kinds of strain configurations are optimal. In addition, it is hard to predict where regions of uniform pseudo-magnetic field will be produced, and if we can expect any magnetic zero mode formations. A further challenge would be to optimize for these two features and create the geometries that generate large regions of uniform PMF and magnetic zero modes that are stable, narrow and fully traverse across the suspended graphene from shuttle to the anchor. The large region of uniformity would allow us to detect the PMF strength using optical methods and the robust magnetic zero mode would enable conducting channels that are topologically protected.

Therefore, without the *a priori* knowledge of optimal geometries, a machine learning approach would greatly enhance geometry discovery (Zhang et al., 2019; Nie et al., 2018). Fig. 7·4 outlines the process flow for our deep learning model. We use a simplified Autoencoder, which has been shown to take in an image, generate a latent representation in the middle, and output a reconstructed image (Hanakata et al., 2020; Hanakata et al., 2018; Hanakata et al., 2016). The machine learning model will achieve two tasks:

- Given a large data set containing geometries and their simulated pseudo-magnetic field, identify and categorize optimal shapes that meet our criteria.
- Given a set of desired attributes of the pseudo-magnetic field distribution, generate geometries according to certain specifications that meet those criteria.

These are demonstrated as paths 1 and 2 in the process flow of Fig. 7·4(a). We will input the graphene geometries in the deep learning model and use the PMF to train the

encoder and decoder. This follows path 1. In order to generate a large set of graphene geometries, we use finite element modeling and python algorithms to draw different geometries under the restrictions of the MEMS device (3 μm suspended region, 1% strain). Fig. 7·4(b) shows geometries simulated by finite element method (top row) and python (bottom row). The finite element geometry generation used the tapered profile previously discussed, and changed the curvature of the sides in a parametric sweep. 600 different geometries were generated using this method. The python geometry generation used a simple rectangular latent space, and changed the number of vertices in the space to draw a geometry. The geometries were constrained to sizes that would allowable by the resolution limit of electron-beam lithography, in order to maintain fabrication compatibility. 1000 unique images were designed using this method.

The resultant PMF under 1% strain was simulated for both these sets of geometries (1600 images in total) using finite element methods. The geometries were inputted in to the deep learning model and randomized. Of the entire data set, 80% was randomly selected as a training set, and 20% was saved for testing. Connected-component labeling and graphing algorithms are used to label the data set, while searching for geometries that match our criteria. The classification algorithms in our deep learning model are then able to identify and demarcate those geometries which meet our criteria for large uniform region of PMF and robust edge mode. Once the algorithm is trained to identify optimal geometries we use the labeled data set as the “ground truth" to train the supervised Autoencoder. We input our own criteria for desired PMF configurations and compute the output geometry through the decoder process, following path 2 in Fig. 7·4(a). During this process, we are trying to minimize the loss function between the input and output geometry through the latent space representation. Prospective additions to the algorithm will aim to remove the need for finite element modeling completely, in order to design geometries and calculate the PMF in one step, all in the same code base. This process flow has the potential to unlock

new geometries with unique PMF features, without the need for human intervention.

7.4 Low-Dimensional Materials Strained using MEMS Actuators

The controlled application of mechanical stresses on low-dimensional membranes has an established technological history. Strain-tunable opto-electronic properties have been thoroughly investigated in “III-V" semiconductor compounds such as tuning emission properties in nanowires (Greil et al., 2016; Signorello et al., 2013; Zardo et al., 2012), application in flexible electronics (Kim et al., 2008; Yang et al., 2012), and quantum optics (Xu et al., 2014; Seo et al., 2016; Sookchoo et al., 2013). Nanomembranes are crystalline materials of thickness ranging from tens of nanometers to microns (Paiella and Lagally, 2018; Chaâbani et al., 2016; Gilperez et al., 1992). Although they are macroscopic when compared to atomically thin, 2D materials, nanomebranes are nonetheless able to withstand significant amounts of strain ($< 5\%$) (Paskiewicz, 2012; Jain et al.,) before failure.

Recently, Wang *et. al* demonstrated the broadband tuning of optical emission using strain in low-dimensional indium gallium arsenide (InGaAs) nanomembranes (Wang et al., 2018; Boztug et al., 2014; Wang and Ma, 2020). InGaAs nanomembranes of thickness $\sim$ 100 nm were affixed to polyimide films. The flexible film was allowed to bulge via pressurized N_2 gas flow while hermetically sealed in a chamber. The film transferred 1.16% biaxial strain to the InGaAs nanomembrane on top, which adhered through hydrogen and van der Waals interaction to its underlying substrate. Observing the PL response as a function strain demonstrated remarkably wide-ranging emission wavelength tunability of Δ250 nm. Beyond this level of applied strain, the nanomembrane experienced slipping from the polyimide film.

Motivated by these remarkable results, I aimed to demonstrate low-dimensional material-integrated MEMS devices for strain-tuning optical emission in InGaAs. The demonstrated strain-capabilities of the MEMS actuator combined with our microstructure material trans-

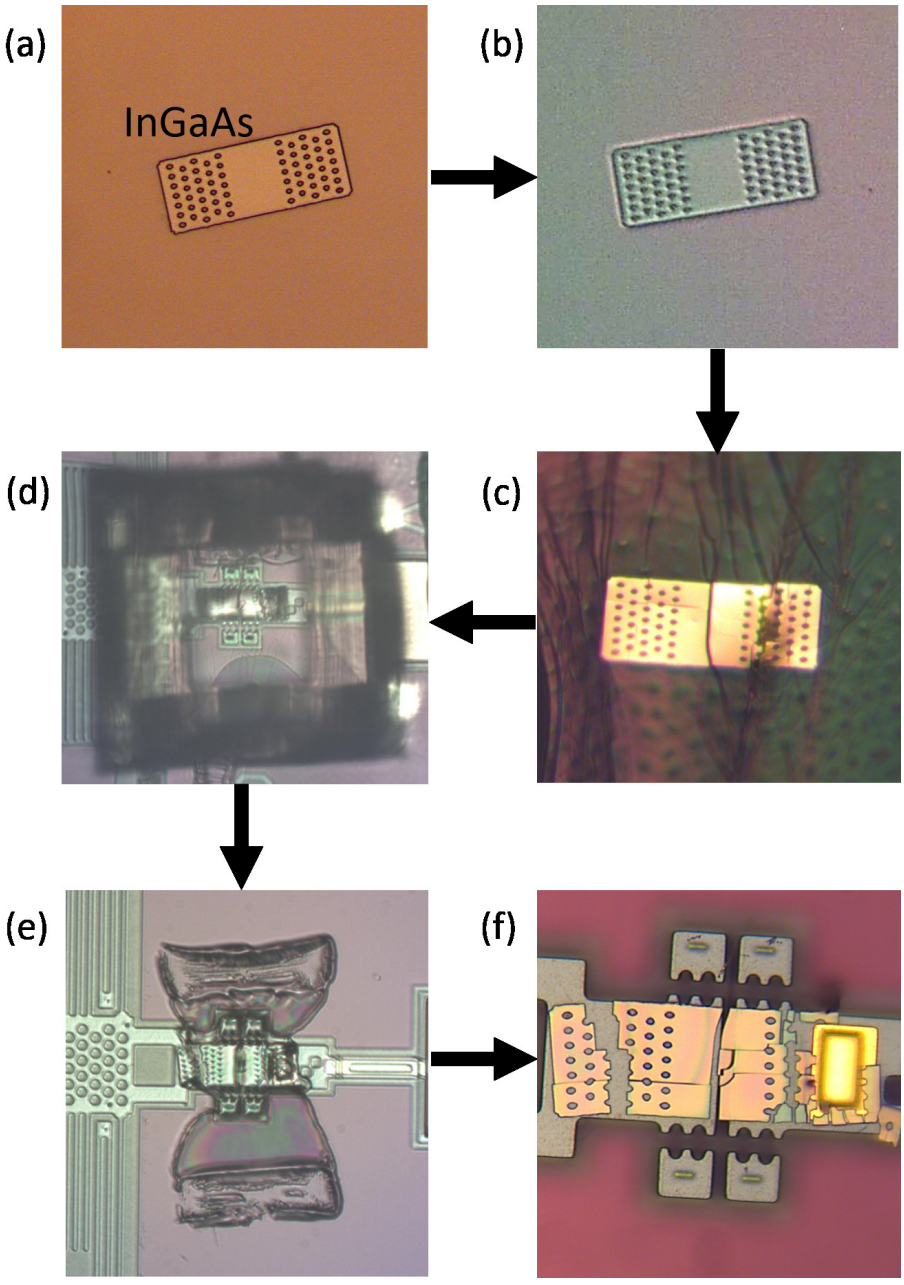

Figure 7-5: Fabrication of InGaAs Nanomembrane integrated MEMS device.

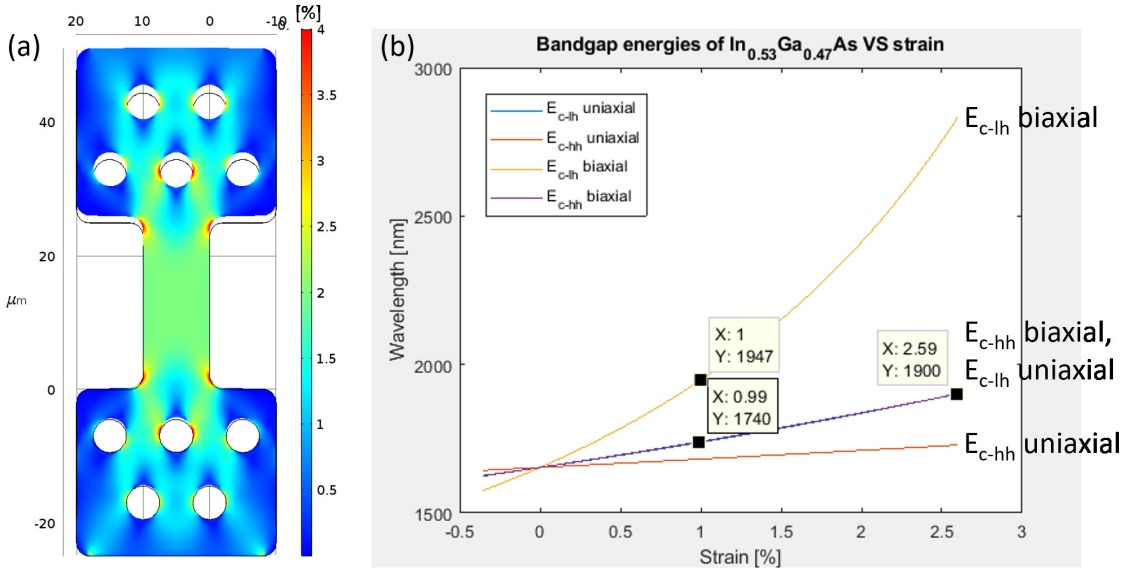

Figure 7·6: Modeling of Strain on InGaAs. (a) FEA modeling uniaxial strain on InGaAs nanomembrane. The suspended region has uniform 2% strain, while corners and edges of rivet holes experience higher strains. (b) Change in bandgap of InGaAs as function of strain, both uniaxial and biaxial.

fer and microrivetting procedures form an optimal road-map to more controllable application of strain on these nanomembranes. This work was done in collaboration with Dr. Xiaowei Wang and the Paiella group at Boston University. In Fig. 7·5, I show optical images of the fabrication process flow to integrate InGaAs with the MEMS device. $In_{0.53}Ga_{0.46}$ is grown via molecular beam epitaxy on sacrificial layers of InAlAs/InP. In order to suitably shape the InGaAs nanomembrane for the MEMS device, we coat with the substrate with a photoresist, and, using a specially designed mask, expose a desired shape to UV light. The exposed “island" of InGaAs is etched in citric acid, as shown in Fig. 7·5(a). Here, the dimensions of the InGaAs are: length $L = 76\ \mu m$, width $w = 30\ \mu m$, and thickness $t = 100\ nm$. $2\mu m$ diameter holes for microrivetting are introduced on either end, while a gap of 25 μm is left to allow for suspension on the 2D strain device stage. Following the microstructure transfer process illustrated in Chapter 5, PPC is spin coated on top of the entire chip as shown in Fig. 7·5(b). In order to release the shaped InGaAs nanomembrane and etch away the sacrificial growth layers, the float release of the PPC+nanomembrane is done in HCl of 3:1 concentration with H_2O, at 40 °C for 1 hour. A surfactant, sodium dodecyl sulfate (SDS), was added to prevent bubbles from forming during release, which could adversely effect with PPC. Fig. 7·5(c) shows the InGaAs nanomembranes released from its substrate, suspended on a PPC membrane. The PPC+nanomembrane is transferred on to the microstructure, which then transfers it on top of the MEMS 2D strain device stage, as shown in Fig. 7·5(d). After taking the PPC through the glass transition temperature and lifting off the microstructure, the InGaAs nanomembrane is succesffully deposited on top of the MEMS device, leaving only PPC residue around the 2D strain device stage (Fig. 7·5(e)). The device is left in acetone overnight and undergoes CPD to dry the MEMS. The resulting InGaAs integrated MEMS device is shown in Fig. 7·5(f).

Clearly, the InGaAs underwent cracking and mechanical failure at some point during the process. I will discuss some ways to improve this fabrication here. Despite the addition

of SDS, the chemical etching of the sacrificial growth layer was a vigorous reaction and may have negatively effected the PPC polymer and wrinkled it. Since InGaAs is much stiffer compared to 2D materials like MoS_2, small fluctuations during the etching or handling of the polymer could have caused cracks to transfer to the nanomembrane, as well. A future modification to this procedure will use a thicker layer of PPC and thinner, more flexible InGaAs membranes. In addition, strain relief cuts will be made to release some of the strain on the nanomembrane. In addition, the CPD will be optimized for sensitive materials.

The fabrication pipeline to integrate InGaAs with MEMS takes a little more effort to perfect. However, theoretical predictions based on our existing knowledge of the experimental framework can be made. In Fig. 7·6(a), I show a simulation of shaped InGaAs under 2% uniaxial strain. I use finite element modeling to simulate the strain, similar to the procedure followed in the previous section with graphene. The shape of the InGaAs is optimized so that there is uniform strain in the gap, and the force needed to strain to 2% is within the limit of the MEMS actuator (4 mN output force). The simulated InGaAs nanomembrane has a length $L = 75\ \mu m$, thickness $t = 100\ nm$, Young's modulus $E = 67$ GPa, Poisson's ratio $\sigma = 0.33$, and density $\rho = 5500\ kg/m^3$. In order to calculate the optimal width of the InGaAs membrane, I first consider the effective spring constant of the nanomembrane from Hooke's law,

$$k_{InGaAs} = \frac{EA}{d} \tag{7.1}$$

where E is Young's Modulus, area $A =$ some width w times thickness t, and $d = 3\ \mu m$ is the gap in the 2D strain device stage. From Eqn. 7.1 and the values previously defined, we can get a spring constant as a function of width w as $k_{InGaAs} = 2.23w[kN/m]$. For 2% strain in a 3 μm gap, the elongation will be $\Delta x = 0.06\ \mu m$. Hence, the force as a function of width required to produce 2% strain in InGaAs will be:

$$F_{app} = k_{InGaAs}\Delta x = 2.23w[\frac{kN}{m}] \times 0.06[\mu m] = 0.134w[mN] \tag{7.2}$$

Hence, the force required to strain InGaAs by 2% scales with the width of the nanomembrane across the gap as $0.134 \times w$ mN. For widths of 10 μ and 20 μm, the force required would be 1.34 mN, and 2.68 mN, respectively. This is comfortably within the maximum output force of the Chevron actuator. For widths $\geq$ 30 μm, the Chevron actuator would need to provide $\geq$ 4.02 mN of force, which is not within its current capability. In Fig. 7·6(a), I show the simulation results of a nanomembrane of 10 μm strained to 2%, with 5 μm diameter microrivet holes on either end. It is clear that the rivet holes and the corners of the nanomembrane experience high strain due to spatial constriction. In order to avoid this, the corners of the membrane should be smooth, and the rivet holes should be sufficiently separated so prevent propagating crack formation. Future device fabrication will use this simulation as a basis for designing the nanomembrane.

In order to understand the effect of strain on the electronics of the nanomembrane, a simulation of bandgap energies vs. strain was conducted by Dr. Xiaowei Wang, as shown in Fig. 7·6(b). This plots the change in bandgap between the conduction band and the strain-split heavy-hole and light-hole valence bands as a function of both uniaxial and biaxial strain on InGaAs. It is clear from the simulation that the degeneracy of the valence band is lifted to a lesser extent for uniaxial strain compared to biaxial strain. With increasing biaxial strain, Wang *et. al.* demonstrated that the electron-light hole recombination tends to increase TM-polarized light emission from the surface of the InGaAs, which decreases the overall integrated emission intensity. Hence, these results show that emission efficiency could significantly improve by applying uniaxial strain as a opposed to biaxial strain.

7.5 Conclusion

The unique capabilities of both nanopillars and MEMS are discussed in the context of their applications in this chapter. For nanopillars, possible exploration of interesting light-matter interactions, including observing the elusive electron-hole droplet state, is a distinct possibility given preliminary results. For MEMS, designer pseudo-magnetic fields and strain-tunable optical emission in low-dimensional materials are on the horizon. I believe that the foundational work laid down by my thesis will help pave the way for these exciting “straintronic" applications.

Chapter 8

Conclusions

In this thesis, I have demonstrated 2 platforms for strain engineering of 2D materials: nanopillars and microelecrtomechanical actuators and the strain-emergent phenomena that arise from deformation on their lattices.

The nanopillars are relatively straightforward to fabricate on SiO_2/Si substrates using electron-beam lithography and reactive ion etching. The resulting pillars discussed in this thesis are square with roughly 250-300 nm side length, 130 nm height, and produced in an array with 7 μm spacing. The standard transfer procedure of multilayer MoS_2 on top encapsulates several nanopillars at a time. The procedure allows the material to tent from the pillar to the substrate, causing uniaxial strain in the suspended region and biaxial strain at the apex of the pillar. The optical characterization using Raman and PL revealed thickness, polarization, effect of laser heating, and interference on the sample. The resultant strain wa 1-2% over 27 different samples. The monolayers showed negligible strain due to conforming closely to the pillar, without a tented region. Finite element modeling was performed in order to correlate tent-length with strain, and simulate the spatial distribution of the strain in 3D. As a result of the strain, excitons and charge carriers were funneled to the apex of the pillar. Non-local PL measurements revealed the interplay between exciton drift from funneling and diffusion in a 2 μm radius around the pillar. The localization of these two carriers resulted in an increase in trion formation on top of the pillar, when the neutral excitons converted to charged trions in the presence of excess charges. The strain funneling of carriers also resulted in an enhancement in dielectric screening atop the pillar.

This caused reduction in binding energy of excitons, and band gap renormalization in the material. As a result, the band-to-band transitions resulted in a dramatic enhancement in the PL from the pillar-strained samples.

MEMS actuators have the power to dynamically strain 2D materials in a controllable, voltage driven way. Fabricated devices showed incredibly controllable output displacement and IV characteristics, and agreed with finite element modeling of the devices. The issue of increasing temperature at the 2D strain device stage has been addressed through implementing a thermal isolation sink which prevented heat from flowing down the device to the sample. Hence, as the device was actuated, the 2D strain device stage remained isothermal. This was confirmed through finite element modeling of the whole device, infrared imaging, and Raman thermometry. The transfer procedure to integrate 2D materials utilized a specialized microstructure fabricated through direct laser writing. The anchoring was improved using gold microrivetting to prevent slipping under actuation. MEMS should ideally provide nanoscale control in strain. However, there are still challenges with the integration. Fabrication yield and repeatability are outstanding issues to be dealt with in order to integrate 2D materials with MEMS. Previously, monolayer MoS_2 integrated with MEMS devices showed 1.3% strain. Here, we expand on the MEMS capabilities by demonstrating 0.3% strain in CVD monolayer graphene and 1.2% strain in few layer exfoliated graphene. The resulting Raman spectra from few layer graphene under strain showed signatures of interlayer slip, which could be exploited to utilize MEMS as a platform to tune layer commensuration.

There are a number of prospective applications from these strain engineering platforms. The nanopillar-strained MoS_2 is an platform way to study electron-hole plasma formation using strain to localize the carriers enough to induce a phase transition. The resulting PL would show a sudden increase in PL intensity and broadening. Future experiments will attempt to controllably induce this transition by changing pillar dimensions, carefully mod-

eling evolution of band structure under train using DFT, and utilizing pump-probe experiments to capture funneling kinetics. From the MEMS, the possibilities of controllably applying strain fields to graphene is a pathway to observing pseudo-magnetic field generation in graphene. Finite element modeling was performed to demonstrate the PMF distribution in graphene under 1% strain. Future computational work will utilize a deep learning model to accelerate the search for desirable graphene geometries according to user-input specifications. Finally, due to the remarkable output force capabilities of MEMS, low dimensional materials like InGaAs can also be strain-engineered. The transfer and anchoring procedure can be adapted to integrate InGaAs on to MEMS, with some alterations to account for the increased stiffness in the thicker material. Band gap engineering using uniaxial strain is an intriguing prospect for InGaAs integrated MEMS devices.

2D materials are a real paradigm shift in the materials world. It is hard to believe that so many wondrous possibilities come from such small a thing. With the controllable application of strain, the tunability of fundamental materials properties and exploration new quantum states becomes accessible. With the methods and results presented here, I hope that road to straintronic devices using nanopillars and MEMS are on the horizon.

Appendix A

MoS_2 on Nanopillars

A.1 Nanopillar Fabrication: Recipes and Process Specifics

Chapter 2 provides a general overview for the nanopillar fabrication process. Here, I provide recipes and specific process parameters in order to aid replication of the experimental setup.

A.1.1 PMMA Recipe

Poly(methyl methacrylate) (PMMA) is a resist polymer which is highly suitable for electron beam lithography of nanopillars. Here, it is used as a positive resist, as the area dosed by the high voltage electrons during EBL is removed under development, leaving unexposed areas behind. The SiO_2/Si substrate is first prepared by plasma ashing (Gas: O_2 10 sccm, Pressure: 200 mTorr, Power: 250 W, Time: 15 minutes) to improve adhesion and cleanliness. In order to facilitate metal lift-off after chromium deposition, the PMMA is spun triple thick.

1. Using 950 A6 PMMA, add a droplet to the substrate suctioned on the spinner.
2. Spin the PMMA to a top speed of 2000 RPM using a ramp of 1000 RPM/s for 45 s.
3. Bake on a hotplate at 180 °C for 1 minute.
4. Repeat spin and bake process 2 more times, for a triple thick PMMA coating on the substrate.

A.1.2 Electron Beam Lithography and Development

Electron beam lithography is used to create the nanopillar array on SiO_2/Si substrate. It is preferable to use EBL for patterning over traditional UV lithography as there is more flexibility in designing shapes and sizes without the need for developing individual masks. The resolution limit of EBL is also smaller: $\sim$ 30 nm feature sizes are feasible with appropriate parameters compared to $\sim$ 100 nm using traditional UV lithography. The lithography space is designed in the NPGS system making use of the DesignCAD software. For the nanopillar system used in 2, an array of square pillars of side length 300 nm, separated by 7 μm is defined. For optimal resolution and sharp features, the EBL setting used are: 30 kV accelerating voltage, 10 μm aperture, 400 $\mu C/cm^2$ area dosage. The patterning is primarily optimized for the Zeiss Supra 40.

Aligning the array such that it is parallel with the sides of the substrate (assuming the substrate is a roughly square chip) will greatly simplify the alignment under a microscope and finding particular areas (such as in the Raman microscope). To do this during patterning, it may be necessary to rotate the SEM sample stage before patterning. One could endeavor to do this in the NPGS software. However, setting the rotation of the sample using the NPGS has proved faulty in the past, due to some small translation error inherent in the communication between the SEM and the NPGS. Instead, initial alignment and rotation should be handled on the SEM using some pre-patterned fiducials on the substrate or on a visible straight edge. The required area is aligned using the cross-hair alignment feature in the Zeiss software, and manual stage rotation using the joystick. Take care to ensure that the NPGS software rotation during patterning is set to zero so that this alignment stays during patterning. Before running the pattern on NPGS, use the on-screen guide for setting rotation angle. Instead of rotating the stage to a desired angle, apply a small a translation so that the calculated rotation is zero degrees. Apply this rotation to the SEM stage and exit out of the patterning run before the exposure step. Check the rotation on the SEM stage

navigation window. If the noted rotation is greater than 0.05 degrees, repeat the above procedure.

Following EBL, the pattern is developed by agitating for 70 seconds in 1:3 methyl isobutyl ketone (MIBK):IPA solution, followed by agitation in IPA for 20 seconds. The sample is dried with N2 gas. As a result, the exposed regions are washed off, leaving square gaps in the PMMA defining the nanopillar array.

A.1.3 Chromium Deposition and Lift-off

A thin layer of chromium acts as a mask for the pillar array. Metal deposition is achieved using electron-beam evaporation. Ensuring that the vacuum remains below 3×10^{-6} Torr prior to deposition and during the evaporation process allows for an even coating of chromium. However, as the chromium is only acting as a mask, and not an adhesive layer for electrical contacts, rough pumping is suitable. Deposit 20 nm of Chromium (Cr) at 2 $\dot{A}/s$ (Step: 1, Power: 12%, Ramp: 60 s, Soak: 120 s, Step: 2, Power: 14.9%, Ramp: 60 s, Soak: 240 s). After deposition, the PMMA is lift-off by agitation in acetone for $\sim$ 20 minutes. The thickness of the PMMA mask should make for sharp edges and ease the lift-off, but may take longer to strip off the substrate.

A.1.4 Reactive Ion Etch and Chromium Etch

The final steps involve formation of the pillars of a desired height by etching the areas uncovered by chromium. Etching down the SiO_2 is achieved through reactive ion etching as opposed to wet-etching (such as through KOH or TMAH) to maintain more control over the height of the pillar. As seen in the discussion in 2, the effect of interference on the optical signal is contingent on the thickness of oxide at the substrate and pillar, hence a controllable etching process is more favorable for fabrication of the pillars. In addition, the chromium capped areas of the substrate remain unaffected by the RIE process step. The RIE procedure is as follows:

1. First, a thorough IPA clean of the RIE chamber is necessary to maintain quality of the etching.

2. Following the IPA clean, the first run in the chamber will be an oxygen plasma clean using 10 sccm O_2, at 200 mTorr pressure and 250 W for 15 minutes.

3. Then, do a test run of the recipe with 50 sccm of CF_4 at 30 mTorr pressure and 100 W for 2 minutes).

4. Finally, add the sample in the chamber and repeat the recipe above.

This recipe etches the substrate down by 130 nm and the RIE makes the sides of the pillars relatively more even when compared to wet-etching methods. Finally, the chromium caps on top of the pillars are removed by agitation in chromium etchant for $\sim$ 1 minute, followed by rinsing in DI H_2O and N_2 drying.

A.2 AFM of fabricated nanopillar

Fig. A·1 shows the AFM characterization of a SiO_2 nanopillar fabricated on Si substrate. In the left AFM image, the measured region is 2.8 μm by 2.8 μm. The right is the cross-sectional height profile of the pillar. The measured pillar height is 130 *nm*, and the width is 300 *nm*.

A.3 Physical Vapor Deposition of MoS_2

The PVD growth, done with the assistance of Zhuofa Chen in the Swan Lab and Metehan Calis in the Bunch Lab at Boston University, undergoes the following process flow:

1. Ramp Step, 20 minutes: Increasing temperature from 20 °C to 900 °C, and increasing pressure from 20 mTorr to 40 mTorr.

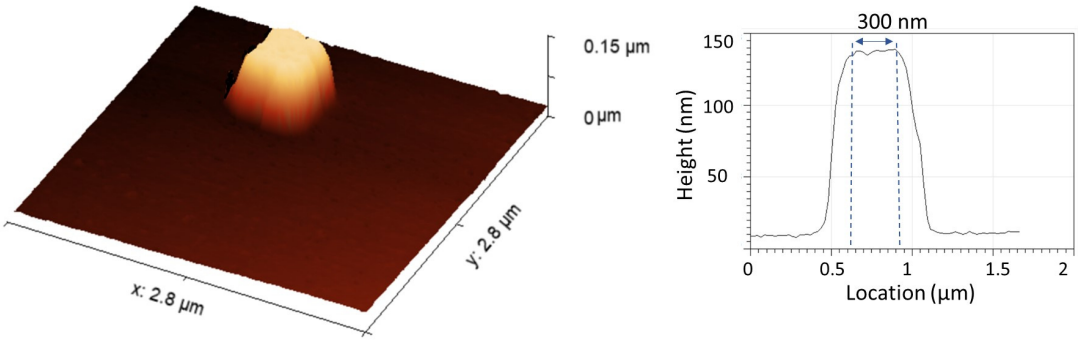

Figure A·1: AFM characterization of a representative pillar.

2. Growth Step, 20 minutes: Temperature remains steady at 900 °C. MoS_2 powder undergoes physical vapor deposition in the growth furnace tube and deposits on the substrate (Fig. 2·2).

3. Cool Down, 1 hr: The temperature gradually reaches room temperature under ambient conditions.

This procedure is reproducible to grow multilayer MoS_2.

A.4 Determining Laser Beam Waist

The transversal intensity profile of a radially symmetric Gaussian beam is described by:

$$I(x,y) = I_0 exp(-\frac{2(x^2+y^2)}{w^2}) \tag{A.1}$$

where I_0 is the peak intensity of the beam centered at the (x_0, y_0), and w is the beam radius, defined as half the spatial distance between diametrically points on the irradiance profile where the intensity is 1/2 (half-width at half maximum).

Walking a Gaussian beam across a “knife edge" is a easy way to determine the diameter of a diffraction limited laser spot. Here, we go across a sharp Au-Si transition on a Si substrate, as shown in Fig. A·2(a), in steps of 100 *nm*. We monitor the Si Raman feature at 520 cm^{-1} across the Au-Si edge. On the Au, the Si feature will be negligible, and will gradually increase in intensity as the beam traverses on to the substrate. Fitting the Si peak with a Fano profile, we extract the intensity of the Si Raman peak as a function of position, as indicated by the red data points in Fig. A·2(b).

The intensity profile can be fitted by an error function, given by:

$$I = I_{bg} + I_0 \times erf(\frac{\sqrt{2}(y-y_0)}{w}) \tag{A.2}$$

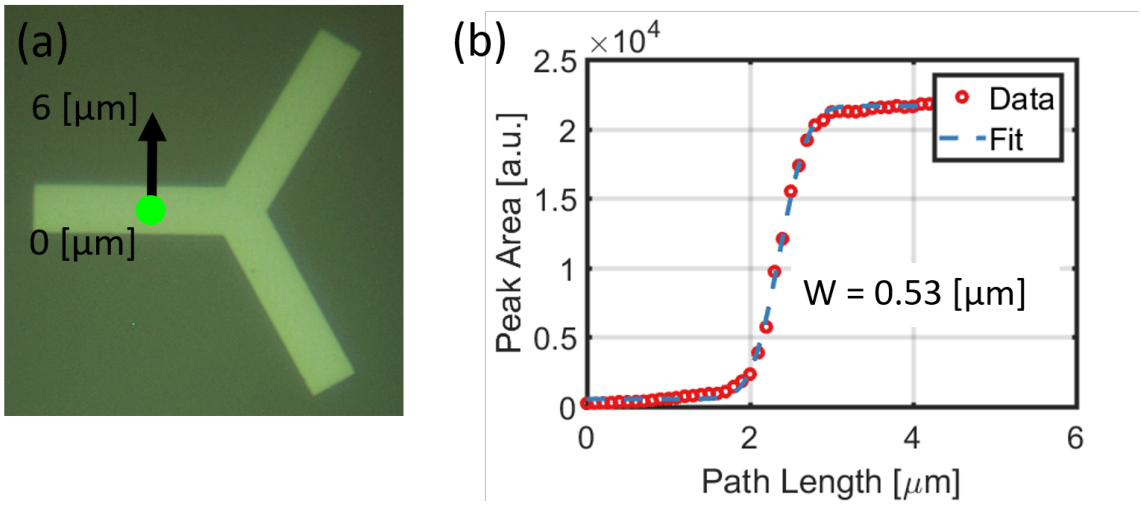

Figure A·2: Beam Waist Determination by Knife Edge Experiment. (a) Gold cross-hairs deposited on a Si substrate. Path of the laser (green point) is indicated by the arrow from 0 μm to 6 μm. (b) Increasing Raman Si intensity as a function of path length. The data is fit with an *erf* function. The beam waist is extracted as $W = 0.53\ \mu m$.

where I_{bg} is the background intensity, y_0 is the position of the scan, and w is the beam radius in μm. The fit is represented by the dashed blue line in Fig. A·2(b). We then extract the beam waist by the best fit to the data. In our experiments, the beam diameter is determined to be 0.53 μm, and is circularly symmetric.

A.5 Fitting Details

The fitting of the Raman and PL spectra was done on MATLAB ™. Voigt line shapes were created using the Faddeeva package (Zaghloul and Ali, 2012).

```
%  Define Voigt function
%       b(1) = Area of peak
%       b(2) = Peak position
%       b(3) = Half Width at Half Max of Lorentz part
%       b(4) = Standard deviation of Gauss part
voigt = @(b,x) b(1)*real(Faddeeva_w((x-b(2)+1i*b(3))/(b(4)*sqrt(2))))/(b(4)*sqrt(2*pi));

% Calculate range of values to plot a fit over
%   vec = vector of data set
%   pad = percent paddingtempS = data{F}(:,4);
fitRange = @(vec,pad) linspace(min(vec)-pad*(max(vec)-min(vec)),...
                               max(vec)+pad*(max(vec)-min(vec)));
% MoS2 PL
% 3 Voight + Linear Background
if pk == 2
    % - Rough peak parameters
    % Trion
    wt = 1.73;
    gt = 0.05;
    %  A Exciton
    w0 = 1.85;
    g0 = 0.05;
    %   B Exciton
    w1 = 1.9;
    g1 = 0.05;
    %
    % - Fit region
    wMin = wt-10*gt;
    wMax = w1+10*g1;
    % - Fit function
    %   3 Voight + Linear Background
    %   b(1) = Area Trion
    %   b(2) = Peak Position Trion, split
    %   b(3) = HWHM Trion
    %   b(4) = Area A
    %   b(6) = HWHM A
    %   b(7) = Area B
    %   b(8) = Peak Position B
    %   b(9) = HWHM B
    %   b(10) = Slope BG
    %   b(11) = Constant BG
    %   b(12) = Gaussian broadening
    fhP = @(b,x) voigt([b(1:3) b(12)],x) + voigt([b(4:6) b(12)],x) + voigt([b(7:9) b(12)],x)...
        + b(10)*x + b(11);
    bInit = [1 wt gt 1 w0 g0 1 w1 g1 0 0 0.002];
    % - Init update
    %   b = Initial fit parameter values
    %   S = Spectra [counts]
    %   w = Energy of spectra
    fhI = @(b,S,E) [pi*g0*max(S(wMin < E & E < wMax))*0.6 b(2) b(3)...
        pi*g1*max(S(wMin < E & E < wMax))*0.4 b(5:12)];
    % - Parameter range
    %   b = Initial fit parameter values

    pMin = @(b) [
         0 1.69 0.00...
         0 1.73 0.000...
         0 1.96 0.000...
         0 -Inf 0];
    pMax = @(b) [
        Inf 1.80 0.1...
        Inf 1.87 0.1...
        Inf 2.1 0.3...
        Inf Inf 1];
end
```

Figure A·3: Fitting PL and Raman of MoS_2 Using Voigt line shapes. 1/3

```
% MoS2 Raman peaks
if pk == 4
     % - Rough peak parameters
    %   E2g
    w0 = 383;
    g0 = 2.5;
    %   Alg
    w1 = 406;
    g1 = 2.5;
    % - Fit region
    wMin = w0-8*g0;
    wMax = w1+8*g1;
    % - Fit function
    %   3 Lorentzians + Linear Background
    %   b(1) = Area 1
    %   b(2) = Peak Position 1
    %   b(3) = HWHM 1
    %   b(4) = Area 2
    %   b(5) = Peak Position 2
    %   b(6) = HWHM 2
    %   b(7) = Constant BG
    %   b(8) = Slope BG
    %   b(9) = Gaussian Broadening
    fhP = @(b,x) voigt([b(1:3) b(9)],x) + voigt([b(4:6) b(9)],x) + b(7)*x + b(8);
    bInit = [1 w0 g0 1 w1 g1 0 0 0.002];
    % - Init update
    %   b = Initial fit parameter values
    %   S = Spectra [counts]
    %   w = Energy of spectra
    fhI = @(b,S,E) [pi*g0*max(S(wMin < E & E < wMax))*0.6 b(2)...
        b(3) pi*g1*max(S(wMin < E & E < wMax))*0.4 b(5:9)];
    % - Parameter range
    %   b = Initial fit parameter values
    pMin = @(b) [
    0 360 0 ...
    0 390 0 ...
    -Inf -Inf 0.00];

pMax = @(b) [
    Inf 400 6 ...
    Inf 410 6 ...
    Inf Inf Inf];
end
```

Figure A·4: Fitting PL and Raman of MoS_2 Using Voigt line shapes. 2/3

```
%% Import Data
%-----------------------
%% Averaging 3 Spectra
%%-------------------
% For Line scans and Maps
% Sum up three spectra, excluding the pillar region.
%% Fit the Data
%-----------------------

Iwf = find(wMin < E & E < wMax);

FitP = zeros(n,length(bInit));
Rnorm = zeros(n,length(bInit));

for f = 1:n
    bInit = fhI(bInit,S(f,:),E);
    [FitP(f,:), Rnorm(f,:)] = lsqcurvefit(fhP,bInit,E(Iwf),Srev(f,Iwf)',...
        pMin(bInit),pMax(bInit),optimset('TolFun',1e-12,'Display','off'));

    if pk == 4
        fh_Raman = @(b,x) voigt(b(1:4),x);
       E2g_Fit(f,:) = fh_Raman(FitP(f,[1,2,3,9]),E(Iwf));
        Alg_Fit(f,:) = fh_Raman(FitP(f,[4,5,6,9]),E(Iwf));

    elseif pk == 2
        fh_Exciton = @(b,x) voigt(b(1:4),x);
        T_Fit(f,:) = fh_Exciton(FitP(f,[1,2,3,12]),E(Iwf));
        A_Fit(f,:) = fh_Exciton(FitP(f,[4,5,6,12]),E(Iwf));
       B_Fit(f,:) = fh_Exciton(FitP(f,[7,8,9,12]),E(Iwf));

    end
end
```

Figure A·5: Fitting PL and Raman of MoS_2 Using Voigt line shapes. 3/3

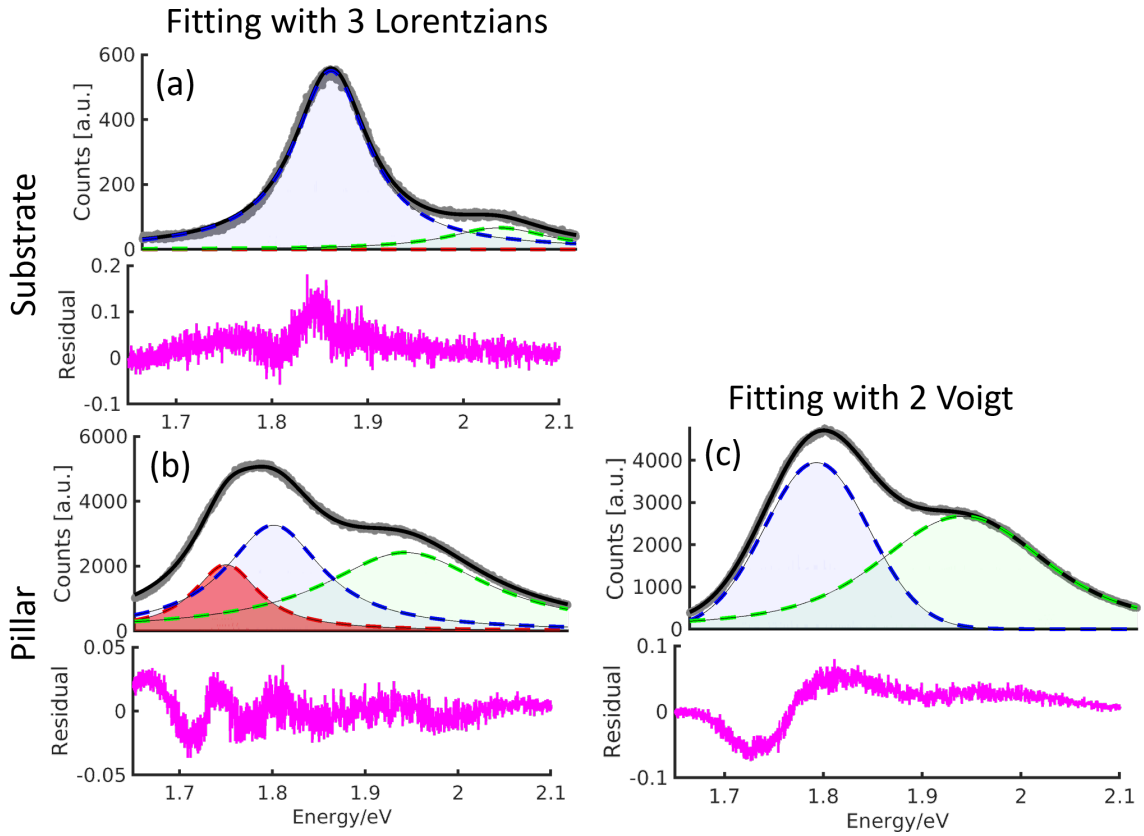

Figure A·6: Fitting PL from strained and unstrained MoS_2. (a&b) PL of MoS_2 is fit using 2 Lorentzian line shapes. The resulting fit on the substrate and pillar shows high residuals. (c) PL on the substrate fit with 2 Voigt functions shows high residuals, especially on the low energy end of the spectrum. This shows that an additional Voigt function should be added to effectively capture the trion peak.

A.6 Laser Power Studies: Additional Data

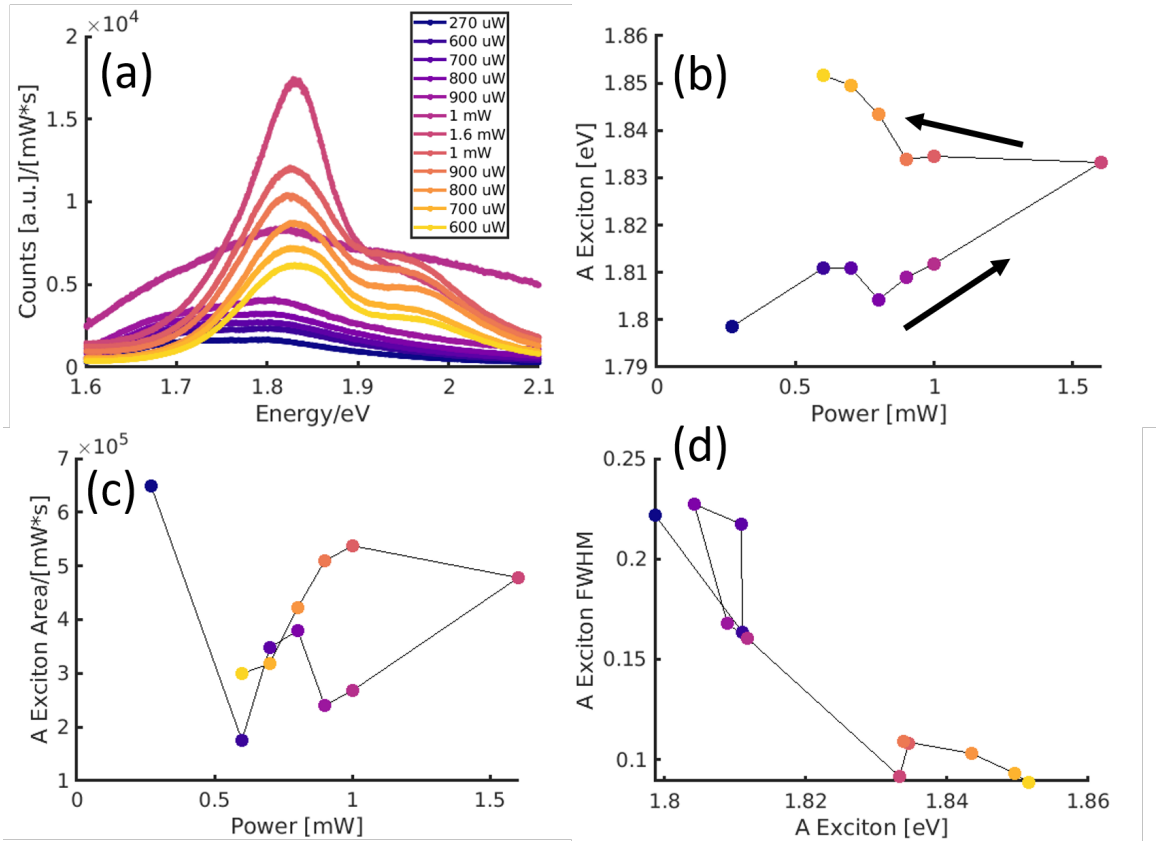

Figure A·7: Laser Power Study: Additional Data

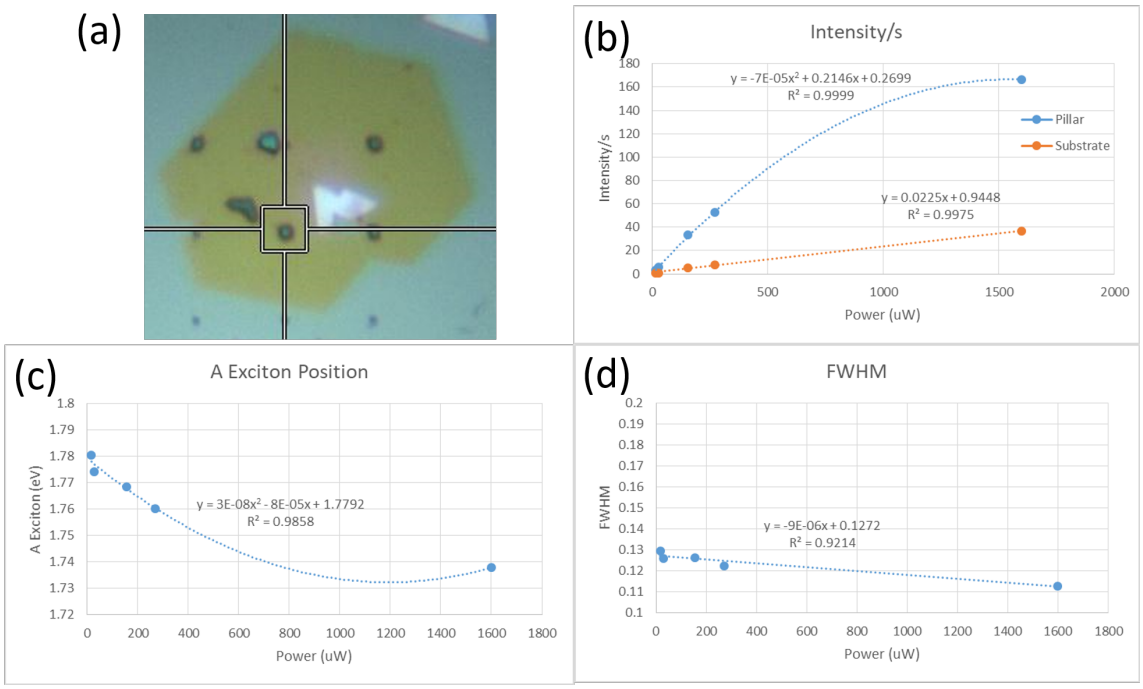

Figure A·8: Laser Power Study: Substrate vs. Pillar

A.7 Polarization Dependent Raman

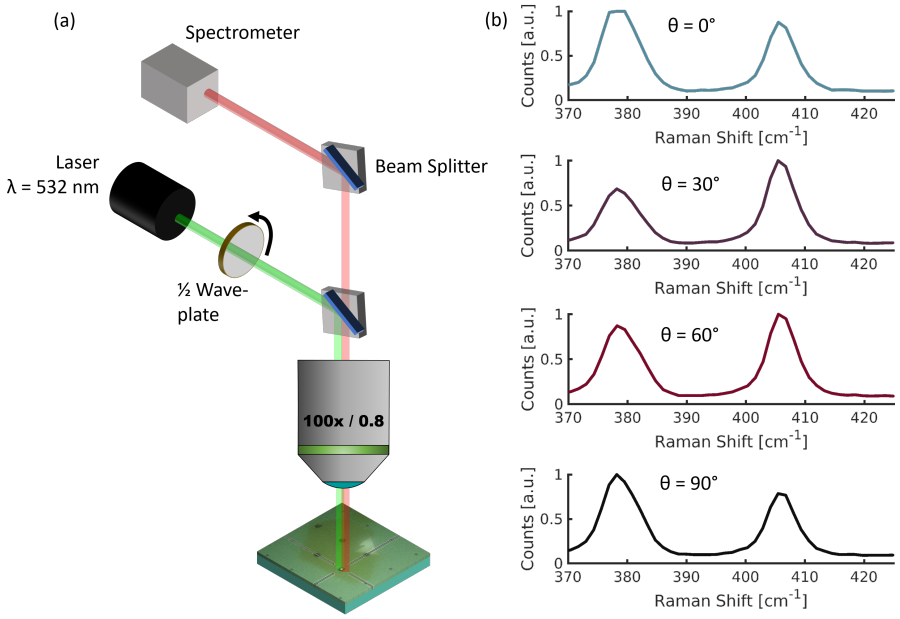

Figure A·9: Polarization Dependent Raman: Intensity, Position, FWHM. (a) Setup for polarized experiments with a 1/2 wave-plate, high NA, 100x objective, beam splitters. (b) Raman for θ =0°to θ =90°.

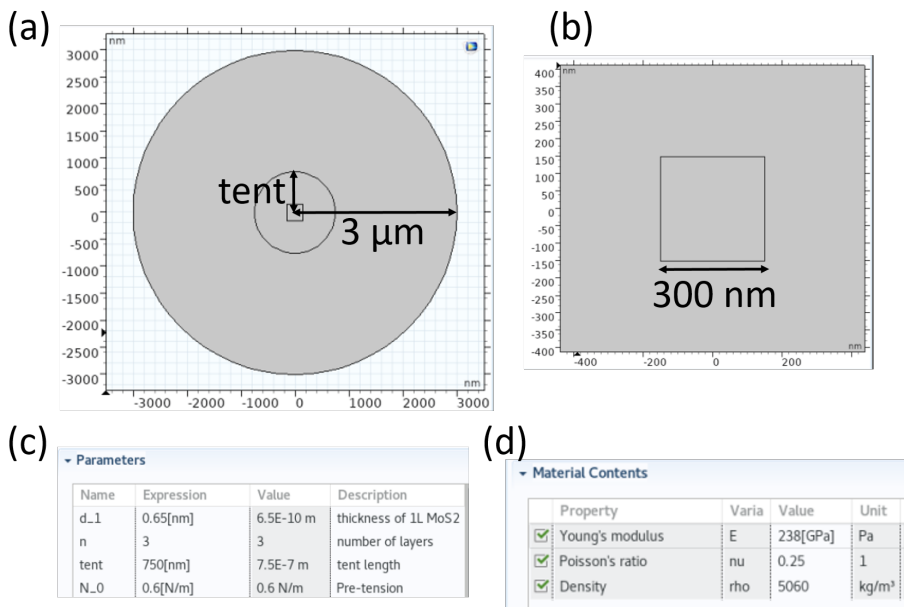

Figure A·10: Geometry and Material Parameters for FEM simulation. (a) Total MoS_2 has a 3 μm radius, and the tent length is allowed to vary. (b) The pillar at the center is square and has a side length of 300 nm (c) List of variables that can be parameterized during the simulation. (d) Material parameters for MoS_2.

A.8 Finite Element Modeling of Multilayer MoS_2 on Nanopillars

This section will detail how to perform the finite element modeling of multilayer MoS_2 on Nanopillars using COMSOL Multiphysics™. Here, only the deformation in the MoS_2 is simulated. The underlying substrate is not simulated. First, choose the 2D space dimension for the geometry. Under Physics selection, choose plate mechanics interface. This interface, along with the geometric nonlinearity introduced during computation, allows us to model thin structures with bending stiffness which undergo out-of-plane deformation, using the Kirchoff theory. Once the physics interface is added, select a Stationary study to compute the results. The calculated deformations are not dependent on time, and will be under static equilibrium.

Once the model is setup, draw the geometry according to Fig. A·10. A circle of radius

$3\mu m$ defines the total area of MoS_2 that the simulation will consider. Define another circle, concentric within the first, of variable radius “tent." This area defines the length of the tent region, as shown in Fig. A·10(a). Finally, add a square of side length 300 nm within the both circles (Fig. A·10(b)). All these shapes are centered at the origin.

In order to parameterize tent length, number of layers, and pre-strain in MoS_2, add these as variable under global parameters to the model, as seen in Fig. A·10(c). The initial values for simulating strain in trilayer MoS_2 uses, $n = 3$, $tent = 750nm$, $N_0 = 0.6[N/m]$. Finally, add material parameters by selecting a blank material and input the values shown in Fig. A·10(d) in the empty slots. As this is a purely structural simulation, only the Young’s Modulus, Poisson’s ratio, and density are needed. Here, we neglect change in the Young’s Modulus and Poisson’s ratio as a function of thickness. These can also be added in order to have a more complete simulation.

Next, move to the Plate interface. We will be considering MoS_2 as linear elastic material where the material properties are isotropic throughout. Under the thickness and offset node, parameterize the thickness of the 2D geometry by inputting $d = n \times d_1$, where n is the number of layers, and $d_1 = 0.65nm$ is the thickness of 1 layer of MoS_2. Next, add two prescribed displacement nodes under the interface. For one node, select prescribed displacement in z and input $u_{0z} = 130nm$, as seen in Fig. A·11(a). Leave all other displacements unselected, and the prescribed rotation as “free." In the model, add this displacement to the region of the MoS_2 in contact with the pillar, as shown in Fig. A·11(b). Repeat this process for the second prescribed displacement node, but this time, select prescribed displacement in z and input $u_{0z} = 0nm$ (Fig. A·11(c)). In the model, add this displacement by selecting the annulus from the tent region to the edge of the defined area of MoS_2, as shown in Fig. A·11(d). These simple additions are all that is needed to model the deformation of the MoS_2 by the nanopillar. By defining only the z displacement for each part of the model, we’re leaving the material free to translate in the xy plane and rotate accordingly.

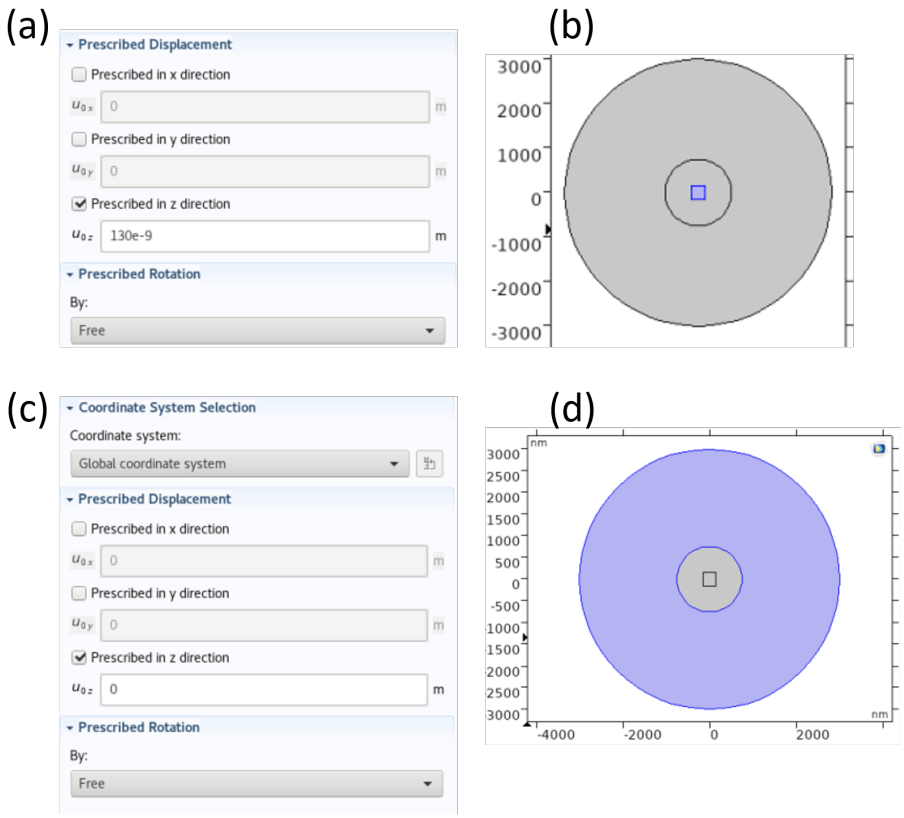

Figure A·11: Plate Interface Definitions (a&b) Prescribed z-displacement of 130 nm applied to the pillar region. (c&d) Prescribed displacement of 0 nm applied to the region from the tent to the edge of the defined area of MoS_2.

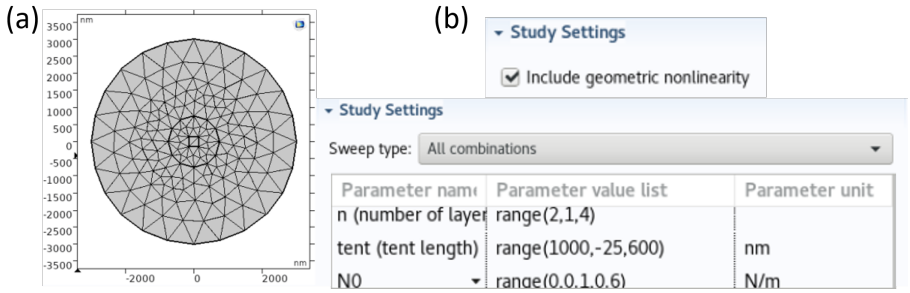

Figure A·12: Mesh and Simulation Settings. (a) A coarse triangular mesh is applied over the whole geometry. (b) Geometric nonlinearity is selected, and parameter ranges for layer number, tent length, and pre-strain in MoS_2 is defined. All combinations of these 3 variables will be performed during the simulation.

In addition, we're leaving the tent region unconstrained, to undergo deformation as it sees fit according to the continuity equations at its boundaries.

Finally, the geometry is meshed according to the desired granularity for the solution. Keep in mind that the a denser mesh necessitates a large number of iterations, and possibly a change in the relative error tolerance for the solution. Generally, a courser mesh should suffice (Fig. A·12(a)). Under Study Settings, "include geometric nonlinearity" must be selected in order to correctly model the large out-of-plane deformations that MoS_2 is subjected to. Finally, add parametric sweep to the study and input the desired variables you want to play with, and the range of values to consider. Since these variable change the geometry of the model at each step, it is not advisable to use an auxiliary sweep for this.

Appendix B

PL Enhancement from Strained MoS_2

B.1 Raman and PL Spectra

Fig. B·1 shows the raw data for Raman and PL spectra for a representative MoS_2 sample on nanopillar, fitted with Voigt profiles. The E^1_{2g} phonon mode describes the in-plane vibration of sulphur atoms, which vibrate opposite to molybdenum atoms in the material, while the A_{1g} phonon mode describes the out-of-plane vibration of sulphur atoms in opposing directions (Bertrand, 1991), as shown in inset of Fig. B·1(a). The PL of MoS_2 arises from transitions around the K(K') point, from exciton(Coehoorn et al., 1987) (blue and green in inset of Fig. B·1(a)) or trion (Mak et al., 2013) recombination (red in inset of Fig. B·1(b)).

When compared to the substrate, both Raman and PL features show red-shift due to strain from the pillar (B·1(b)). In addition, the trion contribution to the PL is significantly increased on the pillar.

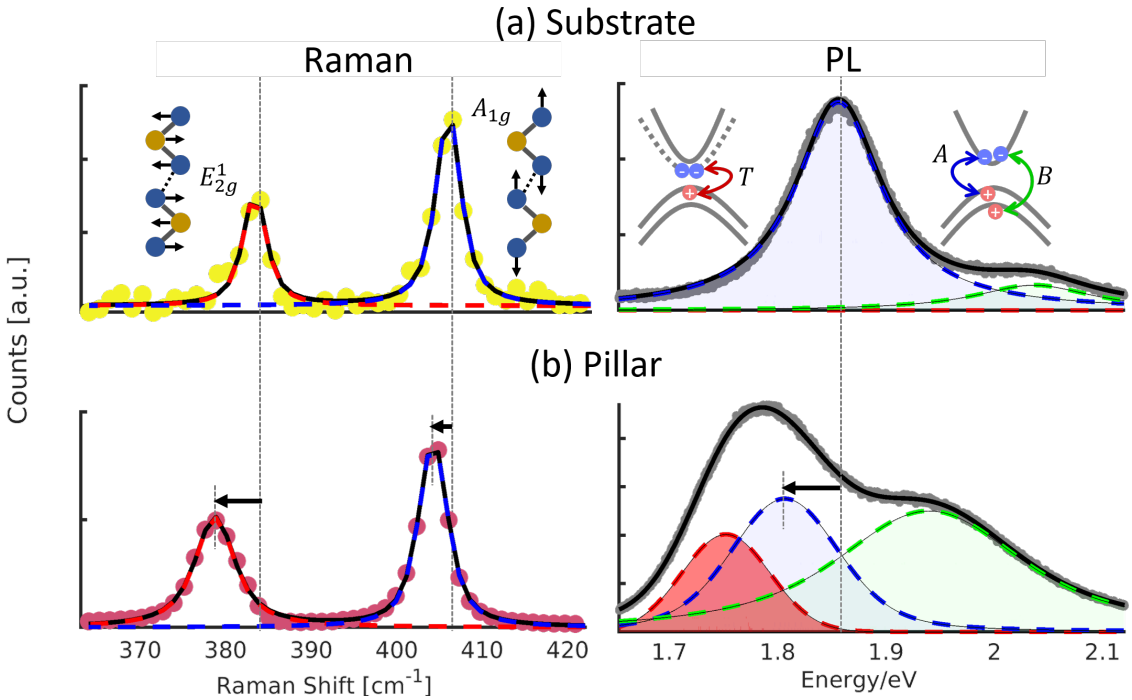

Figure B·1: Raman and PL Spectra of MoS_2. Raman and PL spectra of MoS_2 on the (a) substrate and (b) pillar. The redshift of features is evident in the respective phonon or PL energies. The inset diagrams show the origin of the Raman active modes and exciton and trion features in the PL.

Table B.1: Strain-Charge Correlation Map Parameters

Layer	ω_0		γ		k_n ($\times 10^{13}$ cm^{-2})	
	E^1_{2g}	A_{1g}	E^1_{2g}	A_{1g}	E^1_{2g}	A_{1g}
2	386.7	408.8	0.58	0.17	-0.07	-0.74
3	384.2	407.5	0.41	0.15	-0.035	-0.37
4	384.3	409.2	0.34	0.13	-0.023	-0.24

B.2 Strain-Charge Correlation Map Parameters

B.3 Non-local PL Measurements

532 *nm* light from a solid state laser is focused on the sample using a 100× objective (NA=0.7). The FWHM of the excitation spot is measured to be ∼450 *nm*. The PL is collected by the same objective and passed through a dielectric 550 *nm* long pass filter. The light is then focused onto the spectrometer (Acton SP2300) entrance slit using a 2× tube lens. The slit is left wide open to allow capturing the light coming from the surface of the sample other than the excitation spot. The spectrometer's grating is set at zeroth order to reflect the incoming light without dispersion. Finally, the light is detected by a deep cooled 1340×100 CCD array (PIXIS).

Appendix C

Thermally-isolated MEMS Device

C.1 Derivation of the lumped thermal circuit model for the TIS device

From Fourier's Law, the heat transfer along an element in one dimension is $q = -k\frac{A}{\Delta x}\Delta T$. Using the analogue to electrical circuits, we consider the temperature gradient to be analogous with the voltage difference and heat flow to be analogous with electrical current. Thus, we can set up an Ohm's Law relation for a thermal circuit such that $\Delta T = q \cdot R_{thermal}$. The thermal resistance $R_{thermal}$ can therefore be calculated by $R_{thermal} = \frac{\Delta x}{k \cdot A}$.

We then consider the heat flux in these branches, q_1, q_2, q_3 and q_4, as seen in Fig. C·1. We want $q_1 > q_2$ to shunt the heat flow to the 2D strain device stage whilst simultaneously maintaining the actuator motion by not thermally loading the actuator. Likewise, we want $q_3 < q_4$. Using Thermal Ohm's Law, we can calculate the ratio of heat flux as a ratio of thermal resistances:

$$\frac{q_2}{q_1} = \frac{R_{air,h}}{R_{eq}} \Rightarrow q_2 = q_1 \frac{R_{air,h}}{R_{eq}} \tag{C.1}$$

$$\frac{q_4}{q_3} = \frac{R_{air,w}}{(R_{t,w} + R_{||})} \Rightarrow q_3 = q_4 \frac{(R_{t,w} + R_{||})}{R_{air,w}} \tag{C.2}$$

From Fig. C·1, we can see that $q_2 = q_3 + q_4$. Hence we can also write q_2 as:

$$q_2 = q_4 \frac{(R_{t,w} + R_{||})}{R_{air,w}} + q_4 = q_4 \frac{R_{air,w} + R_{t,w} + R_{||}}{R_{air,w}} \tag{C.3}$$

Also using Thermal Ohm's Law, we can calculate the temperature differential with

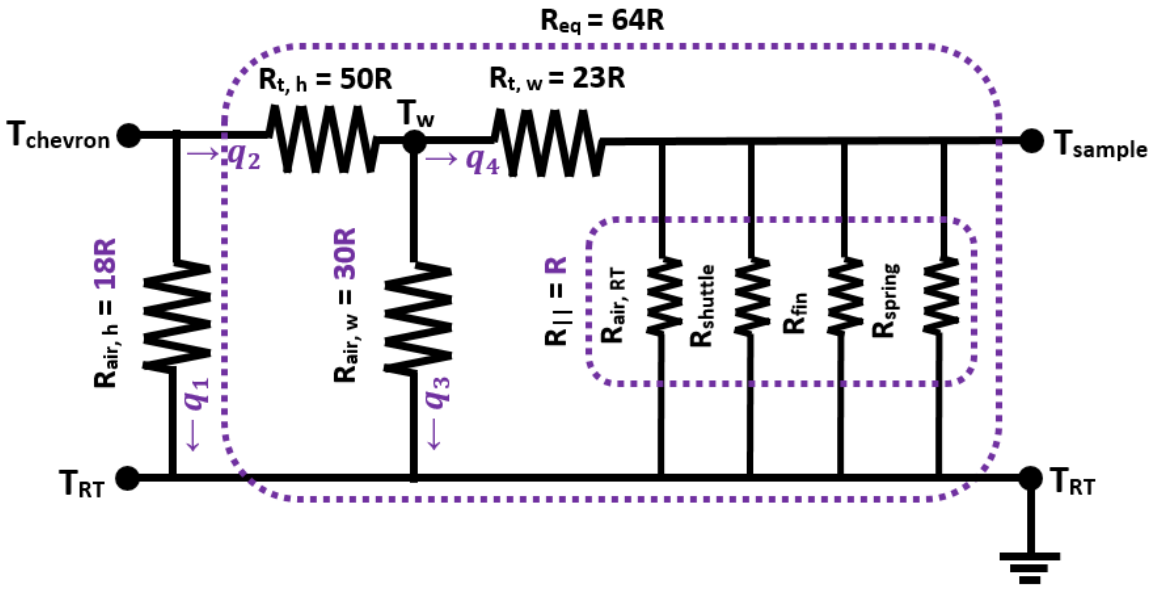

Figure C·1: TIS device as a lumped thermal thermal divider circuit. The tether resistors $R_{t,h}$ and $R_{t,w}$ in red conducts heat through the Si tethers. $R_{air,h}$, $R_{air,w}$ and $R_{air,RT}$ in purple conduct heat from the tether through the air-gap to the substrate (ground), likewise for central shuttle and resistances ($R_{shuttle}$, R_{fin}). R_{spring} conducts heat through the polysilicon and air. The spring conduction through the polysilicon is negligible compared to conduction through air, and hence is neglected in the model. The heat currents are denoted by q_i.

reference to room temperature as:

$$\Delta T_{chevron} = q_1 * R_{air,h} \Rightarrow q_1 = \frac{\Delta T_{chevron}}{R_{air,h}} \tag{C.4}$$

$$\Delta T_{sample} = q_4 * R_{||} \Rightarrow q_4 = \frac{\Delta T_{sample}}{R_{||}} \tag{C.5}$$

Hence, we can rewrite Eqn. (7) using Eqn. (5) and Eq. (8):

$$\frac{\Delta T_{chevron}}{R_{air,h}} \frac{R_{air,h}}{R_{eq}} = \frac{\Delta T_{sample}}{R_{||}} \frac{R_{air,w} + R_{t,w} + R_{||}}{R_{air,w}} \tag{C.6}$$

Finally, simplifying and rearranging Eqn. (10), we can obtain a relationship between temperature at the 2D strain device stage and chevron shuttle:

$$\Delta T_{sample} = \frac{R_{||} R_{air,w}}{R_{eq}(R_{t,w} + R_{||} + R_{air,w})} \Delta T_{chevron} \tag{C.7}$$

C.2 Multiphysics Finite Element Modeling and Analysis

C.3 Measurements

C.4 One-dimensional heat transfer and lumped thermal circuit analysis

Using the resistances calculated in Table C.3 and following the lumped thermal circuit analysis, we derive the relation between T_{sample} and $T_{chevron}$ to be:

$$T_{sample} = 1.5\% \Delta T_{chevron} \tag{C.8}$$

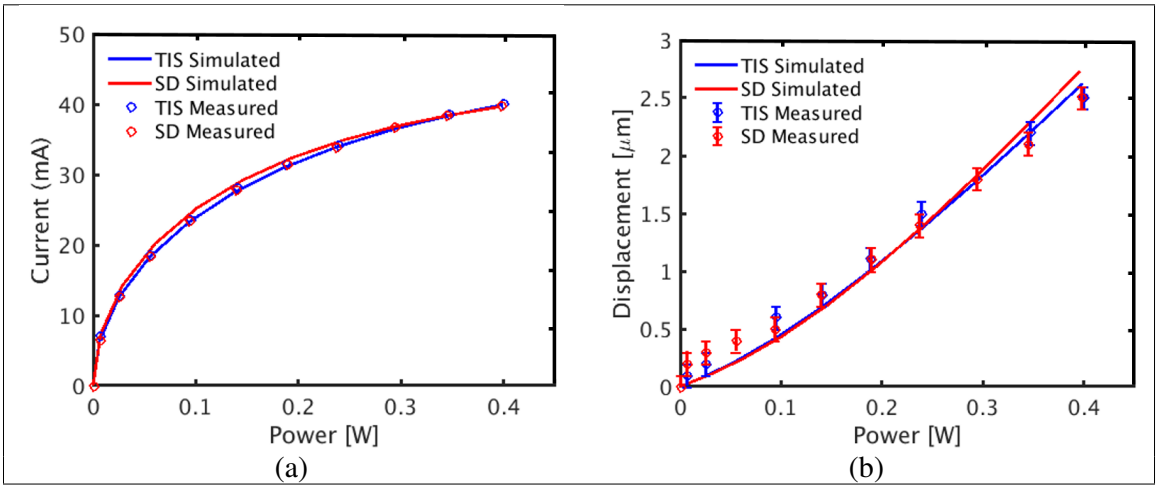

Figure C·2: Comparison of current and output displacment for SD and TIS device. The chevron actuator is powered by applying a voltage in 1 V steps from 0 to 10 V. The displacement and current of the devices are plotted as a function of power. (a) The resulting current of the SD (red dots) and TIS (blue dots) devices is the same. The simulated currents, in the corresponding solid lines, differ slightly from the measured value and can likely be attributed to the differences in resistivity of the fabricated devices. (b) The simulated displacements overlap for the SD (solid red line) and TIS (solid blue line), showing that the chevron beams are not loosing heat in the TIS device compared to the SD device, and hence the actuator motion remains unaffected. The displacement is measured optically using the scalloped verniers on the sides of the 2D strain device stage. The error bars are determined by the size of the camera pixel, 0.2 μm. The measured displacements for both devices (red and blue dots) are also closely matched, within the precision of the optical microscope.

Table C.1: Material Parameters for COMSOL Finite Element Analysis

Material Parameter	**Notation**	**Value**	**Unit**	**Reference**
Room Temperature	T_{RT}	21.4	°C	–
Polysilicon				
Thermal Conductivity	$k_{Si}(T)$	$(21.07\times10^{4})T^{-1.2747}$	$Wm^{-1}K^{-1}$	(Kuang et al., 2002)
Thermal Expansion Coefficient	$\alpha_{Si}(T)$	$(3.725[1-e^{-5.88\times10^{-3}(T-124)}]+(5.548\times10^{-4})T\times10^{-6}$	K^{-1}	(Okada and Tokumaru, 1984)
Resistivity of Poly0, Poly1, Poly2	ρ_0	$1.26\times10^{-5}, 1.97\times10^{-5}, 2.62\times10^{-5}$	$\Omega\cdot m$	PolyMUMPs Run Information
Resistivity Temperature Coefficient	α_0	1.25×10^{-3}	K^{-1}	(Lott et al., 2002)
Electrical Conductivity	$\sigma_{Si}(T)$	$(\rho_0(1+\alpha_0(T-T_{RT})))^{-1}$	$S\cdot m^{-1}$	(Raman et al., 2006)
Density	ρ	2320	$kg\cdot m^{-3}$	COMSOL Multiphysics
Young's Modulus	E	169	*GPa*	" "
Poisson's Ratio	η	0.22	1	" "
Air				
Thermal Conductivity	$k_{air}(T)$	$(3.4288\times10^{-11})T^3-(9.1803\times10^{-8})T^2+(1.2940\times10^{-4})T-5.2076\times10^{-3}$	Wm^{-1}°C^{-1}	(Holman, 1997)

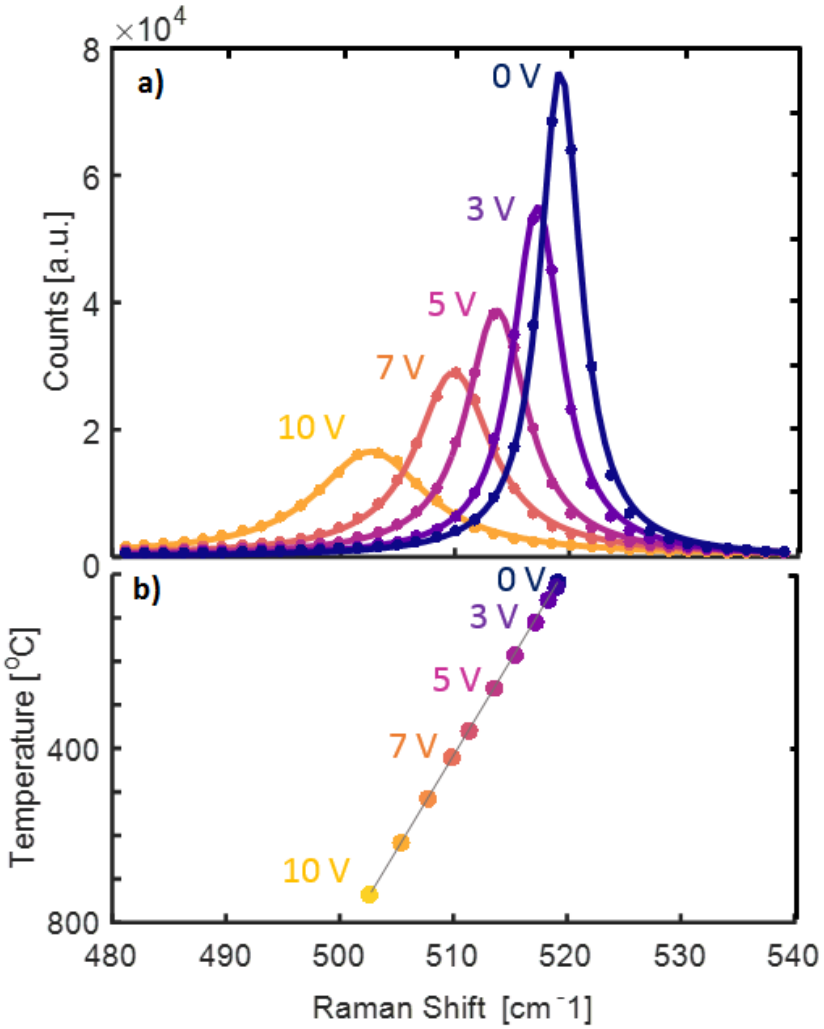

Figure C·3: Actuation voltage-dependent Raman shift measured at the center of a chevron beam. (a) Temperature dependent Si Raman peak. A clear down shift with increasing heating is shown. (b) Relation between Raman Si Stokes peak position to temperature (Abel et al., 2007a).

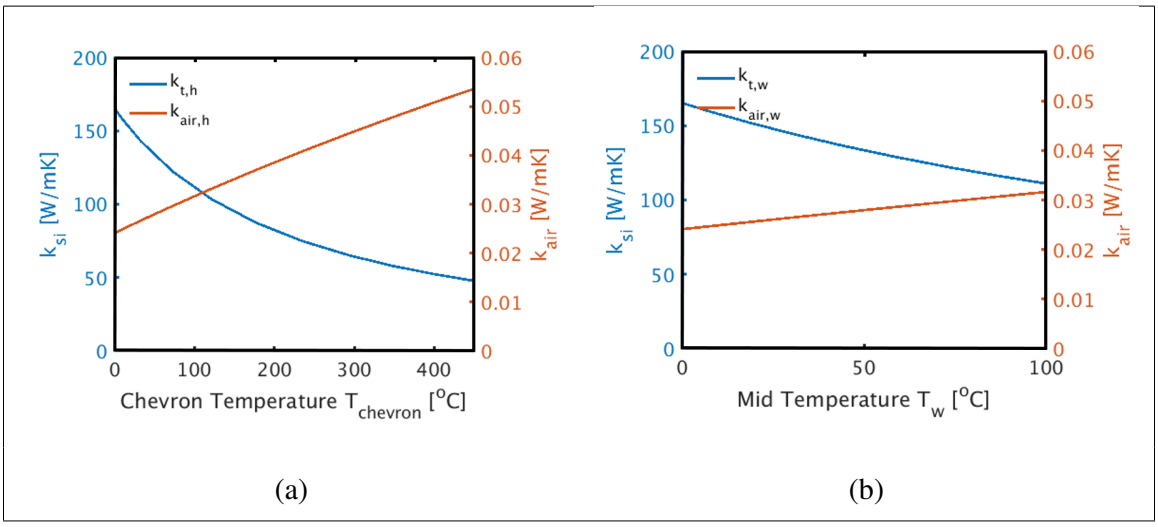

Figure C·4: Thermal conductivity of polysilicon k_{si} and air k_{air} varies as a function of input power as shown. (a) $k_{t,h}$ and $k_{air,h}$ are determined by the temperature of the chevron shuttle, $T_{chevron}$. (b) $k_{t,w}$ and $k_{air,w}$ are determined by the temperature $T_{mid} = \frac{1}{4}T_{chevron} + T_{RT}$. The graphs illustrate how at high T, the heat conduction through the tether is diminished by a factor of 3 while the shunting of heat via air to the substrate becomes twice as effective.

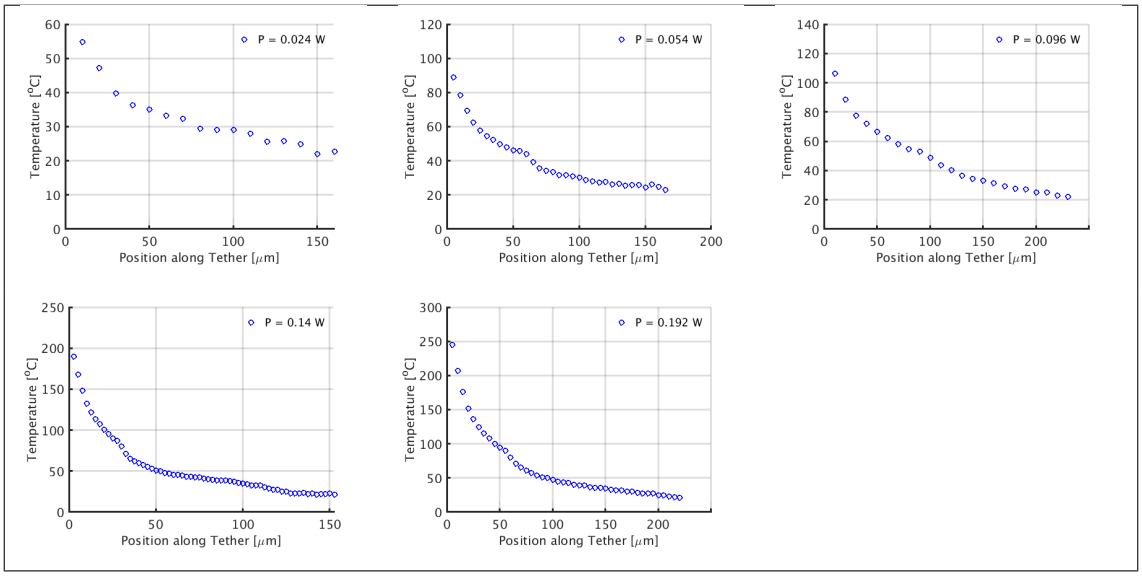

Figure C·5: The temperature is measured along the tether from the chevron shuttle till room temperature using IR thermometry. Input power is limited to 0.192 W (6 V). At lower temperatures, the IR camera cannot pick up contrast between the tether and substrate hence the temperature across the full length of the tether cannot be measured.

Table C.2: Summary of Calculated Thermal Resistances for P = 0.41 W

Resistance	**Temperature**	**Value [K/W]**$\cdot 10^3$	**Approximation**
$R_{t,h}$	$\Delta T_{chevron}$ = 448 °C	347	50R
$R_{t,w}$	$T_w = \frac{1}{4}\Delta T_{chevron}$ = 112 °C	167	24R
$R_{air,h}$	$\Delta T_{chevron}$ = 448 °C	123	18R
$R_{air,w}$	$T_w = \frac{1}{4}\Delta T_{chevron}$ = 112 °C	194	28R
$R_{air,RT}$	T_{RT} = 21 °C	256	37R
R_{fin}	"	25	4R
R_{spring}	"	19	3R
$R_{shuttle}$	"	23	4R
$R_{\|\|}$	-	$R_{air,RT}\|\|R_{fin}\|\|R_{spring}\|\|R_{shuttle} = 7$	R
R_{eq}	-	$R_{t1} + [R_{air,w}\|\|(R_{t2} + R_{\|\|})] = 787$	64R

Table C.3: Summary of Calculated Thermal Resistances for P = 0.14 W

Resistance	**Temperature**	**Value [K/W]**$\cdot 10^3$	**Approximation**
$R_{t,h}$	$\Delta T_{chevron}$ = 241 °C	190	$28R$
$R_{t,w}$	$T_w = \frac{1}{4}\Delta T_{chevron}$ = 44 °C	122	$18R$
$R_{air,h}$	$\Delta T_{chevron}$ = 241 °C	178	$26R$
$R_{air,w}$	$T_w = \frac{1}{4}\Delta T_{chevron}$ = 44 °C	239	$35R$
$R_{air,RT}$	T_{RT} = 21 °C	256	$37R$
R_{fin}	"	25	$4R$
R_{spring}	"	19	$3R$
$R_{shuttle}$	"	23	$4R$
$R_{\|\|}$	-	$R_{air,RT}\|\|R_{fin}\|\|R_{spring}\|\|R_{shuttle} = 7$	R
R_{eq}	-	$R_{t1} + [R_{air,w}\|\|(R_{t2} + R_{\|\|})] = 465$	$41R$

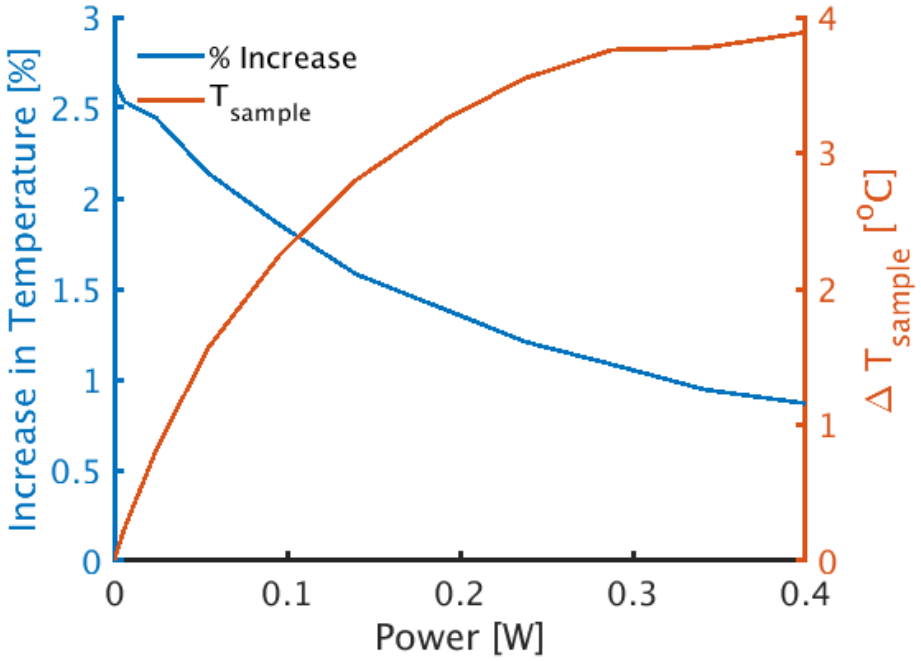

Figure C·6: LCM results. Percentage increase in temperature (%) can be defined as the ratio of increase in temperature at the 2D strain device stage, ΔT_{sample}, and chevron shuttle temperature $\Delta T_{chevron}$. At a maximum input power to the device, 0.4 W (10 V), the LCM predicts that the TIS effectiveness is 0.8 %. This corresponds to a T_{sample} of 25.3 °C, or an increase in temperature ΔT_{sample} = 3.9 °C.

Appendix D

Integration

D.1 PDMS Base Preparation

We use Dow Corning *Sylgard*©184 Silicon Elastomer for our PDMS base. This product was chosen from Dow Corning's line of silicone encapsulants as it is transparent, flexible, has a long pot life, and experiences very little shrinkage through heating. Hence it is a reliable polymer for repeated use in transferring 2D materials. The two part elastomer is mixed 10:1/Base:Curing Agent. The thoroughly mixed silicone blend is poured into a Petri dish at a thickness of 1 mm. The mixture is cured at 150 °C for 10 minutes. More information on the PDMS used can be found in the company's product reference manual.

Using an Xacto knife, a square PDMS block with roughly a 1 mm side length is cut from the master mold and placed on a clean glass slide. Clear tape on top secures the PDMS in place while also mounding the block on top to a domed shape, as seen in Figure D·1. The PDMS block should now have a specific area where point of first contact with a flat substrate would occur.

To find this point of first contact, the PDMS block+glass slide is flipped and slowly brought in contact with a silicon chip. Newton rings start to form as the domed PDMS block makes contact with the underlying substrate, as seen in Figure D·1. The DLW microstructure will be placed in the proximity of the center of these Newton rings, as seen in the next section. Note that this process of identification must be performed slowly and must be stopped as soon as the Newton rings start to form. Going past this point may cause irreversible deformation to the PDMS block and loss of a single point of first contact.

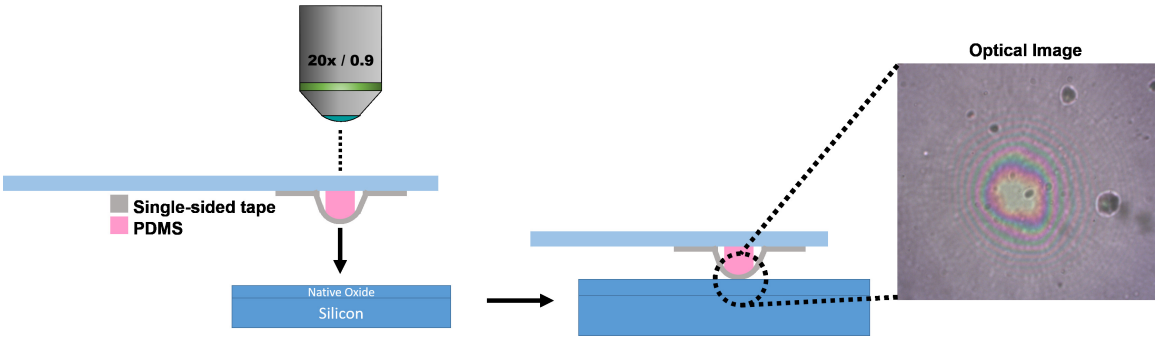

Figure D·1: Identifying highest point of the PDMS Base. The schematic for identifying highest point in PDMS domed by single-sided tape is shown. The domed PDMS is slowly brought in contact with a highly reflective, flat substrate like native oxide. Newton rings start to form around the point of first contact, as seen in the optical image. The center of the Newton rings is always the first point of contact for this setup.

D.2 Direct Laser Written Microstructure

Our transfer procedure starts with designing a specialized microstructure using Solidworks to distribute the stamping force onto the sturdy substrate while limiting the force on the released actuator. Microstructures were fabricated at Boston University using the commercial Nanoscribe Photonic Professional GT System (780 nm, Nanoscribe GmbH) with IP-S photoresist and the 25x NA 1.4 objective. The Nanoscribe system uses a process known as direct laser writing via two-photon polymerization (DLW-TPP), where a femtosecond laser is focused into a volume of liquid photoresist to induce a localized polymerization reaction; this reaction results in solidification of the liquid resist only near the laser focal spot. By moving this focal spot around within the liquid resist, complex 3D parts with sub-micron resolution can be produced. After printing, excess IP-S photoresist was removed by soaking in propylene glycol methyl ether acetate (PGMEA, Sigma Aldrich) for 20 minutes, followed by a brief rinse in NOVEC 7100 (3M) to remove excess PGMEA from the microstructure.

With commercially available direct laser writing (DLW) systems, polymer scaffolds and structures can be designed and custom printed much like in 3D printing. For example, DLW scaffolds have been used as living cell scaffolds in biology (Klein et al., 2010; Scheiwe et al., 2015) and investigating tunable metamaterials (Reeves et al., 2018; Reeves et al., 2019). Computer-aided software like Solidworks can be used to program designs which can then be fabricated using the commercial 2D printing systems. The Nanoscribe Photonic Professional GT system used in our work can achieve sub-micron resolution and print several microstructures in parallel (Jayne et al., 2018).

A CAD schematic of the microstructure is shown in Figure D·2. The design includes two parallel legs 150 μm tall (Figure D·2(c)) and spaced 140 μm apart (Figure D·2(b)), a distance slightly larger than the width of the actuator's 2D Strain Device Stage. During transfer onto the 2D strain device stage, the legs of the microstructure make contact with

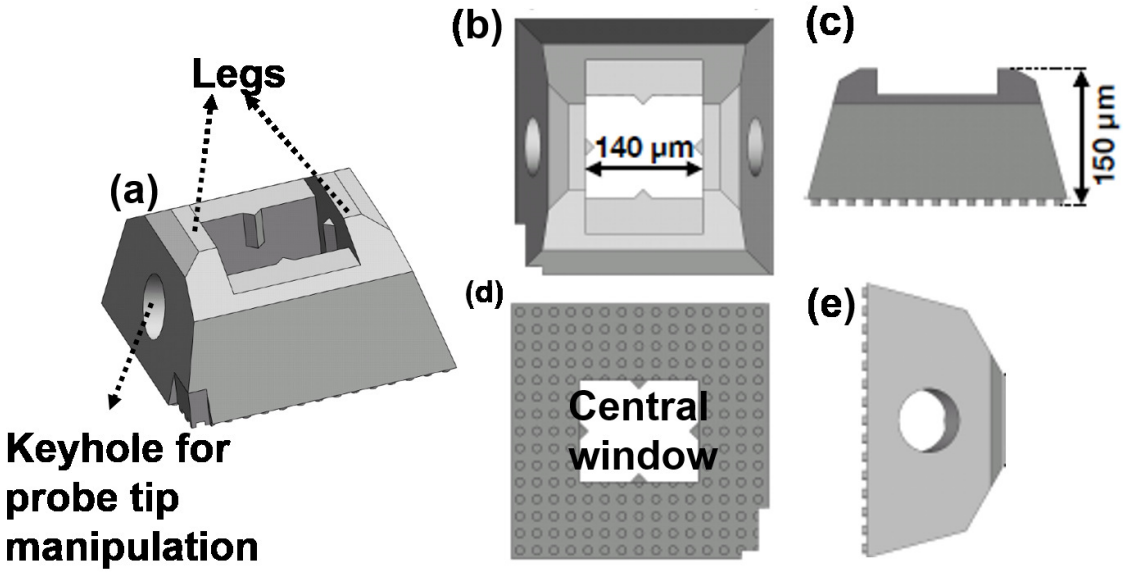

Figure D·2: CAD diagram of the 3D polymer microstructure, different views and dimensions. (a) A keyhole in its side is designed for inserting a probe tip to move the microstructure. The legs are the only points of the microstructure that make contact with the substrate. (b&c) The legs are separated by 140 μm, giving ample room for transferring on the 2D strain device stage. The microstructure's height, 150 μm, is high enough to ensure that it is the only part of the transfer system to make contact with the target substrate. (d) The central window allows for a wide view of the target substrate during transfer, which allows precision alignment of the 2D material. (e) The contact area of the legs are 10 μm x 100 μm- a significantly reduced area of contact compared to other transfer methods.

the silicon nitride substrate, leaving the released MEMS device unaffected by the transfer.

The microstructure can be picked up and moved using a probe inserted into the keyhole at its side, as indicated in Figure D·2(a). At its base, The microstructure is 900 μm^2. As seen in the bottom up view (Figure D·2(d)), the microstructure has a large central window of about 140 μm x 100 μm, which allows for precise placement of 2D materials using a microscope objective. The base of contains arrays of cylindrical pedestals 5 μm tall (Figure D·2(e)). These pedestals allow for wicking of UV curable glue introduced to the base, attaching the microstructure to the conventionally used domed PDMS transfer system. The microstructures are completely re-usable for successive transfers as they undergo no damage during transfer.

D.3 Assembling the Microstructure onto the PDMS Base

The microstructure is fabricated on silicon chips. It can be easily picked up and manipulated using a probe tip. Figure D·3 shows a microstructure lifted off of it's silicon substrate using a probe tip. Controlled using a micromanipulator, the probe tip allows us to place the microstructure on the domed PDMS base precisely at the location of it's highest point, previously determined.

After placing the microstructure on the PDMS base, a micropipette introduces UV curable glue at its base. We use World Precision Instruments©MicroTip Pre-Pulled pipettes with a 10 μm tip attached to a home-built micro-manipulator with pressurized ejection system.

The pedestals at the base of the microstructure ensure that the glue is wicked evenly only around the periphery of the microstructure, leaving the center window clear. We use Norland Optical Adhesive 81, a suitable adhesive for precise bonding of polymers. The adhesive is cured using a long wavelength UV light (320-400 nm) source for 1 minute 40 seconds. Notably, the cured adhesive does not degrade by typical solvents like acetone or

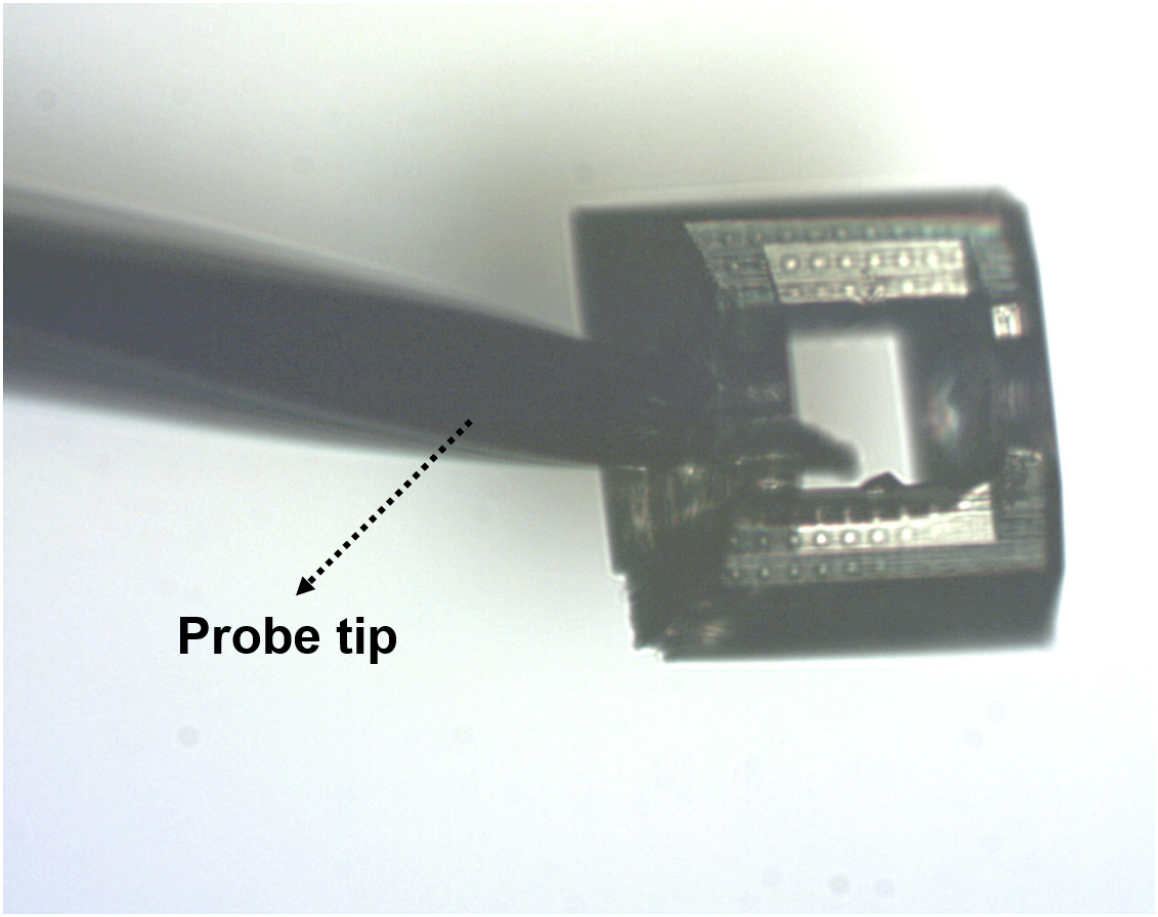

Figure D·3: Probe Tip Manipulation of Microstructure. This optical image shows how a probe tip inserted into the side hole of the microstructure can be used to lift and move it.

isopropyl alcohol. This allows us to reliably clean and reuse the microstructure assembly. Figure D·4 shows the micropipette setup in our transfer station micro-manipulator, and the optical image shows a microstructure glued on to the PDMS base.

D.4 PPC Spin-Coat

We use Poly(propylene carbonate) (PPC) from Millipore Sigma (CAS Number 25511-85-7). Originally in the form of pellets, 2g of PPC is dissolved in 20 ml of Anisole to prepare the polymer for spin-coating. We spin-coat PPC using the spin parameters found in Table D.1. Using these process parameters, we obtain consistent PPC films of 1 μm thickness.

Step	Process	Value
1	Ramp	500 rpm/s
	Speed	3000 rpm
	Time	60 s
2	Ramp	-500 rpm/s
	Speed	0 rpm/s
	Time	5 s

Table D.1: PPC Spin-Coat Process Parameters.

D.5 Float Release to obtain PPC+2D Material membrane

Figure D·5 shows the procedure to lift 2D materials off a growth substrate using a polymer membrane. The desired flake to transfer is first isolated on the substrate by making strain relief cuts in to the PPC (Figure D·5(a)). In order to lift the flake for transfer, we use a single sided tape with a small square hole (4 mm^2) positioned around the flake of interest, as shown in Figure D·5 (b). The setup is then attached to a 3D printed transfer frame. The frame allows us to suspend this assembly (SiO_2, MoS_2, polymer) in DI water in order to delaminate the 2D material from the SiO_2/Si substrate. As a result, we achieve a free-standing film of MoS_2 and PPC polymer, easily identifiable using the strain relief cuts. Optical images of this process can be found in the Figure D·8 and Figure D·7.

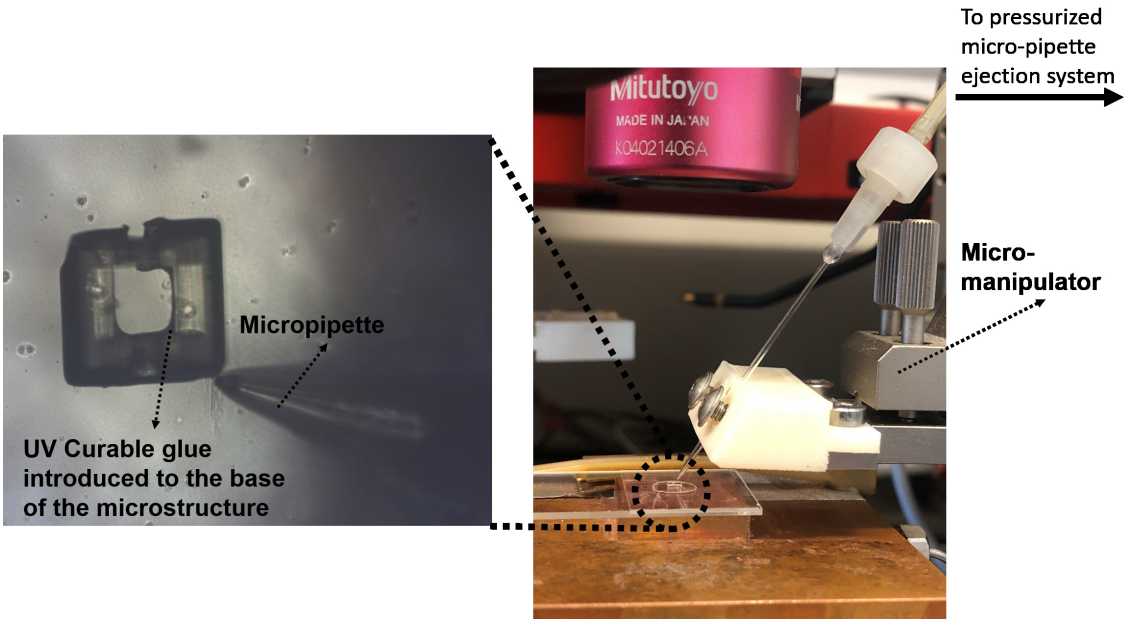

Figure D·4: Micropipette UV Curable Glue to the Base of the Microstructure. This optical image shows the micropippette which introduces UV curable glue to the base of the microstructure. The glue wicks evenly underneath the microstructure, leaving the central window clear. After curing the glue under UV light, the microstructure is bonded to the PDMS base.

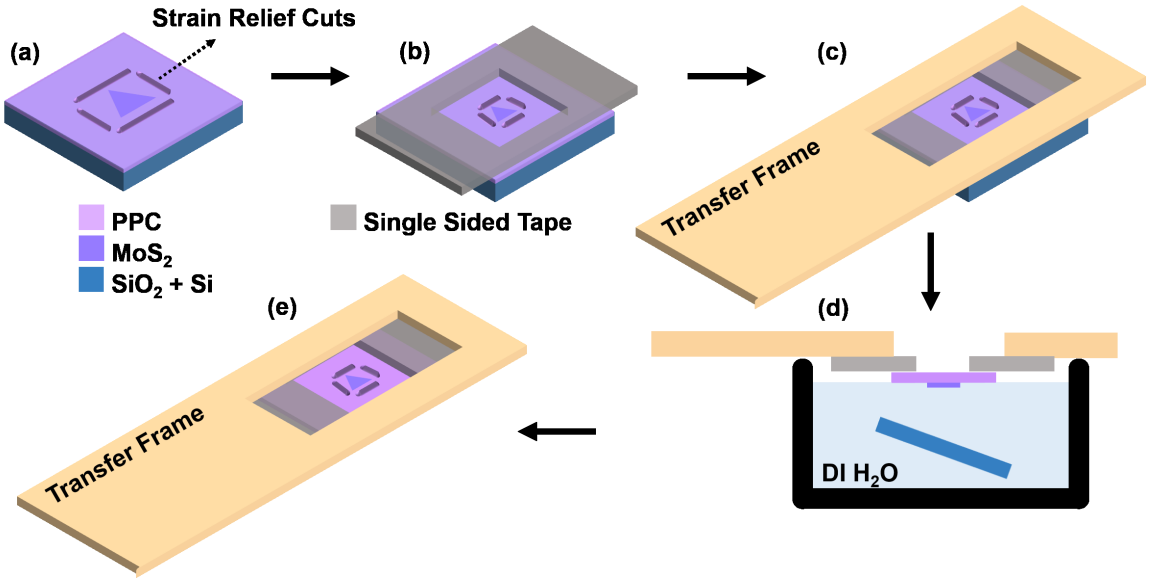

Figure D·5: 2D Material Prepared for Transfer on to the Microstructure. (a) Strain relief cuts are made in the PPC around a suitable flake, spaced 140 μm apart, i.e., the separation of the microstructure legs. (b) Single sided tape with a window cut out framing the flake and strain relief cuts, is place with the adhesive side facing the chip. (c) A 3D printed transfer frame is attached to the top of the chip with double-sided tape. (d) The transfer frame is balanced on a petri dish containing DI water, with the SiO_2 chip just under the water meniscus. After around 30 minutes, the MoS_2 and PPC delaminates from the chip. (e) The result is a transfer frame with a membrane of PPC and MoS_2.

D.6 2D Material Precision Transfer Station

Our Precision Transfer Station is setup to facilitate transfer of 2D materials from their growth substrate to any target substrate. It includes a RTD stage temperature controller and Thermal Stage to allow heating and cooling of the stage as needed. The micro-manipulators provide xyz translation with submicron accuracy and can be fitted with custom-built additions to be used with probe-tips, glass slides, transfer frames, and micro-pipettes. The long-working distance microscope and camera allows in-situ monitoring during the transfer process.

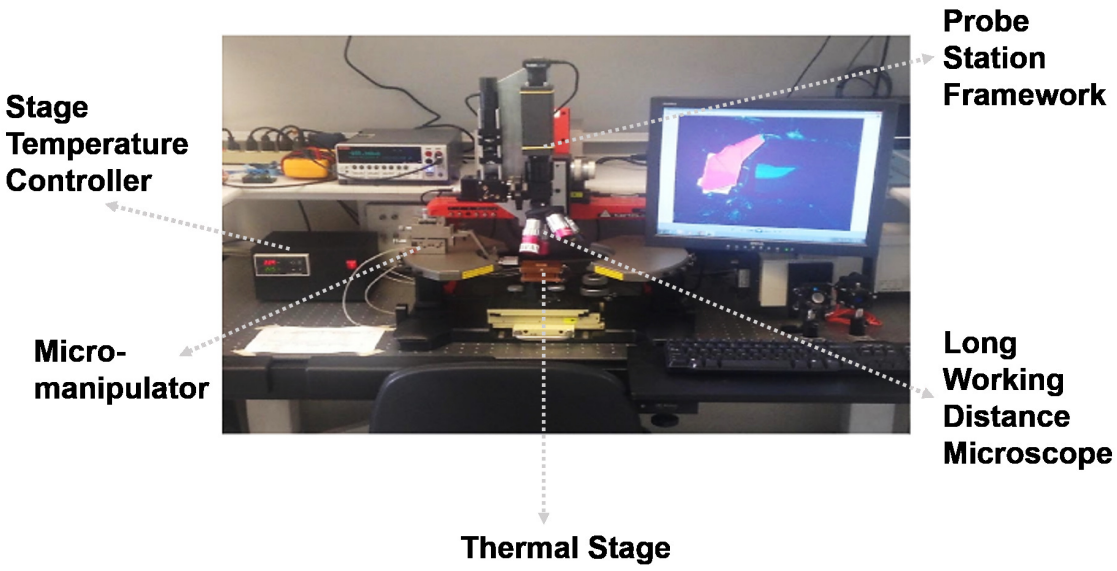

Figure D·6: 2D Material Precision Transfer Station.

D.7 Optical Images of Transfer Process

Here we show optical images during the transfer process of monolayer MoS_2 and FLG on to the MEMS. Figure D·7 and D·8 shows optical images of the transfer process. The procedure is the same for both materials. Figure D·7(a) Monolayer MoS_2 is grown by PVD on SiO_2 and a flake of suitable size is identified. (b) PPC is spun on top of the chip, and a probe tip is used to make strain relief cuts, framing the flake. The cuts are about the width of the legs of the microstructure (100 μm). Using the float release method described earlier, the membrane of PPC+MoS_2 is lifted off the SiO_2 and is attached to a transfer frame. (c) shows the membrane transferred on top of the microstructure, situated such that the strain relief cuts are aligned with the edge of the window and the MoS_2 is at its center. (d,e) The membrane on the microstructure is aligned over the 2D strain device stage. The window through the center of the microstructure allows for precision placement of the 2D film. From the interference pattern that forms, we know that the membrane has made contact with the substrate. Now the stage is heated from 60 °C to 90 °C, in small steps so as to make minor adjustments as the copper stage expands. The interference pattern continues to evolve durin the heating process. (f) A 90 °C the PPC has gone through its glass transition temperature and flows off the microstructure. The PPC and FLG remain on the MEMS device as the microstructure is lifted away. (g) The PPC is then removed using acetone followed up critical point drying in liquid CO_2. The monolayer MoS_2, here outlined in purple to aid the eye, is left behind undisturbed.

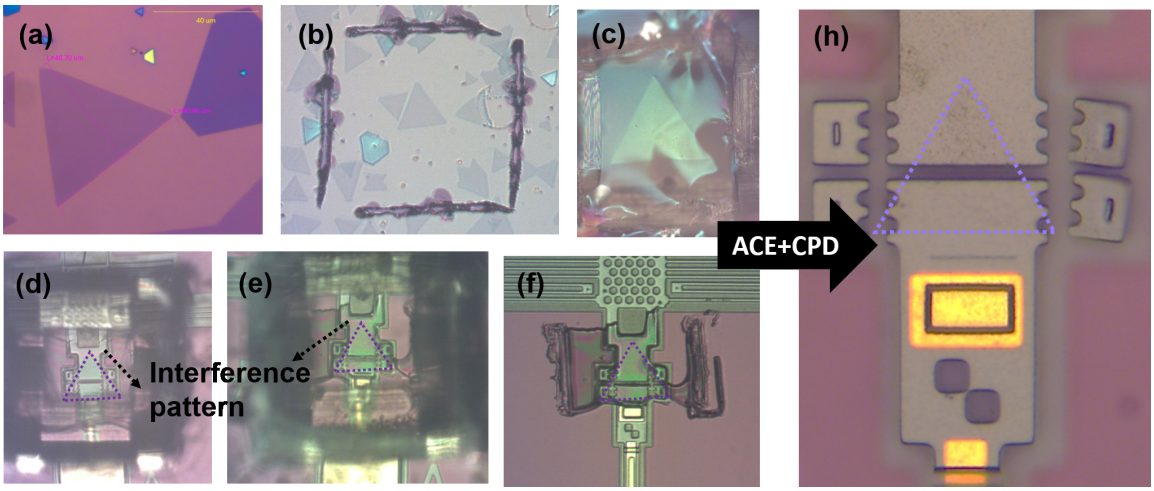

Figure D·7: Optical Images of Monolayer MoS_2 Transfer Process

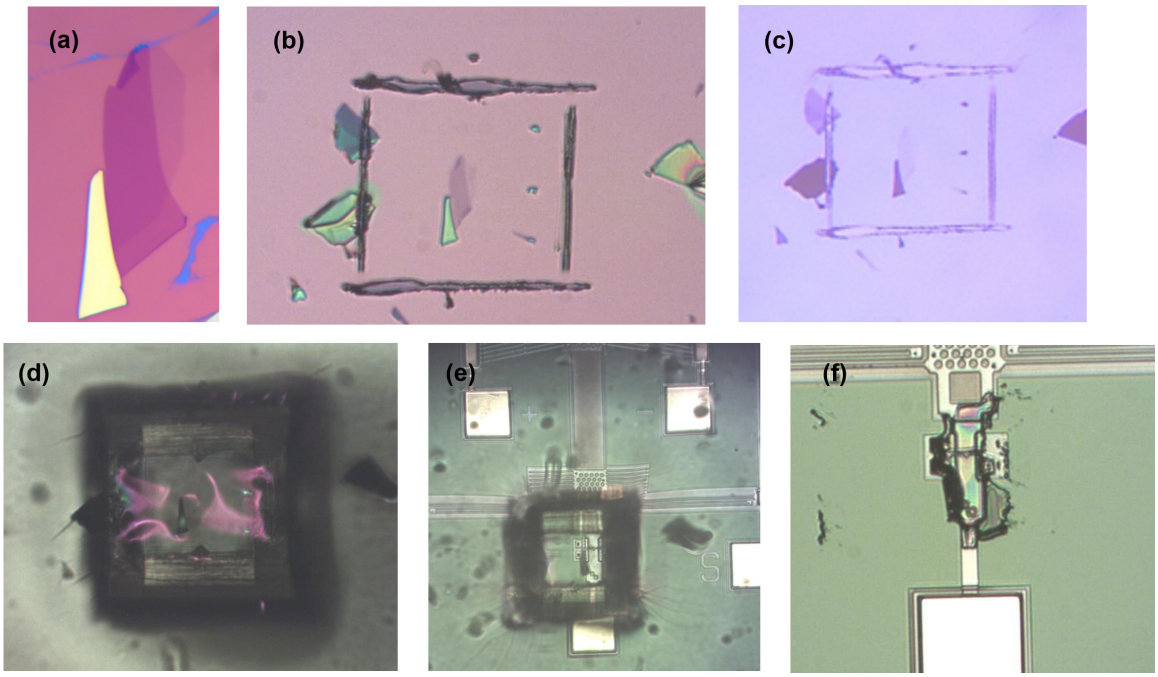

Figure D·8: Optical Images of Few Layer Graphene Transfer Process

D.7.1 PL and Raman Intensity Maps

The intensity maps of the PL and Raman demonstrate high intensity and uniformity through suspended. Closer to the edges of the gap, the intensity starts to weaken due to changing interference conditions. Finally, the intensity drops off at the supported ends, due to substrate interference effects. The PL is lower in the area close to center where a small few-layer region can be found. This is because few-layer MoS_2 is an indirect bandgap system, showing less photoluminescence (Splendiani et al., 2010).

D.7.2 Device Trials, Transfer Procedure Yield, and Common Pitfalls

The transfer procedure can be broadly reclassified into three process steps. Step 1 is transfer of the 2D material from growth substrate to the microstructure via a polymer membrane. Step 2 is the transfer of the 2D material onto to the MEMS using the microstructure. Step 3 is the acetone removal of the polymer and critical point drying of the MEMS device to achieve a clean, suspended 2D material on the 2D strain device stage. The overview of the device trials can be visualized in Figure D·10. In total, the transfer procedure was tested 47 times to transfer and suspend 2D material onto movable MEMS actuators. Of those trials, 43 made it through Step 1, giving a process step yield of 91.5%. Step 2 was cleared by 35 devices, which is a yield of 74.5%. Step 3 was cleared by 18 devices out of 47, which is a process step yield of 38.3%. The process steps utilizing the microstructure have an extremely high success rate. The final process step is crucial to the overall success of the device, and can be improved with mechanically stronger material growth or more careful critical point drying. Below, we summarize the common pitfalls at each process step that could reduce the yield. Apart from these technical details, user experience will also affect the yield of successful transfers.

Step 1 - Transfer to Microstructure. Common Pitfalls:

- Strain relief cuts in the PPC could elongate or connect during float release or during

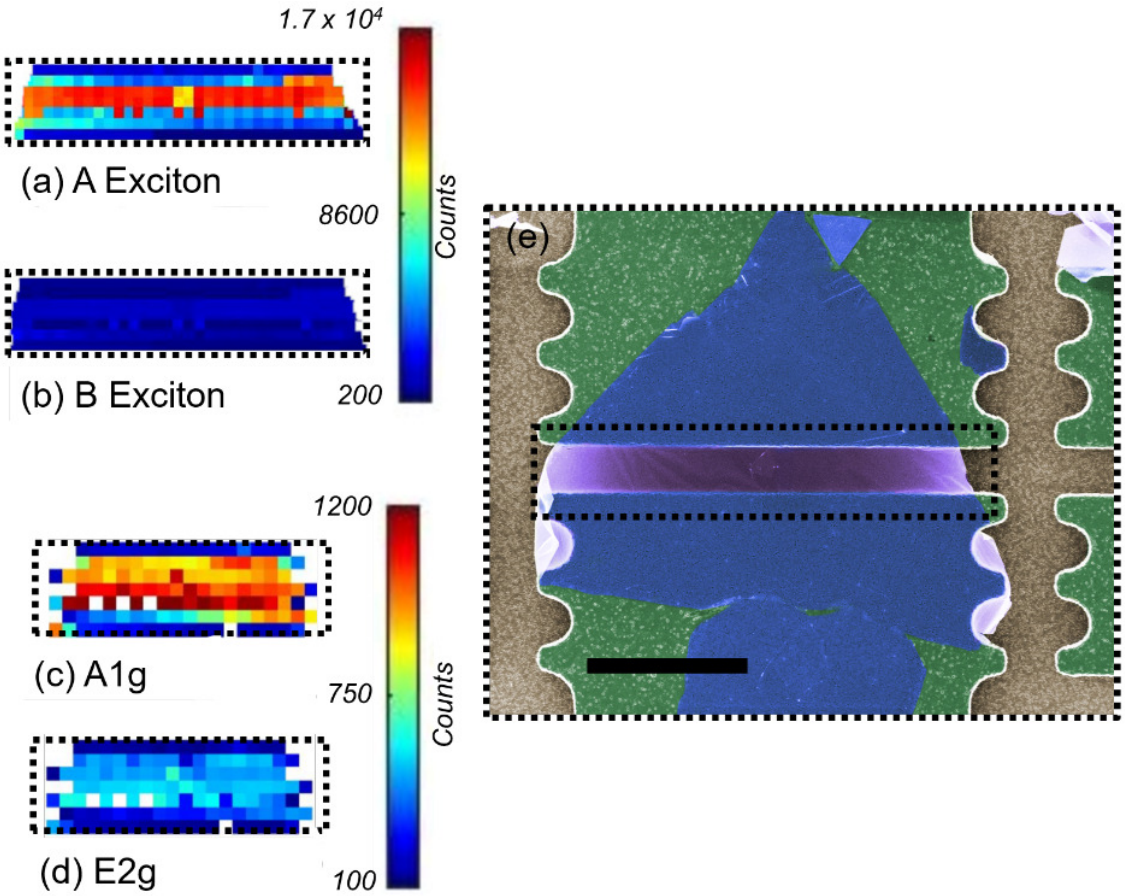

Figure D·9: PL and Raman Intensity Mapping on MoS_2 (a) and (b) are the intensities of the A and B excitons, obtained by fitting the mapped region. The intensity maps show that the suspended area has high PL intensity, with a small few layer growth in the center where the PL is weaker. (c) and (d) are the intensities of the E^1_{2g} and A_{1g} phonon modes, obtained by using a Voigt on the mapped region. The intensity maps show similar behavior to that of the PL in the corresponding region. Scale bar is 10 μm.

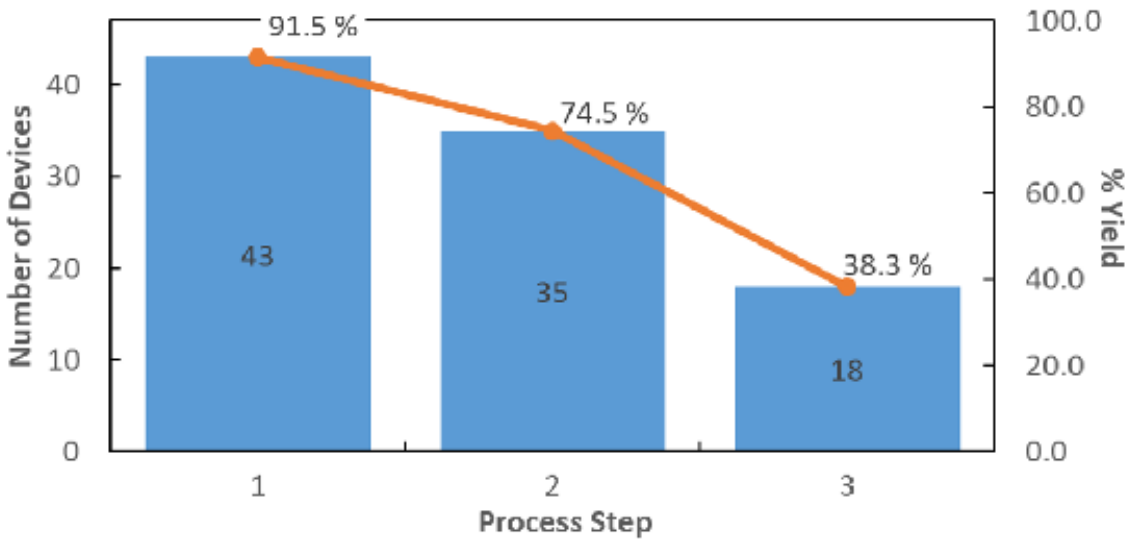

Figure D·10: Overview of Device Trials

transfer onto the microstructure. This could cause the membrane to wrinkle and fold, or tear away completely.

- 2D material contrast against the PPC could be very low, especially for monolayer graphene. Aligning the material in the center of the microstructure window can be difficult.

Possible Solutions:

- Care and practice is needed when making strain relief cuts, so they are sufficiently far apart from each other. During transfer, the ostructure on the thermal stage can be heated slightly (30-40 °C) to “heal" the elongated cuts.

- The thickness of the PPC film can be increased slightly by varying the spin parameters, which may provide improved contrast for very thin materials.

Step 2 - Transfer to MEMS. Common Pitfalls:

- The material starts to move or slip off the target substrate when being transferred with the microstructure.

- The microstructure might not be the highest point of contact. This will happen with repeated and harsh deformation of the underlying mounded PDMS block.

Possible Solutions:

- This could happen due to insufficient contact or because of the expansion of the thermal stage moving the underlying substrate. Smaller step sizes in increasing temperature combined with small adjustments of the stage positioning could help with this. Unfortunately, insufficient contact is difficult to correct.

- During normal procedure, this error may start to arise when the microstructure has been repeatedly used for over 100 transfer. It is an indication that a new microstructure transfer system needs to be prepared.

Step 3 - Polymer Removal and Critical Point Drying. Common Pitfalls:

- The suspended material is broken up after CPD.
- There is no material evident on the MEMS device after CPD.

Possible Solutions:

- This is an indication that more mechanically strong material is needed. For CVD or PVD growths, changing precursor ratios or growth parameters could help increase the mechanically strength of the material.
- This indicates that the adhesion strength between the material and the MEMS polysilicon substrate was insufficient during the drying process. The MEMS substrate could be treated chemically or plasma ashed to increase the adhesion of the 2D material. A turbulent CPD cycle could also cause the material to wash away. The flow of acetone or liquid CO_2 will need to be adjusted during the CPD process.

D.7.3 Comparison to As-Grown MoS_2 on SiO_2

MoS_2 for this work was grown by PVD on SiO_2. Figure D·11 shows spatially resolved PL mapping and exciton energy histogram of an MoS_2 flake grown on SiO_2 (optical image is in the inset). The intensity (Figure D·11(a,c)) maps shows some variation due areas of contamination on the the material from the growth process. The exciton energy positions (Figure D·11(b,d)) are uniform throughout the sample. From the histogram of the A and B exciton energy positions (Figure D·11(e)), we see that the A exciton centered at 1.84 ± 0.009 eV, which is similar to that of MoS_2 on MEMS transferred by our process. The B exicton is, centered around 2.00 ± 0.005 eV, slightly higher than suspended MoS_2.

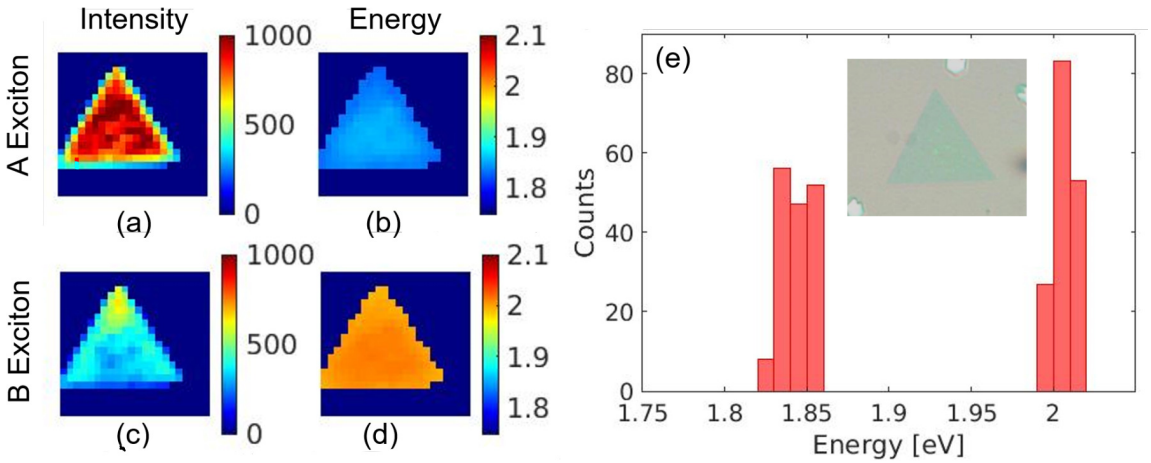

Figure D·11: PL Spectra and Histogram of As-grown MoS_2. Lorentzian fitting was used to obtain information from the PL spectra of as-grown MoS_2 on SiO_2. (a) and (c) are the intensities of the A and B excitons, obtained by fitting the mapped region. (b) and (d) are the positions of the A and B exictons. (e) is the histogram of the exciton energy positions. The inset shows the optical image of the 2D material as-grown on MoS_2.

Appendix E

MEMS Strained 2D Materials

E.1 Graphene RIE

For best results, etching graphene with Argon (not Oxygen) produces cleaner and more defined shapes without damaging the material. This is because as Argon is heavier than Oxygen and within the magnetic field of the RIE, the etching is more directional and there is less under-etching of the exposed suspended graphene. Check the log book for the instrument before starting. I have found that if previous users have used the machine for a long run, the next user faces some unpredictability in their run. Hence, the recipe times for seasoning the chamber need to be adjusted accordingly, in order to "stabilize" the instrument for your run. In addition, more attention should be paid to cleaning the chamber if the previous run was a long one.

1. RIE chamber should be vented and vigorously cleaned using IPA prior to use.

2. To burn off any residue from prior runs, the chamber needs to be cleaned using 15 sccm oxygen plasma for at least 15 minutes, at a power of 250 W, at 200 mTorr pressure.

3. Glass sides will be used to align and keep the MEMS in place during the etching process. Clean 4 glass slides with IPA and place in the center of the chamber. To season the chamber for Argon, you will need run the recipe that you use for etching for a longer time to get the flow rate and power to be optimal right away. This is crucial as we are etching for a very short amount of time, so need to capitalize on

every second and reduce the "booting" time in the beginning of the run. Run the instrument with Argon gas of 10 sccm, at a power of 30 W, with a pressure of 50 mTorr for at least 5 minutes.

4. Finally, add the sample to the center of the chamber and align with the glass sides. Centering the MEMS is essential, as the RIE chamber seems to have an unequal etch rate across the chamber. The etch recipe for the MEMS with graphene will be the same as the previous recipe, except the etch time will be 20 seconds. The instrument takes approximately 5 seconds to boot up to full power and pressure, as well as auto-correct for overshooting. The actual most effective etching will be done after approximately 7 seconds. Considering the current state of the RIE, this was the optimal etch time to get rid of the graphene in the selective area.

The final comment I can make here is that the RIE is an inherently unpredictable machine. The same recipe ends up yielding different results depending on the day or the hour, and can potentially destroy 3 days worth of work. Don't get discouraged! I hope tips here can help alleviate at least some of the unpredictable behavior.

E.2 Metal Deposition

The process for prepping the CHA to deposit metal follows what was detail in Appendix A.1.3. The recipe is changed to the following:

- Deposit an adhesive layer of 20 nm Chromium at 2 $\dot{A}/s$.
    1. Power 12%, Ramp: 60 s, Soak: 120 s.
    2. Power 15%, Ramp: 60 s, Soak: 240 s.
- Deposit 100 nm of Gold at 1 $\dot{A}/s$.
    1. Power 12%, Ramp: 60 s, Soak: 120 s.

2. Power 16%, Ramp: 90 s, Soak: 150 s.

The Chromium degrades if it remains uncapped, so refrain for using only a Chromium layer for riveting. In addition, another unknown factor seems to affect the metal layer, as in at least one device the metal "popped" off the substrate after a day in ambient conditions.

E.3 Raman Setup

514 nm light from Ar+ laser is focused on the sample using a long working distance 100x Mitutoyo lens, with 0.7 NA. The spectrometer used a 1800 l/mm grating. The FWHM of the laser is 500 nm.

E.4 Monolayer Device Degradation

The device G11 CFNP2 degraded unexpectedly under ambient conditions. This happened over the course of Day 1 of experiments, although changes were slight enough that I only really realized the issue in retrospect. The main culprit seemed to be the cracking metal rivets under ambient condition, as seen in Fig. E·1, the issue effects not only graphene across the gap but also the suspended shuttle of the device.

E.5 Procedure for Obtaining PMMA Films

PMMA films are obtained using PVP dissolved as a sacrificial polymer on SiO2/Si chips. I use the 950 A6 for the free-standing PMMA films. Make sure to check the expiration date on the PMMA as it can effect the quality of the films substantially.

1. PVP is spun on the SiO2/Si substrate to a top speed of 4000 rpm, accelerated at 1200 rpm/s for 60 seconds.

2. The PVP is baked on a hotplate at 90 °for 60 s.

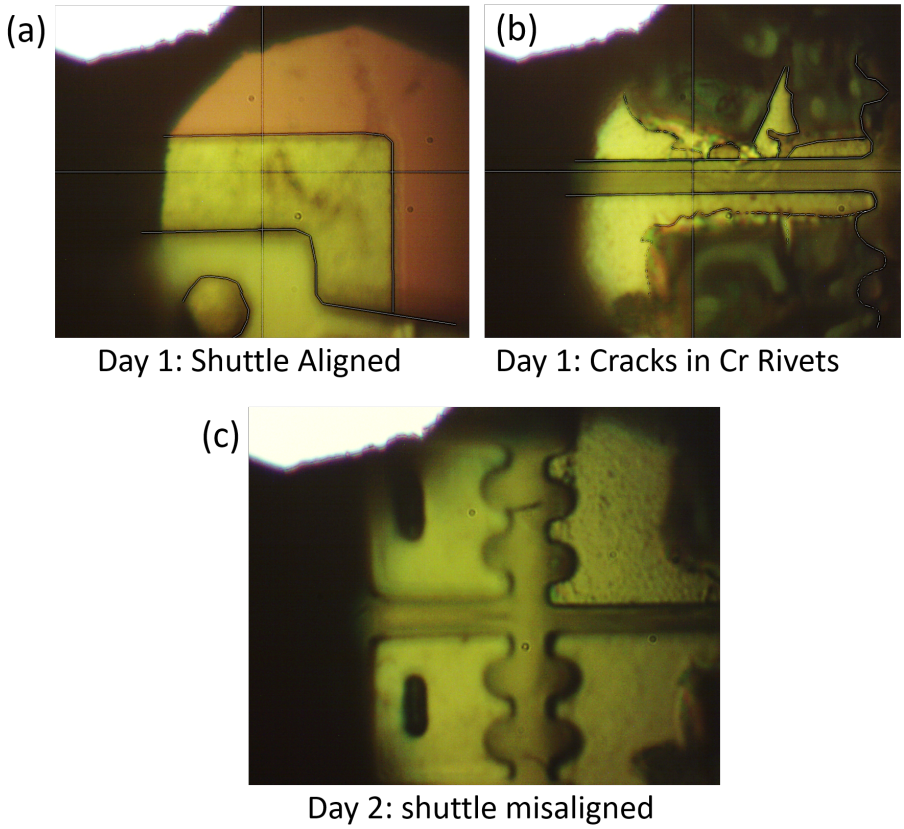

Figure E·1: Degradation of G11 CFNP2. (a) Day 1: Optical image of the MEMS device shows the Chevron shuttle aligned with the markers. (b) End of Day 1: Cracks appear in the riveting metal. (c) Day 2: 2D strain device stage shows significant misalignment. Interestingly, the suspended shuttle seems to be dragged toward the anchor side, shortening the gap.

3. Triple thick PMMA is spun on top of the PVP using the recipe detailed in Appendix A.1.1.

4. A tape mask containing a hole slightly larger than the side length of the subdie, ~ 2 mm, is placed on the PMMA. Again, a large window in the tape mask can be unstable when handling the film.

5. The tape mask and substrate is affixed to a transfer frame and float released in DI H_2O. The PVP dissolves in ~ 1 hour. The substrate does not always fall away from the film, but if it starts to release from the corners of the film it can be coaxed away from it using tweezers.

6. After release, the film should be dried in the desiccator for at least 24 hours before use.

E.6 Pitfalls and Prospective Improvements

The integration of 2D materials and MEMS is an arduous journey with many steps. Each step has its perils, and through the law of diminishing returns, the device yield ends up being quite low. As mentioned in Section 6.2 of this chapter, the best fabrication route is to maximize number of device that are co-fabricated. I gratefully acknowledge J. Christopher who worked out so many kinks in the fabrication process, and really for building the process from the ground up. Here, I hope to add to the trove of fabrication expertise he began, by looking at some pitfalls that still exist in the fabrication pipeline, and some options to improve device yield.

E.6.1 RIE Process

The reactive ion etching process has to be improved during the etching step after the EBL+Development. As seen in Fig. 6·6, the graphene is not completely removed dur-

ing the process and could be a cause of non-ideal behavior in the device when electrically actuated. In any case, the remaining graphene is added residue that the device could do without. The best course for improvement would be to try different etching recipes, increasing time in increments of 5 seconds. This should be attempted on samples of CVD graphene transferred over SiO_2, with a simple pattern made on it using EBL. This would save time and save MEMS devices from being destroyed.

Despite your best efforts, the pattern may get destroyed. The RIE machine has a tendency to be inconsistent in etching. The only course of action here to is to be extremely thorough in cleaning the chamber, positioning your device in the center of the chamber, and doing a trial run of the recipe (maybe more than once) in order to "season" the RIE.

E.6.2 MEMS Design

A consideration to be made about the MEMS itself is the sharp edges on either side of the gap of the 2D strain device stage. The straight edges can be points of strain concentration or areas where the material may tear. Fortunately, I have included several devices with smoother edges that should be prioritized for future design runs.

E.6.3 Graphene Quality

Clearly, the quality of the graphene is a real bottleneck to fabrication. Of all the commercial CVD graphene I have tried, GrollTex seems to be the most mechanically viable. It still has issues with strength. It is not very easy to know *a priori* if graphene or MoS_2 will be strong enough to mechanically withstand the entire fabrication process. One way to test mechanical viability of a growth is to do a quick transfer over a substrate with holes, all the way through to CPD. Another suggestion to maintain an unbroken graphene region across the gap is to make the region smaller. Graphene that spans the entire width of the 2D strain device stage ($\sim 30\,\mu m$) might be too large to remain viable during the fabrication process. Any small nicks or cracks propagate very quickly under straining the material,

which simply will tear the material. The downside is that smaller regions means there is lesser area to optically investigate.

E.6.4 PMMA Cleanliness

PMMA is the primary source of residue during the fabrication process for these devices. It is an exceptional transfer and lithography polymer, however it is incredibly difficult to remove completely after curing. Issues also arise when releasing large parts of the MEMS device during EBL and development. In the ACE bath some PMMA may detach, float, and land in inopportune areas such as on the Chevron shuttle, the tethers, or the 2D strain device stage. A final issue is PMMA getting under the MEMS device and preventing its motion. Unfortunately, I have not been able to ascertain at what point during the process this could happen.

The best assurance here is to ensure that the polymer is completely washed away in acetone. It must be soaked in acetone for as long as possible, usually $>$ 24 hrs. The last 1-2 hours of the acetone bath should be on the hotplate at 60 °C. Remember to keep the MEMS device in the CPD canister during this whole process and that the beaker with ACE is covered at all times. Many a time, I have forgotten to cover the beaker and the acetone readily evaporated, damaging the suspended 2D material. In order to avoid floating PMMA pieces, it may be better to release an entire square surface area containing the MEMS device. The trade-off is that the EBL process will take very long.

E.6.5 EBL Misalignment

A slight misalignment on during the EBL has been a source of great consternation for me towards the end of my device fabrication runs. If one peruses through my graphene and MoS_2 device trials, one will notice a steady displacement of the rivet holes on the anchor and shuttle side with each run. If the issue persists, trial runs on PMMA on bare substrates should be done. Calculate any misalignment against some preset markers, and add the

displacement during EBL on the MEMS. I'm not sure how else to address this besides carefully following the tips in Appendix A.1.2, and quickly bring up any alignment issues to Anlee.

E.6.6 Shadow Mask

During etching of the shadow mask under the focus ion beam, I have started to make the gap between the windows as large as 10 μm. This way the gap will definitely be covered. In addition, the windows themselves can be made smaller, which will prevent any deposition over the edge of the device at the slightest misalignment of the shadow mask. When putting the MEMS device in the chuck, S1818 can easily spill on to the device from overflowing. Take extreme caution in depositing only the tiniest droplet of S1818 for fixing in the chuck.

After affixing the shadow mask in PHO 810, carefully bring it to the clean room (PHO 817) for metal deposition. Remember that the chuck is strongly magnetic, meaning it will snap to most of the tables in the clean room and misalign the mask on the MEMS. Be careful where you're placing the sample on a surface in the clean room. Check for misalignment immediately under the microscope in the clean room.

E.6.7 Metal Deposition Issues

The final issue is an abnormal one that I've yet to fully troubleshoot, as it only happened abruptly in one device. Unfortunately for me, that device was the on that really worked, barring this issue. So in order to prevent a good device and hard work from being destroyed in even these rare circumstances, a suitable fix would be to lay down on a layer of gold on top of the anchor and shuttle prior to transferring any 2D material using PMMA and EBL. After depositing gold for microriveting, the on top and the gold on the bottom might merge to create a tighter hold on the material.

References

Abbas, K., Alaie, S., and Leseman, Z. C. (2012). Design and characterization of a low temperature gradient and large displacement thermal actuators for in situ mechanical testing of nanoscale materials. *Journal of Micromechanics and Microengineering*, 22(12):125027.

Abedrabbo, S., Hensel, J., a.T. Fiory, Sopori, B., Chen, W., and Ravindra, N. (1998). Perspectives on emissivity measurements and modeling in silicon. *Materials Science in Semiconductor Processing*, 1(3-4):187–193.

Abel, M. R., Graham, S., Serrano, J. R., Kearney, S. P., and Phinney, L. M. (2007a). Raman Thermometry of Polysilicon Microelectro- mechanical Systems in the Presence of an Evolving Stress. *Journal of Heat Transfer*, 129(3):329.

Abel, M. R., Wright, T. L., King, W. P., and Graham, S. (2007b). Thermal metrology of silicon microstructures using Raman spectroscopy. *IEEE Transactions on Components and Packaging Technologies*, 30(2):200–208.

Anagnostopoulos, G., Androulidakis, C., Koukaras, E. N., Tsoukleri, G., Polyzos, I., Parthenios, J., Papagelis, K., and Galiotis, C. (2015). Stress transfer mechanisms at the submicron level for graphene/polymer systems. *ACS Applied Materials and Interfaces*, 7(7):4216–4223.

Anagnostopoulos, G., Sygellou, L., Paterakis, G., Polyzos, I., Aggelopoulos, C. A., and Galiotis, C. (2019). Enhancing the adhesion of graphene to polymer substrates by controlled defect formation. *Nanotechnology*, 30(1).

Anasori, B., Xie, Y., Beidaghi, M., Lu, J., Hosler, B. C., Hultman, L., Kent, P. R., Gogotsi, Y., and Barsoum, M. W. (2015). Two-Dimensional, Ordered, Double Transition Metals Carbides (MXenes). *ACS Nano*, 9(10):9507–9516.

Androulidakis, C., Sourlantzis, D., Koukaras, E. N., Manikas, A. C., and Galiotis, C. (2019). Stress-transfer from polymer substrates to monolayer and few-layer graphenes. *Nanoscale Advances*, 1(12):4972–4980.

Ardekani, H., Younts, R., Yu, Y., Cao, L., and Gundogdu, K. (2019). Reversible Photoluminescence Tuning by Defect Passivation via Laser Irradiation on Aged Monolayer MoS_2. *ACS Applied Materials and Interfaces*, 11(41):38240–38246.

Arp, T. B., Pleskot, D., Aji, V., and Gabor, N. M. (2017). 2D condensate of electrons and holes in ultrathin MoTe2 photocells. *arXiv*, pages 1–40.

Bataller, A. W., Younts, R. A., Rustagi, A., Yu, Y., Ardekani, H., Kemper, A., Cao, L., and Gundogdu, K. (2019). Dense Electron–Hole Plasma Formation and Ultralong Charge Lifetime in Monolayer MoS_2 via Material Tuning. *Nano Letters*, 19:1104–1111.

Bernal, J. D. (1924). The Structure of Graphite. *Proceedings of the Royal Society of London. Series A, Containing Papers of a Mathematical and Physical Character*, 106(740):749–773.

Bertolazzi, S., Brivio, J., and Kis, A. (2011). Stretching and breaking of ultrathin MoS_2. *ACS Nano*, 5(12):9703–9709.

Bertrand, P. A. (1991). Surface-phonon dispersion of MoS_2. *Physical Review B*, 44(11): 5745–5749.

Blees, M. K., Barnard, A. W., Rose, P. A., Roberts, S. P., McGill, K. L., Huang, P. Y., Ruyack, A. R., Kevek, J. W., Kobrin, B., Muller, D. A., and McEuen, P. L. (2015). Graphene kirigami. *Nature*, 524(7564):204–207.

Blundo, E., Felici, M., Yildirim, T., Pettinari, G., Tedeschi, D., Miriametro, A., Liu, B., Ma, W., Lu, Y., and Polimeni, A. (2020). Evidence of the direct-to-indirect band gap transition in strained two-dimensional WS_2, MoS_2, and WSe_2. *Physical Review Research*, 2(1):012024.

Boztug, C., Sánchez-Pérez, J. R., Cavallo, F., Lagally, M. G., and Paiella, R. (2014). Strained-germanium nanostructures for infrared photonics. *ACS Nano*, 8(4):3136–3151.

Brown, J. J., Suk, J. W., Singh, G., Baca, A. I., Dikin, D. A., Ruoff, R. S., and Bright, V. M. (2009). Microsystem for nanofiber electromechanical measurements. *Sensors and Actuators, A: Physical*, 155(1):1–7.

Cao, K., Feng, S., Han, Y., Gao, L., Hue Ly, T., Xu, Z., and Lu, Y. (2020). Elastic straining of free-standing monolayer graphene. *Nature Communications*, 11(1):1–7.

Cao, Y., Fatemi, V., Demir, A., Fang, S., Tomarken, S. L., Luo, J. Y., Sanchez-Yamagishi, J. D., Watanabe, K., Taniguchi, T., Kaxiras, E., Ashoori, R. C., and Jarillo-Herrero, P. (2018a). Correlated insulator behaviour at half-filling in magic-angle graphene superlattices. *Nature*, 556(7699):80–84.

Cao, Y., Fatemi, V., Fang, S., Watanabe, K., Taniguchi, T., Kaxiras, E., and Jarillo-Herrero, P. (2018b). Unconventional superconductivity in magic-angle graphene superlattices. *Nature*, 556(7699):43–50.

Castellanos-Gomez, A., Agrat, N., and Rubio-Bollinger, G. (2010). Optical identification of atomically thin dichalcogenide crystals. *Applied Physics Letters*, 96(21):94–97.

Castellanos-Gomez, A., Roldán, R., Cappelluti, E., Buscema, M., Guinea, F., Van Der Zant, H. S., and Steele, G. A. (2013). Local strain engineering in atomically thin MoS_2. *Nano Letters*, 13(11):5361–5366.

Chaâbani, W., Melliti, A., Moadhen, A., Maaref, M. A., Testelin, C., Lemaître, A., and Oueslati, M. (2016). Theoretical Model and Experimental Study of Effects of Rapid Thermal Annealing on Self-assembled In(Ga)As/GaAs Quantum Dots. *Silicon*, 8(1):1–9.

Chae, W. H., Cain, J. D., Hanson, E. D., Murthy, A. A., and Dravid, V. P. (2017). Substrate-induced strain and charge doping in CVD-grown monolayer MoS_2. *Applied Physics Letters*, 111(14):143106.

Chakraborty, B., Bera, A., Muthu, D. V., Bhowmick, S., Waghmare, U. V., and Sood, A. K. (2012). Symmetry-dependent phonon renormalization in monolayer MoS_2 transistor. *Physical Review B - Condensed Matter and Materials Physics*, 85(16):161403.

Chaste, J., Missaoui, A., Huang, S., Henck, H., Ben Aziza, Z., Ferlazzo, L., Naylor, C., Balan, A., Johnson, A. T., Braive, R., and Ouerghi, A. (2018). Intrinsic Properties of Suspended MoS_2 on SiO_2/Si Pillar Arrays for Nanomechanics and Optics. *ACS Nano*, 12(4):3235–3242.

Chen, J., Walther, J. H., and Koumoutsakos, P. (2014). Strain Engineering of Kapitza Resistance in Few-Layer Graphene. *Nano Letters*, 14:819–825.

Chen, J.-H., Jang, C., Xiao, S., Ishigami, M., and Fuhrer, M. S. (2008). Intrinsic and extrinsic performance limits of graphene devices on sio 2. *Nature nanotechnology*, 3(4):206–209.

Cheng, Y. C., Zhu, Z. Y., Huang, G. S., and Schwingenschlögl, U. (2011). Grüneisen parameter of the G mode of strained monolayer graphene. *Physical Review B - Condensed Matter and Materials Physics*, 83(11):1–5.

Chernikov, A., Berkelbach, T. C., Hill, H. M., Rigosi, A., Li, Y., Aslan, O. B., Reichman, D. R., Hybertsen, M. S., and Heinz, T. F. (2014). Exciton binding energy and nonhydrogenic Rydberg series in monolayer WS_2. *Physical Review Letters*, 113(7):1–5.

Chernikov, A., Ruppert, C., Hill, H. M., Rigosi, A. F., and Heinz, T. F. (2015a). Population inversion and giant bandgap renormalization in atomically thin WS_2 layers. *Nature Photonics*, 9(7):466–470.

Chernikov, A., Van Der Zande, A. M., Hill, H. M., Rigosi, A. F., Velauthapillai, A., Hone, J., and Heinz, T. F. (2015b). Electrical Tuning of Exciton Binding Energies in Monolayer WS_2. *Physical Review Letters*, 115(12):126802.

Choi, S.-M., Jhi, S.-H., and Son, Y.-W. (2010). Effects of strain on electronic properties of graphene. *Physical Review B*, 81(8):081407.

Christopher, J., Vutukuru, M., Lloyd, D., Bunch, J., Goldberg, B., Bishop, D., and Swan, A. Monolayer MoS_2 Strained to 1.3% with a microelectromechanical system. *Journal of Microelectromechanical Systems*, 28(2):254–263.

Christopher, J. W., Goldberg, B. B., and Swan, A. K. (2017). Long tailed trions in monolayer MoS_2: Temperature dependent asymmetry and resulting red-shift of trion photoluminescence spectra. *Scientific Reports*, 7(1):1–8.

Coehoorn, R., Haas, C., and De Groot, R. A. (1987). Electronic structure of $MoSe_2$, MoS_2, and WSe_2. II. The nature of the optical band gaps. *Physical Review B*, 35(12):6203–6206.

Cong, C., Yu, T., Sato, K., Shang, J., Saito, R., Dresselhaus, G. F., and Dresselhaus, M. S. (2011). Raman Characterization of ABA- and ABC-Stacked Trilayer Graphene. *ACS Nano*, 5(11):8760–8768.

Conley, H. J., Wang, B., Ziegler, J. I., Haglund, R. F., Pantelides, S. T., and Bolotin, K. I. (2013). Bandgap engineering of strained monolayer and bilayer MoS_2. *Nano Letters*, 13(8):3626–3630.

Cowen, A., Hardy, B., Mahadevan, R., and Wilcenski, S. (2013). PolyMUMPs Design Handbook a MUMPs® process. *MEMSCAP Inc*.

Dean, C. R., Young, A. F., Meric, I., Lee, C., Wang, L., Sorgenfrei, S., Watanabe, K., Taniguchi, T., Kim, P., Shepard, K. L., and Hone, J. (2010). Boron nitride substrates for high-quality graphene electronics. *Nature Nanotechnology*, 5(10):722–726.

Espinosa, H. D., Zhu, Y., and Moldovan, N. (2007). Design and operation of a MEMS-based material testing system for nanomechanical characterization. *Journal of Microelectromechanical Systems*, 16(5):1219–1231.

Fechine, G. J., Martin-Fernandez, I., Yiapanis, G., Bentini, R., Kulkarni, E. S., Bof De Oliveira, R. V., Hu, X., Yarovsky, I., Castro Neto, A. H., and Özyilmaz, B. (2015). Direct dry transfer of chemical vapor deposition graphene to polymeric substrates. *Carbon*, 83:224–231.

Feng, J., Qian, X., Huang, C. W., and Li, J. (2012). Strain-engineered artificial atom as a broad-spectrum solar energy funnel. *Nature Photonics*, 6(12):866–872.

Fernández, M., Chen, T. L., Chang, T., Zhu, B., Marchena, M., Wagner, F., Johnson, B., Mazumder, P., Lee, R., Pruneri, V., and Arliguie, T. (2018). Dry transfer of graphene to dielectrics and flexible substrates using polyimide as a transparent and stable intermediate layer. *2D Materials*, 5(3):035022.

Ferrari, A. C. (2007). Raman spectroscopy of graphene and graphite: Disorder, electron-phonon coupling, doping and nonadiabatic effects. *Solid State Communications*, 143(1-2):47–57.

Ferrari, A. C. and Basko, D. M. (2013). Raman spectroscopy as a versatile tool for studying the properties of graphene. *Nature Nanotechnology*, 8(4):235–246.

Ferrari, A. C., Meyer, J. C., Scardaci, V., Casiraghi, C., Lazzeri, M., Mauri, F., Piscanec, S., Jiang, D., Novoselov, K. S., Roth, S., and Geim, A. K. (2006). Raman spectrum of graphene and graphene layers. *Physical Review Letters*, 97(18):1–4.

Frank, I. W., Tanenbaum, D. M., Van der Zande, A. M., and McEuen, P. L. (2007). Mechanical properties of suspended graphene sheets. *Journal of Vacuum Science and Technology B*, 25(6):2558–2561.

Fu, X., Su, C., Fu, Q., Zhu, X., Zhu, R., Liu, C., Liao, Z., Xu, J., Guo, W., Feng, J., Li, J., and Yu, D. (2014). Tailoring exciton dynamics by elastic strain-gradient in semiconductors. *Advanced Materials*, 26(16):2572–2579.

Gao, S., Liang, Y., Spataru, C. D., and Yang, L. (2016). Dynamical Excitonic Effects in Doped Two-Dimensional Semiconductors. *Nano Letters*, 16(9):5568–5573.

Gao, S. and Yang, L. (2017). Renormalization of the quasiparticle band gap in doped two-dimensional materials from many-body calculations. *Physical Review B*, 96(15):155410.

Geim, A. and Novoselov, K. (2007). The rise of graphene. *Nature Materials*, 6:183–191.

Geisberger, A. A., Sarkar, N., Ellis, M., and Skidmore, G. D. (2003). Electrothermal properties and modeling of polysilicon microthermal actuators. *Journal of Microelectromechanical Systems*, 12(4):513–523.

Ghani, T., Armstrong, M., Auth, C., Bost, M., Charvat, P., Glass, G., Hoffmann, T., Johnson, K., Kenyon, C., Klaus, J., McIntyre, B., Mistry, K., Murthy, A., Sandford, J., Silberstein, M., Sivakumar, S., Smith, P., Zawadzki, K., Thompson, S., and Bohr, M. (2003). A 90nm high volume manufacturing logic technology featuring novel 45nm gate length strained silicon cmos transistors. In *IEEE International Electron Devices Meeting 2003*, pages 11.6.1–11.6.3.

Gilperez, J. M., Gonzalez-Sanz, F., Calleja, E., Munoz, E., Calleja, J. M., Mestres, N., Castagne, J., and Barbier, E. (1992). Photoluminescence and Raman analysis of strain and composition in InGaAs/AlGaAs pseudomorphic heterostructures. *Semiconductor Science and Technology*, 7(4):562–566.

Goldsche, M., Sonntag, J., Khodkov, T., Verbiest, G. J., Reichardt, S., Neumann, C., Ouaj, T., von den Driesch, N., Buca, D., and Stampfer, C. (2018). Tailoring Mechanically Tunable Strain Fields in Graphene. *Nano Letters*, page acs.nanolett.7b04774.

Golovynskyi, S., Irfan, I., Bosi, M., Seravalli, L., Datsenko, O. I., Golovynska, I., Li, B., Lin, D., and Qu, J. (2020). Exciton and trion in few-layer MoS_2: Thickness- and temperature-dependent photoluminescence. *Applied Surface Science*, 515(January):146033.

Gong, L., Young, R. J., Kinloch, I. A., Haigh, S. J., Warner, J. H., Hinks, J. A., Xu, Z., Li, L., Ding, F., Riaz, I., Jalil, R., and Novoselov, K. S. (2013). Reversible loss of bernal stacking during the deformation of few-layer graphene in nanocomposites. *ACS Nano*, 7(8):7287–7294.

Gong, L., Young, R. J., Kinloch, I. A., Riaz, I., Jalil, R., and Novoselov, K. S. (2012). Optimizing the reinforcement of polymer-based nanocomposites by graphene. *ACS Nano*, 6(3):2086–2095.

González, J., Guinea, F., and Vozmediano, M. (1994). Non-fermi liquid behavior of electrons in the half-filled honeycomb lattice (a renormalization group approach). *Nuclear Physics B*, 424(3):595–618.

Gorbar, E. V., Gusynin, V. P., Miransky, V. A., and Shovkovy, I. A. (2002). Magnetic field driven metal-insulator phase transition in planar systems. *Physical Review B - Condensed Matter and Materials Physics*, 66(4):451081–4510822.

Greil, J., Assali, S., Isono, Y., Belabbes, A., Bechstedt, F., Valega MacKenzie, F. O., Silov, A. Y., Bakkers, E. P., and Haverkort, J. E. (2016). Optical properties of strained wurtzite gallium phosphide nanowires. *Nano Letters*, 16(6):3703–3709.

Guinea, F., Geim, A. K., Katsnelson, M. I., and Novoselov, K. S. (2010). Generating quantizing pseudomagnetic fields by bending graphene ribbons. *Physical Review B - Condensed Matter and Materials Physics*, 81(3):1–5.

Hanakata, P. Z., Cubuk, E. D., Campbell, D. K., and Park, H. S. (2020). Forward and inverse design of kirigami via supervised autoencoder. *Physical Review Research*, 2(4):1–6.

Hanakata, P. Z., Cubuk, E. D., Campbell, D. K., Park, H. S., Wang, S., Huang, S., Wang, Q., Peng, L., and Zhao, W. (2018). Accelerated Search and Design of Stretchable Graphene Kirigami Using Machine Learning. *Physical Review Letters*, 121(25):255304.

Hanakata, P. Z., Qi, Z., Campbell, D. K., and Park, H. S. (2016). Highly stretchable MoS2 kirigami. *Nanoscale*, 8(1):458–463.

Harats, M. G., Kirchhof, J. N., Qiao, M., Greben, K., and Bolotin, K. I. (2020). Dynamics and efficient conversion of excitons to trions in non-uniformly strained monolayer WS_2. *Nature Photonics*, 14(5):324–329.

He, K., Poole, C., Mak, K. F., and Shan, J. (2013). Experimental demonstration of continuous electronic structure tuning via strain in atomically thin MoS2. *Nano Letters*, 13(6):2931–2936.

Hicks, C. W., Barber, M. E., Edkins, S. D., Brodsky, D. O., and Mackenzie, A. P. (2014). Piezoelectric-based apparatus for strain tuning. *Review of Scientific Instruments*, 85(6).

Holman, J. (1997). *Heat Transfer*. McGraw-Hill.

Hsu, C., Teague, M. L., Wang, J., and Yeh, N. (2020). Nanoscale strain engineering of giant pseudo-magnetic fields , valley polarization , and topological channels in graphene. *Science Advances*, 6(19).

Huang, Y., Sutter, E., Shi, N. N., Zheng, J., Yang, T., Englund, D., Gao, H. J., and Sutter, P. (2015). Reliable Exfoliation of Large-Area High-Quality Flakes of Graphene and Other Two-Dimensional Materials. *ACS Nano*, 9(11):10612–10620.

Hui, Y. Y., Liu, X., Jie, W., Chan, N. Y., Hao, J., Hsu, Y. T., Li, L. J., Guo, W., and Lau, S. P. (2013). Exceptional tunability of band energy in a compressively strained trilayer MoS2 sheet. *ACS Nano*, 7(8):7126–7131.

Jain, S., Willander, M., and Overstraeten, R. V. *Compound Semiconductors Strained Layers and Devices*, volume 7 of *Electronic Materials Series*. Springer US, 1 edition.

Javey, A., Uddin, S. Z., Kim, H., Lorenzon, M., Yeh, M., Lien, D. H., Barnard, E. S., Htoon, H., and Weber-Bargioni, A. (2020). Neutral exciton diffusion in monolayer MoS_2. *ACS Nano*, 14(10):13433–13440.

Jayne, R. K., Stark, T. J., Reeves, J. B., Bishop, D. J., and White, A. E. (2018). Dynamic Actuation of Soft 3D Micromechanical Structures Using Micro-Electromechanical Systems (MEMS). *Advanced Materials Technologies*, 3(3):1–6.

Kane, C. L. and Mele, E. J. (2004). Electron interactions and scaling relations for optical excitations in carbon nanotubes. *Physical Review Letters*, 93(19):197402.

Kearney, S. P., Phinney, L. M., and Baker, M. S. (2006). Spatially resolved temperature mapping of electrothermal actuators by surface Raman scattering. *Journal of Microelectromechanical Systems*, 15(2):314–321.

Kern, J., Niehues, I., Tonndorf, P., Schmidt, R., Wigger, D., Schneider, R., Stiehm, T., Michaelis de Vasconcellos, S., Reiter, D. E., Kuhn, T., and Bratschitsch, R. (2016). Nanoscale Positioning of Single-Photon Emitters in Atomically Thin WSe_2. *Advanced Materials*, 28(33):7101–7105.

Khveshchenko, D. V. (2001). Ghost excitonic insulator transition in layered graphite. *Physical Review Letters*, 87(24):246802–1–246802–4.

Kim, D.-H., Ahn, J.-H., Choi, W. M., Kim, H.-S., Kim, T.-H., Song, J., Huang, Y. Y., Liu, Z., Lu, C., and Rogers, J. A. (2008). Stretchable and foldable silicon integrated circuits. *Science*, 320(5875):507–511.

Kim, H., Ko, H., Kim, S. M., and Rho, H. (2020). Polarization-dependent anisotropic Raman response of CVD-grown vertically stacked MoS2 layers. *Journal of Raman Spectroscopy*, 51(5):774–780.

Kinoshita, K. and Moriya, R. (2019). Dry release transfer of graphene and few-layer h-BN by utilizing thermoplasticity of polypropylene carbonate. *npj 2D Materials and Applications*, (January):4–6.

Kitt, A. L., Qi, Z., Rémi, S., Park, H. S., Swan, A. K., and Goldberg, B. B. (2013). How graphene slides: Measurement and theory of strain-dependent frictional forces between graphene and SiO2. *Nano Letters*, 13(6):2605–2610.

Klar, P., Lidorikis, E., Eckmann, A., Verzhbitskiy, I. A., Ferrari, A. C., and Casiraghi, C. (2013). Raman scattering efficiency of graphene. *Physical Review B - Condensed Matter and Materials Physics*, 87(20):1–12.

Klein, F., Striebel, T., Fischer, J., Jiang, Z., Franz, C. M., Von Freymann, G., Wegener, M., and Bastmeyer, M. (2010). Elastic fully three-dimensional microstructure scaffolds for cell force measurements. *Advanced Materials*, 22(8):868–871.

Kojima, K., Lim, H. E., Liu, Z., Zhang, W., Saito, T., Nakanishi, Y., Endo, T., Kobayashi, Y., Watanabe, K., Taniguchi, T., Matsuda, K., Maniwa, Y., Miyauchi, Y., and Miyata, Y. (2019). Restoring the intrinsic optical properties of CVD-grown MoS_2 monolayers and their heterostructures. *Nanoscale*, 11(27):12798–12803.

Kovalchuk, S., Harats, M. G., López-Polín, G., Kirchhof, J. N., Höflich, K., and Bolotin, K. I. (2020). Neutral and charged excitons interplay in non-uniformly strain-engineered WS_2. *2D Materials*, 7(3):035024.

Kuang, Y., Huang, Q. A., and Lee, N. K. S. (2002). Numerical simulation of a polysilicon thermal flexure actuator. *Microsystem Technologies*, 8(1):17–21.

Kumar, S., Kaczmarczyk, A., and Gerardot, B. D. (2015). Strain-Induced Spatial and Spectral Isolation of Quantum Emitters in Mono- and Bilayer WSe_2. *Nano Letters*, 15(11):7567–7573.

Landau, L. D. (1937). Zur theorie der phasenumwandlungen ii. *Physikalische Zeitschrift der Sowjetunion*, 11(545):26–35.

Lee, C., Wei, X., Kysar, J. W., and Hone, J. (2008). Measurement of the elastic properties and intrinsic strength of monolayer graphene. *Science (New York, N.Y.)*, 321(5887):385–388.

Lee, C., Yan, H., Brus, L. E., Heinz, T. F., Hone, . J., and Ryu, S. (2010). Anomalous Lattice Vibrations of Single- and Few-Layer MoS_2. *ACS Nano*, 4(5):2695–2700.

Lee, J. E., Ahn, G., Shim, J., Lee, Y. S., and Ryu, S. (2012). Optical separation of mechanical strain from charge doping in graphene. *Nature Communications*, 3(May):1024.

Leong, W. S., Wang, H., Yeo, J., Martin-Martinez, F. J., Zubair, A., Shen, P. C., Mao, Y., Palacios, T., Buehler, M. J., Hong, J. Y., and Kong, J. (2019). Paraffin-enabled graphene transfer. *Nature Communications*, 10(1):1–8.

Levy, N., Burke, S. A., Meaker, K. L., Panlasigui, M., Zettl, A., Guinea, F., Neto, A. H. C., and Crommie, M. F. (2010). Strain-Induced Pseudo–Magnetic Fields Greater Than 300 Tesla in Graphene Nanobubbles. *Science*, 329(5991).

Li, H., Contryman, A. W., Qian, X., Ardakani, S. M., Gong, Y., Wang, X., Weisse, J. M., Lee, C. H., Zhao, J., Ajayan, P. M., Li, J., Manoharan, H. C., and Zheng, X. (2015). Optoelectronic crystal of artificial atoms in strain-textured molybdenum disulphide. *Nature Communications*, 6(May):7381.

Li, H., Zhang, Q., Yap, C. C. R., Tay, B. K., Edwin, T. H. T., Olivier, A., and Baillargeat, D. (2012). From bulk to monolayer MoS_2: Evolution of Raman scattering. *Advanced Functional Materials*, 22(7):1385–1390.

Li, X., Zhu, Y., Cai, W., Borysiak, M., Han, B., Chen, D., Piner, R. D., Colomba, L., and Ruoff, R. S. (2009). Transfer of large-area graphene films for high-performance transparent conductive electrodes. *Nano Letters*, 9(12):4359–4363.

Liang, X., Sperling, B. A., Calizo, I., Cheng, G., Hacker, C. A., Zhang, Q., Obeng, Y., Yan, K., Peng, H., Li, Q., Zhu, X., Yuan, H., Hight Walker, A. R., Liu, Z., Peng, L. M., and Richter, C. A. (2011). Toward clean and crackless transfer of graphene. *ACS Nano*, 5(11):9144–9153.

Lien, D. H., Amani, M., Desai, S. B., Ahn, G. H., Han, K., He, J. H., Ager, J. W., Wu, M. C., and Javey, A. (2018). Large-area and bright pulsed electroluminescence in monolayer semiconductors. *Nature Communications*, 9(1):1229.

Lien, D. H., Uddin, S. Z., Yeh, M., Amani, M., Kim, H., Ager, J. W., Yablonovitch, E., and Javey, A. (2019). Electrical suppression of all nonradiative recombination pathways in monolayer semiconductors. *Science*, 364(6439):468–471.

Lin, Y., Ling, X., Yu, L., Huang, S., Hsu, A. L., Lee, Y. H., Kong, J., Dresselhaus, M. S., and Palacios, T. (2014). Dielectric screening of excitons and trions in single-layer MoS_2. *Nano Letters*, 14(10):5569–5576.

Lin, Y. C., Jin, C., Lee, J. C., Jen, S. F., Suenaga, K., and Chiu, P. W. (2011). Clean transfer of graphene for isolation and suspension. *ACS Nano*, 5(3):2362–2368.

Liu, G.-B., Shan, W.-Y., Yao, Y., Yao, W., and Xiao, D. (2013). Three-band tight-binding model for monolayers of group-vib transition metal dichalcogenides. *Physical Review B*, 88:085433.

Liu, Y., Guo, J., Zhu, E., Liao, L., Lee, S. J., Ding, M., Shakir, I., Gambin, V., Huang, Y., and Duan, X. (2018). Approaching the Schottky-Mott limit in van der Waals metal-semiconductor junctions. *Nature*, 557(7707):696–700.

Lloyd, D., Liu, X., Christopher, J. W., Cantley, L., Wadehra, A., Kim, B. L., Goldberg, B. B., Swan, A. K., and Bunch, J. S. (2016). Band Gap Engineering with Ultralarge Biaxial Strains in Suspended Monolayer MoS2. *Nano Letters*, 16(9):5836–5841.

Lott, C. D., McLain, T. W., Harb, J. N., and Howell, L. L. (2002). Modeling the thermal behavior of a surface-micromachined linear-displacement thermomechanical microactuator. *Sensors and Actuators, A: Physical*, 101(1-2):239–250.

Lu, S., Dikin, D. A., Zhang, S., Fisher, F. T., Lee, J., and Ruoff, R. S. (2004). Realization of nanoscale resolution with a micromachined thermally actuated testing stage. *Review of Scientific Instruments*, 75(6):2154–2162.

Lu, S., Guo, Z., Ding, W., and Ruoff, R. S. (2006). Analysis of a microelectromechanical system testing stage for tensile loading of nanostructures. *Review of Scientific Instruments*, 77(5).

Mak, K. F., He, K., Lee, C., Lee, G. H., Hone, J., Heinz, T. F., and Shan, J. (2013). Tightly bound trions in monolayer MoS_2. *Nature Materials*, 12(3):207–211.

Mak, K. F., Sfeir, M. Y., Misewich, J. A., and Heinza, T. F. (2010a). The evolution of electronic structure in few-layer graphene revealed by optical spectroscopy. *Proceedings of the National Academy of Sciences of the United States of America*, 107(34):14999–15004.

Mak, K. F., Shan, J., and Heinz, T. F. (2010b). Electronic structure of few-layer graphene: Experimental demonstration of strong dependence on stacking sequence. *Physical Review Letters*, 104(17):1–4.

Mangu, V. S., Zamiri, M., Brueck, S. R., and Cavallo, F. (2017). Strain engineering, efficient excitonic photoluminescence, and exciton funnelling in unmodified MoS_2 nanosheets. *Nanoscale*, 9(43):16602–16606.

Marta, B., Leordean, C., Istvan, T., Botiz, I., and Astilean, S. (2016). Efficient etching-free transfer of high quality, large-area CVD grown graphene onto polyvinyl alcohol films. *Applied Surface Science*, 363:613–618.

Martins, L. G., Song, Y., Zeng, T., Dresselhaus, M. S., Kong, J., and Araujo, P. T. (2013). Direct transfer of graphene onto flexible substrates. *Proceedings of the National Academy of Sciences of the United States of America*, 110(44):17762–17767.

McConnell, A. D., Uma, S., and Goodson, K. E. (2001). Thermal conductivity of doped polysilicon layers. *Journal of Microelectromechanical Systems*, 10(3):360–369.

McCreary, A., Ghosh, R., Amani, M., Wang, J., Duerloo, K. A. N., Sharma, A., Jarvis, K., Reed, E. J., Dongare, A. M., Banerjee, S. K., Terrones, M., Namburu, R. R., and Dubey, M. (2016). Effects of Uniaxial and Biaxial Strain on Few-Layered Terrace Structures of MoS_2 Grown by Vapor Transport. *ACS Nano*, 10(3):3186–3197.

Mermin, N. D. (1968). Crystalline Order in Two Dimensions. *Physical Review*, 176(1):250–254.

Metzger, C., Rémi, S., Liu, M., Kusminskiy, S. V., Castro Neto, A. H., Swan, A. K., and Goldberg, B. B. (2010). Biaxial strain in graphene adhered to shallow depressions. *Nano Letters*, 10(1):6–10.

Michail, A., Delikoukos, N., Parthenios, J., Galiotis, C., and Papagelis, K. (2016). Optical detection of strain and doping inhomogeneities in single layer MoS_2. *Applied Physics Letters*, 108(17):173102.

Miller, B., Parzinger, E., Vernickel, A., Holleitner, A. W., and Wurstbauer, U. (2015). Photogating of mono- and few-layer MoS_2. *Applied Physics Letters*, 106(12):122103.

Mistry, K., Armstrong, M., Auth, C., Cea, S., Coan, T., Ghani, T., Hoffmann, T., Murthy, A., Sandford, J., Shaheed, R., Zawadzki, K., Zhang, K., Thompson, S., and Bohra, M. (2004). Delaying forever: Uniaxial strained silicon transistors in a 90nm CMOS technology. *Digest of Technical Papers - Symposium on VLSI Technology*, (May 2014):50–51.

Mohiuddin, T. M., Lombardo, A., Nair, R. R., Bonetti, A., Savini, G., Jalil, R., Bonini, N., Basko, D. M., Galiotis, C., Marzari, N., Novoselov, K. S., Geim, A. K., and Ferrari, A. C. (2009). Uniaxial strain in graphene by Raman spectroscopy: G peak splitting, Grüneisen parameters, and sample orientation. *Physical Review B - Condensed Matter and Materials Physics*, 79(20):205433.

Moon, H., Grosso, G., Chakraborty, C., Peng, C., Taniguchi, T., Watanabe, K., and Englund, D. (2020). Dynamic Exciton Funneling by Local Strain Control in a Monolayer Semiconductor. *Nano Letters*, 20(9):6791–6797.

Morozov, S. V., Novoselov, K. S., Katsnelson, M. I., Schedin, F., Elias, D. C., Jaszczak, J. A., and Geim, A. K. (2008). Giant intrinsic carrier mobilities in graphene and its bilayer. *Physical Review Letters*, 100(1):11–14.

Mouri, S., Miyauchi, Y., and Matsuda, K. (2013). Tunable photoluminescence of monolayer MoS_2 via chemical doping. *Nano Letters*, 13(12):5944–5948.

Mueller, N. S., Heeg, S., Alvarez, M. P., Kusch, P., Wasserroth, S., Clark, N., Schedin, F., Parthenios, J., Papagelis, K., Galiotis, C., Kalbáč, M., Vijayaraghavan, A., Huebner, U., Gorbachev, R., Frank, O., and Reich, S. (2017). Evaluating arbitrary strain configurations and doping in graphene with Raman spectroscopy. *arXiv*.

Nagai, M. and Kuwata-Gonokami, M. (2002). Electron-hole liquid formation by exciton and biexciton resonant excitation in CuCl. *Journal of Luminescence*, 100(1-4):233–242.

Naguib, M., Mochalin, V. N., Barsoum, M. W., and Gogotsi, Y. (2014). 25th anniversary article: Mxenes: A new family of two-dimensional materials. *Advanced Materials*, 26(7):992–1005.

Naraghi, M., Chasiotis, I., Kahn, H., Wen, Y., and Dzenis, Y. (2007). Novel method for mechanical characterization of polymeric nanofibers. *Review of Scientific Instruments*, 78(8).

Neto, A. H. C., Guinea, F., Peres, N. M. R., Novoselov, K. S., and Geim, A. K. (2007). The electronic properties of graphene. *Reviews of Modern Physics*, 81(March):109–162.

Newaz, A. K., Puzyrev, Y. S., Wang, B., Pantelides, S. T., and Bolotin, K. I. (2012). Probing charge scattering mechanisms in suspended graphene by varying its dielectric environment. *Nature Communications*, 3:734.

Ni, Z., Wang, Y., Yu, T., and Shen, Z. (2008). Raman spectroscopy and imaging of graphene. *Nano Research*, 1(4):273–291.

Nie, Z., Jiang, H., and Kara, L. B. (2018). Deep Learning for Stress Field Prediction Using Convolutional Neural Networks. *CoRR*, abs/1808.0.

Novoselov, K. S., Geim, A. K., Morozov, S. V., D. Jiang, Y. Z., Dubonos, S. V., Grigorieva, I. V., and Firsov, A. A. (2004). Electric Field Effect in Atomically Thin Carbon Films. *Science*, 306(5696):666–669.

Novoselov, K. S., Geim, A. K., Morozov, S. V., Jiang, D., Katsnelson, M. I., Grigorieva, I. V., Dubonos, S. V., and Firsov, A. A. (2005a). Two-dimensional gas of massless Dirac fermions in graphene. *Nature*, 438(7065):197–200.

Novoselov, K. S., Jiang, D., Schedin, F., Booth, T. J., Khotkevich, V. V., Morozov, S. V., and Geim, A. K. (2005b). Two-dimensional atomic crystals. *Proceedings of the National Academy of Sciences of the United States of America*, 102(30):10451–10453.

Novoselov, K. S., Jiang, Z., Zhang, Y., Morozov, S. V., Stormer, H. L., Zeitler, U., Maan, J. C., Boebinger, G. S., Kim, P., and Geim, A. K. (2007). Room-Temperature Quantum Hall Effect in Graphene. *Science*, 315(5817):1379–1379.

Okada, Y. and Tokumaru, Y. (1984). Precise determination of lattice parameter and thermal expansion coefficient of silicon between 300 and 1500 K. *Journal of Applied Physics*, 56(2):314–320.

Paiella, R. and Lagally, M. G. (2018). Optical properties of tensilely strained Ge nanomembranes. *Nanomaterials*, 8(6):1–10.

Pant, B., Allen, B. L., Zhu, T., Gall, K., and Pierron, O. N. (2011). A versatile microelectromechanical system for nanomechanical testing. *Applied Physics Letters*, 98(5):4–7.

Pant, B., Choi, S., Baumert, E. K., Allen, B. L., Graham, S., Gall, K., and Pierron, O. N. (2012). MEMS-Based Nanomechanics: Influence of MEMS Design on Test Temperature. *Experimental Mechanics*, 52(6):607–617.

Paskiewicz, D. M. (2012). *Elastic strain engineering in silicon and silicon-germanium nanomembranes*. PhD thesis, The University of Wisconsin - Madison.

Peierls, R. (1935). Quelques propriétés typiques des corps solides. *Annales de l'institut Henri Poincaré*, 5(3):177–222.

Pereira, V. M. and Castro Neto, A. H. (2009). Strain Engineering of Graphene's Electronic Structure. *Physical Review Letters*, 103(4):1–4.

Pizzocchero, F., Gammelgaard, L., Jessen, B. S., Caridad, M., Wang, L., Hone, J., Bøggild, P., and Booth, T. J. (2016). The hot pick-up technique for batch assembly of van der Waals heterostructures. *Nature Communications*, 7(11894).

Polyzos, I., Bianchi, M., Rizzi, L., Koukaras, E. N., Parthenios, J., Papagelis, K., Sordan, R., and Galiotis, C. (2015). Suspended monolayer graphene under true uniaxial deformation. *Nanoscale*, 7(30):13033–13042.

Posener, D. (1959). The Shape of Spectral Lines: Tables of the Voigt Profile. *Australian Journal of Physics*, 12(2):184.

Pulizzi, F., Thijssen, W. H., Christianen, P. C., Maan, J. C., Yakovlev, D. R., Ossau, W., Wojtowicz, T., Karczewski, G., and Kossut, J. (2001). Motion of neutral and negatively charged excitons in high magnetic fields. *Physica B: Condensed Matter*, 298(1-4):397–401.

Qin, Q. and Zhu, Y. (2013). Temperature control in thermal microactuators with applications to in-situ nanomechanical testing. *Applied Physics Letters*, 102(1).

Que, L., Park, J.-S., and Gianchandani, Y. (1999). Bent-beam electro-thermal actuators for high force applications. *Technical Digest. IEEE International MEMS 99 Conference. Twelfth IEEE International Conference on Micro Electro Mechanical Systems (Cat. No.99CH36291)*, (608):31–36.

Raja, A., Chaves, A., Yu, J., Arefe, G., Hill, H. M., Rigosi, A. F., Berkelbach, T. C., Nagler, P., Schüller, C., Korn, T., Nuckolls, C., Hone, J., Brus, L. E., Heinz, T. F., Reichman, D. R., and Chernikov, A. (2017). Coulomb engineering of the bandgap and excitons in two-dimensional materials. *Nature Communications*, 8(May):15251.

Raman, M. S., Kifle, T., Bhattacharya, E., and Bhat, K. N. (2006). Physical model for the resistivity and temperature coefficient of resistivity in heavily doped polysilicon. *IEEE Transactions on Electron Devices*.

Ramasubramaniam, A. (2012). Large excitonic effects in monolayers of molybdenum and tungsten dichalcogenides. *Physical Review B*, 86:115409.

Reeves, J. B., Jayne, R. K., Barrett, L., White, A. E., and Bishop, D. J. (2019). Fabrication of multi-material 3D structures by the integration of direct laser writing and MEMS stencil patterning. *Nanoscale*, 11(7):3268–3274.

Reeves, J. B., Jayne, R. K., Stark, T. J., Barrett, L. K., White, A. E., and Bishop, D. J. (2018). Tunable Infrared Metasurface on a Soft Polymer Scaffold. *Nano Letters*, 18(5):2802–2806.

Reina, A., Son, H., Jiao, L., Fan, B., Dresselhaus, M. S., Liu, Z. F., and Kong, J. (2008). Transferring and identification of single- and few-layer graphene on arbitrary substrates. *Journal of Physical Chemistry C*, 112(46):17741–17744.

Rosati, R., Brem, S., Perea-Causin, R., Schmidt, R., Niehues, I., Michaelis De Vasconcellos, S., Bratschitsch, R., and Malic, E. (2021). Strain-dependent exciton diffusion in transition metal dichalcogenides. *2D Materials*, 8(1):015030.

Ross, J. S., Klement, P., Jones, A. M., Ghimire, N. J., Yan, J., Mandrus, D. G., Taniguchi, T., Watanabe, K., Kitamura, K., Yao, W., Cobden, D. H., and Xu, X. (2014). Electrically tunable excitonic light-emitting diodes based on monolayer WSe_2 p-n junctions. *Nature Nanotechnology*, 9(4):268–272.

Rustagi, A. and Kemper, A. F. (2018). Theoretical Phase Diagram for the Room-Temperature Electron-Hole Liquid in Photoexcited Quasi-Two-Dimensional Monolayer MoS2. *Nano Letters*, 18(1):455–459.

Saleh, M. E., Beuth, J. L., Picard, Y. N., and De Boer, M. P. (2015). In Situ Platform for Isothermal Testing of Thin-Film Mechanical Properties Using Thermal Actuators. *Journal of Microelectromechanical Systems*, 24(6):2008–2018.

Sarua, A., Ji, H., Kuball, M., Uren, M. J., Martin, T., Hilton, K. P., Balmer, R. S., Self-heating, A., and Gan, A. (2006). Integrated Micro-Raman / Infrared Thermography Probe for Monitoring of Self-Heating in AlGaN / GaN Transistor Structures. *Ieee Transactions on Electron Devices*, 53(10):2438–2447.

Sato, T. (1967). Spectral Emissivity of Silicon. *Materials Science in Semiconductor Processing*, 6(3):339–347.

Scheiwe, A. C., Frank, S. C., Autenrieth, T. J., Bastmeyer, M., and Wegener, M. (2015). Subcellular stretch-induced cytoskeletal response of single fibroblasts within 3D designer scaffolds. *Biomaterials*, 44:186–194.

Schomerus, H. and Fal, V. I. (2013). Transport Signatures of Pseudomagnetic Landau Levels in Strained Graphene Ribbons. *Physical Review Letters*, 110(June):1–5.

Seo, J.-H., Zhang, K., Kim, M., Zhao, D., Yang, H., Zhou, W., and Ma, Z. (2016). Flexible phototransistors based on single-crystalline silicon nanomembranes. *Advanced Optical Materials*, 4(1):120–125.

Sercombe, D., Schwarz, S., Pozo-Zamudio, O. D., Liu, F., Robinson, B. J., Chekhovich, E. A., Tartakovskii, I. I., Kolosov, O., and Tartakovskii, A. I. (2013). Optical investigation of the natural electron doping in thin MoS_2 films deposited on dielectric substrates. *Scientific Reports*, 3:3489.

Serrano, J. R., Phinney, L. M., and Kearney, S. P. (2006). Micro-Raman thermometry of thermal flexure actuators. *Journal of Micromechanics and Microengineering*, 16(7):1128–1134.

Settnes, M., Garcia, J. H., and Roche, S. (2017). Valley-polarized quantum transport generated by gauge fields in graphene. *2D Materials*, 4(3).

Settnes, M., Leconte, N., Barrios-Vargas, J. E., Jauho, A. P., and Roche, S. (2016a). Quantum transport in graphene in presence of strain-induced pseudo-Landau levels. *2D Materials*, 3(3).

Settnes, M., Power, S. R., and Jauho, A. P. (2016b). Pseudomagnetic fields and triaxial strain in graphene. *Physical Review B - Condensed Matter and Materials Physics*, 93(3):1–8.

Shah, J., Combescot, M., and Dayem, A. H. (1977). Investigation of exciton-plasma mott transition in Si. *Physical Review Letters*, 38(25):1497–1500.

Shibuta, Y. and Elliott, J. A. (2011). Interaction between two graphene sheets with a turbostratic orientational relationship. *Chemical Physics Letters*, 512(4-6):146–150.

Shivayogimath, A., Whelan, P. R., MacKenzie, D. M., Luo, B., Huang, D., Luo, D., Wang, M., Gammelgaard, L., Shi, H., Ruoff, R. S., Bøggild, P., and Booth, T. J. (2019). Do-It-Yourself Transfer of Large-Area Graphene Using an Office Laminator and Water. *Chemistry of Materials*, 31(7):2328–2336.

Signorello, G., Karg, S., Björk, M. T., Gotsmann, B., and Riel, H. (2013). Tuning the light emission from GaAs nanowires over 290 meV with uniaxial strain. *Nano Letters*, 13(3):917–924.

Sinclair, M. (2000). A high force low area MEMS thermal actuator. *ITHERM 2000. The Seventh Intersociety Conference on Thermal and Thermomechanical Phenomena in Electronic Systems (Cat. No.00CH37069)*, 1:127–132.

Smausz, T., Kondász, B., Gera, T., Ajtai, T., Utry, N., Pintér, M., Kiss-Albert, G., Budai, J., Bozóki, Z., Szabó, G., and Hopp, B. (2017). Determination of UV–visible–NIR absorption coefficient of graphite bulk using direct and indirect methods. *Applied Physics A: Materials Science and Processing*, 123(10).

Smith, C. S. (1954). Piezoresistance effect in germanium and silicon. *Physical Review*, 94(1):42–49.

Snoke, D. (2008). Predicting the ionization threshold for carriers in excited semiconductors. *Solid State Communications*, 146(1-2):73–77.

Sookchoo, P., Sudradjat, F. F., Kiefer, A. M., Durmaz, H., Paiella, R., and Lagally, M. G. (2013). Strain Engineered SiGe Multiple- Quantum-Well Nanomembranes for Far-Infrared Intersubband Device Applications. *ACS Nano*, 7(3):2326–2334.

Soule, D. E. and Nezbeda, C. W. (1968). Direct Basal-Plane Shear in Single-Crystal Graphite. *Journal of Applied Physics*, 39(11):5122–5139.

Spataru, C. D. and Léonard, F. (2010). Tunable band gaps and excitons in doped semiconducting carbon nanotubes made possible by acoustic plasmons. *Physical Review Letters*, 104(17):1–4.

Splendiani, A., Sun, L., Zhang, Y., Li, T., Kim, J., Chim, C. Y., Galli, G., and Wang, F. (2010). Emerging photoluminescence in monolayer MoS_2. *Nano Letters*, 10(4):1271–1275.

Sreenivasulu, B., Ramji, B. R., and Nagaral, M. (2018). A Review on Graphene Reinforced Polymer Matrix Composites. *Materials Today: Proceedings*, 5(1):2419–2428.

Srikar, V. T., Swan, A. K., Ünlü, M. S., Goldberg, B. B., and Spearing, S. M. (2003). Micro-Raman measurements of bending stresses in micromachined silicon flexures. *Journal of Microelectromechanical Systems*, 12(6):779–787.

Staehli, J. L. (1976). Electron–hole droplet formation kinetics in pure germanium. *physica status solidi (b)*, 75(2):451–463.

Stegmann, T. and Szpak, N. (2016). Current flow paths in deformed graphene: From quantum transport to classical trajectories in curved space. *New Journal of Physics*, 18(5).

Steinhoff, A., Florian, M., Rösner, M., Schönhoff, G., Wehling, T. O., and Jahnke, F. (2017). Exciton fission in monolayer transition metal dichalcogenide semiconductors. *Nature Communications*, 8(1).

Suk, J. W., Kitt, A., Magnuson, C. W., Hao, Y., Ahmed, S., An, J., Swan, A. K., Goldberg, B. B., and Ruoff, R. S. (2011). Transfer of CVD-grown monolayer graphene onto arbitrary substrates. *ACS Nano*, 5(9):6916–6924.

Tas, N., Sonnenberg, T., Jansen, H., Legtenberg, R., and Elwenspoek, M. (1996). Stiction in surface micromachining. *Journal of Micromechanics and Microengineering*, 6(4):385–397.

Tiberj, A., Camara, N., Godignon, P., and Camassel, J. (2011). Micro-Raman and microtransmission imaging of epitaxial graphene grown on the Si and C faces of 6H-SiC. *Nanoscale Research Letters*, 6:1–9.

Torche, A., Mauri, F., Charlier, J.-C., and Calandra, M. (2017). First-principles determination of the raman fingerprint of rhombohedral graphite. *Phyical Review Materials*, 1:041001.

Tsoukleri, G., Parthenios, J., Papagelis, K., Jalil, R., Ferrari, A. C., Geim, A. K., Novoselov, K. S., and Galiotis, C. (2009). Subjecting a graphene monolayer to tension and compression. *Small*, 5(21):2397–2402.

Tyurnina, A. V., Bandurin, D. A., Khestanova, E., Kravets, V. G., Koperski, M., Guinea, F., Grigorenko, A. N., Geim, A. K., and Grigorieva, I. V. (2019). Strained Bubbles in van der Waals Heterostructures as Local Emitters of Photoluminescence with Adjustable Wavelength. *ACS Photonics*, 6(2):516–524.

Uchoa, B. and Barlas, Y. (2013). Superconducting states in pseudo-Landau-levels of strained graphene. *Physical Review Letters*, 111(4):1–5.

Ulrich, C., Anastassakis, E., Syassen, K., Debernardi, A., and Cardona, M. (1997). Lifetime of phonons in semiconductors under pressure. *Physical Review Letters*, 78(7):1283–1286.

Unuchek, D., Ciarrocchi, A., Avsar, A., Watanabe, K., Taniguchi, T., and Kis, A. (2018). Room-temperature electrical control of exciton flux in a van der Waals heterostructure. *Nature*, 560(7718):340–344.

Velasco, J., Zhao, Z., Zhang, H., Wang, F., Wang, Z., Kratz, P., Jing, L., Bao, W., Shi, J., and Lau, C. N. (2011). Suspension and measurement of graphene and Bi2Se3 thin crystals. *Nanotechnology*, 22(28).

Velasco, J. V., Liu, G., Bao, W., and Lau, C. N. (2009). Electrical transport in high-quality graphene pnp junctions. *New Journal of Physics*, 11.

Verbiest, G. J., Brinker, S., and Stampfer, C. (2015). Uniformity of the pseudomagnetic field in strained graphene. *Physical Review B - Condensed Matter and Materials Physics*, 92(7):1–7.

Vutukuru, M., Christopher, J., Pollock, C., Bishop, D., and Swan, A. (2019). Modeling and thermal metrology of thermally isolated MEMS electrothermal actuators for strain engineering of 2D materials in air. *Journal of Microelectromechanical Systems*, 28(3):550–557.

Wallace, P. R. (1947). The band theory of graphite. *Physical Review*, 71(9):622–634.

Wang, G., Dai, Z., Liu, L., Hu, H., Dai, Q., and Zhang, Z. (2016). Tuning the Interfacial Mechanical Behaviors of Monolayer Graphene/PMMA Nanocomposites. *ACS Applied Materials and Interfaces*, 8(34):22554–22562.

Wang, Q. H., Kalantar-Zadeh, K., Kis, A., Coleman, J. N., and Strano, M. S. (2012). Electronics and optoelectronics of two-dimensional transition metal dichalcogenides. *Nature Nanotechnology*, 7(11):699–712.

Wang, W. and Ma, X. (2020). Strain-Induced Trapping of Indirect Excitons in $MoSe_2$/WSe_2 Heterostructures . *ACS Photonics*, 7(9):2460–2467.

Wang, X., Cui, X., Bhat, A., Savage, D. E., Reno, J. L., Lagally, M. G., and Paiella, R. (2018). Ultrawide strain-tuning of light emission from InGaAs nanomembranes. *Applied Physics Letters*, 113(20).

Wang, X., Tantiwanichapan, K., Christopher, J. W., Paiella, R., and Swan, A. K. (2015). Uniaxial Strain Redistribution in Corrugated Graphene: Clamping, Sliding, Friction, and 2D Band Splitting. *Nano Letters*, 15(9):5969–5975.

Wang, Y., Cong, C., Qiu, C., and Yu, T. (2013). Raman spectroscopy study of lattice vibration and crystallographic orientation of monolayer mos2 under uniaxial strain. *Small*, 9(17):2857–2861.

Wood, J. D., Doidge, G. P., Carrion, E. A., Koepke, J. C., Kaitz, J. A., Datye, I., Behnam, A., Hewaparakrama, J., Aruin, B., Chen, Y., Dong, H., Haasch, R. T., Lyding, J. W., and Pop, E. (2015). Annealing free, clean graphene transfer using alternative polymer scaffolds. *Nanotechnology*, 26(5).

Xie, J., Inaba, T., Sugiyama, R., and Homma, Y. (2012). Intrinsic diffusion length of excitons in long single-walled carbon nanotubes from photoluminescence spectra. *Physical Review B - Condensed Matter and Materials Physics*, 85(8):085434.

Xu, X., Subbaraman, H., Chakravarty, S., Hosseini, A., and Covey, J. (2014). Flexible Single-Crystal Silicon Nanomembrane Photonic Crystal Cavity. *ACS Nano*, 8(12):12265–12271.

Yang, C., Gao, Y., Qin, C., Liang, X., Han, S., Zhang, G., Chen, R., Hu, J., Xiao, L., and Jia, S. (2019). All-optical reversible manipulation of exciton and trion emissions in monolayer WS_2. *Nanomaterials*, 10(23):1–12.

Yang, H., Zhao, D., Chuwongin, S., Seo, J. H., Yang, W., Shuai, Y., Berggren, J., Hammar, M., Ma, Z., and Zhou, W. (2012). Transfer-printed stacked nanomembrane lasers on silicon. *Nature Photonics*, 6(9):615–620.

Yang, S. Y., Oh, J. G., Jung, D. Y., Choi, H. K., Yu, C. H., Shin, J., Choi, C. G., Cho, B. J., and Choi, S. Y. (2015). Metal-etching-free direct delamination and transfer of single-layer graphene with a high degree of freedom. *Small*, 11(2):175–181.

Ye, W., Mukherjee, S., and MacDonald, N. C. (1998). Optimal shape design of an electrostatic comb drive in microelectromechanical systems. *Journal of Microelectromechanical Systems*, 7(1):16–26.

Ye, Y., Wong, Z. J., Lu, X., Ni, X., Zhu, H., Chen, X., Wang, Y., and Zhang, X. (2015). Monolayer excitonic laser. *Nature Photonics*, 9(11):733–737.

Yoon, D., Moon, H., Son, Y. W., Choi, J. S., Park, B. H., Cha, Y. H., Kim, Y. D., and Cheong, H. (2009). Interference effect on Raman spectrum of graphene on SiO_2/Si. *Physical Review B - Condensed Matter and Materials Physics*, 80(12):125422.

Yu, Y., Bataller, A., Younts, R., Yu, Y., Li, G., Puretzky, A., Geohegan, D., Gundogdu, K., and Cao, L. (2019). Room-Temperature Electron–Hole Liquid in Monolayer MoS_2. *ACS Nano*, 13(9):10351–10358.

Yu, Y., Yu, Y., Li, G., Puretzky, A. A., Geohegan, D. B., and Cao, L. (2020). Giant enhancement of exciton diffusivity in two-dimensional semiconductors. *Science Advances*, 6(51):4–11.

Zaghloul, M. R. and Ali, A. N. (2012). Algorithm 916: Computing the faddeyeva and voigt functions. *ACM Transactions on Mathematical Software*, 38(2).

Zardo, I., Yazji, S., Marini, C., Uccelli, E., Fontcuberta I Morral, A., Abstreiter, G., and Postorino, P. (2012). Pressure tuning of the optical properties of GaAs nanowires. *ACS Nano*, 6(4):3284–3291.

Zhai, L. X., Wang, Y., and Liu, J. J. (2012). Screening effect on the binding energy of the exciton in quantum wires. *Journal of Applied Physics*, 112(3):6–12.

Zhang, D. B., Seifert, G., and Chang, K. (2014a). Strain-induced pseudomagnetic fields in twisted graphene nanoribbons. *Physical Review Letters*, 112(9):1–5.

Zhang, G., Güell, A. G., Kirkman, P. M., Lazenby, R. A., Miller, T. S., and Unwin, P. R. (2016). Versatile Polymer-Free Graphene Transfer Method and Applications. *ACS Applied Materials and Interfaces*, 8(12):8008–8016.

Zhang, H., Wan, Y., Diego, S., and Wang, W. (2015). Interference effect on optical signals of monolayer MoS_2. *Applied Physics Letters*, 107(September):101904.

Zhang, X. P., Huang, C., and Cazalilla, M. A. (2017). Valley Hall effect and nonlocal transport in strained graphene. *2D Materials*, 4(2).

Zhang, Y. B., Tan, Y. W., Stormer, H. L., and Kim, P. (2005). Experimental observation of the quantum Hall effect and Berry's phase in graphene. *Nature*, 438(7065):201–204.

Zhang, Y. J., Oka, T., Suzuki, R., Ye, J. T., and Iwasa, Y. (2014b). Electrically Switchable Chiral Light-Emitting Transistor. *Science*, 344(May):725–729.

Zhang, Z., Hong, Y., Hou, B., Zhang, Z., Negahban, M., and Zhang, J. (2019). Accelerated discoveries of mechanical properties of graphene using machine learning and high-throughput computation. *Carbon*, 148:115–123.

Zhang, Z. M. (2000). Surface Temperature Measurment of Optical Techniques. *Annual Review of Heat Transfer*, 11:351–411.

Zhou, L., Wang, Y., and Cao, G. (2013). Estimating the elastic properties of few-layer graphene from the free-standing indentation response. *Journal of Physics Condensed Matter*, 25(47).

Zhu, S., Huang, Y., Klimov, N. N., Newell, D. B., Zhitenev, N. B., Stroscio, J. A., Solares, S. D., and Li, T. (2014). Pseudomagnetic fields in a locally strained graphene drumhead. *Physical Review B*, 90(7):075426.

Zhu, S., Stroscio, J. A., and Li, T. (2015). Programmable Extreme Pseudomagnetic Fields in Graphene by a Uniaxial Stretch. *Physical Review Letters*, 115(24):245501.

Zhu, Y. and Chang, T.-H. (2015). A review of microelectromechanical systems for nanoscale mechanical characterization. *Journal of Micromechanics and Microengineering*, 25(9):93001.

Zhu, Y., Corigliano, A., and Espinosa, H. D. (2006). A Thermal Actuator for Nanoscale In Situ Microscopy Testing: Design and Characterization. *Journal of Micromechanics and Microengineering*, 16(2):242–253.

Zhu, Y. and Espinosa, H. D. (2005). An electromechanical material testing system for in situ electron microscopy and applications. *Proceedings of the National Academy of Sciences*, 102(41):14503–14508.

Zipfel, J., Kulig, M., Perea-Causín, R., Brem, S., Ziegler, J. D., Rosati, R., Taniguchi, T., Watanabe, K., Glazov, M. M., Malic, E., and Chernikov, A. (2020). Exciton diffusion in monolayer semiconductors with suppressed disorder. *Physical Review B*, 101(11):1–20.

CURRICULUM VITAE